Spray Deposition for Plastic Electronics

Kirsty Ann Roy

Imperial College London

Department of Physics

Submitted for the degree of Doctor of Philosophy

January 4, 2017

I declare that the contents of this thesis are a result of my own work at Imperial College London and that, except where specific reference is made, the contents of this thesis has not been submitted, either wholly or in part, to satisfy any degree requirement at this or any other university.

Kirsty Ann Roy

Acknowledgements

Firstly I'd like to thank my supervisor Dr. Martyn McLachlan in particular for paying my wage, finding me somewhere to live and providing beer at any given opportunity. I would also like to thank the McLachlan group for their support and friendly faces when I first joined Imperial.

The work presented in this thesis would not have been possible without the guidance and resources of the de Mello group, to whom I am truly thankful. In particular James, for his help with all things concerning design and construction and for patiently helping me learn how to code. I can only imagine how painful a process this must have been. Thank you Tom for teaching me the magical ways of a chemistry lab and for your daily support and much appreciated words of advice. Thanks also to Siva, Wenmin and Baz for sweet potato fries and mayonnaise in hbar.

I am hugely indebted to Simon Turner, who managed to translate my highly specific, non-technical design requirements into finished, functional products. Neil was somewhat of a savior during the final stages of my Phd, participating in many device based discussions and providing essential help with device fabrication.

For all the fun times and for making the tough times bearable, thanks to the friends I've made on the DTC, especially Chaz, Matt and Jeeves. Thanks also to Alex for being an awesome friend and scientist. Fond memories of our trips to American Apparel, posh birthday lunches, and dancing and singing everywhere (without fail) will remain with me forever.

Thanks to my parents Sarah and Roger, who have been unfailingly supportive and encouraging over the years, and to my sister Hayley and the puppies Buzz and Izzie

for providing essential cuddles and emotional support. Finally thanks to John who has probably experienced the worst of ”writing-up Kirsty” without much reward. I look forward to our expanding future.

Abstract

Spray deposition is a promising technique for the solution processing of plastic electronic devices due to its potential for high-speed, large-scale device fabrication using low capital cost equipment. Most recent reports of spray-deposited electronic devices have used ultrasonic systems for film deposition to minimise surface roughness, but such systems suffer from low materials throughput, and are consequently ill-suited to industrial manufacturing. Gas-driven spray-heads enable higher throughput materials delivery but can result in an unacceptably rough film due to the large, broadly distributed droplet sizes that are often generated and the hard-impact nature of the deposition process.

This thesis describes a new automated gas-driven spray coater for the controlled deposition of a broad variety of solution processed electronic materials. It is specifically suited to the deposition of polymer films such as poly(3-hexylthiophene) (P3HT), overcoming many of the usual disadvantages of conventional gas-driven spray coaters. Key features of the system include: a novel, high performance 3D-printed spray-head for the generation of ultrafine sprays; full three-dimensional position and velocity control of the spray-head; integrated temperature control; and independent control of solution and gas flow rates.

To determine the optimum solution composition for spray-deposition of P3HT films, the aggregation and gelation dynamics of various P3HT/o-xylene solutions were first investigated by static light scattering. On the basis of these measurements, we conclude that dilute solutions (with polymer concentration $<$5 mg/ml) of low ($\leq$20 kg/mol) molecular weight polymer containing a small amount of a secondary solvent are optimal for avoiding gelation and clogging of the spay-head. For higher weight material, heating of the solution is necessary to avoid gelation.

The thesis also describes the development of an optical profiling technique for the characterisation of polymer films, which provides a fast method for quantitatively characterising the uniformity of large-area, thin polymer films. Using this technique, we were able to confirm that the spray-deposition system yields high quality, thin semiconducting polymer films, allowing for the controlled fabrication of active layers in organic photovoltaic devices from non-chlorinated solvents. The influence of solution composition and deposition variables such as gas pressure, solvent composition and substrate temperature were investigated, and optimised conditions for the deposition of high quality (device-grade) thin P3HT films were thereby identified.

A maximum device efficiency of 4.0 % was achieved for the spray-deposited bulk heterojunction P3HT:fullerene films processed from xylene. The results indicate that, providing the active layer is continuous, high device efficiency may be achieved even with relatively rough films, spray-coated from non-chlorinated processing solvents.

Contents

Acknowledgements **vii**

Abstract **ix**

1 Introduction **1**

1.1 Organic electronics 1

1.2 Solution processing of electronic materials 2

1.3 Spray coating 5

1.3.1 Atomisation 9

1.3.2 Surface tension and solution spreading 14

1.3.3 Drop impact 22

1.4 Drying of thin films and droplets 25

1.4.1 Evaporation rates of drops 26

1.4.2 Pattern formations in drying films and droplets 28

1.5 Summary 35

2 Design and characterisation of an automated pressurised spray deposition rig **37**

2.1 Design of a spray-head for the controlled deposition of semiconducting polymer solutions 38

2.2 Droplet characterisation by optical microscopy 42

2.3 Influence of the nozzle parameters on droplet size distribution 45

2.3.1 Carrier gas velocity 45

2.3.2 Solution flow rate 48

2.3.3 Capillary size 50

2.3.4 Pressure and ultrasonic spray: a rough comparison 51

2.4 Development of a spray-deposition rig 52
  2.4.1 Rig design 52
  2.4.2 Automating spray deposition 55
  2.4.3 Motor characterisation 60
  2.4.4 Hotplate characterisation 61
2.5 Summary 64

3 Characterising spray-deposited polymer films 65

3.1 Optical microscopy 65
3.2 Atomic force microscopy 67
3.3 Optical profiling of polymer films 69
  3.3.1 Measurement principle 69
  3.3.2 Design of an optical profiling rig 71
  3.3.3 Evaluation of the measurement accuracy 79
  3.3.4 Spin coated polymer films 81
  3.3.5 Reproducibility of spray deposited polymer films 84
  3.3.6 Large area uniformity of spray-deposited polymer films 84
  3.3.7 Drying patterns of drop-cast polymer films 84
  3.3.8 Summary 86

4 Spray-deposition of organic semiconductor films 88

4.1 Ink composition 88
  4.1.1 Gel temperature measurement 89
  4.1.2 Molecular weight 90
  4.1.3 Concentration 94
  4.1.4 Use of a secondary solvent 95
4.2 The effect of ink composition on film uniformity 98
  4.2.1 Molecular weight 98
  4.2.2 Concentration 102
  4.2.3 Co-solvent systems 108
4.3 The effect of spray parameters on film uniformity 111
  4.3.1 Carrier gas flow rate 111
  4.3.2 Solution flow rate 113

4.3.3 Raster speed 117
4.3.4 Temperature 119
4.4 Summary 122

5 Organic photovoltaics 124
5.1 Organic heterojunctions 124
5.2 Current-voltage characteristics 127
5.2.1 Dark conditions 127
5.2.2 Under illumination 129
5.3 Characterising device performance 130
5.4 Loss mechanisms 131
5.5 Spray-deposited organic bulk heterojunction solar cells 132
5.6 OPV fabrication 135
5.7 Characteristics of spray-deposited P3HT:PCBM blends 137

6 Conclusions and Further Work 145
6.1 Conclusions 145
6.2 Further optimisation of spray-deposited polymer films 148
6.3 Exploiting the functionality and additional applications of the spray-rig 148
6.4 Combining polymer synthesis with spray deposition 149

References 151

7 Appendix 1: Molecular weight distribution 165

8 Appendix 2: Arduino code for spray automation 167
8.1 Main controller: Arduino Yun 167
8.2 Secondary controller: Arduino Uno 177
8.3 Hotplate controller: Arduino Uno 184

List of Figures

1.1 The molecular structure of (a) o-xylene, the processing solvent used in this thesis and (b) poly(3-hexylthiophene), the semiconducting polymer used in this thesis. 5

1.2 Schematic of the atomisation process for ultrasonic and gas-driven spray-heads. 7

1.4 Overview of the film-formation process of spray-deposition, adapted from [24]. 9

1.5 A schematic (a) and photograph [27] (b) showing the break-up of a liquid cylinder into droplets. 10

1.6 Photographs and schematics showing the atomisation of a liquid cylinder in an air stream. Drop sizes are much smaller than the jet diameter and break-up starts at the nozzle exit. (a) Shows the break-up of dyed water jet, surrounded by a coaxial sheath of fast-flowing air, adapted from [33]. (b) Shows a schematic of the same process, adapted from [33]. (c) Shows a close-up of the droplet formation process due to collapse of a ligament, taken from [34]. 12

1.7 Competing pressures during atomisation. 13

1.8 Schematic of a liquid droplet resting on a substrate. Gravitational forces are weak for a small droplet so the surface of the droplet takes on a spherical cap shape. The contact angle θ is defined by the balance of interfacial forces. 15

1.9 A schematic demonstrating how the surface energy of an interface is determined by: the adhesive forces between the liquid and the solid (a) and the cohesive forces within the liquid (b). 18

1.10 Time-lapse photographs showing different outcomes that can occur when a droplet impacts on a dry surface. Taken from [42] 23
1.11 Evaporation modes of sessile droplets on a surface. Left: Pinning leads to evaporation at constant contact area. Right: receding leads to evaporation at constant contact angle. 26
1.12 Droplet evaporation. (a) Volume change of a sessile water drop during evaporation in pinning mode (blue) and in receding mode (red dashed), taken from [49]. Pinned droplets evaporate faster than receding droplets. (b) Probability of escape for vapour molecules at two different sites on the surface of a droplet for diffusion-controlled evaporation. The random trajectory of a vapour molecule is more likely to result in a return to the surface if the starting point is far away from the edge of the droplet. Adapted from [50]. 27
1.13 (a) ring deposit of a dried coffee droplet, taken from [55]. (b) schematic of the outward evaporation-induced flow inside a sessile droplet and the resultant material distribution of a dried deposit. An internal flow is generated inside the droplet as a result of evaporation that carries the fluid towards the edges. 29
1.14 A plot showing how the height, ζ, of the final droplet shape varies with the position, ξ, of the gelation region, for three different ratios, Φ, of solution concentration in the liquid phase to solution concentration in the gel phase: 0.4, 0.6 and 0.8, given by equation 1.45 and taken from [61] 30
1.15 Time-dependent velocity fields of capillary vs Marangoni flows, taken from [66]. Marangoni flow produces an inward flow that counters the outward evaporation-induced flow for sessile droplets during the pinned stage. 32
1.16 A schematic of pattern formation as a result of solution dewetting. (left) The "orange peel" effect, caused by the stick-slip behaviour of a lightly pinned droplet as a result of mechanical instabilities at the droplet edge as it dries. (right) "Mountain" formation caused by the inward flow of solute as a result of the droplet receding droplet as it dries. 33

1.17 A schematic to show skin formation and buckling. (left) Thin gel-like skin formation caused by the rapid evaporation of solvent from the surface of a pinned droplet. (right) Subsequent buckling of the skin layer due to a decrease in pressure inside the droplet as it continues to dry. . 35

2.1 A schematic comparing the atomisation process in two common types of gas-driven spray-head. (a) a common pressure-driven spray-head where the solution and gas are mixed internally and (b) a coaxial spray-head where they are mixed externally. 39

2.2 Three dimensional rendering of the coaxial spray-head designed for the deposition of semiconducting polymer solutions. (a) Exterior image showing the detachable nozzle (b) cross-sectional image showing the position of the capillary and the path taken by the carrier gas before exiting the nozzle. 40

2.3 Front-on view of the spray-head, showing the narrow capillary protruding slightly from the orifice of the spray-head. 41

2.4 Optical microscopy images of a sparsely populated film of dried polymer droplets deposited via spray-deposition. (a) raw image and (b) an annotated version to demonstrate how each drop was identified and measured in imageJ. 43

2.5 Optical microscopy images of sparsely populated films of droplets deposited via spray-deposition, using different spay-head operating parameters. (a,b,c) raw images (d,e,f) annotated images. The images show the broad range of droplet sizes. 44

2.6 Photographs taken from ref [93], demonstrating the atomisation of a liquid cylinder using a coaxial spray-head by a carrier gas with velocities in the range 0-300 m/s. 46

2.7 Histograms showing droplet size distributions for dried P3HT polymer films obtained using different gas velocities/flow rates, with a constant liquid flow rate of 50 μL/min. The numbers at the top and bottom right hand corner of each histogram are the gas velocity in m/s and gas flow rate in Lpm, respectively. 47

2.8 Histograms showing the distribution of droplet diameter for different solution flow rates. The number at the top right hand corner of each histogram is the solution flow rate in μL/min. The gas flow rate and capillary diameter were fixed at 20 Lpm and 150 μm, respectively. . . . 49
2.9 Histograms showing the droplet size distributions for different capillary diameters at fixed gas and liquid flow rates of 20 Lpm and 50 μL/min. The number at the top right hand corner of each histogram is the capillary diameter in μm. 50
2.10 Histograms showing size distribution for droplets generated by my gas-driven spray-head (green) and an ultrasonic spray-head by sono-tek (red) [16]. 51
2.11 An annotated photograph of the spray-deposition rig. 53
2.12 Schematic of the x-y-z gantry used to manoeuvre the spray-head comprising (a) a main stage for x-control and (b) a secondary stage for y-z-control. The two stages were attached together in positions indicated by the red x. 54
2.13 The three modes of operation of the spray-deposition rig. (a) single-solution mode (b) multi-solution mode and (c) multi-spray-head mode. 55
2.14 A flowchart showing the program structure of the code used to automate the spray-deposition process. 59
2.15 Plots showing how the x-y positioning of the spray head can be used to create a variety of patterns including (a) a raster pattern and (b) a spiral. 60
2.16 A plot showing the distance of travel over which the velocity of the spray-head was constant, when operated at a constant acceleration of 12.7 cm/s^2, for velocities of 5, 10 and 18 cm/s. 61
2.17 (a) A photograph of the hotplate showing the recessed areas designed to secure the substrates. (b) A temperature map of the hotplate at 100 °C. 62
2.18 A plot showing the transient response of the hotplate during heating and cooling using optimised PID gain parameters. 63

3.1 Optical micrographs of two spray-deposited films, deposited using very different operating parameters. For images (a) and (b) the concentration of P3HT was 5 mg/ml, the solution flow rate was 50 μL/min, and the raster speed was 2.54 cm/s. For images (c) and (d) the concentration of P3HT was 20 mg/ml, the solution flow rate was 200 μL/min, and the raster speed was 0.254 cm/s. 66
3.2 A characteristic atomic force microscopy image of a spray-deposited film of P3HT, showing droplet-shaped surface features. 68
3.3 A schematic showing the loss of light intensity in passing through an infinitesimal slice of absorbing medium. 70
3.4 Thickness dependence of the optical absorbance of P3HT films at 470nm. Data is shown for films processed by spin coating from chloroform, toluene, chlorobenzene and dichlorobenzene. Taken from [100]. 71
3.5 A schematic of the system used to obtain spatially-resolved absorbance maps of large-area polymer films. (a) Setup for measuring the background image, Φ_{bck}. (b) Setup for measuring the sample image, Φ_{film}. . 72
3.6 The substrate (a), background (b), and dark (c) images obtained from the rig shown in figure 3.5. The three images are used to create an absorbance map (d) of the film via equation 3.8. 74
3.7 Histograms showing the distributions in absorbance for neutral density filters with optical densities of (a) 0.5 (b) 1.0 (c) 1.5 and (d) 2.0, calculated using equation 3.1, with 1, 10 and 50 averages. 76
3.8 A plot showing the standard deviation of the distributions in absorbance vs. the number of averages taken for each of the images used in the absorbance calculation. The data was obtained using a OD 1.0 neutral density filter. 77
3.9 Plots for neutral density filters showing how (a) the standard deviation and (b) the relative standard deviation of the absorbance distributions varies optical density, for 1, 10 and 50 averages. 78

3.10 Plots showing the filtered emission spectrum of the lamp, the absorption spectrum of the absorbing medium and the sensitivity of the (green) detector in the Pi camera (a) and the true absorbance and the estimated absorbance against normalised film thickness (b). 80
3.11 Absorbance distributions for spin-coated P3HT films of varying thickness, obtained by casting at different speeds from solutions of varying concentrations. 82
3.12 Plots showing the standard deviation (a) and relative standard deviation (b) of the absorbance distribution versus the mean optical density for the spin-coated films of P3HT. 83
3.13 Left: The distributions in absorbance for ten spray-coated films deposited using identical processing parameters. Right: Plots showing the (top) standard deviation and (bottom) relative standard deviation of the distribution for each film. 83
3.14 (a) Absorbance map of a large-area (2.6 cm x 2 cm) spray-coated film, each quartile was measured separately. (b) Absorbance distributions for each quartile of the film. Plots showing the mean optical density (c) and standard deviation (d) extracted from (b). 85
3.15 The substrate (a), background (b), and dark (c) images used to create 2D (d) and 3D (e) absorbance maps of a drop-cast film. 86

4.1 (a) Schematic of the instrument (developed by Dr. Siva Krishnadasan) used to measured the gel temperature of solutions. (b) A typical trace obtained using the light-scattering instrument, showing three regimes: (1) at the highest temperatures the polymer is in solution; (2) as the solution cools aggregation of solid nucleates occurs; (3) further cooling leads to gelation of the polymer solution. 91
4.2 Traces obtained using the light scattering instrument for 10 mg/ml solutions of P3HT (in o-xylene) with molecular weights of (a) 21 (b) 40 (c) 65 and (d) 90 kg/mol. The arrows on each graph indicate the onset of aggregation (OA), the onset of gelation (OG), and complete gelation (CG), where they could be determined. 92

4.3 A plot showing the temperatures at which aggregation (green squares) and gelation (red circles) begin, and gelation ends (purple diamonds), for molecular weights in the range 40-90 kg/mol. 93

4.4 Traces obtained using the light-scattering instrument for 90 kg/mol molecular weight P3HT solutions (in o-xylene) with polymer concentrations of (a) 5 (b) 10 (c) 15 and (d) 20 mg/ml. The arrows on each graph indicate the onset of aggregation (OA), the onset of gelation (OG) and complete gelation (CG), where they could be determined. 95

4.5 A plot showing the temperatures at which aggregation (green squares) and gelation (red circles) begin, and gelation ends (purple diamonds), for 90 kg/mol molecular weight P3HT and solution concentrations of 5-20 mg/ml. 96

4.6 Traces obtained using the light-scattering instrument for 10 mg/ml solutions of 90 kg/mol molecular weight P3HT (in o-xylene/indane mixtures) with indane concentrations of (a) 0 (b) 20 (c) 40 (d) 50 (e) 75 and (d) 100 %. The arrows on each graph indicate the onset of aggregation (OA), the onset of gelation (OG) and complete gelation (CG), where they could be determined. 97

4.7 A plot showing the temperatures at which aggregation (green squares) and gelation (red circles) begin, and gelation ends (purple diamonds), for 10 mg/ml concentrations of 90 kg/mol molecular weight P3HT in o-xylene with indane concentrations in the range 0-100 %. 97

4.8 Absorbance maps of drop-cast P3HT films deposited from 5 mg/ml solutions in o-xylene with molecular weights of (a) 20 (b) 40 (c) 65 and (d) 90 kg/mol. A clear shift in the drying pattern from coffee-stained to mound-shaped is evident as the molecular weight of the P3HT increases. 99

4.9 Absorbance histograms of films spray-deposited from 5 mg/ml solutions of P3HT (in o-xylene) with molecular weights in the range 20 to 90 kg/mol, using a solution flow rate of 200 μL/min, a gas flow rate of 20 Lpm, and a raster speed of 7.62 mm/s. The molecular weight of the P3HT in kg/mol is indicated at the top right hand corner of each histogram. 100

4.10 Plots showing how the mean optical density (a), the standard deviation (b) and the relative standard deviation (c) of each film varies with the molecular weight of P3HT. (Data extracted from distributions shown in figure 4.9). 101
4.11 Optical microscopy images of spray-coated films deposited from solutions of (a) 20 and (b) 90 kg/mol molecular weight P3HT in o-xylene. In both cases droplet-shaped surface features can be seen with "patchy" material distribution. 102
4.12 Absorbance maps of drop-cast films of 20 kg/mol (a-c) 40 kg/mol (d-f) 65 kg/mol (g-i) and 90 kg/mol (j-l) P3HT solutions in o-xylene, for different solution concentrations. 103
4.13 3D absorbance maps of drop-cast films deposited from solutions of 20 kg/mol molecular weight P3HT in o-xylene at polymer concentrations of 5 mg/ml (a) 10 mg/ml (b) and 20 mg/ml (c). The maps show a gradual transition from coffee-stained to mound-shaped film formation on increasing the concentration of the solution. 104
4.14 Absorbance histograms of films that were spray-deposited from solutions of 90 kg/mol molecular weight P3HT, using a solution flow rate of 200 μL/min, a gas flow rate of 20 Lpm, a raster speed of 10.16 mm/s and solutions concentrations in the range 1 to 7 mg/ml as indicated above each histogram. 105
4.15 Plots showing how the mean optical density (a) the standard deviation (b) and the relative standard deviation (c) of the absorbance distributions vary with increasing solution concentration. (d) shows the relative standard deviation versus the mean optical density. 106
4.16 Optical microscopy images comparing the surface morphology of spray-coated films deposited from solution concentrations of 5 mg/ml (a) 10 mg/ml (b) and 20 mg/ml (c). 107
4.17 Absorbance maps of drop-cast 90 kg/mol P3HT films deposited from 3 mg/ml o-xylene/indane solutions, of varying indane content. 109

4.18 Absorbance histograms of 90 kg/mol P3HT films that were spray-deposited from 3 mg/ml solutions, using a gas flow rate of 20 Lpm, raster speed of 7.62 mm/s, solution flow rate of 200 μL/min and indane concentration in the range 0-30 % as indicated at the top right hand corner of each histogram. 110

4.19 Plots showing how the mean optical density (a) the standard deviation (b) and the relative standard deviation (c) of the absorbance distributions of spray-deposited P3HT films varies with increasing indane concentration. 111

4.20 Left: absorbance histograms of 90 kg/mol P3HT films that were spray-deposited from 5 mg/ml solutions in o-xylene at room temperature, using a solution flow rate of 200 μL/min, raster speed of 12.7 mm/s and gas flow rate in the range 5-25 Lpm as indicated in the right top hand corner of each histogram. Right: the corresponding absorbance maps of each of the films. 112

4.21 Plots showing how the mean optical density (a) the standard deviation (b) and the relative standard deviation (c) of the absorbance distributions of spray-deposited films varies with gas flow rate. Data was extracted from figure 4.20 114

4.22 Absorbance histograms of 90 kg/mol P3HT films that were spray-deposited from 5 mg/ml solutions, using a gas flow rate of 20 Lpm, raster speed of 10.16 mm/s and solution flow rate in the range 50-400 μL/min as indicated above each histogram. 114

4.23 Plots showing how the mean optical density (a) the standard deviation (b) and the relative standard deviation (c) of the absorbance distributions vary with increasing solution flow rate. (d) shows how the relative standard deviation varies with respect to the mean optical density of each film. 115

4.24 Optical microscopy image showing the effect of solution "pooling" on a spray-deposited film. Pooling was caused by using a high solution flow rate of 800 μL/min. 116

4.25 Absorbance histograms of 90 kg/mol P3HT films spray-deposited from 5 mg/ml o-xylene solutions, using a solution flow rate of 200 μL/min, gas flow rate of 20 Lpm, and various raster speeds in the range 2.5-15.2 mm/s as indicated above each histogram. 117
4.26 Plots showing how the mean optical density (a) the standard deviation (b) and the relative standard deviation (c) of the absorbance distributions vary with increasing raster speed. (d) shows how the relative standard deviation varies with respect to the mean optical density of each film. . 118
4.27 Absorbance maps of drop-cast films deposited from 5 mg/ml o-xyelene solutions, using 90 kg/mol P3HT at substrate temperatures of (a) 20 (b) 40 (c) 60 (d) 80 (e) 120 and (f) 160 °C. 120
4.28 Left: absorbance histograms of 90 kg/mol P3HT films that were spray-deposited from 5 mg/ml solutions in o-xylene, using a solution flow rate of 200 μL/min, gas flow rate of 20 Lpm, raster speed of 12.7 mm/s, and substrate temperatures in the range 20-160 °C as indicated in the right top hand corner of each histogram. Right: the corresponding absorbance maps of each of the films. 121
4.29 Plots showing how the mean optical density (a) the standard deviation (b) and the relative standard deviation (c) of the absorbance distributions of spray-deposited P3HT films vary with increasing substrate temperature. 122

5.1 (a) Exciton dissociation into free charge carriers at the bulk heterojunction (b-c) A simple model of a bulk heterojunction organic solar cell, where the polymer/fullerene blend is presented as a single semiconductor, with its HOMO derived from the polymer and its LUMO from the fullerene. The organic layer is sandwiched between electrodes with differing work functions. At equilibrium, the Fermi levels of the electrodes equalise, thus developing a "built-in" electric field. 125
5.2 A schematic diagram illustrating the direction of current flow at various applied voltages, taken from [114]. 128
5.3 Current density vs. voltage (J-V) of a solar cell. 130
5.4 An equivalent circuit diagram for the photodiodes. 131

5.5 Substate patterns for the anode, ITO (a) and the cathode, Al (b) and a schematic showing the composite materials of the OPV device stack (c). 136
5.6 Absorbance histograms of 90 kg/mol P3HT films spray-deposited from 1.25 mg/ml o-xylene/ODT solutions, using a gas flow rate of 20 Lpm, raster speed of 5.1 mm/s and solution flow rates of (a) 100 (b) 125 (c) 150 and (d) 200 μL/min. Plots showing how the mean optical density (e) of the absorbance distributions vary with increasing solution flow rate and how the standard deviation (f) and the relative standard deviation (g) varies with respect to the mean optical density of each film. 138
5.7 Atomic force microscopy images of the spray-deposited active layers, each showing droplet-shaped surface features. 139
5.8 A plot showing the RMS roughness of each spray-deposited active layer as determined by AFM with respect to the mean optical density of the film. 139
5.9 Current density versus voltage curves for four devices with spray-deposited active layers of varying OD under illumination and in the dark (a,b). A table (below) showing the corresponding device parameters. 140
5.10 Plots showing how the (a) FF, (b) V_{OC}, (c) J_{SC}, (d) PCE and (e) R_{SH} of each device varies with the spray-deposited active layer thickness. (f) A plot showing how the J_{SC} of each device varies with the percentage of photons absorbed (determined from the mean optical density of each film) by each active layer. 141
5.11 The corrected photocurrent for the four 12 mm^2 devices of varying OD, whose "RAW" J-V characteristics are shown in figure 5.9. The corrected photocurrent of each device was calculated by subtracting the dark current from the photocurrent. 142
5.12 Plots showing the variation of (a) FF, (b) V_{OC}, (c) J_{SC} and (d) PCE with pixel area, using spray-deposited P3HT:PCBM active layers with an optimised optical density of 0.47. 143
5.13 J-V characteristics of the best (PCE) performing spray-coated device, and the corresponding device performance parameters. 144

7.1 Series of RI-SEC chromatograms for the various molecular weights of P3HT used in this thesis. 165

8.1 Schematic showing the electrical connections between the Arduino Yun and the motors responsible for the motion of the spray nozzle. [1] Arduino Yun. [2] EasyDriver, stepper motor drivers (Sprakfun). [3] Stepper motor responsible for motion along the *x*-axis. [4] Stepper motor responsible for motion along the *y*-axis. [5] Linear actuator (Firgelli) responsible for motion along the *z*-axis (RobotShop). 168

8.2 Schematic showing the electrical connections associated with the secondary controller. [1] Arduino Yun. [2] Secondary controller (Arduino uno). [3] 1.8″ Colour TFT LCD display (Adafruit). [4] Dual rate syringe pump (Harvard Apparatus). [5] Mass flow controller (Sierra). 177

8.3 Schematic showing the electrical connections between the Arduino Uno and the hotplate apparatus. [1] Arduino Uno. [2] Solid state relay. [3] Thermocouple Amplifier MAX31855 (Adafruit). 184

1 Introduction

1.1 Organic electronics

Organic electronics is a field of research concerned with the design, synthesis, characterisation, and application of semiconducting organic materials to electronic devices. Unlike conventional inorganic semiconductors, organic semiconductors are constructed from predominantly carbon-based small molecules or polymers. Their semiconducting properties arise from the delocalised pi bonding system between the constituent carbon atoms. Organic electronics has the potential to become one of the major technologies of the twenty-first century, by enabling flexible, light-weight devices that can be fabricated over large areas using low cost printing methods [1] - advantages that are unmatched by conventional inorganic technologies. Currently, this potential remains unrealised and, despite the vast amount of research to date, most organic electronic devices are still at a relatively early stage of technological development.

Organic materials have been successfully used as the active materials in a broad range of devices including light emitting diodes, transistors, solar cells and biosensors. Typical devices consist of layers of different electronic materials that are stacked sequentially. Individual layers may be formed from a single material or from several blended materials that together provide the desired combination of chemical, physical, mechanical and/or electronic properties. The appropriate choice of materials in each layer depends on the primary function of that layer within the device. For instance, the layer (or material within a layer) may inject or extract charges, transport holes or electrons, absorb or emit light (within a specific wavelength range), or act as an insulator or dielectric. Beyond organic semiconductors, there is a variety of other complementary printable electronic materials that can be incorporated into the ″organic device″, including semiconducting metal oxides (most notably the electron conductors ZnO and TiO_2, and the hole conductors ITO, V_2O_5, WO_3 and MoO_3 [2], carbon nanostructures (including carbon nanotubes and graphene) [3], and metallic nanostructures (including copper and silver nanowires) [4]). The effectiveness of a material in fulfilling its role within a layer/device depends on both the intrinsic properties of the material (relative to its neighbouring layers) and on the electrical, structural and morphological properties of the film it forms. These properties are often heavily influenced by the deposition process.

1.2 Solution processing of electronic materials

The realisation of ultra low cost organic electronic devices is dependent on the development of effective roll-to-roll ($R2R$) processing methods for depositing the layers in the device stack. Unlike conventional batch fabrication procedures, roll-to-roll processing allows for the continuous production of large-area devices and modules, using an uninterrupted sequence of inline processing steps (as few as possible), reducing fabrication costs. Solution-phase coating and printing methods are considered most amenable to roll-to-roll coating, although a few attempts have been made to extend evaporative methods to roll-to-roll coating [5].

The principle challenge in R2R coating is to find fast solution-phase deposition methods for each layer that are capable of providing ″high-quality″ films. Some of the requirements for the films are common to all of the layers in a device, e.g. homogeneity and the absence of pinholes; others are specific to the function of that layer and the materials used (e.g. the thickness, crystallinity, pattern resolution, surface morphology, surface topography and/or molecular orientation). The best choice of coating or printing technique for a given layer depends on both the process of film formation during deposition and the composition of the ″ink″ from which the layer is to be deposited, e.g. solute, solvent, molecular weight, concentration, viscosity.

Most solution-based film-forming techniques involve the evaporation of solvent, leaving behind a solid film of the solute. The simplest method for forming a film involves depositing a pool of solution on a substrate and allowing it to dry by evaporation (a technique known as drop-casting). However this approach is slow and the drying process leads to the formation of inhomogeneous films. A simple improvement is spin-coating, in which the solution is deposited onto a secured substate that rotates at typical speeds between 1000 and 5000 r.p.m [6]. Spin-coating provides remarkably uniform films with (route-mean square) roughnesses that can be less than 1 nm [7]. Whilst spin-coating is not amenable to roll-to-roll processing, the excellent uniformity it can deliver has led to its widespread use in small-scale device fabrication, where the principle concern is the uniformity of the deposition method (as opposed to its scalability). As such, spin-coated films and devices provide a useful standard against which films and devices made by other methods may be compared.

There are many film-forming techniques available that have already been developed for high volume, *R*2*R* processing of paper, plastic and textile materials. Several of these have been successfully used for fabricating organic devices. Some of the most promising *R*2*R* techniques for organic devices include: slot-die coating [8], gravure coating [9], spray coating [10] and screen printing [11]. Slot-die coating forces ink through a slot, onto a substrate. Gravure coating transfers ink from an engraved surface onto a substate. Screen printing uses a ″squeegee″ to transfer ink through a mesh, onto a substrate. And spray-coating atomises the ink solution into droplets, which are directed towards a substate.

Each of the above techniques places different constraints on the composition of the ink that can be reliably deposited (see table 1.1). For example screen printing is best suited to the deposition of thick layers from high viscosity, non-volatile solutions. Typical examples include metal inks (for electrodes) and insulating polymers (e.g. dielectric layers). Gravure and slot-die methods are better suited to the deposition of thin layers from low viscosity solutions. There are occasional reports of complete transistors or solar cells being fabricated by a single process such as screen printing [12], however the use of a single technique for depositing every layer results in inevitable compromises,

	Inkjet	Screen	Slot-die	Gravure	Spray
Resolution (μm)	>50	>100	~1000	>20	~1000
Layer thickness (μm)	1-500	10-500	10-250	5-80	1-500
Ink viscosity (cP)	1-40	500-50 000	10-10 000	50-200	10-1000
Maximum throughput (m^2s^{-1})	>50	>100	>1000	>100 000	>60 000

Table 1.1: Comparison of printing specifications for common printing methods taken from [13].

resulting in poor final device performance. It is likely that any industrial approach to fabricating devices will use a variety of deposition techniques for the different layers.

For most deposition techniques, it is essential to find good solvents for the material being printed, which is not always straight forward. Most semiconducting polymers for instance, exhibit poor solubility in common industrially accepted processing solvents [14]. Consequently, for the majority of reported organic devices, the active layer film has been cast from a chlorinated solvent such as chlorobenzene. In side by side comparisons, devices processed using chlorinated solvents typically perform better than those processed using less harmful (non-chlorinated) solvents such as toluene and xylene due to decreased surface roughness and improved nanoscale morphology. Furthermore, the poor solubility of organic semiconductors in non-chlorinated solvents can result in gelation of the solution, with the polymer forming large-scale aggregates that extend (percolate) through the entire liquid in the solution, resulting in a a solid-like gel. The tendency for non-chlorinated solutions to gel increases viscosity and causes clogging of printing machinery, limiting the range of viable processing solvents available. The continuing widespread use of chlorinated (and more generally halogenated) solvents in solution processing of organic devices is a major obstacle to large-scale, roll-to-roll manufacturing of organic devices at an industrial level, as strict environmental and safety regulations restrict the use of such solvents. For this reason, methods for solution processing electronic materials from non-chlorinated solvents are urgently needed.

The most commonly used, environmentally friendly solvents in the conventional (non-electronic) printing industry systems based on toluene or isomers of xylene. Xylenes

(a) o-xylene (b) P3HT

Figure 1.1: The molecular structure of (a) o-xylene, the processing solvent used in this thesis and (b) poly(3-hexylthiophene), the semiconducting polymer used in this thesis.

have a better solubility for organic semiconductors than toluene and are, therefore, usually preferred. For this reason, I have selected o-xylene as the solvent for the work described in this thesis. I have selected poly(3-hexylthiophene) (P3HT), one of the most prominent organic materials reported in organic photovoltaic literature [15], as a semiconducting polymer due to its ready availability in a wide range of molecular weights. It is likely however, that the broad results presented in this thesis are applicable to many other semiconducting polymer and solvent systems.

1.3 Spray coating

One technique that is of particular interest for organic electronics is spray-coating. Spray-coating entails the formation of a fine mist of droplets (an aerosol) from an ink solution, which is then directed towards the surface that is to be coated. In the ideal case, the wet droplets coalesce on the substrate to form a thin liquid film that subsequently dries into a continuous solid layer.

Fast processing speeds of up to 100 m/min [13], coupled with the low capital cost of the equipment, make spray coating an attractive technique for large-area roll-to-roll deposition. Spray-coating produces relatively little waste, unlike undirected techniques such as spin-coating or vapour deposition, where most of the material is lost to surrounding areas. It is also relatively insensitive to the nature of the surface it is coating, providing good coverage on both smooth and rough surfaces even if they are not particularly wettable. Furthermore, compared to other more widely studied *R*2*R* printing/coating techniques, ink preparation is typically simple since a wide range of ink viscosities can be tolerated (see table 1.1).

The two main methods for generating an aerosol rely on a high-pressure gas or ultrasonic vibrations to atomise or "nebulise" the liquid, as illustrated in figure 1.2. In a typical gas-driven system, a fast-moving stream of compressed gas creates a localised reduction in pressure across the outlet of a reservoir containing the printing ink at atmospheric pressure. The solution is nebulised as it exits the nozzle, and is further dispersed into a fine mist by the high velocity carrier gas, which serves the dual role of creating the spray mist and propelling the droplets to the target. In ultrasonic systems, the surface of the spray-head is made to vibrate at ultrasonic frequencies ($\sim$35 KHz) using a piezoelectric quartz crystal, driven by a sinusoidal drive voltage [16]. When liquid is deposited into the spray-head, standing waves of liquid are formed on its surface, with thin regularly spaced filaments of liquid protruding from the vibrating surface. For sufficiently large amplitude oscillations, the waves separate into droplets which are carried to the substrate by a gas flow. The gas flow is typically slower than that used in pressure-driven systems, resulting in lower impact deposition that may sometimes lead to smoother films.

The ink viscosity is an important parameter for both pressurised and ultrasonic systems. Higher solution viscosities require more energy to nebulise the solution (which reduces the maximum achievable flow rate), and influence the drying behaviour of the solution. There is therefore an upper limit on the solution viscosity that can be successfully sprayed. Higher viscosity solutions are also more likely to foul or clog the spray-head. Pressurised systems are typically more susceptible to such problems as nebulisation requires the ink to be forced through a small orifice where the risk of clogging is high [16]. Compared with other solution deposition techniques, however, the limitation on ink viscosity is rather minor, with typical acceptable viscosities lying in the range 10 to 1000 cP [13].

The volatility of the solvent is also an important consideration. If the solvent dries too quickly, the droplets may dry before reaching the substrate surface, a phenomena know

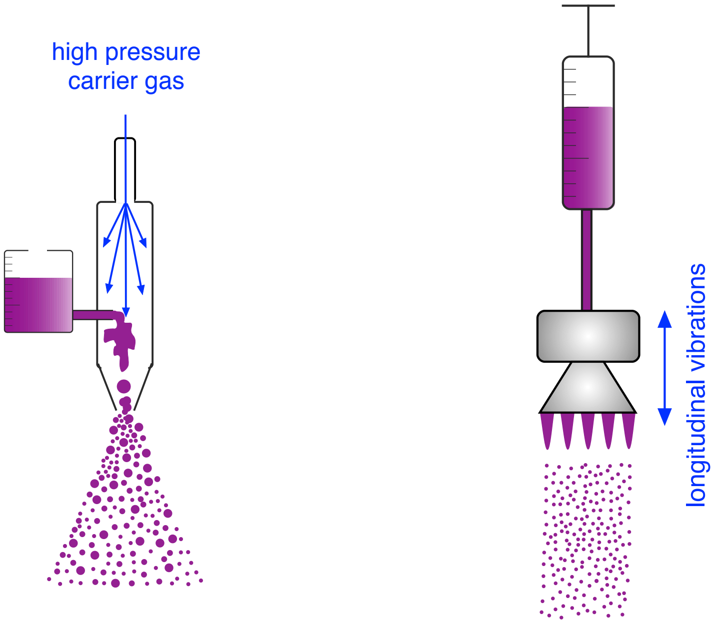

(a) Gas-driven spray-head

(b) Ultrasonic spray-head

Figure 1.2: Schematic of the atomisation process for ultrasonic and gas-driven spray-heads.

as ”spray-drying” [17]. If on the other hand the solvent dries too slowly, a puddle of liquid may form and become distorted under the pressure of the carrier gas, leading to poor film uniformity. This process is sometimes referred to as ”pooling” [18]. The rate of solvent evaporation depends on many environmental factors such as temperature, atmospheric pressure, and air movement. The challenge in spray-coating is to adjust these (and other) parameters to ensure that the material arrives at the substrate in solution, and thereafter dries at an appropriate rate to yield a high quality film.

Spray-coating has been widely applied in multiple areas including medicine, food, electronics, cosmetics, and textiles due to its low cost, high throughput and versatility. These same advantages also make it an attractive technique for organic electronics. Indeed, spray-coating has been widely deployed for the deposition of electronically active nano-particulates from suspension, e.g. carbon nanotubes [19], graphene [20], and metal nanoparticles [21] and metal nanowires [22]. It has also been widely used for the deposition of metal oxides from thermally labile precursor materials [23]. These

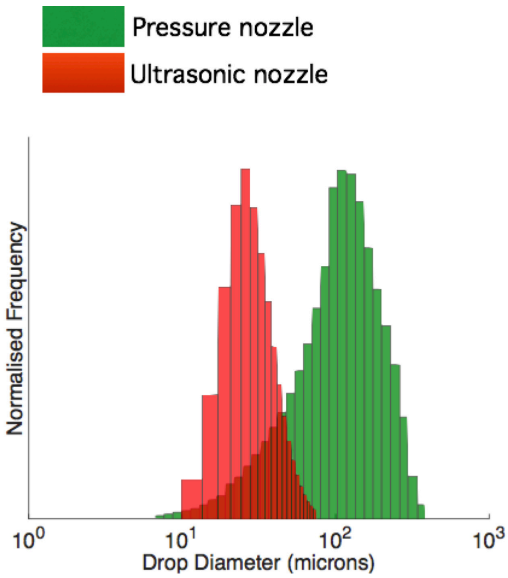

Figure 1.3: Typical droplet size distributions for ultrasonic and gas-driven spray-coating systems. It is often argued that ultrasonic systems generate smaller droplets, leading to more uniform films. Adapted from [16]

materials have been predominantly used for electrodes or electron/hole transport layers, which are relatively ”forgiving” with respect to smoothness, purity and microscopic ordering. There are far fewer examples of spray-coating being applied to the deposition of the active layer, where poor film quality can strongly impair device function. Applying spray-coating to polymer layers raises a number of additional challenges which are rarely encountered with particulate suspensions and arise in part from the high viscosities of polymer solutions, which can cause spray-head clogging and generate complex drying patterns. In this thesis I describe the development of a spray deposition system for polymer active layer, that is capable of delivering state-of-the-art performance in OPV devices, with efficiencies comparable to those obtained using spin-coating. A second aim of this thesis is to explore whether the widespread assumption that ultrasonic systems are better suited to electronic device fabrication than gas-driven systems is correct and whether smooth, device grade films can be prepared via gas-driven spray coating techniques. In the next section I describe in detail the principles of atomisation in a gas-driven system, with a view to developing an optimised gas-driven spray head that is capable of delivering comparable or superior performance to ultrasonic methods.

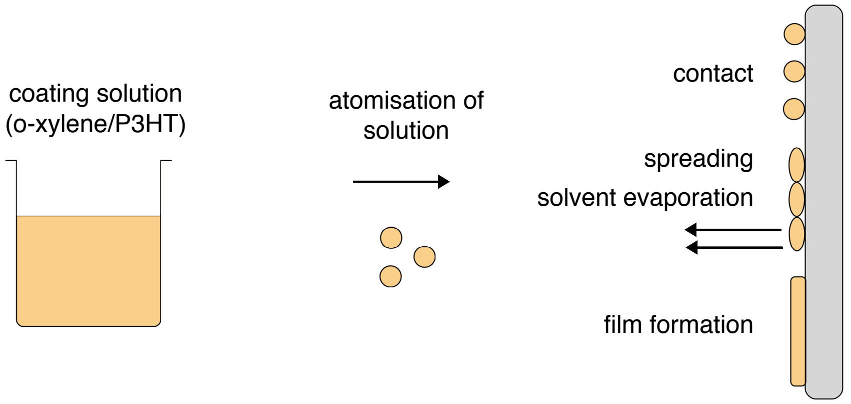

Figure 1.4: Overview of the film-formation process of spray-deposition, adapted from [24].

The overall process of film formation via spray-coating can be broken down into several steps as illustrated in figure 1.4. First the solution is atomised into a fine mist of droplets, which are then delivered to a surface using a carrier gas. Upon impacting the surface, the droplets spread and coalesce with neighbouring droplets, after which the solvent evaporates from the solution to form a dry, solid film. Each step is considered separately, in the rest of this chapter.

1.3.1 Atomisation

The size and shape of droplets in a spray mist can affect the surface roughness and uniformity of the deposited film [25, 26]. Smaller droplets($< 50\ \mu$m) are preferable for attaining a smooth film, but obtaining a narrow size distribution in which no large droplets are present can be difficult because the droplets are formed stochastically from disruption of a liquid stream. The method of droplet formation for ultrasonic systems is at face level a more controllable process than that of a gas-driven system, where liquid is sheared in all directions after being forced through a nozzle (see below). Hence, it has been widely argued that gas-driven systems are incapable of matching the narrow size and shape distributions of ultrasonic systems [16]. There are, however, good reasons why it would be beneficial to develop gas-driven systems for electronic materials deposition and in particular, polymer deposition. Such systems are better suited to high-viscosity solutions [17], and can handle higher solution flow rates than ultrasonic systems, allowing faster processing speeds [17].

The collapse of a liquid column

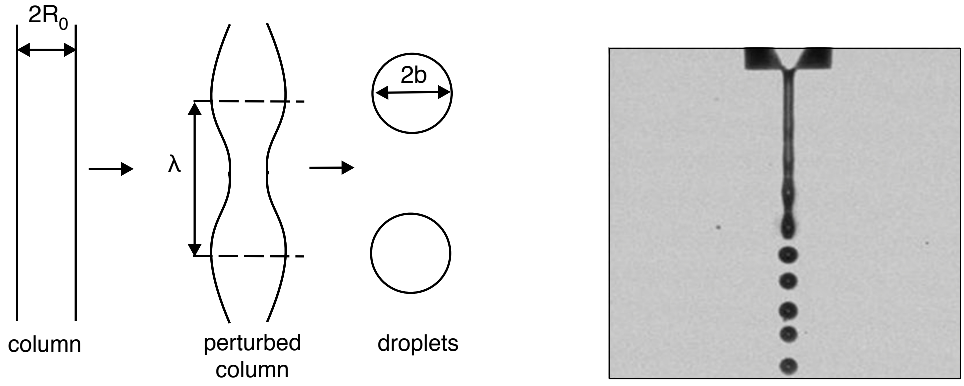

(a) (b)

Figure 1.5: A schematic (a) and photograph [27] (b) showing the break-up of a liquid cylinder into droplets.

The break-up of a liquid cylinder is the starting point for understanding the process of droplet formation in a spray-head. Edme Mariotte and Félix Savarat were the first to report that a free-flowing liquid column is inherently unstable, and will eventually break up into a train of droplets [28]. They observed that the column would develop periodic undulations, which would grow in size until the column broke up into discrete droplets (see figure 1.5a). This instability arises from a reduction in the total surface area (and hence surface energy) of a cylindrical column of liquid upon an axisymmetric (undulating) change in shape. This concept was first explained by Plateau [29] and more famously (and in greater detail) by Lord Rayleigh [30, 31].

Srolovitz and Safran [32] have provided a particularly simple geometric explanation of liquid column instability, which we repeat here. We first consider a long liquid cylinder of radius, R, whose surface is perturbed axisymmetrically with a wavelength, λ, eventually forming a row of droplets of radius, b (see figure 1.5a). The volume per wavelength of the cylinder can be equated with the volume of each droplet such that

$$\frac{4}{3}\pi b^3 = \pi R^2 \lambda \tag{1.1}$$

The droplet radius is therefore given by

$$b = \left(\frac{3R^2\lambda}{4}\right)^{\frac{1}{3}} \tag{1.2}$$

The free energy of a system is equal to its surface area multiplied by its surface tension, γ. Therefore the free energy, E_c, per wavelength of the initial cylinder is given by

$$E_c = 2\pi R\lambda\gamma \tag{1.3}$$

and the free energy, E_d, of the droplets is

$$E_d = 4\pi b^2\gamma \tag{1.4}$$

For the liquid column to break up into droplets, the cylinder must have a larger free energy than the row of droplets ($E_c > E_d$) from which it follows that

$$\lambda > \frac{9R}{2} \tag{1.5}$$

In other words, a liquid column is unstable to perturbations that have a wavelength greater than five times the radius of the column. By substituting equation 1.5 into equation 1.2, it follows that the minimum resulting droplet radius, b_{min}, is given by

$$b_{min} = \frac{3R}{2} \tag{1.6}$$

Hence the liquid column will spontaneously break up into discrete droplets whose radii are slightly larger than that of the column. From a practical perspective it is difficult to work with liquid streams narrower than 25 μm in radius, giving rise to a minimum droplet radius of $\sim$40 μm. This is at the upper limit of what can reliably be used for plastic electronics.

Atomisation in an air stream

To break up a droplet further, an external disrupting influence is required. The pressure caused by the disruption should be larger than the pressure inside the droplet, which has its origins in the stabilising influence of the surface tension, γ. From Laplace's law, the pressure due to the surface tension is given by

$$P_{ST} = \frac{2\gamma}{b} \tag{1.7}$$

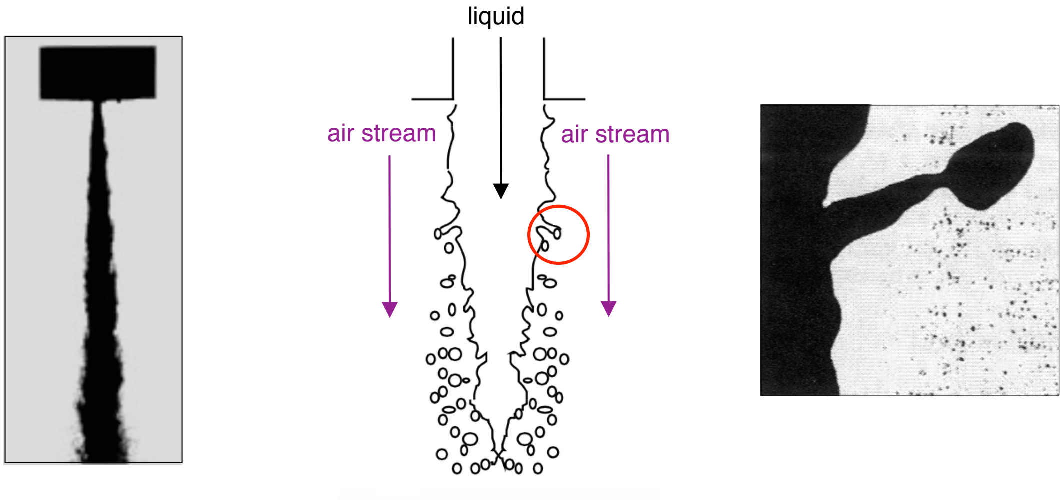

(a) (b) (c)

Figure 1.6: Photographs and schematics showing the atomisation of a liquid cylinder in an air stream. Drop sizes are much smaller than the jet diameter and break-up starts at the nozzle exit. (a) Shows the break-up of dyed water jet, surrounded by a coaxial sheath of fast-flowing air, adapted from [33]. (b) Shows a schematic of the same process, adapted from [33]. (c) Shows a close-up of the droplet formation process due to collapse of a ligament, taken from [34].

Interpreting the dynamic pressure, $P_{dynamic}$, of a flowing gas as its kinetic energy per unit volume, we can write

$$P_{dynamic} = \frac{1}{2}mv^2 \times n \tag{1.8}$$

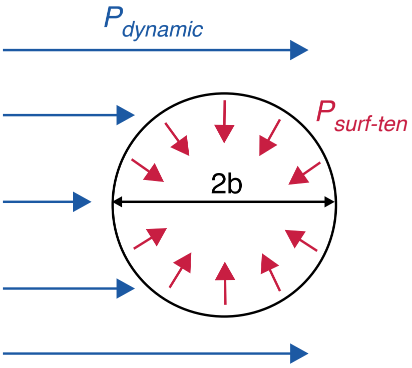

Figure 1.7: Competing pressures during atomisation.

where m is the mass of the gas molecules, n is the number of molecules per unit volume and v is the linear velocity of the gas molecules. Rewriting n in terms of the density, ρ, of the gas we obtain

$$P_{dynamic} = \frac{1}{2}\rho v^2 \tag{1.9}$$

Accounting for aerodynamic drag this becomes

$$P_{dynamic} = \frac{1}{2}\rho_{drag}\rho v^2 \tag{1.10}$$

where ρ_{drag} is the drag coefficient of the spherical droplet (which has a value of ∼1 in turbulent gas flow).

The shape of the droplet will distort and ultimately disrupt if the dynamic pressure is greater than the surface tension pressure ($P_{ST} = \frac{2\gamma}{b}$). Hence we can define a critical droplet size, $b_{critical}$ above which droplet break up is possible

$$P_{dynamic} \geq P_{ST} \rightarrow b_{critical} = \left(\frac{4\gamma}{\rho_{drag}\rho v^2}\right) \tag{1.11}$$

Liquid droplets in a high velocity gas flow will divide and continue to subdivide until they fall below the critical size. At this point the surface tension pressure (P_{ST}) is sufficiently high (due to the strong curvature of the surface) to maintain the spherical shape of the droplet and prevent further disintegration.

1.3.2 Surface tension and solution spreading

Following droplet formation and upon impacting the surface, the droplets must spread and coalesce with neighbouring droplets, to coat the surface of the substate. (For simplicity, the effect of droplet impact on film formation is discussed in the next section). The ink properties required for successful coating of a surface have been widely studied for conventional inks and coatings. Some properties such as the allowed range of viscosities and boiling points relate to the choice of coating technique, while others relate to the interaction of the ink with the surface of the substrate [35]. As noted above, spray coating is tolerant to a broad range of ink viscosities, and it is not difficult to find solvents with suitable boiling points. In practice, therefore, the ink/surface interactions tend to be the most important consideration when selecting a solvent and formulating an ink. In particular, the ink must wet the surface well so that individual droplets can form smooth, level films, and the wet drops must coalesce to form a continuous film that extends over the entire coating surface [24]. For coalescence to occur, droplets must be deposited in close proximity and then spread until they make physical contact with their immediate neighbours. Their ability to spread is determined by the degree to which they wet the surface. For these reasons, both the polymer ink and the substrate surface must be suitably matched.

When a small droplet (subject to negligible gravitational forces) is gently deposited on a flat substrate, the exposed surface will adopt a spherical geometry to minimise its surface area (and hence its surface energy). The resultant shape is known as a spherical cap (see figure 1.8). Using simple geometry, it is possible to relate the height h of the spherical cap to its in-plane radius a and contact angle θ:

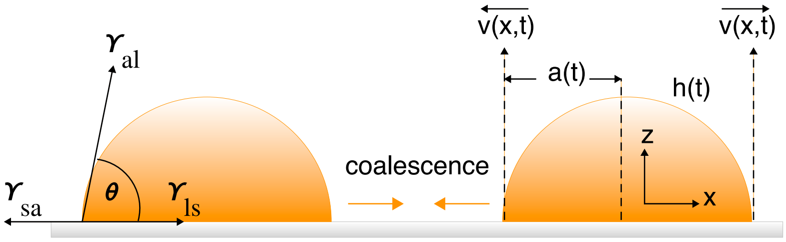

Figure 1.8: Schematic of a liquid droplet resting on a substrate. Gravitational forces are weak for a small droplet so the surface of the droplet takes on a spherical cap shape. The contact angle θ is defined by the balance of interfacial forces.

$$a(t) = h(t)\frac{\sin\theta}{1-\cos\theta} \tag{1.12}$$

where t, is the time, and which for small values of θ simplifies to

$$a(t) = h(t)\frac{\theta + \cdots}{1 - \left(1 - \frac{\theta^2}{2!} + \cdots\right)} \approx \frac{2h(t)}{\theta} \tag{1.13}$$

Assuming evaporation is slow compared to the spreading time, it can also be shown that $h(t)$ and $a(t)$ are related to the (fixed) droplet volume V by:

$$V = \frac{\pi}{2}h(t)a^2(t) \tag{1.14}$$

Immediately after the placement of the drop, the contact area between the droplet and the substrate will be small, resulting in a large contact angle. However, if the liquid readily wets the substrate, it will then spread to reduce the total surface energy of the system, with a increasing at the expense of h and θ. As the droplet spreads, three factors must be taken into account to understand how the surface energy changes: the increased contact area between the liquid and the substrate ΔA_{ls} (+ve); the reduced contact area between the substrate and the air ΔA_{sa} = -ΔA_{ls} (-ve); and the increased contact area between the liquid and the air ΔA_{la} (+ve). For an infinitesimal spreading of the droplet, the change in the surface energy ΔE is given by:

$$\Delta E = \gamma_{ls}\Delta A_{ls} + \gamma_{sa}\Delta A_{sa} + \gamma_{al}\Delta A_{al} \tag{1.15}$$

where γ_{ls}, γ_{sa} and γ_{al} are the interfacial energies (per unit area) at the liquid-solid, solid-air, and air-liquid interfaces respectively. The energy change (ΔE) may be rewritten as:

$$\Delta E = (\gamma_{ls} - \gamma_{sa})\Delta A_{ls} + \gamma_{al}\Delta A_{al} \tag{1.16}$$

For a spherical cap of fixed volume, it can be shown geometrically that

$$\Delta A_{al} = \Delta A_{ls}\cos\theta \tag{1.17}$$

Hence

$$\Delta E = (\gamma_{ls} - \gamma_{sa})\Delta A_{ls} + \gamma_{al}\Delta A_{ls}\cos\theta \tag{1.18}$$

The drop will continue to spread as long as ΔE is negative, i.e. as long as

$$\gamma_{ls} - \gamma_{sa} + \gamma_{al}\cos\theta \leq 0 \tag{1.19}$$

from which it follows that

$$\cos\theta \leq \frac{\gamma_{sa} - \gamma_{ls}}{\gamma_{al}} \tag{1.20}$$

Equilibrium is reached when the surface energy is minimised, and any further spreading would cause an overall increase in surface energy (due to an excessive increase in the contact area between the droplet and the air). Under these conditions, we obtain Young's equation relating the equilibrium contact angle θ_e to the three surface energies:

$$\gamma_{al} \cos\theta_e = \gamma_{sa} - \gamma_{ls} \tag{1.21}$$

Since surface energies are positive quantities (under normal circumstances), it follows that $\cos\theta_e$ is negative if $\gamma_{sa} < \gamma_{ls}$. In these circumstances a contact angle greater than ninety degrees is observed and the liquid is said to be *non*-wetting. If $\gamma_{sa} \geq \gamma_{ls}$, then $\cos\theta_e \geq 0$. The equilibrium angle is now smaller than ninety degrees, and the liquid is said to *partially* wet the substrate. From Young's equation, it is evident that larger values of γ_{al} correspond to smaller values of $\cos\theta_e$, i.e. to larger diameter droplets with larger equilibrium contact angles. All else being equal, liquids with low surface tensions therefore spread more than those with high surface tensions.

When $\theta_e = 0$ complete wetting occurs, and the liquid spreads out into a thin microscopic film of large surface area. It follows from Young's equation that complete wetting occurs when

$$\gamma_{al} = \gamma_{sa} - \gamma_{ls} \tag{1.22}$$

or

$$\gamma_{sa} - \gamma_{ls} - \gamma_{al} = 0 \tag{1.23}$$

In practice, complete wetting of a liquid on a dry substrate will occur whenever

$$\gamma_{sa} - \gamma_{ls} - \gamma_{al} \geq 0 \tag{1.24}$$

and it is convenient to define a "spreading coefficient" [36]

$$S = \gamma_{sa} - \gamma_{ls} - \gamma_{al} \tag{1.25}$$

Complete wetting occurs for all positive values of S, with larger values of S promoting wider spreading of the liquid. (Note, even with complete wetting, the liquid cannot spread indefinitely since the final liquid film has a finite thickness).

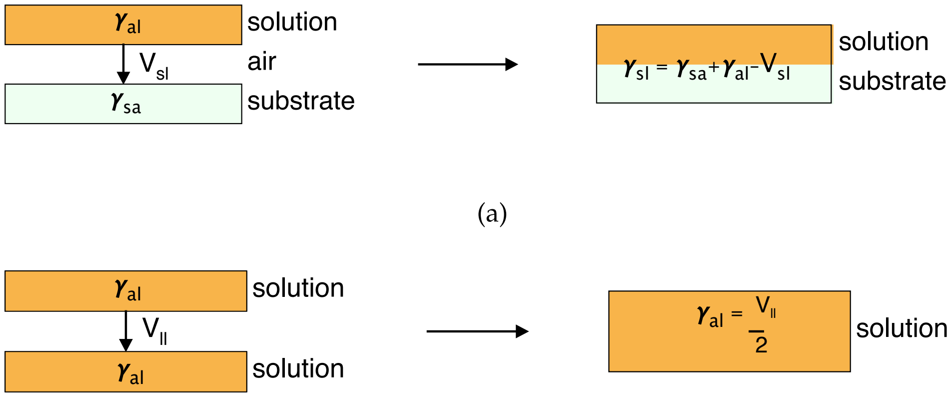

(a)

(b)

Figure 1.9: A schematic demonstrating how the surface energy of an interface is determined by: the adhesive forces between the liquid and the solid (a) and the cohesive forces within the liquid (b).

The spreading parameter, S, can be rewritten in terms of adhesive forces between the liquid and solid and cohesive forces within the liquid. To do this, we start by considering a solid and a liquid that are separated by an air gap (shown in figure 1.9a). The total surface energy (per unit area) will be γ_{sa} + γ_{al}. If the liquid and solid are now brought into contact, attractive Van der Waals forces will lower the total surface energy by amount $-V_{sl}$ per unit area. The total surface energy of the solid-liquid interface will therefore be

$$\gamma_{sl} = \gamma_{sa} + \gamma_{al} - V_{sl} \tag{1.26}$$

In a similar way, when two liquids are brought together, attractive forces between the liquid molecules will lower their surface energy by an amount $-V_{ll}$ (shown in figure 1.9b). Starting with a surface energy per unit area of $2\gamma_{al}$ for the separated liquids, we finish up with zero interfacial energy, and we can therefore write:

$$0 = 2\gamma_{al} - V_{ll} \rightarrow \gamma_{al} = \frac{V_{ll}}{2} \tag{1.27}$$

Substituting equations 1.26 and 1.27 into equation 1.25 we obtain:

$$S \geq 0 \rightarrow \left[\gamma_{sl} - \frac{V_{ll}}{2} + V_{sl}\right] - \gamma_{sl} - \frac{V_{ll}}{2} \geq 0 \rightarrow V_{sl} \geq V_{ll} \tag{1.28}$$

In other words for *complete* wetting to occur, the adhesive energy, V_{ls}, per unit area between the solid and liquid must outweigh the attractive energy, V_{ll}, per unit area between the liquid molecules.

Complete wetting typically occurs when depositing onto "high-energy" surfaces formed from "hard" solids with strong covalent, ionic or metallic bonds [37]. Typical surfaces energies for such materials lie in the range 500 to 5000 ergs/cm^2 (1 erg/cm^2 = 10^{-7} J/cm^2) [38]. Glass substrates and metal oxide layers are the most frequently encountered high energy surfaces in organic device fabrication. Plastic substrates and (previously deposited) organic layers have low surface energies of order 10 ergs/cm^2, meaning wetting is typically only partial. For partial wetting, $0 \leq \cos\theta_e \leq 1$, and it follows from equation 1.21 (Young's equation) that

$$0 \leq \frac{\gamma_{sa} - \gamma_{sl}}{\gamma_{al}} \leq 1 \tag{1.29}$$

Hence, substituting equations 1.26 and 1.27 into equation 1.29, we obtain

$$0 \leq \frac{V_{sl} - \frac{1}{2}V_{ll}}{\frac{1}{2}V_{ll}} \leq 1 \tag{1.30}$$

which re-arranges to give

$$\frac{1}{2} \leq \frac{V_{sl}}{V_{ll}} \leq 1 \tag{1.31}$$

Hence, the condition for partial wetting is that the attractive solid-liquid interactions, V_{sl}, should be at least half the value of the (attractive) liquid-liquid interactions, V_{ll}. Again, it is clear that a liquid with low interfacial tension due to weak intermolecular bonding will more readily wet a surface than one with high interfacial tension.

To a first approximation the Van der Waals couplings V_{sl} and V_{ll} are proportional to the polarisabilities of the solid, α_s, and liquid, α_l [35].

$$V_{ls} = \kappa \alpha_l \alpha_s \tag{1.32}$$

$$V_{ll} = \kappa \alpha_l \alpha_l \tag{1.33}$$

where the proportionality constant κ is approximately the same in both cases. Hence it follows from equation 1.31 that for partial wetting

$$\alpha_l \leq 2\alpha_s \tag{1.34}$$

Hence, since from equation 1.27, $\gamma = \frac{V_{ll}}{2}$, we obtain

$$\gamma_c^{partial} \leq 2\kappa\alpha_s^2 \tag{1.35}$$

At this level of approximation, it follows that there is a critical value, $\gamma_c^{partial}$, of the surface tension for each substrate material that depends only on the properties of the solid surface. Providing the liquid has a surface tension below this critical value, the liquid will partially wet the surface. Following an equivalent argument, we find that complete wetting is obtained when the surface tension is lower than a critical value γ_c^{full} where

$$\gamma_c^{full} \leq \frac{1}{2}\kappa\alpha_s^2 \tag{1.36}$$

As the surface tension of the liquid is reduced (e.g. by changing solvent or addition of surfactants) from $\gamma_c^{partial}$ to γ_c^{full} the contact angle reduces steadily until complete wetting is obtained.

The wettability of the organic solvents used to process electronic materials is usually sufficiently good for solution spreading on a glass substrate. Relative to water, which has a high surface tension of ∼72 mN/m (at 25°C), o-xylene has an extremely low surface tension of ∼30.1 mN/m (at 20°C). This is slightly lower than that of the commonly used chlorinated solvent, orthodichlorobenzene (oDCB), which has a surface tension of 36.7 mN/m (at 25°C). The choice of processing solvent used in this thesis, therefore, promotes droplet spreading which increases the likelihood of droplet coalescence and film formation during spray-deposition.

Hysteresis in the contact angle

From the above discussion, we expect the same final contact angle irrespective of whether the droplet is spreading (advancing) or contracting (receding). In practice, for most real surfaces, different contact angles are observed for the two cases, with the advancing and receding angles being respectively larger and smaller than the equilibrium angle [39]. To understand this, we return to equation 1.18, from which it follows that, at a contact angle θ away from equilibrium, the "driving force", F, for droplet spreading is given by

$$F = -\frac{\Delta E}{\Delta A_{ls}} = -(\gamma_{ls} - \gamma_{sa} + \gamma_{al}\cos\theta) \tag{1.37}$$

which using equation 1.21 reduces to

$$F(\theta) = \gamma_{al}(\cos\theta_e - \cos\theta) \tag{1.38}$$

For a real surface that is rough and/or chemically inhomogeneous, frictional forces are present that oppose the motion of the droplet. The droplet will therefore continue to spread or recede only as long as the driving force $F(\theta)$ is large enough to overcome the frictional force $R(\theta)$, i.e.

$$F(\theta) = |\gamma_{al}(\cos\theta_e - \cos\theta)| > R(\theta) \tag{1.39}$$

It follows that a spreading (advancing) droplet that starts off with an initial contact angle in excess of the equilibrium contact angle ($\theta > \theta_e$) will spread to a final angle θ_a that is greater than the equilibrium contact angle by a finite (non-zero) amount so as to ensure that $|(\cos\theta_e - \cos\theta)|$ is of sufficient magnitude to satisfy equation 1.40. By contrast, a receding droplet that starts off with an initial contact angle θ_r that is smaller than the equilibrium contact angle will contract to a final angle that is smaller than the equilibrium contact angle by a finite (non-zero) amount. Hence,

$$\theta_r < \theta_e < \theta_a \tag{1.40}$$

The spreading of a droplet on a surface affects the rate of solvent evaporation from the solution and the drying patterns that occur as a result (as discussed in detail in section 1.4). Thus, as I will discuss later, hysteresis in the contact angle is an important consideration for the formation of smooth thin films.

1.3.3 Drop impact

In drop-casting, the liquid is placed onto the substrate gently and then spreads under the influence of the competing interfacial forces, as discussed in the previous section. In spray-coating, by contrast, the droplet is driven to the substrate using a carrier gas of a known velocity v_{gas}. In principle, this can be beneficial for achieving a uniform film since it can enhance droplet spreading and so increase the likelihood of coalescence. In practice, however, the impact of the drop on the surface can result in a variety of different outcomes depending on factors such as the velocity and direction of the impact relative to the surface, the drop size, the properties of the liquid (namely density, viscosity and surface tension) [40], and the roughness and wettability of the solid surface [41]. The various outcomes, which are shown in figure 1.10, can strongly influence the roughness of the final film.

The spreading of the droplet after impact can be separated into two stages: a kinematic stage and a secondary spreading [40]. During the kinematic stage, the kinetic energy of the droplet is partly dissipated by viscous forces in the liquid (that raise the

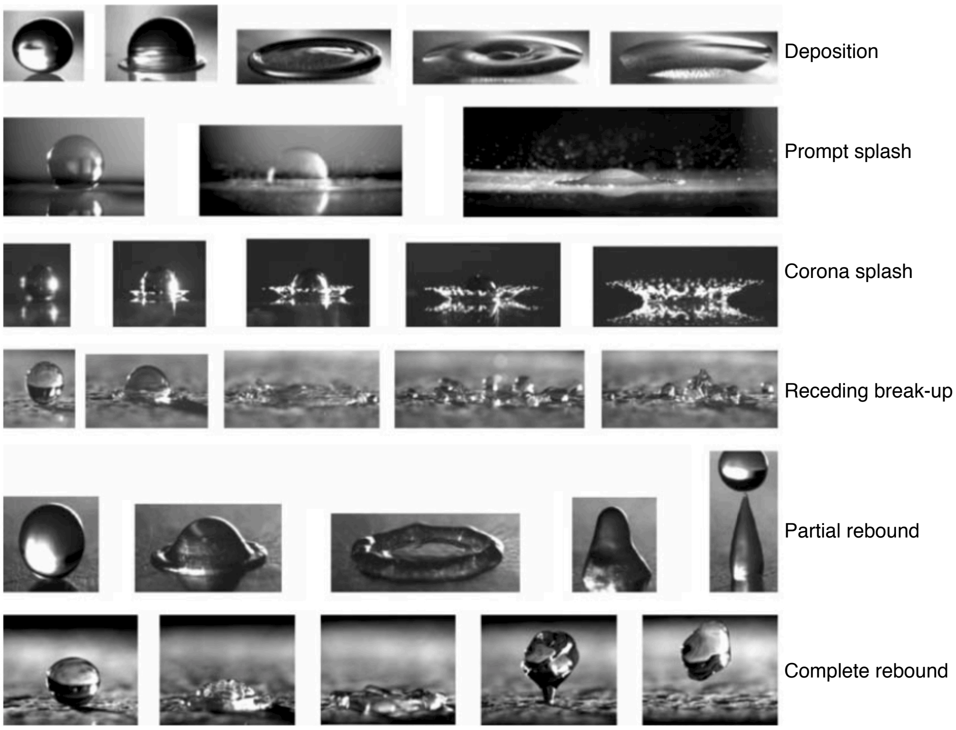

Figure 1.10: Time-lapse photographs showing different outcomes that can occur when a droplet impacts on a dry surface. Taken from [42]

temperature of the droplet) and partly converted into an increased surface energy due to an increased surface area. If the viscous forces dissipate most of the available kinetic energy, the drop may continue to spread across the substrate surface until the equilibrium radius is reached as with static deposition, leading to the *deposition* outcome shown in figure 1.10. However, if the kinetic energy of the impacting drop is high, the diameter of the spreading drop may overshoot the equilibrium value during the kinematic stage, after which the drop may recede toward the point of impact due to capillary forces. If the receding motion of the shrinking droplet is sufficiently slow, it will be arrested when the droplet reaches its equilibrium diameter. However at high receding velocities the droplet may break into several drops leading to the *receding break-up* scenario. Or, if it remains intact, the solution may be squeezed upward from the surface, resulting in *partial* or *complete rebound*. Outcomes where the drop undergoes receding break-up or partial or complete rebound during the secondary spreading stage are often characteristic of non-wettable surfaces. They are therefore unlikely to occur if the surface and the solvent are selected carefully such that $\gamma_{sl} \leq \gamma_{sg}$ (the condition for wetting).

Prompt splash and *corona splash* [43] correspond to break up of the droplet after overshoot during the kinematic spreading stage, and are promoted by a high impact velocity ($> \sim 5$ ms^{-1}) and a rough substrate surface. The typical range of impact velocities for spray-coating is 0.5-8.5 ms^{-1} [44]. Therefore both splashing and *deposition* scenarios are possible outcomes during spraying. Deposition can be expected to give smoother films and is therefore the preferred outcome.

A splashing parameter K has been proposed to characterise the transition between the spreading and the splashing regimes [45]. K is determined from the product of two dynamic dimensionless numbers that describe droplet behaviour. The Reynolds number, R_e (1.41), is a ratio of inertial forces to viscous forces, and the Weber number, W_e (1.42), is a ratio of inertial forces to capillary forces.

$$R_e = \frac{\rho d v_0}{\eta} \tag{1.41}$$

$$W_e = \frac{\rho d v_0^2}{\gamma} \tag{1.42}$$

$$K = W_e^{\frac{1}{2}} R_e^{\frac{1}{4}} \tag{1.43}$$

where v_0, is the impact velocity of the droplet, ρ, η, and γ, are the liquid density, the viscosity and the surface tension for a solution-air interface, and d, is the initial droplet diameter. In the case of water, it has been shown that for values of K above a critical value (57.7), splashing is observed, and for lower values, deposition is observed instead [45].

This relationship implies that the occurrence of splashing is most strongly dependent on impact velocity ($K \sim v_0^{\frac{5}{4}}$), with a significant dependency also on droplet density and size, ($K \sim \rho^{\frac{3}{4}}, d^{\frac{3}{4}}$). For spray coating, where the impact velocity is often extremely high ($\sim$8.5 ms^{-1}), this is potentially problematic. In order to reduce splashing, the droplet size and density must be low to compensate for a high impact velocity. Splashing can also be prevented by using a solution with a large surface tension ($K \sim \gamma^{-\frac{1}{2}}$) and a large viscosity ($K \sim \eta^{-\frac{1}{4}}$). However, excessively high solution viscosities are best avoided in spray-coating as they can lead to blockages within the nozzle and increase the energy required for atomisation, necessitating a faster flowing gas stream that will in turn increase the likelihood of splashing. Large surface tensions are also undesirable as they hinder solution spreading on the substrate.

It has been argued elsewhere by Rioboo et al. that the thresholds between the various scenarios in figure 1.10 cannot be quantified in terms of dimensionless numbers (such as the Weber and Reynolds number) as they do not take into account the wettability and roughness of the substrate [46]. Therefore, in practice it is easier to take an empirical approach, choosing a gas velocity that is high enough to form small droplets, but low enough to avoid splashing.

1.4 Drying of thin films and droplets

Once the droplets have deposited on the substrate and (ideally) coalesced, the volume of the solution starts to decrease as the solvent evaporates, eventually leaving behind a thin polymer layer. On drying, various patterns may form in the solid film, causing spray-coated films to exhibit highly structured non-uniform features. In this section we discuss the process of drying and some of the patterns that may result.

The process of solvent evaporation follows two separate steps: a phase change of the solvent, from liquid to vapour (which is dependent on the rate at which molecules cross the liquid-air interface), and the transport of vapour molecules away from the drop into the surrounding air (this process is a combination of diffusive and convective transport). If one process is much slower than the other it will control the evaporation process. If phase change is the rate-limiting step, the evaporation rate will be uniform over the surface. If on the other hand, escape of vapour molecules is the rate-limiting step, the evaporation rate will be strongly dependent on the geometry of the film (this is explained in section 1.4.1). In this thesis I consider the evaporation of o-xylene from thin films and droplets ($\leq$ 1 mm in diameter), for which the diffusive transport of o-xylene vapour in the surrounding air is rate-limiting [47].

For a large, flat expanse of solution, formed e.g. by the coalescence of numerous proximate droplets, the evaporation rate will be constant across the deposit, resulting in the formation of a uniform, featureless film. However, coalescence between deposited droplets is not guaranteed during spray deposition, and it is therefore necessary to consider the evaporation profiles of individual droplets. In contrast to large films, the edge region accounts for an appreciable fraction of a droplet and edge effects strongly influence the drying behaviour. This in turn can lead to a rich variety of drying patterns in the final solid films.

1.4.1 Evaporation rates of drops

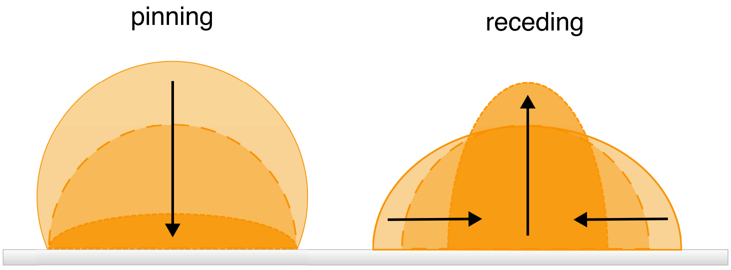

Figure 1.11: Evaporation modes of sessile droplets on a surface. Left: Pinning leads to evaporation at constant contact area. Right: receding leads to evaporation at constant contact angle.

As a droplet dries, the edge (or perimeter) may either recede from its (normal) equilibrium position or pin [48] as shown in figure 1.11. In the case where the droplet recedes as it dries, it is observed to display a constant contact angle and diminishing contact area between the solution and substrate. Alternatively, in circumstances where the substrate is rough or there are impurities in the solution, the liquid perimeter (or contact line) will pin at its original position. This result is a reducing contact angle and a constant contact area between the film and the substrate. Receding and pinning are extreme modes of evaporation, and it is not unusual for the two modes to occur alternatively (stick/slip behaviour) or even simultaneously on different portions of the liquid. Since real surfaces always exhibit some inhomogeneities, edge pinning is

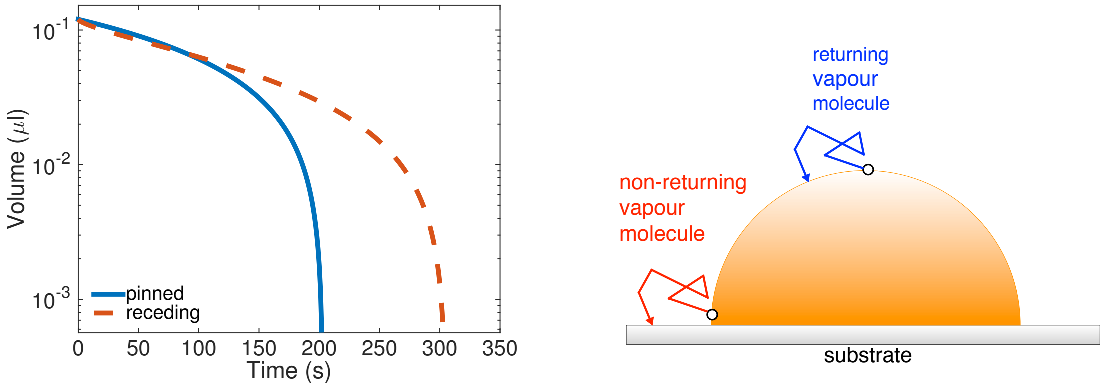

(a)

(b)

Figure 1.12: Droplet evaporation. (a) Volume change of a sessile water drop during evaporation in pinning mode (blue) and in receding mode (red dashed), taken from [49]. Pinned droplets evaporate faster than receding droplets. (b) Probability of escape for vapour molecules at two different sites on the surface of a droplet for diffusion-controlled evaporation. The random trajectory of a vapour molecule is more likely to result in a return to the surface if the starting point is far away from the edge of the droplet. Adapted from [50].

the more commonly observed effect. Receding is a secondary effect, and so the initial instance of drying often proceeds from a pinned position.

Early measurements by Morse [51, 52] on the drying of an iodine drop on a surface indicated, that the mass evaporation rate ($\frac{\partial m}{\partial t}$) is proportional to the radius, a, of the droplet and not to its surface area (as would naively be expected) such that:

$$-\frac{\partial m}{\partial t} = ka \tag{1.44}$$

where k is the heat conductivity of the gas. Since then, many studies have been conducted on droplets of various compositions and dimensions which have confirmed the wide applicability of equation 1.44 [53, 54]. When considering evaporating droplets of organic liquids, Picknett and Bexton found that the instantaneous evaporation rate is dependent on the shape of the droplet as it dries [48]. When the film is pinned, the rate falls relatively slowly since the droplet radius is fixed. However when the film recedes, the evaporation rate diminishes steadily over the lifetime of the drop, resulting in a longer drying time. This is demonstrated graphically in figure 1.12a.

Hu and Larson rationalised this behaviour by showing that the local evaporation rate is highest at the edge of a droplet. This is because a vapour molecule at the edge of a droplet has a higher probability of escaping the surface than one in the centre. This concept is demonstrated in figure 1.12b, where the random walk path of a vapour molecule close to the edge and close to the centre are depicted. As discussed in the next section, the enhanced evaporation rate at the droplet edge has profound implications for the drying patterns of solid films formed from solutions and dispersions.

1.4.2 Pattern formations in drying films and droplets

The final profile of a dried film is affected by multiple parameters, including the chemical composition of the printing ink, the droplet size, the nature of the impact, the influence of the substrate surface and the non-uniform evaporation rate. The drying dynamics of droplets are rather complex, and are responsible for pattern effects such as coffee staining, mound formation, skin formation, and buckling instabilities; all of which are discussed in this section. While such phenomena are challenging to control and avoid, they must nonetheless be addressed if smooth films are to be deposited.

Coffee staining

If the evaporation of solvent is slow and the solution is dilute, an internal flow within the liquid phase can result in one of the most extensively discussed drying patterns in the scientific literature: the classic ”coffee ring” [55]. The feature derives its name from the observation that coffee spilt on a flat surface dries in a manner that leaves coffee particulates preferentially located in a ring around the edge of the initial spill, with the centre largely devoid of solids. This was first explained by Deegan et al, who attributed the effect to capillary flow [50, 55]. As the droplet dries, it remains pinned at the edge where it experiences an enhanced evaporation rate for the reasons explained above. Consequently, the solution concentration increases fastest close to the edge (or contact line), causing the local dissolved/suspended material to precipitate. The depletion of material from the solution at the droplet edge induces a replenishing flow of material from the bulk of the droplet to the edge, where a progressive build-up of material occurs due to continued deposition as illustrated in figure 1.13.

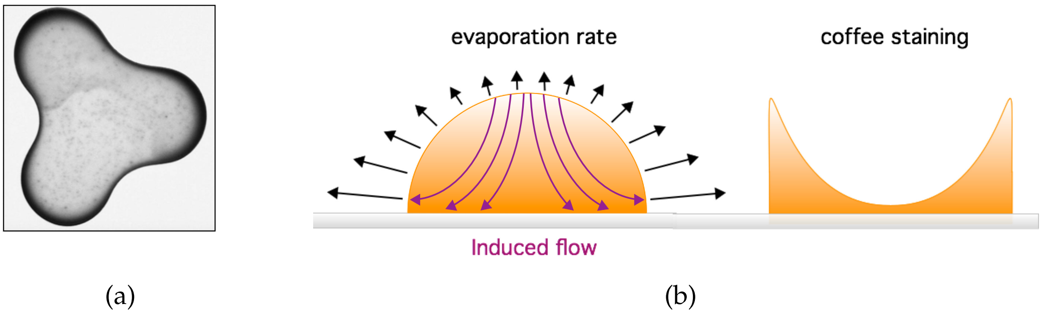

(a) (b)

Figure 1.13: (a) ring deposit of a dried coffee droplet, taken from [55]. (b) schematic of the outward evaporation-induced flow inside a sessile droplet and the resultant material distribution of a dried deposit. An internal flow is generated inside the droplet as a result of evaporation that carries the fluid towards the edges.

”Coffee staining” is a common occurrence in films formed from pinned droplets, and is not limited to colloidal dispersions such as coffee particulates. Fairhurst et al discussed the drying of aqueous solutions of poly(ethylene oxide) (PEO) in a series of publications [56–58]. They showed that polymer solutions behave in a similar manner to colloidal dispersions, with the polymer building up at the edge of the droplet as it dries. Coffee-staining is problematic for spray-coating as it prevents the formation of uniform films, resulting instead in ”dappled” or ”cratered” coatings. Techniques for avoiding coffee-staining are therefore of interest when it is required to deposit smooth films by spray-coating.

Mound formation

Coffee-staining is the most common, but not the only outcome observed with drying polymer solutions. Jung et al [59] investigated the effects of initial polymer concentration, initial drop size and evaporation conditions on the drying patterns of polymer films. They found (in agreement with Ozawa et al. [60]) that the final deposits were frequently mound or basin-shaped in addition to the classic coffee stain. They attributed these features to gelation of the polymer solution. If the solution concentration was sufficiently high (or became sufficiently high during evaporation), the droplet would start to gel. They suggested that an important shape-determining parameter was the amount of polymer left in the solution when gelation at the pinned edge began. If the initial polymer concentration was low, it would take a long time for the droplet to gel since evaporation would start when the solution was far from saturation. By the time gelation had started at the edge of the droplet, most of the polymer would already have been brought to the edge by the outward flow, leaving very little polymer in the bulk solution. The result after complete drying would therefore be a thin basin-like structure (depending on the amount of polymer remaining at gelation onset). Higher initial polymer concentrations by contrast would lead to earlier gelation at a time when a large amount of polymer was still present in the solution. If gelation occurred only at the edge, the solute would travel as before from the centre towards the edge, however if the bulk solution viscosity increased rapidly as solvent was lost, the outward capillary flow would be suppressed, weakening the coffee stain effect and causing a central mound shape in the final dried film.

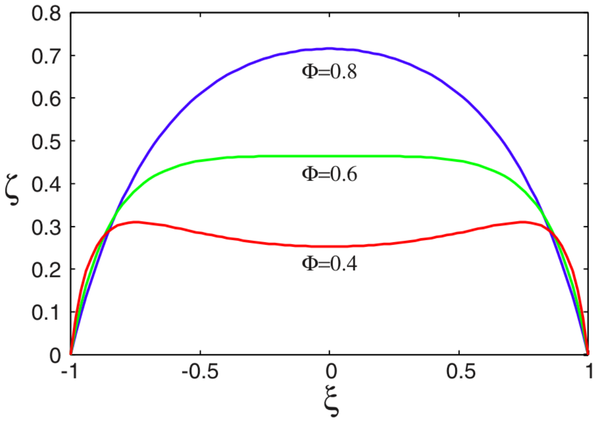

Figure 1.14: A plot showing how the height, ζ, of the final droplet shape varies with the position, ξ, of the gelation region, for three different ratios, Φ, of solution concentration in the liquid phase to solution concentration in the gel phase: 0.4, 0.6 and 0.8, given by equation 1.45 and taken from [61]

Okuzono et al [61] modelled the droplet shape as a function of the initial polymer concentration of the solution by solving the 2D Navier Stokes equation in the lubrication limit. They were able to account for both basin-shaped and mounded features, see figure 1.14. They reported that the height, ζ, of the final drop shape could be described as a function of the position, ξ, of the gelation region and the ratio, Φ, of the solution concentration in the liquid phase to the solution concentration in the gel phase as follows:

$$\zeta = \frac{\Phi^{-1}(1-\xi^2)}{[\xi^2 + \Phi^{-1}(1-\xi^2)]^{\frac{5}{2}}} \tag{1.45}$$

Therefore, deliberately encouraging gelation offers a potential means of preventing coffee-staining, with factors such as the evaporation rate (influenced by the solution/-substrate temperature), solution concentration, and choice of solvent, all playing an important role.

Marangoni flows

Coffee-staining occurs in single solvent droplets that exhibit a constant surface tension over the entire gas/liquid interface. However, the surface tension can be varied by the addition of a surfactant [62], secondary liquid [63, 64], or solute [65]. In the case of a secondary liquid that has a very different boiling point than the primary solvent, a surface tension gradient may be generated by the preferential evaporation of the more volatile solvent at the droplet edge. Depending on whether the more volatile solvent has a higher or lower surface tension than the other solvent, the gradient will either point in-to or out-from the centre. The remaining liquid will move towards the region of higher surface tension to reduce the surface energy, thus draining liquid from the region of lower surface tension. This behaviour is familiar in everyday life from a swirled glass of wine, which is predominantly a mixture of water and ethanol. When the wall of the glass is coated with a thin layer of wine, ethanol (which has a lower interfacial tension with glass) evaporates preferentially, leaving behind water (which has a higher interfacial tension). Ethanol then passes from the bulk of the wine to coat the glass, causing so-called "tears" to form. Visually, one observes wine climbing the walls of the glass. In general, this local replenishment of lost solvent is observed for any mixture where the more volatile component of the liquid has the lower surface tension.

Surface tension gradients can also be generated by local differences in temperature. In this case the resultant motion of liquid is usually called Marangoni convection or thermocapillary flow [66–68]. Hu and Larson showed that, for simple (single component) organic solvents such as octane, solute deposition ocurred preferentially at the centre of the droplet, due to a recirculatory flow driven by surface-tension gradients due to temperature differences caused by non-uniform evaporation. They suggested that such Marangoni flows could be used to counteract coffee staining by redirecting solute back to the centre of the drop [69]. The competing (capillary and Marangoni) flows for a pinned droplet are demonstrated in figure 1.15.

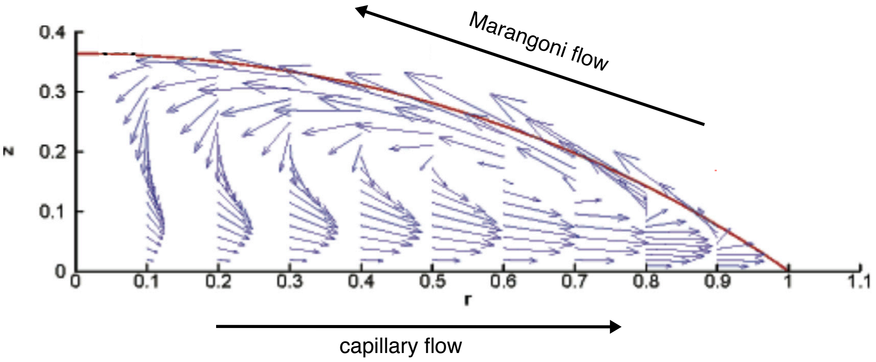

Figure 1.15: Time-dependent velocity fields of capillary vs Marangoni flows, taken from [66]. Marangoni flow produces an inward flow that counters the outward evaporation-induced flow for sessile droplets during the pinned stage.

Dewetting

There are many cases in which the edge does not stay pinned throughout the entire process of evaporation. In some cases the edge may pin and de-pin multiple times, which is referred to as stick-slip behaviour. The stick-slip behaviour of drying droplets containing particle suspensions has been widely investigated [70–73]. If the film is only lightly pinned, then a coffee stain will form at the initial contact edge due to particle deposition, but subsequent de-pinning will cause the contact line to recede inwards due to the diminishing solvent volume (caused by evaporation). The droplet may again become pinned to the substrate, causing a second coffee ring to form at the new contact edge. If this stick-slip process occurs repeatedly, multiple ring formation will occur as the film edge intermittently jumps towards the centre, leaving solid deposits behind as it does so. The resulting pattern which is sometimes referred to as an ”orange peel” pattern, is shown in figure 1.16. Multiple ring formation has also been observed in bacterial colonies [74] and collagen solutions [75], where it was found that the motion of the droplet edge is coupled to both the concentration of the solution and the rate of evaporation. (Neither study explained the mechanism through which the motion of the contact line was controlled by these variables).

The stick-slip behaviour can be explained in terms of competing forces at the contact line in response to solvent evaporation [70]. These forces include a frictional force which the contact line feels when the particles flow from the inside of the drop to the drop boundary (outward flow), and a surface tension force of the solution (inward flow). It has been suggested that these local, opposing forces may generate mechanical instabilities responsible for the ’slip’ motion.

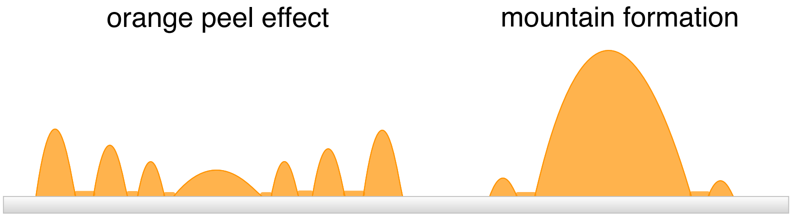

Figure 1.16: A schematic of pattern formation as a result of solution dewetting. (left) The ”orange peel” effect, caused by the stick-slip behaviour of a lightly pinned droplet as a result of mechanical instabilities at the droplet edge as it dries. (right) ”Mountain” formation caused by the inward flow of solute as a result of the droplet receding droplet as it dries.

In the case where the drop’s edge freely recedes (i.e. the droplet is not pinned), height changes near the edge of the drop due to evaporation, are larger than height changes at the centre. This has been shown to push fluid radially inward as the drop evaporates [73]. Li et al found that drops containing poly(ethylene glycol) recede during the majority of their evaporation and only show contact line pinning at early times [72]. This results in the formation of mountain-like deposits (see figure 1.16) in the centre of the drop instead of the usual coffee stain morphology. (Note: It has also been reported that receding drying drops of poly(ethylene oxide) form mountain-like patterns in which the droplet is raised by solid deposits as it dries [57, 58]. In these cases however, the unusual mountain-like shape was attributed to the ability of PEO to precipitate semi-crystalline spherulites at high concentrations, and was not related to the drying process itself).

Skin formation and buckling

For large expanses of solution where the evaporation rate is roughly uniform across the entire surface, or for very fast evaporation of solvent from a pinned drop, one-dimensional vertical drying is sometimes observed in which the solute concentration increases near the surface, causing a thin gel-like skin to appear [76–79]. Sheetz et al. for instance, reported the formation of a skin layer at the top of a drying paint film, which hindered further evaporation and so slowed down the process of film formation [80]. When skin formation occurs, the shape of the final dried film is strongly affected by the growth of the skin phase. Films formed by skin formation are typically found to have rougher surfaces than those formed in other ways (since the skin has a tendency to wrinkle during drying to relieve internal stresses).

In the specific case of concentrated polymer solutions that undergo both skin formation and pinning, subsequent buckling of the skin is a likely outcome, causing a dimple to form in the centre of the dried film [81]. As the solvent continues to evaporate following skin formation and the volume of the drop continues to decrease, so too does the pressure inside the droplet. When the internal pressure drops below a critical value, the droplet cannot maintain a spherical shape and may buckle inwards to form a dimple. (Note, the profile of the final polymer film is influenced by the mechanical properties of the skin, and several other deformed drop profiles can also result [82–84]). Both skin formation and buckling are shown in figure 1.17.

For droplets pinned at the contact line, the roughening effect of skin formation (and buckling) occurs in addition to the outward radial flow of solvent responsible for the coffee stain effect, during evaporation. Skin formation is therefore likely to be an undesirable process from the prospective of device fabrication (where increased roughness increases the risk of shunting).

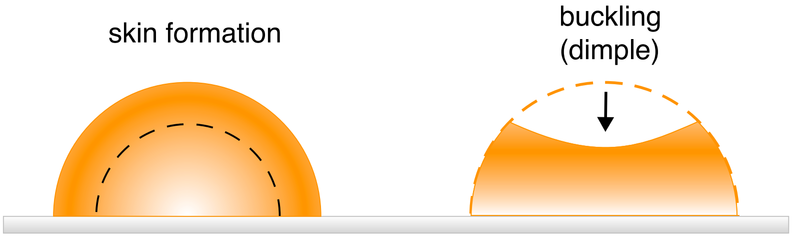

Figure 1.17: A schematic to show skin formation and buckling. (left) Thin gel-like skin formation caused by the rapid evaporation of solvent from the surface of a pinned droplet. (right) Subsequent buckling of the skin layer due to a decrease in pressure inside the droplet as it continues to dry.

1.5 Summary

In this section we have considered various processes that may affect the quality of polymer films formed by spray-coating. Film formation by spray-deposition is dependent on various factors including: effective atomisation of the solution by the spray-head, the nature of the impact of the drop on the substrate, the spreading of the solution onto a substrate, and non-uniformities in solvent evaporation. Forming a good quality film requires a combination of conditions to be met. Firstly, the size of the droplets generated in the atomisation process should be small (<40 μm) with a narrow size distribution. Splashing upon impact should be avoided to maintain a narrow droplet size distribution, and solutions with low surface tensions should be used to enable droplet spreading and thus, promote droplet coalescence. Finally, any outward flow of material (as a result of non-uniformities in solvent evaporation) should be counteracted to prevent non-uniform material distribution within films. These conditions may be met by careful design/selection of the spray-head, tailoring of the ink composition and optimisation of the deposition parameters. In this thesis I aim to do this for spray films of P3HT cast from the non-chlorinated solvent o-xylene.

2 Design and characterisation of an automated pressurised spray deposition rig

The wide range of spray coating applications described in the previous chapter, has led to numerous designs, especially in relation to the design of the nozzle (or ”spray head”) where the spray is generated and dispensed. The optimal nozzle design is application dependent, and is influenced by the properties of the fluid being sprayed (e.g. its viscosity and volatility), the environment in which it is sprayed (e.g. ambient conditions or high pressure and/or high temperature) and the spray duration (e.g. milliseconds or hours).

It is instructive to consider two applications with very different requirements: the distribution of pesticides in agriculture, and the injection of fuel into the combustion chamber of an engine. For the deposition of pesticides, the spray system must deliver liquid to the ground with broadly uniform coverage whilst minimising evaporation during droplet transport. Here, the droplets must be large enough to avoid appreciable evaporation but the exact size distribution of the droplets is of little importance. In combustion, by contrast, drop size is critical and must be minimised to create a large surface area to enhance fuel evaporation. Droplet velocity is also important and must be tailored to provide the desired fuel-air mixing, while avoiding surface deposits and undesirable exhaust emissions. Nozzle designs for the two applications are consequently very different. A flat-fan nozzle is employed for depositing pesticides. The fan-shaped nozzle causes the liquid to form a large sheet that subsequently breaks up into drops upon contact with a flat surface attached to the spray-head. High pressure carrier gases are avoided to prevent unwanted droplet evaporation. For fuel injection, by contrast, a high velocity jet of liquid is injected into a highly pressurised turbulent gas, which causes the liquid stream to disintegrate into tiny droplets. Hence, although a spray mist of some description is formed in both cases, the characteristics of the mists are quite different, and are tailored to the needs of their own particular application. If applied to pesticide distribution, the fine mist from a fuel-injection spray-head would disperse and evaporate before contacting the ground. On the other hand, if applied to fuel injection, the large drops formed by the flat-fan spray nozzle would make insufficient interfacial contact with the air to achieve efficient combustion.

This thesis is specifically concerned with the the deposition of very thin (∼100 nm) conjugated polymer films by spray coating, which is a particular challenge since the films must be uniform, continuous and relatively smooth for device applications. The nozzle plays a large role in determining the roughness and uniformity of the final film, and should be designed to achieve the optimum film characteristics.

In this chapter I describe the design and characterisation of a pressurised spray nozzle for the deposition of thin polymer films for organic electronic devices. A key objective was to develop a spray-coating system that would operate controllably and reproducibly in a fully automated manner. When properly implemented, automation can provide precise control over key operating parameters, eliminating human errors that would otherwise lead to operational variance. The design of the rig and the procedures used to automate it are documented in this chapter.

2.1 Design of a spray-head for the controlled deposition of semiconducting polymer solutions

Much of the previous work on spray deposition of polymer films has used high pressure, gas-driven airbrushes similar or identical to those used in spray painting. As described in section 1.3, airbrushes of this kind use a fast-moving stream of

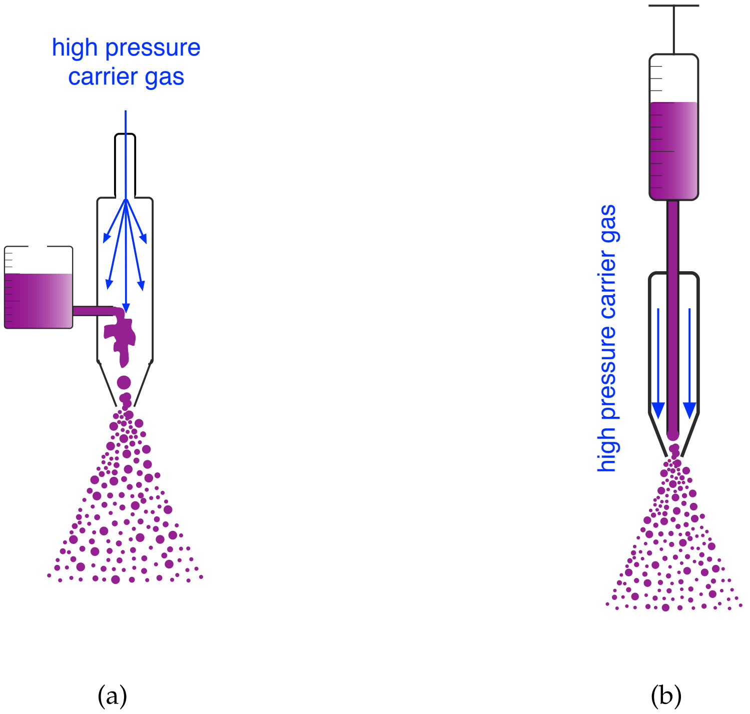

(a) (b)

Figure 2.1: A schematic comparing the atomisation process in two common types of gas-driven spray-head. (a) a common pressure-driven spray-head where the solution and gas are mixed internally and (b) a coaxial spray-head where they are mixed externally.

compressed gas, to create a reduction in pressure at the outlet of a reservoir containing the printing ink. The ink solution is nebulised inside the spray-head as it interacts with the compressed gas and the resultant mist is carried by the gas, out of the spray-head (through a narrow orifice) and towards the surface being coated. This method is widely used for coating of commodity materials since coating systems of this kind are relatively inexpensive (∼ £100) and provide adequate uniformity for many applications. Unfortunately, conventional airbrushes are poorly suited to organic device fabrication: whilst the roughness and uniformity of films produced using a pressurised gas-driven nozzle are adequate for painting applications, where films are often many microns thick, the sub-micron film thicknesses and nano-scale uniformity required for organic devices are extremely difficult to achieve with a standard airbrush.

It has been suggested that the main reason for the poor film quality is the inability of gas-driven nozzles to produce small enough droplets (with a sufficiently narrow size distribution) to form uniform, smooth films. On this basis, ultrasonic spray-heads have been proposed as a more suitable technology for organic device fabrication [16] due to their ability to generate very small droplets ($\leq 50\ \mu$m). However this reasoning is based on a side-by-side comparison of ultrasonic systems with one particular design of gas-driven spray-head. As noted in the previous chapter, numerous designs of gas-driven spray-heads have been developed, some of which are capable of producing extremely fine spray mists. Most notably, the formation of an ultrafine mist is critical to the operation of fuel-injection systems [85], which are all pressure driven in nature. It is therefore reasonable to speculate that some types of gas-driven spray-heads might be capable of generating sufficiently small droplets to obtain films of acceptable quality for organic electronic device applications.

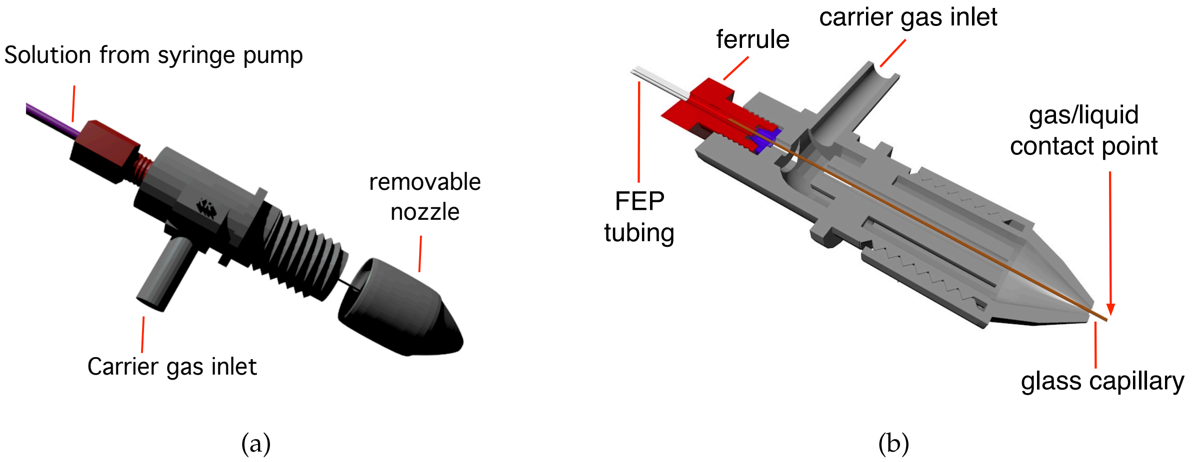

(a)

(b)

Figure 2.2: Three dimensional rendering of the coaxial spray-head designed for the deposition of semiconducting polymer solutions. (a) Exterior image showing the detachable nozzle (b) cross-sectional image showing the position of the capillary and the path taken by the carrier gas before exiting the nozzle.

Based on the general principles of atomisation set out in the previous chapter, I chose to base my work on a co-axial spray-head design, in which a relatively slow-moving jet of liquid is injected coaxially into a surrounding sheath of fast-flowing turbulent carrier gas. The structure of the spray-head I designed is shown in figure 2.2. The main body of the spray-head was 3D-printed in Nylon. Printing was outsourced to the online 3D-printing company, Sculpteo. The shell of the spray-head included inlet manifolds for the carrier gas and solution. A syringe pump was used to inject solution into a central glass capillary that ran along the axis of the spray-head. To avoid excessive back-pressures, the capillary itself was not connected directly to the syringe pump, but via an intervening length of wide-bore (100 μm) fluorinated ethylene propylene (FEP) tubing. The connection between the tubing and the capillary was made using a leak-tight ferrule. The total length of the capillary was approximately 7 cm, sufficient to develop a fully parabolic flow, as discussed in section 1.3.1. When liquid emerges from a capillary outlet the flow switches from parabolic to plug, causing a redistribution of the kinetic energy from the centre to the periphery [86]. This process is believed to aid atomisation via a mechanism known as "bursting" breakup. The spray-head was designed to exploit this process, and hence achieves a finer mist. The interior of the spray-head was hollow (except for the central capillary), with a diameter of ~1 cm. A side inlet was used to deliver dry nitrogen gas from a flow-regulated cylinder using a mass flow controller. The end of the spray-head (the nozzle) was a screw-threaded attachment that narrowed to a 1-3 mm orifice at it's end. The nozzle aperture was used to control the shape and breadth of the resulting spray mist [87]. The large inner bore of the main housing combined with its tapering to a narrow orifice helped to promote turbulence in the gas flow. The tip of the capillary extended approximately 1.5 mm beyond the orifice so that mixing of the liquid and gas streams occurred outside the housing. This design was chosen to avoid coating the interior of the spray-head with material, and hence prevent clogging.

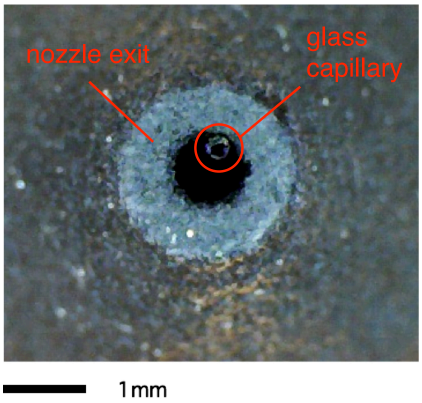

Figure 2.3: Front-on view of the spray-head, showing the narrow capillary protruding slightly from the orifice of the spray-head.

A front-on view of the spray-head is shown in figure 2.3, where both the gas and solution outlets are clearly visible. The nozzle was not in use when the photograph was taken and the capillary can be seen resting to one side of the nozzle. However, when in use, the high velocity carrier gas centres the gas capillary, ensuring uniform flow of the carrier gas across the full perimeter of the solution outlet.

The chosen design offers several advantages over the more widely used spray-head shown in figure 2.2a that mixes solution and gas internally: smaller droplet sizes can be achieved, viscous solutions and dispersions are more easily atomised, and blockage is less likely since the solution does not contact the nozzle. Furthermore, the gas pressure can be varied to produce the desired atomisation without changing the liquid flow rate or pressure. In the conventional spray-head design of figure 2.2a, the liquid flow rate increases as the gas flow rate is increased.

2.2 Droplet characterisation by optical microscopy

Characterising droplets in a spray mist is challenging because the high droplet density and high droplet velocities complicate experimental measurements. With sufficient care, properties such as the drop velocity, momentum and volume flux can be determined at different positions within the spray [88]. However for the work in this study, I focused only on the size distribution of the droplets.

Various methods for determining droplet size have been reported in the literature. The three most widely used techniques are laser diffraction [89], phase Doppler imaging [90, 91] and optical imaging [92]. These methods are used to measure droplets within a spray mist, and can be classified as either spatial (measuring the drops in a finite volume), or flux-based (sampling continually over a measurement cross-section). Laser diffraction is a spatial sampling method which relies on Fraunhofer diffraction caused by the light interacting with the drops in the spray. The scattering angle of the diffraction pattern is inversely related to the size of the drop. The phase Doppler method is flux-based and involves creating an interference pattern from two intersecting laser beams, resulting in a region of alternating light and dark fringes. A droplet passing through this region scatters light with an angular and temporal intensity distribution which is characteristic of the size, refractive index, and velocity of the droplet. The optical imaging method is the simplest; it uses a pulsed light, laser or strobe, to generate a shadow image, which is used to determine the size of the drop in the measurement volume.

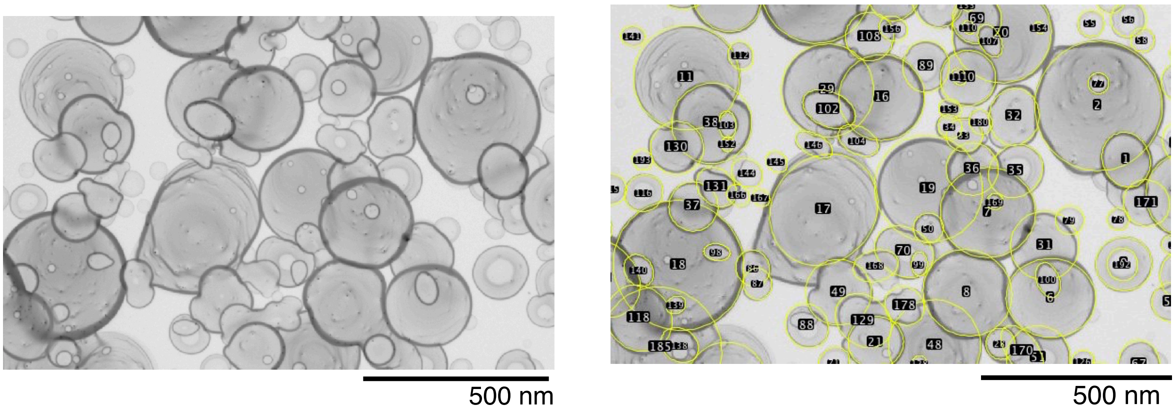

(a) (b)

Figure 2.4: Optical microscopy images of a sparsely populated film of dried polymer droplets deposited via spray-deposition. (a) raw image and (b) an annotated version to demonstrate how each drop was identified and measured in imageJ.

The above methods are used to characterise the droplets in the spray mist. Since my interest here was in spray coating, i.e. the formation of thin films on a surface, it is more instructive and far simpler to make static optical measurements of the dried droplet deposits on a surface. For the reasons discussed in section section 1.2, this thesis is specifically concerned with spray-coating of the well characterised semiconducting polymer (P3HT) from the non-chlorinated solvent o-xylene. To characterise the size of droplets generated by the spray-head, high resolution images of sparse droplet deposits of P3HT on glass sprayed from o-xylene were obtained using an Olympus BX51 optical microscope. A typical image, representative of these sparse droplet patterns, is shown in figure 2.4a (the exact deposition conditions need not concern us here). Droplet size distributions were determined using image analysis software (ImageJ) in a manual counting mode. Each droplet was fitted by eye to an ellipse, from which the semi-major and semi-minor axes were extracted and averaged to provide a mean droplet diameter. For each image, ~400 separate droplets were measured to determine the overall size distribution. An image illustrating the analysis process is shown in figure 2.4b. Here, elliptical fits for every droplet in the optical microscope image are shown together with a label showing the droplet number.

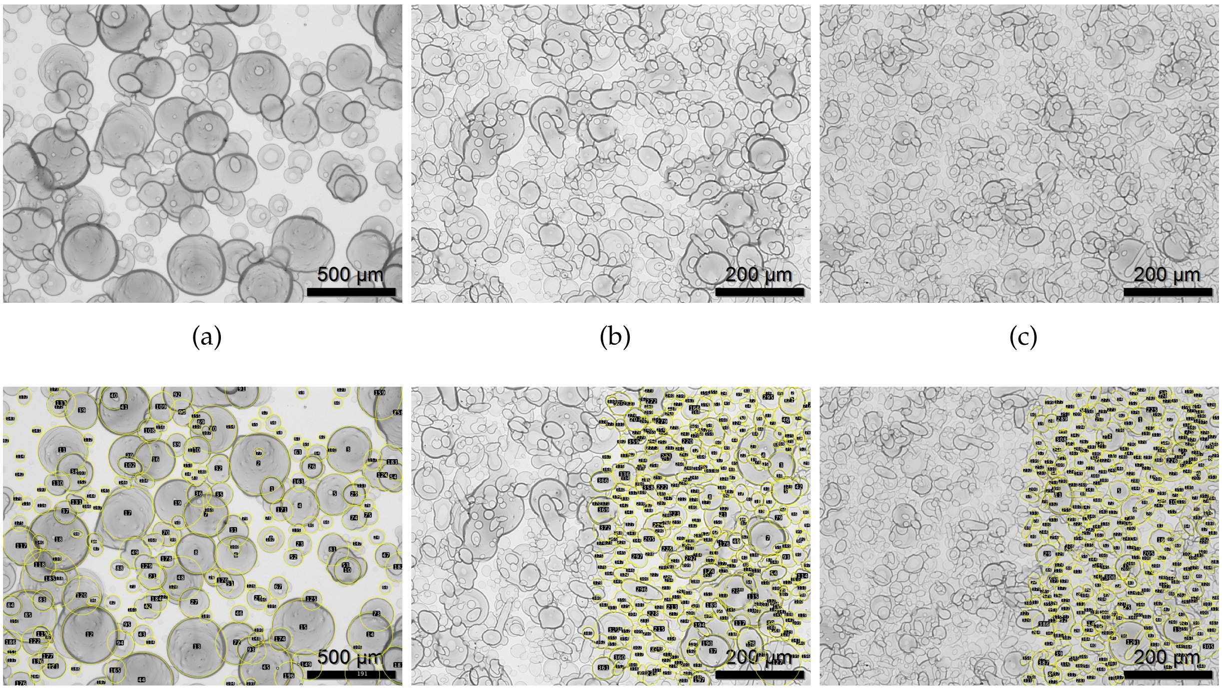

(a) (b) (c)

(d) (e) (f)

Figure 2.5: Optical microscopy images of sparsely populated films of droplets deposited via spray-deposition, using different spay-head operating parameters. (a,b,c) raw images (d,e,f) annotated images. The images show the broad range of droplet sizes.

We will show later that the droplet size distribution is strongly dependent on the chosen spray conditions. Figures 2.5a- 2.5c, shows transmission mode microscope images for substantially different sized droplets obtained under different spray conditions. Figures 2.5d-2.5f, show the corresponding elliptical fits. On the basis of these fits, it is possible to plot droplet size distributions of the form shown in the (see e.g. figure 2.7) next section.

Whilst the largest droplets in figure 2.5a are easily measured, as the droplet size decreases to $\leq$10 μm, the measurement becomes more difficult. Although the diameters of many of the observed droplets in figure 2.5f are in the range of 10 μm, there is considerable uncertainty in the extracted diameter values, and the extracted size distributions diameters should be treated with a degree of caution. In the following sections, we will use this imaging technique to understand the influences of various spray parameters on the droplet size distribution.

Finally we note that, beyond information about the size distributions, the droplet micrographs also provide useful information concerning the material distribution within the droplets. The darker areas in the images are a result of increased light absorption by the deposited film, and are indicative of a localised build up of material. Dark areas are clearly visible around the perimeter of the drops, indicating substantial coffee staining (see section 1.4.2).

2.3 Influence of the nozzle parameters on droplet size distribution

2.3.1 Carrier gas velocity

The velocity of the carrier gas is one of the most important parameters for controlling the droplet size. The influence of the gas velocity, u_g, may be understood in terms of the dimensionless gas Reynolds number, Re_g (equation 2.1), which also depends on the diameter, y, of the nozzle aperture and the density, ρ_g, and the viscosity, η_g of the gas:

$$Re_g = \frac{y \rho_g u_g}{\eta_g} \tag{2.1}$$

To obtain a finely atomised spray, a high gas Reynolds number ($>10^4$) is required since the gas must be sufficiently turbulent to break up the uniform jet of liquid emerging from the capillary. Given that η_g and y are typically fixed parameters that do not change during the course of a spray-run, the most effective way to achieve a high gas Reynolds number is to increase the velocity and/or density, ρ_g of the gas.

A previous study by Mayer [93] into the use of coaxial spray-heads (for fuel injection) demonstrated experimentally that the application of a carrier gas to a fluid column caused detachment of liquid in the form of ligaments and droplets. As the gas velocity was increased, the fluid stream was increasingly disrupted until eventually a fine spray was produced close to the fluid exit. Photographs of the liquid column are shown in figure 2.6 for different gas velocities in the range 0 to 300 m/s.

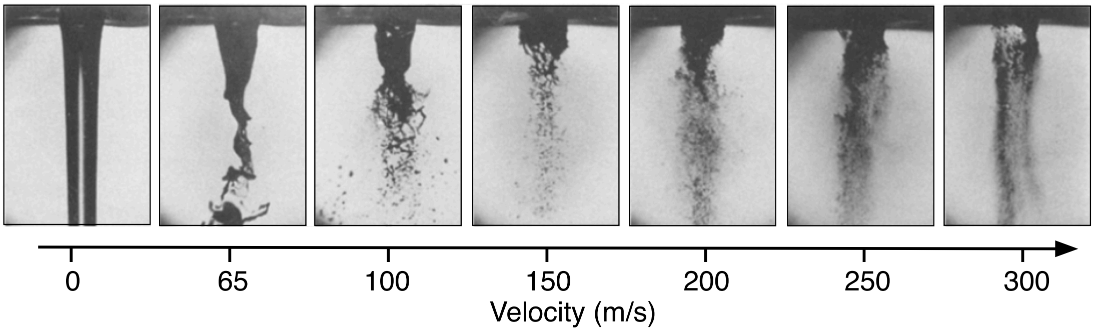

Figure 2.6: Photographs taken from ref [93], demonstrating the atomisation of a liquid cylinder using a coaxial spray-head by a carrier gas with velocities in the range 0-300 m/s.

The same study showed that increasing the gas pressure inside the (sealed) chamber into which the liquid was injected (while holding the gas velocity constant) caused finer droplets to be produced, consistent with the increasing gas Reynolds number. For spray-coating, pressure-controlled environments should be avoided, for the sake of simplicity. Hence, the spray characteristics must be controlled using the gas velocity alone.

Figure 2.7 shows size distributions for dried P3HT droplets on glass using various nitrogen flow rates in the range 5 to 25 Lpm for a nozzle aperture of 1 mm and a fixed liquid flow rate of 400 μL/min. For all of the measurements reported in this thesis, the end of the capillary was fixed at a height 8 cm above the substrate. The histograms were obtained using the method described in section 2.2. Table 2.1 shows the corresponding gas velocity and Reynolds number for each flow rate used.

In accordance with the discussion above, higher nitrogen flow rates produced smaller droplets with narrower size distributions (shown in figure 2.7). The most noticeable change occurred when increasing the gas flow rate from 5 to 10 Lpm, with the average drop diameter decreasing from 130 to 29 μm respectively, and the standard deviation in droplet sizes falling from 77 to 18. This large transition is consistent with the Reynolds gas number being <10000 for the gas flow rate of 5 Lpm, and >10000 for the gas flow rate of 10 Lpm. Although the mean size and width of the size distribution decreased

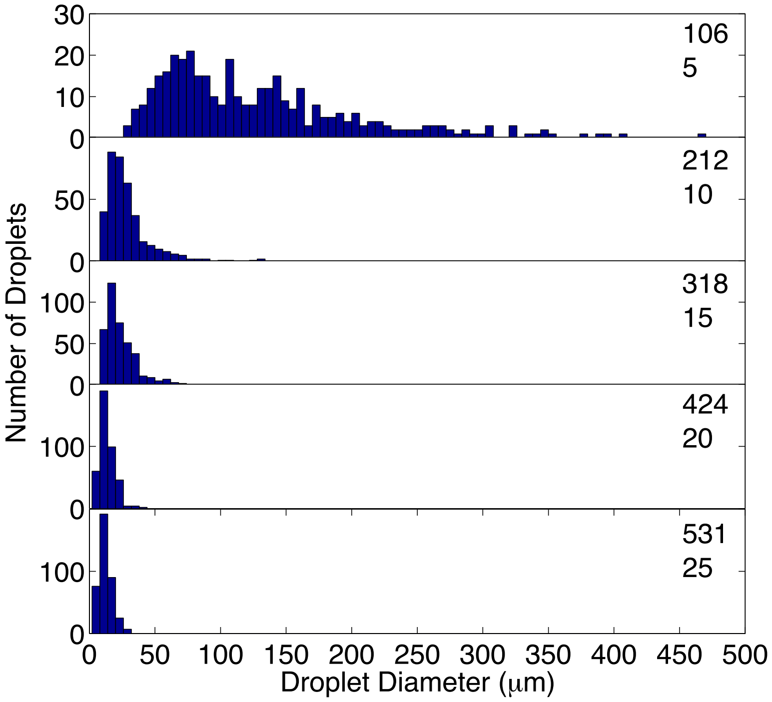

Figure 2.7: Histograms showing droplet size distributions for dried P3HT polymer films obtained using different gas velocities/flow rates, with a constant liquid flow rate of 50 μL/min. The numbers at the top and bottom right hand corner of each histogram are the gas velocity in m/s and gas flow rate in Lpm, respectively.

Gas flow rate (lpm)	Gas velocity (m/s)	Reynolds number
5	106	7 033
10	212	14 065
15	318	21 097
20	424	28 130
25	531	35 229

Table 2.1: Conversion of carrier-gas flow rates to linear velocities and gas Reynolds numbers.

continuously with increasing gas flow rate, flow rates higher than 25 Lpm could not be investigated as it became difficult to secure the substrate in place. It is worth noting however, that the difference in the drop size distributions between gas flow rates of 20 and 25 Lpm was very small, suggesting that impractically high flow rates would be needed to achieve appreciably finer droplets. In addition, using excessively high gas flow rates can cause problems such as "spray drying" and "pooling" (as discussed in section 1.3). Hence, it appears that a flow rate of ∼20 Lpm offers a good compromise between achieving a small droplet size and avoiding these complications.

2.3.2 Solution flow rate

In principle the flow rate of the solution as it exits the nozzle can also influence the atomisation process, and therefore affect the droplet characteristics. However, the liquid flow rate is only likely to play a substantial role when the liquid flow is turbulent, leading to ligament formation at the surface of the liquid column (see section 1.3.1). To understand whether the liquid jet emerging from the capillary is laminar or turbulent, one can calculate the liquid Reynolds number, Re_l (equation 2.2), where d_l, is the diameter of the solution outlet (i.e. the glass capillary), ρ_l, is the solution density and η_l, is the solution viscosity.

$$Re_l = \frac{d_l \rho_l u_l}{\eta_l} \tag{2.2}$$

The aforementioned study by Mayer [93] showed that a slow-flowing stream of water with a low liquid reynolds number of 800, would emerge from a 2 mm outlet as a continuous column, with a smooth surface (in the absence of a carrier gas). However, for water jets with high liquid Reynolds numbers greater than 10000, surface distortions were observed that resulted in the spontaneous detachment of droplets from the liquid column. A commensurate reduction in the droplet size was observed in the presence of a carrier gas.

It follows from equation 2.2 that an upper limit estimate for the liquid Reynolds number can be obtained by considering a pure stream of o-xylene. (The viscosity of any P3HT solution, although not measured directly, will be higher than that of o-xylene, resulting in a lower Reynolds number). Due to the limitations of the syringe pump used for this work, I was restricted to using liquid flow rates of 800 μL/min or less. Even at the highest liquid flow rate of 800 μL/min, the liquid Reynolds number is ≈ 90, implying the liquid jet is broadly laminar for all flow rates tested. Hence the liquid flow rate was not expected to strongly influence the droplet size distribution. The liquid velocity does affect the relative velocity of the liquid and gas and hence the gas velocity used in the calculation of the gas Reynolds number (equation 2.1). However, since the gas velocity is of order 100 m/s compared to 1 m/s for the liquid, the effect of the liquid velocity is negligible.

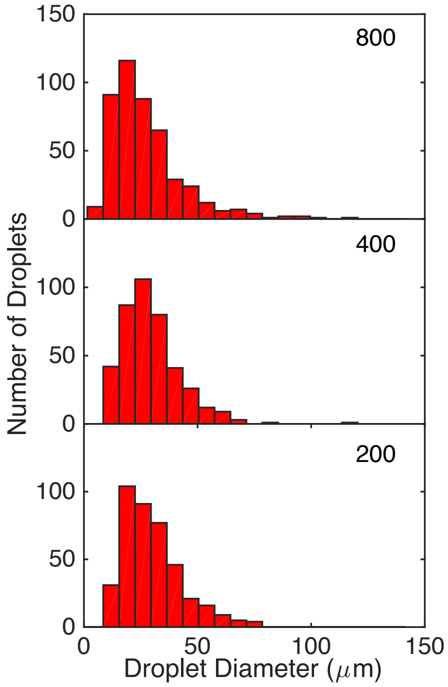

Figure 2.8: Histograms showing the distribution of droplet diameter for different solution flow rates. The number at the top right hand corner of each histogram is the solution flow rate in μL/min. The gas flow rate and capillary diameter were fixed at 20 Lpm and 150 μm, respectively.

Figure 2.8 shows the drop size and size distribution for a constant high velocity carrier gas (424 m/s) and a range of solution flow rates (200, 400 and 800 $\mu L/min$ or 0.43, 0.85 and 1.70 m/s). For the range of velocities shown, both the distribution of droplet sizes and the average droplet size were relatively unaffected by the solution flow rate. The insensitivity of the droplet size distribution to the properties of the solution suggests the solution composition can be optimised in terms of forming smooth films during drying without affecting the atomisation process, thus simplifying the task of ink formation.

2.3.3 Capillary size

The diameter of the liquid column is another factor that may potentially affect the droplet size distribution, since it affects the amount of interfacial contact between the gas and the liquid. There is inconsistency in the literature about the effect of the liquid jet diameter (d_i) on droplet size. Loranzetto and Lefebvre [94] observed, in agreement with Nukiyama and Tanasawa [95], that d_i had little influence on the droplet diameter for low viscosity liquids. Rizk and Lefebvre [96] found that the droplet diameter showed a slight increase with the diameter of the liquid column, but Varga et al observed the opposite [97]. An attempt to reconcile these conflicting observations was made by Jiang et al. [98], who showed (in agreement with Liu et al. [99]) that different behaviour could be observed depending on the liquid jet diameter, and liquid/gas mass flux ratio.

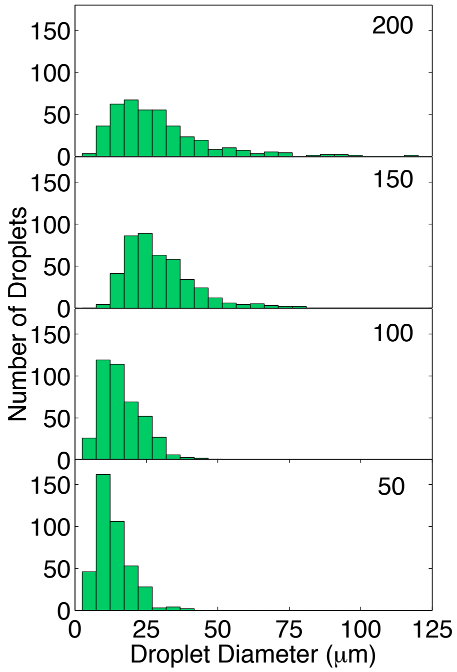

Figure 2.9: Histograms showing the droplet size distributions for different capillary diameters at fixed gas and liquid flow rates of 20 Lpm and 50 μL/min. The number at the top right hand corner of each histogram is the capillary diameter in μm.

Figure 2.9 shows the droplet size and distribution for capillary diameters in the range 50-200 μm. In this case, there is a gradual reduction in droplet size with diminishing capillary diameter. However, due to the limitations of the syringe pump, it was not possible to use capillaries smaller than 50 μm, and so the droplet size distribution could not be improved further using this parameter.

2.3.4 Pressure and ultrasonic spray: a rough comparison

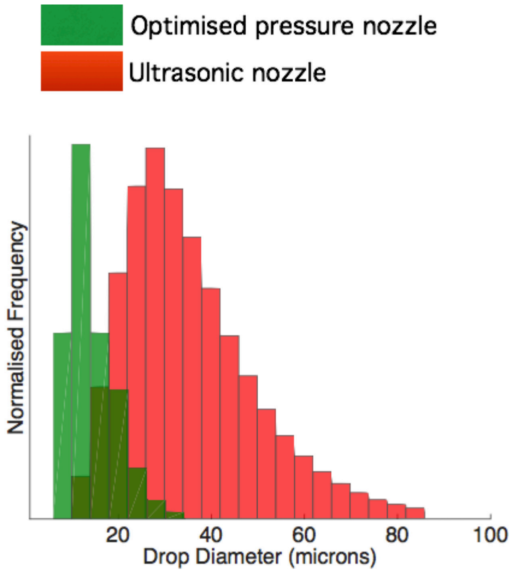

Figure 2.10: Histograms showing size distribution for droplets generated by my gas-driven spray-head (green) and an ultrasonic spray-head by sono-tek (red) [16].

It is often argued that gas-driven spray systems do not compare well with ultrasonic systems in terms of the smallest achievable droplet size. It is therefore interesting to compare the droplet sizes achieved using the spray-head described above with those obtained using a typical ultrasonic nozzle. In the above studies, I found that a glass capillary diameter of 50 μm and a nitrogen flow rate of 25 Lmp yielded the smallest droplets. For comparative purposes the size distribution obtained under these conditions is shown in figure 2.10, alongside the size distribution of droplets produced from water using an ultrasonic spray head, taken from a leading manufacturers' marketing material. Although the histograms relate to different liquids and will have been measured using different techniques, it is evident that the size distribution obtained using the coaxial nozzle is substantially narrower (with a much lower mean droplet size) than for the ultrasonic system. Hence, if the assumption of small droplets being a pre-requisite for attaining smooth uniform films, is correct, it seems feasible that gas-driven spray-heads should also be capable of producing high quality films.

2.4 Development of a spray-deposition rig

Designing of a spray-head that is capable of finely atomising solutions is not the sole requirement for large-area organic device fabrication. In addition, the spray-head must be reliably transported across the coating surface to provide even coverage of the substrate. The spray-deposition system must also operate reproducibly and controllably, in a fully automated manner, minimising the possibility of human error. In the following sections I discuss the design of a complete self-contained system (rig) for spray-deposition and the procedures used to automate it.

2.4.1 Rig design

The spray deposition rig was mounted in a fumehood and comprised an exterior case, an $x - y - z$ gantry for 3-dimensional nozzle motion, and a hotplate. The exterior case was formed from a combination of aluminium framing (Rexroth) and panels of transparent polycarbonate, and served the dual role of shielding the fumehood from the spray, and shielding the spray and the coating surface from the strong convection currents generated by the extraction of the fumehood. An annotated photograph of the finished spray deposition rig can be seen in figure 2.11.

The x-y-z gantry comprised two laser-cut, acrylic stages. The main stage (see figure 2.12a) was attached to four ball bushing bearings that ran along two aluminium, linear guide rails, which were attached to either end of the top of the exterior case (forming the x-axis). Motion along the x-axis was achieved using a pulley system, consisting of two pulley belts (that ran parallel to the linear guides), driven by four stepper motors that operated in sync with one another. The main stage was attached to the pulley belts in four separate positions to ensure smooth motion. As the motors rotated, the pulley belts moved linearly, carrying the main stage along the linear guide rails. The secondary stage (see figure 2.12b) was attached to the bottom of the main stage (as indicated by the red x in figure 2.12), and enabled motion along the y-axis using a similar pulley system (oriented in a perpendicular direction) to that explained above. A linear actuator was also attached to the bottom of the secondary stage, which

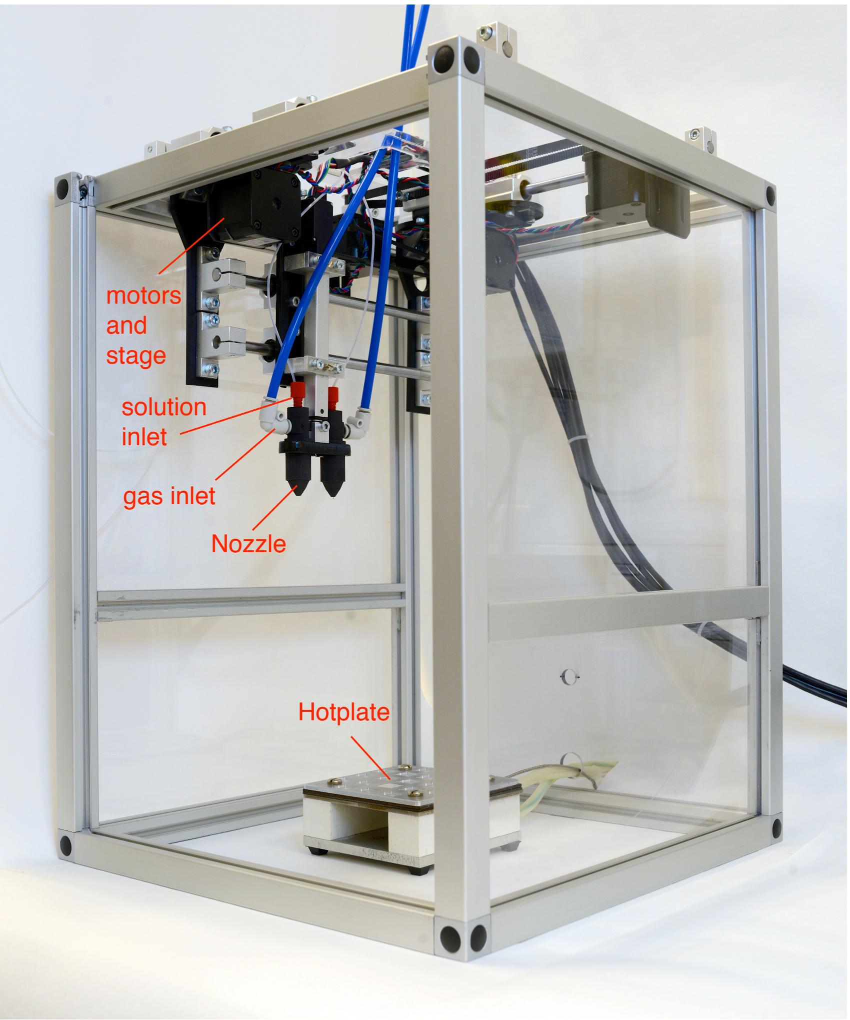

Figure 2.11: An annotated photograph of the spray-deposition rig.

held two spray nozzles and provided motion in the z direction. For the work reported here however, the height was fixed at a constant value of 8 cm above the substrate.

The temperature of the substrate has a strong influence on the final film. A temperature-controlled hotplate was therefore built to hold the substrates. The hotplate consisted of a commercially sourced, temperature-uniform hotplate (Watlow) onto which was secured a 10 cm^2 sheet of aluminium with appropriately shaped 0.5 mm deep recesses for securing the substrates. In addition to allowing the deposition temperature to be controlled, the hotplate also provided the option for post-deposition annealing. An RS232 interface allowed the temperature to be controlled remotely by custom software (see section 2.4.4).

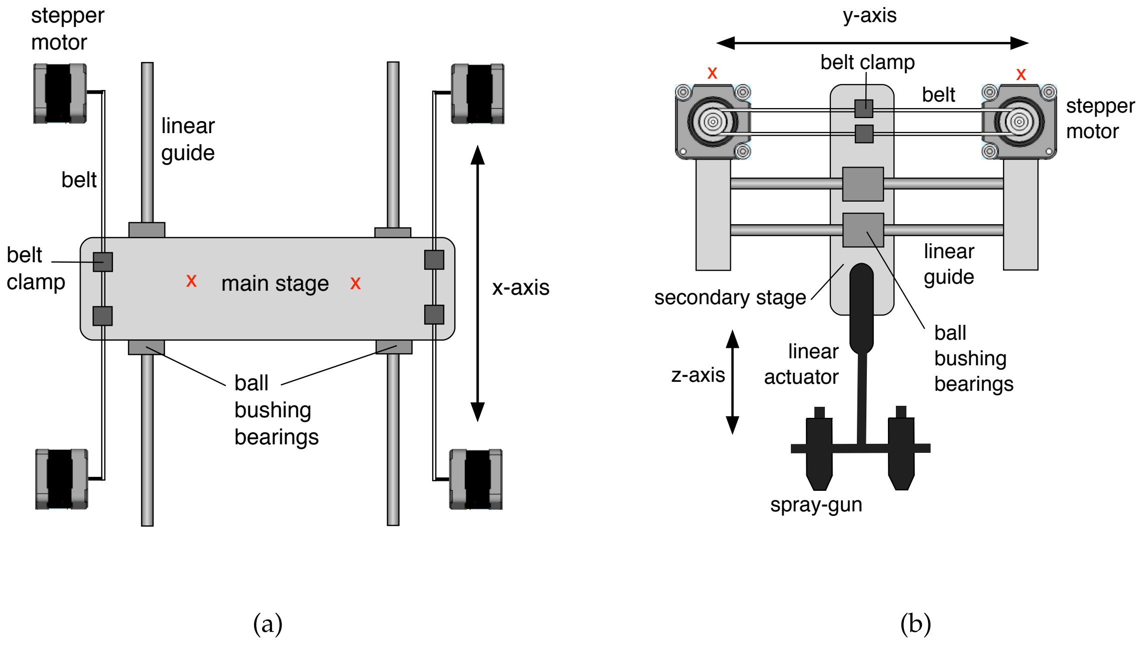

Figure 2.12: Schematic of the x-y-z gantry used to manoeuvre the spray-head comprising (a) a main stage for x-control and (b) a secondary stage for y-z-control. The two stages were attached together in positions indicated by the red x.

The rig was designed to operate in three different deposition modes: single-solution mode, multi-solution mode and multi-spray-head mode. In single-solution mode, a single solution was deposited from a single spray-head. In multi-solution mode, two or more separate solutions were mixed inline using a Y-shaped mixer and then passed into a single spray-head. This mode enabled precise control over solution concentration (by mixing a solution with pure solvent or two solutions of different concentrations). It also enabled solution doping by changing the delivery rates of two different solutions, one containing the solution to be doped and the other containing the dopant. The final mode involved the use of two (or more) separate spray-heads and solution channels to allow several films of different materials to be deposited sequentially. This was achieved by a simple multiplication of the single-solution mode of operation. This multiple-spray-head mode was developed to allow multiple functional layers of a device to be deposited by spray-coating. The work presented in this thesis used the single and multiple-solution modes of operation only.

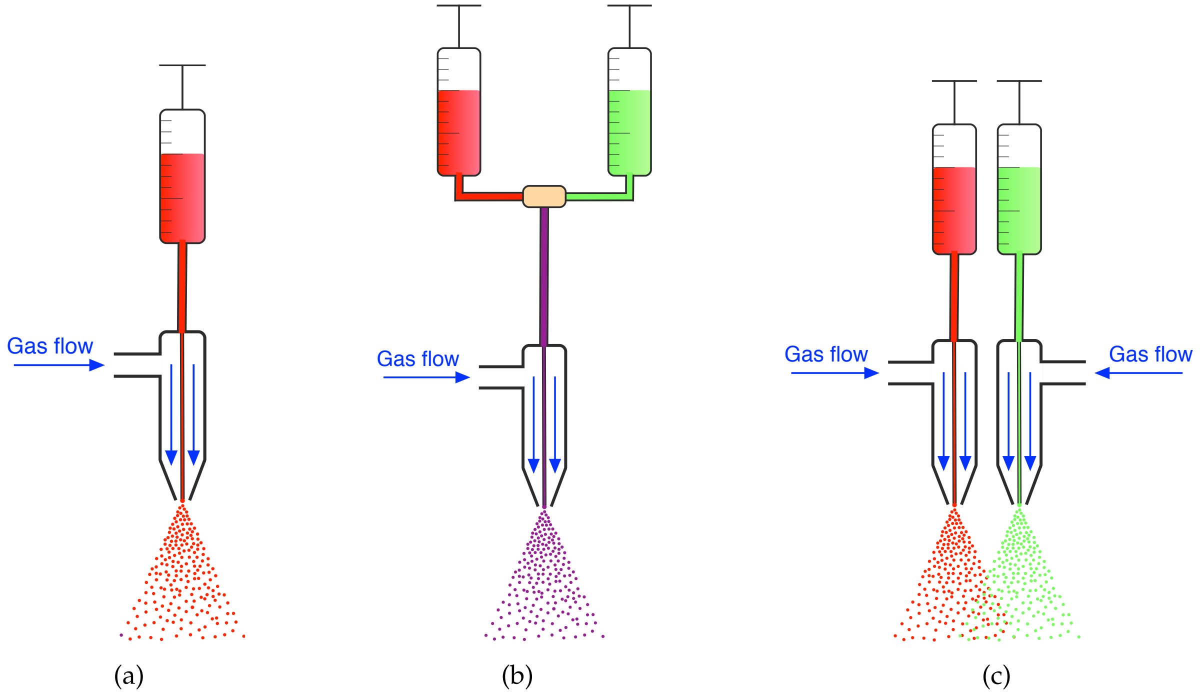

(a) (b) (c)

Figure 2.13: The three modes of operation of the spray-deposition rig. (a) single-solution mode (b) multi-solution mode and (c) multi-spray-head mode.

2.4.2 Automating spray deposition

Arduino-based microcontrollers (Yun and Uno) were used to remotely control the mass flow controller, syringe pumps, motors and hotplate, using the Arduino ”processing language” (which is based on C/C++). The Arduino boards are low cost microcontrollers that are capable of reading analogue or digital inputs from sensors and controlling motors, actuators and other physical outputs. They are also able to communicate with standard shop-bought, commercial instrumentation using a wide variety of hardware protocols. Their low cost (< £ 50) and small footprint (∼ 7 x 6 cm) made them an appropriate choice for use within a fumehood where space is limited and there is a risk of damage due to spillages.

A flowchart explaining the structure of the software program used to automate the spray system is shown in figure 2.14; it identifies subroutines for each of the separate processes, and shows how they work together to form a coherent routine for spray deposition. In brief, the routine starts by setting the relevant deposition variables, namely: carrier gas type, and flow rate, syringe size, solution flow rate, motor speed, spray height, and hotplate temperature. The heater on the hotplate is activated, and the software waits for the hotplate to stabilise at the target temperature. The spray nozzle is set in motion (see below), and the solution and gas are injected into the spray head at the required flow rates using the syringe pump and mass flow controller, respectively. Once the coating process has completed, the motors return back to their "home" positions, the hotplate is either set to a desired annealing temperature or set to cool to ambient temperature, and the gas and solution flow rates are set to zero.

The mass flow controller and syringe pumps were controlled using the Arduino "SoftwareSerial" library, which implements serial communication using two general purpose input/output (GPIO) pins on the Arduino board. Two separate GPIO pins are required for each serial line (i.e. for each instrument being controlled), one is used to send data and the other is used to receive data in accordance with the RS232 protocol. The syringe pump and mass flow controller were controlled using simple ASCII commands as specified in their corresponding user manuals.

Automation of the motors and hotplate was more complex, requiring additional hardware or substantial onboard processing on the Arduino microcontroller. The stepper motors used for *x*-*y* positioning of the spray head were bipolar stepper motors, controlled using two separate pairs of coils. When two (approximately) sinusoidal signals (90° out of phase with each other) are applied to the coils, the rotor rotates at a constant angular velocity between adjacent step positions. Freezing the signals applied to the two coils causes the stepper motor to hold its instantaneous position. Hence speed and position control can be readily achieved by controlling the drive signal to the stepper motor. Generating the requisite sine waves requires substantial processing power and consumes considerable current, so it is convenient to offload this duty onto a separate controller. The option chosen here was an "EasyDriver" stepper motor controller which uses two GPIO pins of the microcontroller to set direction and advance one step or microstep. To ensure smooth motion and avoid "jolting" or "overshooting" of the linear stage, the motors must accelerate/decelerate smoothly from/to rest (see below). For this purpose a prewritten software library "AccelStepper" was employed. The Accelstepper library was used to communicate with the EasyDriver motor Shield, and so control the position, velocity, acceleration and direction of the stepper motors. For the motors used in the rig, one microstep corresponded to a linear travelling distance of 0.0254 mm, thus providing relatively high resolution motion.

The proportional integral derivative (PID) library was used to control the temperature of the hotplate. The code generates an output variable on the basis of two input variables: a process variable, PV (in this case the current temperature), and a setpoint, SP (the target temperature). The current temperature was measured using a K-type thermocouple, which was connected to a thermocouple reader (Adafruit MAX31855K). The target temperature, was defined within the code and the output variable, generated by the PID library, controlled the power to the hotplate via a solid-state relay. The PID library (and PID algorithms in general) uses three user defined tuning parameters (k_p, k_i, k_d) to control how the output is adjusted in order to drive the input towards the setpoint:

$$Output = k_p e(t) + k_i \int_0^t e(t)dt + k_d \frac{d}{dt} e(t) \tag{2.3}$$

where the "error", $e(t)$ is given by

$$e(t) = SP(t) - PV(t) \tag{2.4}$$

The proportional term generates an output that increases proportionally with the deviation from the setpoint. However, since the proportional term falls to zero when the error is zero (causing the heater to switch off), a controller that used only proportional control would always reach a steady state value that fell short of the setpoint. The integral term has the effect of eliminating the steady-state error, but it can make the transient response slower and can lead to unwanted overshoots or oscillations. The derivative term has the effect of reducing the overshoot and improving the transient response, but is very sensitive to noise, and is frequently set to zero in practice. The PID values used to control the hotplate were determined automatically using the Arduino PID Autotune library which involved changing the PID output, observing how the input responded, and subsequently back-calculating the tuning parameters until the desired transient heating characteristics were achieved.

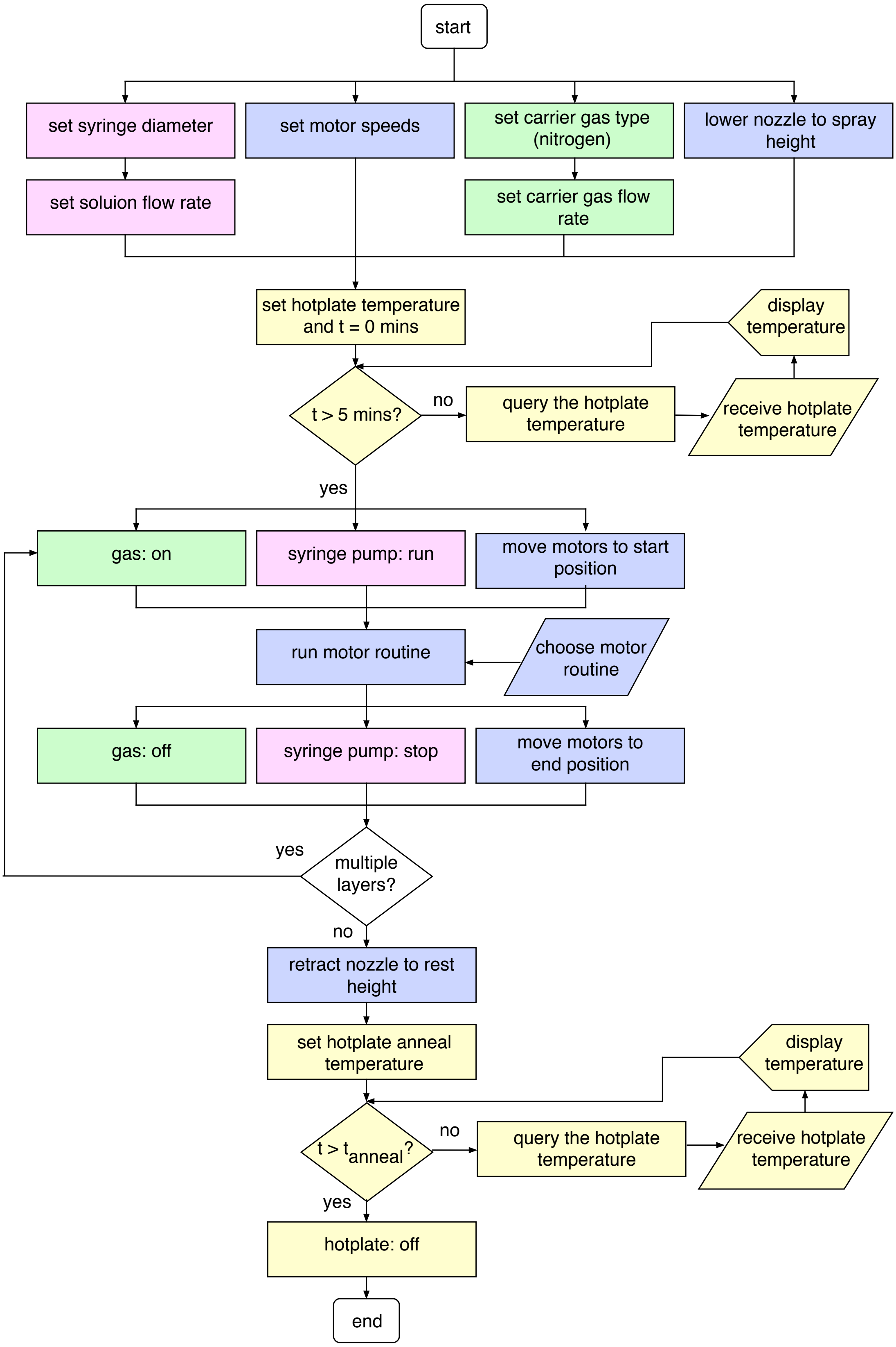

Figure 2.14: A flowchart showing the program structure of the code used to automate the spray-deposition process.

2.4.3 Motor characterisation

Using the AccelStepper library, precise control over the x-y positioning of the nozzle can be readily achieved, allowing a multitude of spray patterns to be realised. In principle, any shape that can be described as a function of x and y, can be sprayed. The conventional raster motion used for spray coating is shown in figure 2.15a. However, it is also straightforward to define more complex geometric patterns such as the spiral in figure 2.15b. The resolution of the chosen spray pattern is limited by both the radius of the spray cone (which is determined by the nozzle height and aperture size), and the smallest distance travelled in a single step of the motor (0.0254 mm). Patterning on the millimetre scale is achievable, but for the purpose of film formation without patterning (and thus for the films documented in this thesis) a raster motion was employed.

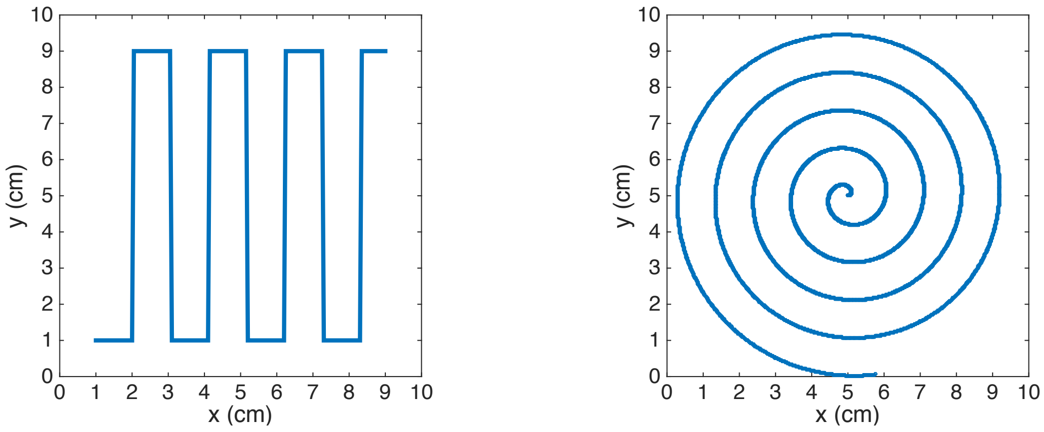

(a)

(b)

Figure 2.15: Plots showing how the x-y positioning of the spray head can be used to create a variety of patterns including (a) a raster pattern and (b) a spiral.

The scan speed of the rig is an important deposition parameter. It is desirable to process at fast speeds, but to form films of uniform thickness, the motion of the spray-head should be smooth, continuous and of a constant velocity. The frequently changing direction of the nozzle during rastering requires the motors to accelerate/decelerate smoothly to avoid any jolting behaviour of the nozzle at the extremes of the raster. It follows that there is an inevitable compromise between the deposition speed and the width over which coating is uniform (see figure 2.16).

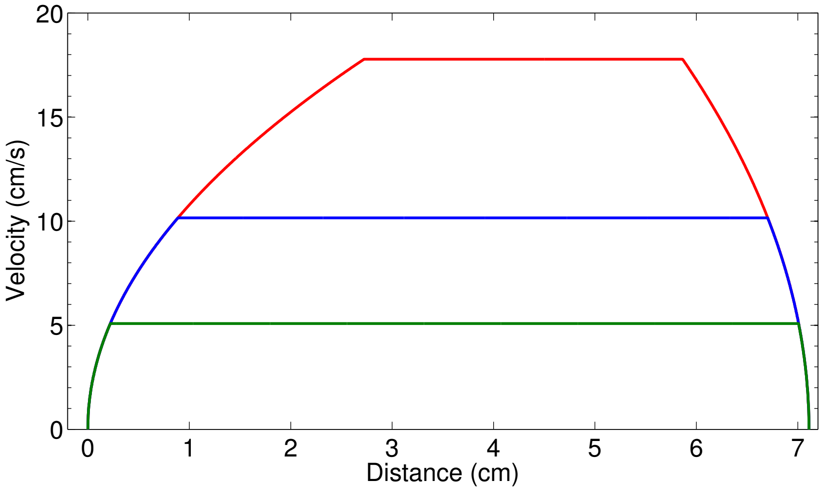

Figure 2.16: A plot showing the distance of travel over which the velocity of the spray-head was constant, when operated at a constant acceleration of 12.7 cm/s^2, for velocities of 5, 10 and 18 cm/s.

It was found that, when accelerating from a stationary start position, the motion of the nozzle was smooth and continuous up to a maximum motor acceleration of 50,000 steps/s^2 or a=12.7 cm/s^2 (above which jolting was observed). The faster the target velocity, $v(t)$, the longer the distance, $s(t)$, required to reach that velocity and the smaller the width of uniform coating $\left(s(t) = \frac{v^2}{2a}\right)$. The distance required to accelerate to the target velocity was determined for a range of velocities which are shown in figure 2.16. Here it is seen that for the spray-head to reach a constant velocity of 18 cm/s, ∼2.5 cm clearance is needed. For a large coating area, as for example used in large-scale coating lines, this clearance distance is insignificant. However, for the small coating area of roughly 10 cm^2 used here, the clearance distance is relatively large, and must be taken into account when spraying at high velocities. (Note, this clearance is required in both directions, so for a target speed of 18 cm/s and a raster length of 10 cm, only 5 cm is usable).

2.4.4 Hotplate characterisation

As previously described, the hotplate was adapted from a shop-bought hotplate by attaching a 2.5 mm thick aluminium sheet (with recesses) to the surface of a uniform Watlow heating panel. The sheet was required to hold the substrates in place at high

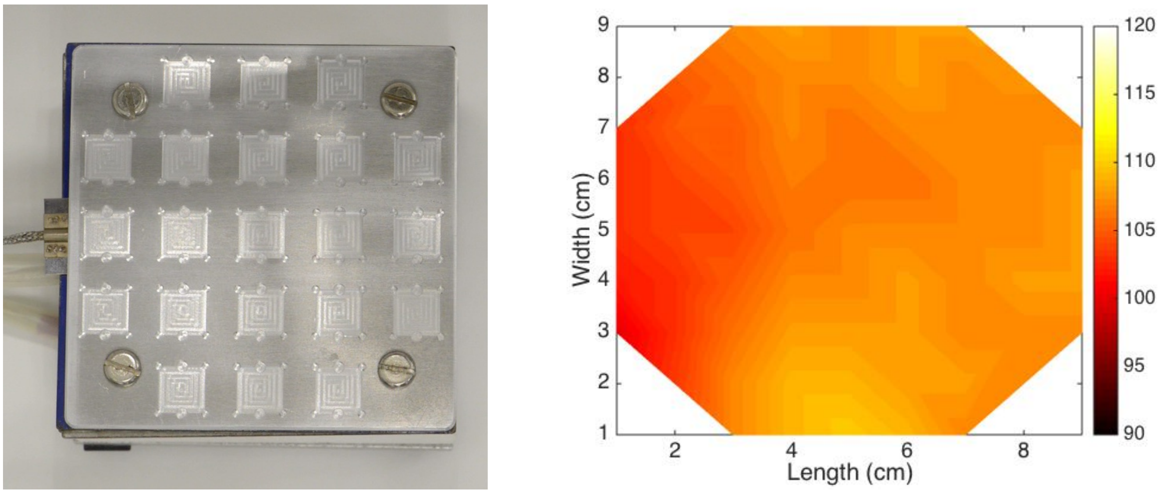

(a)

(b)

Figure 2.17: (a) A photograph of the hotplate showing the recessed areas designed to secure the substrates. (b) A temperature map of the hotplate at 100 °C.

gas velocities. A flat K-type thermocouple was wedged tightly between the surface of the Watlow panel and the aluminium layer to monitor the temperature of the heater. Once stabilised, the temperature of the surface was measured using a surface temperature probe at 21 uniformly spaced positions on the hotplate using a setpoint temperature of 100 °*C*. The temperature distribution across the surface of the hotplate was fairly uniform, with each temperature measurement being within 10 % of the setpoint temperature. A temperature map was formed from these measurements and is shown in figure 2.17. From this map, it is evident that the leftmost 3 cm of the hotplate (close to the position of the thermocouple) was slightly lower in temperature than the rest of the plate. This is due to the presence of the thermocouple, which reduces the contact between the surface of the Watlow hotplate and the aluminium sheet. This was not considered to be a significant problem as the difference in temperature between this region and the rest of the hotplate was small.

Ideally the hotplate should respond rapidly to changes in the target temperature. The time required for the hotplate to heat or cool to a specified temperature should be as short as possible as it adds to the overall processing time for the deposition process. At the same time, it is important not to heat too quickly as this can cause the temperature of the hotplate to overshoot its target, potentially damaging the polymer film (since the annealing temperature is often close to the temperature at which the polymer degrades). The hotplate should ideally reach its target temperature monotonically without significantly overshooting the temperature. Both the speed and settling time of heating and cooling are dependent upon the PID values chosen in the code used to control the Watlow heater, as explained in section 2.4.2.

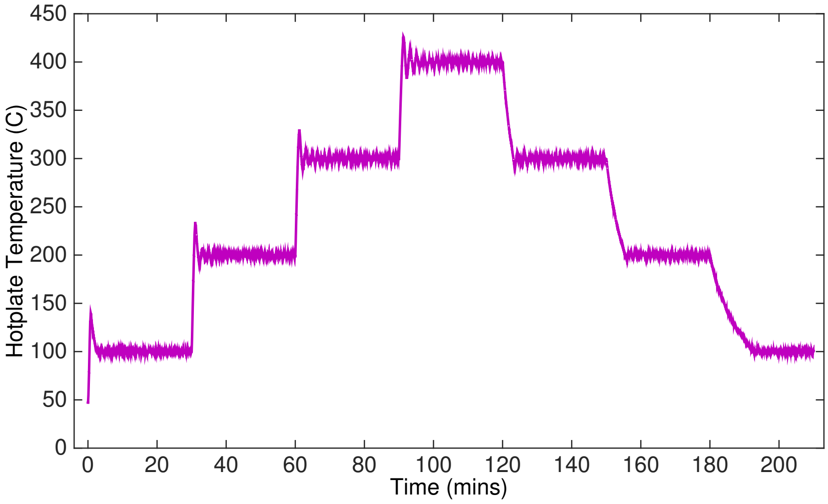

Figure 2.18: A plot showing the transient response of the hotplate during heating and cooling using optimised PID gain parameters.

Figure 2.18 shows the transient response of the hotplate during heating and cooling using optimised PID gain parameters determined by the autotuning library. On heating, the temperature overshot the setpoint temperature by approximately 30 °C, but recovered within one minute. The overall time taken for the temperature to stabilise was less than 5 minutes for the range of temperatures measured (100 °C - 400 °C). No undershoot was observed on cooling since there was no active cooling of the hotplate, (cooling was solely due to heat loss to the ambient). For the same reason, the time taken to stabilise at the target temperature increased slightly as the setpoint approached room temperature. The stabilisation time was in all cases less than 10 minutes and was therefore considered reasonable. The code controlling the spray coater ensured coating would not begin until the hotplate had stabilised at its target temperature.

2.5 Summary

In this chapter I have discussed the development of an automated gas-driven spray-deposition system, specifically for the deposition of thin semiconducting polymer films. A rational design for a gas-driven spray-head was proposed and shown to be capable of generating suitably small droplets with mean diameters down to 18 μm. The average droplet size was shown to decrease on increasing the carrier-gas velocity and decreasing the ink-outlet capillary diameter, but varying the solution flow rate had no observable effect. Moreover, the average size and size distribution of droplets generated with the new spray-head design, under optimum operating conditions, were found to be comparable to those generated using more complex ultrasonic spray-heads. This suggests that contrary to common assertions in the literature, gas-driven spray-heads should be as capable as ultrasonic systems of depositing smooth, homogenous polymer films. I finally discussed the design of a rig to enable fully-automated spray-deposition, with fine control over operating parameters including spray-head positioning, transportation speed, and hotplate temperature.

3 Characterising spray-deposited polymer films

The surface roughness and film uniformity have a strong influence on the performance of organic devices. Experimental methods for obtaining information about the profile of the surface are therefore critical for determining optimal spray conditions. Surface roughness can be determined in many ways, ranging from detailed nm-resolution topographical information from scanning probe techniques such as atomic force microscopy, to simple low resolution information from optical or fluorescence microscopy. At the very least, it is necessary to ensure macroscopic uniformity of the films, avoiding pin holes that would lead to catastrophic shorting between the anode and the cathode in a device. In this section I describe the techniques used to characterise the spray-deposited polymer films presented in this thesis.

3.1 Optical microscopy

Optical microscopy was used to image each spray-deposited film using an Olympus BX51 optical microscope (see section 2.2). All spray-deposited films exhibited micron-sized surface features that matched the shape of the discrete droplets described in the previous chapter. Although features of this kind were observed in all of the films presented in this thesis (as well as sprayed films reported in the literature), their size and prominence were extremely sensitive to the operating parameters of the spray-head, rig variables (such as motor speed and height of the spray-head), substrate temperature, and solution composition. For instance, figure 3.1 shows high and low magnification optical microscope images of a thin film of 21 kg/mol P3HT, sprayed at a fast rastering rate of 25.4 mm/s, from a low concentration (5 mg/ml) solution (figures 3.1a and 3.1b), and a thick film of the same molecular weight P3HT, sprayed at a low rastering rate of 1.27 mm/s, from a high concentration (20 mg/ml) solution (figures 3.1c and 3.1d). The height of the spray-head from the substrate was ∼10 cm in both cases, and the substrate was held at room temperature. Whilst droplet-shaped surface features were observed in both cases, the visual appearance of the films was very different. For reasons discussed in detail in section 1.4, the former conditions result in a thin strongly coffee-stained deposition, while the latter give rise to a more uniform film.

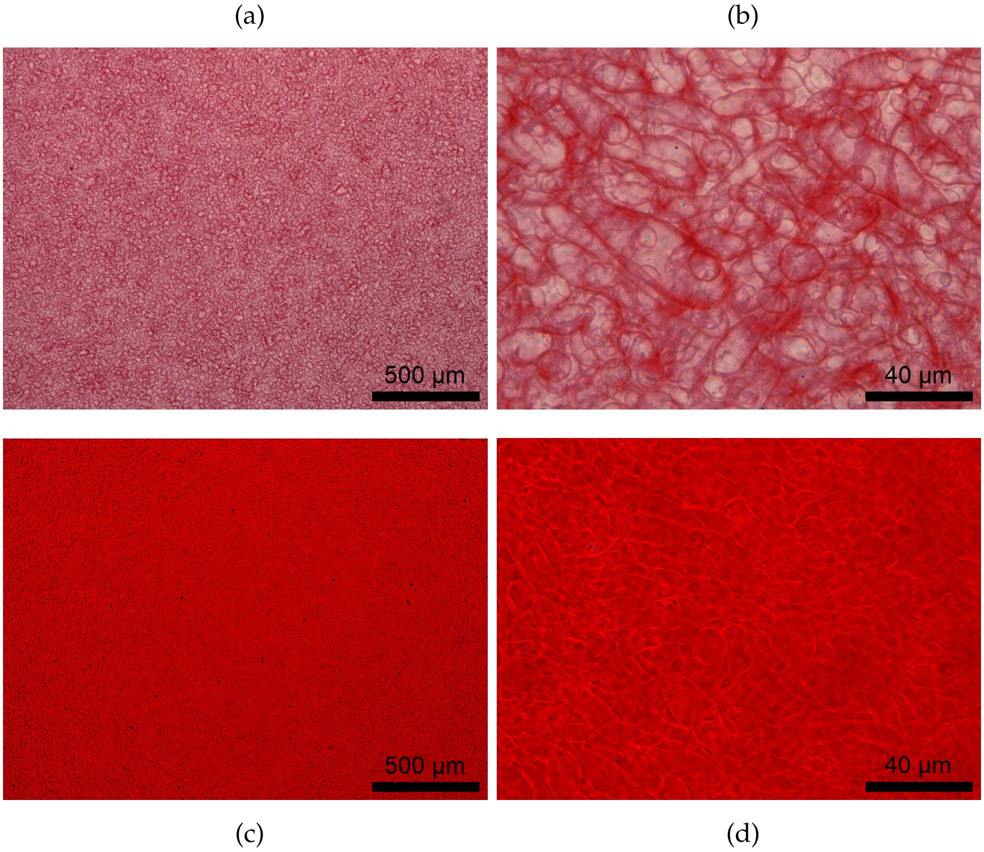

Figure 3.1: Optical micrographs of two spray-deposited films, deposited using very different operating parameters. For images (a) and (b) the concentration of P3HT was 5 mg/ml, the solution flow rate was 50 μL/min, and the raster speed was 2.54 cm/s. For images (c) and (d) the concentration of P3HT was 20 mg/ml, the solution flow rate was 200 μL/min, and the raster speed was 0.254 cm/s.

Optical microscopy provides only qualitative information about the film quality. Whilst there are clearly large differences in the appearance of the two films, these are difficult to quantify. Alternative techniques are therefore required to provide quantitative or semi-quantitative information about the surface profile.

3.2 Atomic force microscopy

Atomic force microscopy (AFM) is routinely used to investigate the surface topography of polymer films with a typical in-plane resolution 1-1000 nm that greatly outperforms optical microscopy. The technique involves the use of a sharp silicon tip which is rastered across the surface of a substrate. The tip is supported on a cantilever, the back of which reflects a laser beam onto a quadrant photodiode. As the tip interacts with the substrate, it exerts attractive or repulsive forces on the cantilever, causing it to bend. This bending in turn causes the laser to be reflected onto different parts of the photodiode, allowing the tip-substrate interaction to be measured. The technique provides a quantitative mapping of film topography, from which the root mean square roughness (RMS) can be obtained. This mode of operation is known as ”contact mode” AFM, and is heavily influenced by frictional and adhesive forces, which can damage samples and distort image data.

Alternatively, it is possible to work in ”tapping-mode” where the tip only touches the surface for a short time, thus avoiding the issue of drag across the surface. Typical tapping-mode operation is carried out using amplitude modulation detection with a lock-in amplifier. The cantilever is made to oscillate up and down at or near its resonance frequency by a small piezoelectric element mounted in the AFM tip holder. Forces acting on the cantilever when the tip comes close to the surface (Van der Waals forces, dipole-dipole interactions, electrostatic forces, etc), cause the amplitude of the oscillation to decrease as the tip gets closer to the sample. An electronic servo uses the piezoelectric actuator to control the height of the cantilever above the sample. The servo adjusts the tip height to maintain a constant amplitude as the cantilever is

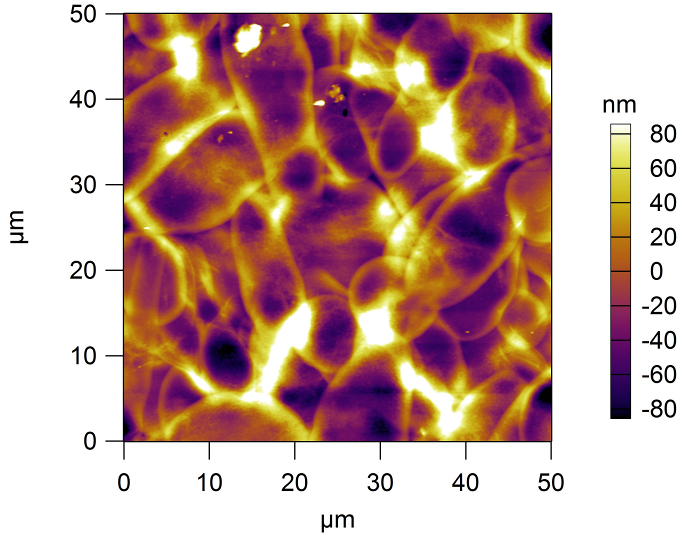

Figure 3.2: A characteristic atomic force microscopy image of a spray-deposited film of P3HT, showing droplet-shaped surface features.

scanned over the sample. A tapping AFM image is produced by imaging the force of the intermittent contacts of the tip with the sample surface.

The AFM images presented in this thesis were recorded by Alex Ramadan using a MFP-3D AFM (Oxford Instruments Asylum Research, Santa Barbara, USA) in AC mode (tapping mode) using Olympus AC240-TS silicon tips. Figure 3.2 shows a tapping-mode AFM image for a typical spray-deposited film of P3HT, deposited using my spray-coater. The droplet-shaped features observed here are consistent with those observed using optical microscopy, confirming a build-up of material along the perimeter of the droplet. From these measurements, the surface roughnesses (RMS) of the spray-deposited films were calculated to be in the region of $\sim$ 20-50 nm, depending on the film thickness and processing parameters. Whilst these values are relatively high compared to spin-coated polymer thin films (RMS $\sim$ 4 nm), they are broadly comparable to other spray-deposited polymer films reported in the literature, which range from $\sim$10 nm for the very best ultrasonically deposited films to >70 nm for films sprayed using hand-held gas-driven nozzles (for films that are approximately 100 nm in thickness).

Although AFM provides a quantitative measure of film roughness, it is a slow, linear process best suited to small ($\ll$100 μm x 100 μm) areas. For the work described in this thesis, I required a much faster method that would allow me to map out the uniformity of films of area up to 1 cm^2. The optical method described below was developed to address this need.

3.3 Optical profiling of polymer films

3.3.1 Measurement principle

The technique I used has its origin in the Beer-Lambert law for optical absorption, which states that the intensity of light transmitted through a material (I_t) diminishes exponentially with distance

$$I_t(x) = I_0 exp(-kx) \tag{3.1}$$

where I_0 is the intensity of the incident light, x is the distance from the front of the sample and k is a proportionality constant known as the absorption coefficient. This can be explained by considering the situation in figure 3.3. Here, light with intensity I_0 strikes the sample perpendicular to the surface and passes through a thickness/path-length b, which contains N absorbing molecules/cm^3, causing the intensity of the light to reduce to I_t. If we consider a cross-section of the sample having an area S and an infinitesimal thickness dz, located at a distance z from the surface, the number of molecules present in the infinitesimal block is

$$NSdz \tag{3.2}$$

If each of these molecules has a cross-sectional area, σ, the fractional area of each molecule (where light gets absorbed) is $\frac{\sigma}{S}$, and the total fractional area for all molecules in the block is therefore

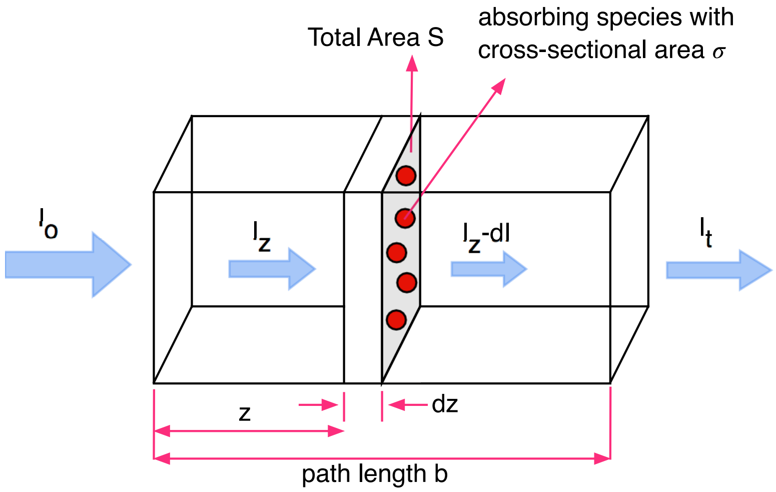

Figure 3.3: A schematic showing the loss of light intensity in passing through an infinitesimal slice of absorbing medium.

$$\sigma N dz \tag{3.3}$$

If I_z is the intensity of the light entering the infinitesimal block and dI is the change in intensity due to the absorbing molecules, the fraction of light absorbed can be written as $\frac{dI}{I_z}$. Since the probability of light striking a molecule is equal to the fractional area presented by the molecules, it follows that

$$-\frac{dI}{I_z} = \sigma N dz \tag{3.4}$$

Integrating this equation between the limits z=0 to z=b gives:

$$-\ln\left(\frac{I_t}{I_0}\right) = \sigma N b \tag{3.5}$$

By taking exponents of this equation we arrive back at equation 3.1, where the absorption coefficient, $k = \sigma N$. This can be re-expressed in logarithms of base 10 as:

$$b = -\frac{1}{\sigma N}\log_e(10)\log_{10}\left(\frac{I_t}{I_0}\right) \tag{3.6}$$

from which it follows that

$$b \propto -\log_{10}\left(\frac{I_t}{I_0}\right) \tag{3.7}$$

where the expression on the right hand side is known as the absorbance, A. Assuming all parts of the film have the same absorption coefficient, k, we can map out the thickness, b, of a film by measuring its absorbance at uniformly spaced points. The linearity between absorbance and film thickness has been confirmed experimentally for spin coated thin films of P3HT, using Atomic Force Microscopy. This behaviour was shown to hold true for films deposited from a variety of solvents [100], as can be seen in figure 3.4. Similar behaviour has also been observed for other conjugated polymers including electrodeposited PEDOT [101], indicating that for many conjugated polymers, interference effects do not cause any deviation from Beer-Lambert behaviour.

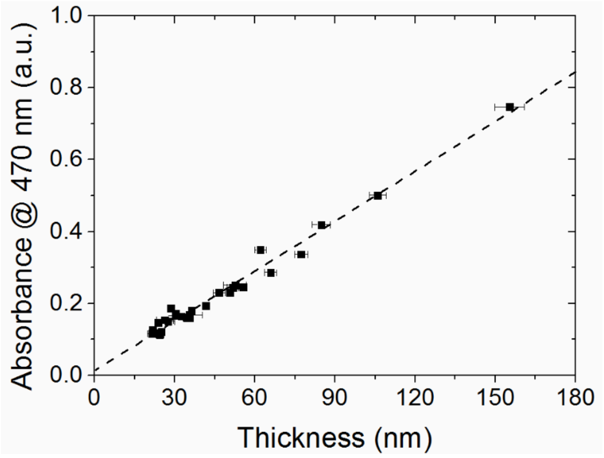

Figure 3.4: Thickness dependence of the optical absorbance of P3HT films at 470nm. Data is shown for films processed by spin coating from chloroform, toluene, chlorobenzene and dichlorobenzene. Taken from [100].

3.3.2 Design of an optical profiling rig

A simple optical setup was used to map out the absorbance of the films and hence determine their spacial uniformity. A band-pass filter centred at 540 nm was placed on top of a white light photography box (MedaLight) to provide a large illumination source with a relatively narrow wavelength range between 450 and 650 nm. A Raspberry Pi camera (five megapixel fixed-focus) was positioned a short distance (1-2 cm) above the filter, with sufficient clearance to allow a coated or uncoated glass slide to be inserted between the two. The lens of the camera was adjusted to obtain a sharp focused image, Φ, of the upper surface of the glass substrate on the camera sensor. A schematic of the setup is shown in figure 3.5.

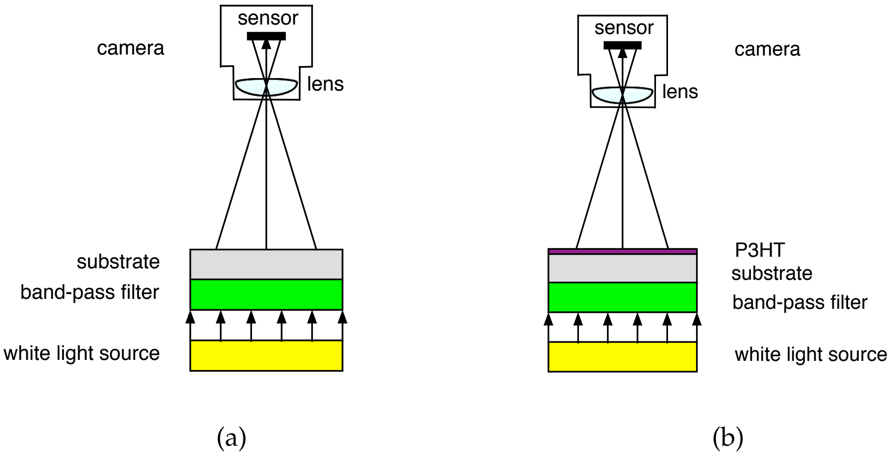

Figure 3.5: A schematic of the system used to obtain spatially-resolved absorbance maps of large-area polymer films. (a) Setup for measuring the background image, Φ_{bck}. (b) Setup for measuring the sample image, Φ_{film}.

The method is based on a two dimensional absorption measurement, calculated from three photographic images. The first image Φ_{film}, was obtained with the coated substrate in place and the light box on. The second image, Φ_{bck}, was obtained with an uncoated substrate in place and the light box on. The final image, Φ_{dark}, was obtained with the light box off. For the work reported here, all images were obtained using a low-cost Pi camera and Raspberry Pi computer, costing approximately £ 50 in total. Unlike conventional absorption spectroscopy, the incident light was not monochromatic but comprised a fixed range of wavelengths that were chosen to broadly cover the absorption spectrum of P3HT (400-650 nm). This has implications for the accuracy of the measurement as described below, but for now we treat the signal as if it were obtained at a single wavelength. For each of the 10-bit images used in the measurement, the signal recorded by each pixel on the Pi camera image sensor corresponds to a different spatial location on the film, and is digitised into 1024 discrete levels. These intensity values (levels) are used to calculate the absorbance, A, for each of the pixels in the substrate image using the following equation:

$$A = -\log_{10}\left(\frac{\Phi_{film} - \Phi_{dark}}{\Phi_{back} - \Phi_{dark}}\right) \tag{3.8}$$

The measurement relies on each pixel detecting the same area of the light source for each of the images. For this reason, care must be taken to fix all optical components in place and to avoid misalignment during insertion or removal of the glass slides. Using the absorbance values calculated from each pixel, a two dimensional map is generated of the absorbance across the film. Figure 3.6 demonstrates this process for a spray-coated film of P3HT; the substrate, background and dark images are shown in figures 3.6a, 3.6b, and 3.6c, respectively and the absorbance map of the film is shown in figure 3.6d. Importantly, if we make the assumption that the absorption spectrum of the deposited material is the same everywhere (irrespective of film thickness or how the film has dried), it follows from equation 3.7 that the absorbance map is also a map of film topography since the absorbance is proportional to the film thickness, b.

The absorbance map of the film therefore provides a simple and rapid way to quantitatively measure film uniformity. For a smooth, continuous, uniform film, the absorbance values measured using each pixel will be very similar and follow a narrow Gaussian distribution. For a rough or uneven film however, the absorbance values will show large variations, leading to a broadening of the distribution. The standard deviation and relative standard deviation in the measured absorbance, are the principal figures of merit I used to characterise and optimise my spray-deposited films. The standard deviation measures the root-mean-squared variation in absorbance about the mean. The relative standard deviation is defined as the ratio of the standard deviation to the mean absorbance, and provides a useful means of comparing film uniformity in films of different thickness. The spatial resolution and precision of the measurement are important, since they determine the smallest features (both horizontal and vertical) that can be resolved using this approach, and thus determine the limitations of this technique for measuring film uniformity.

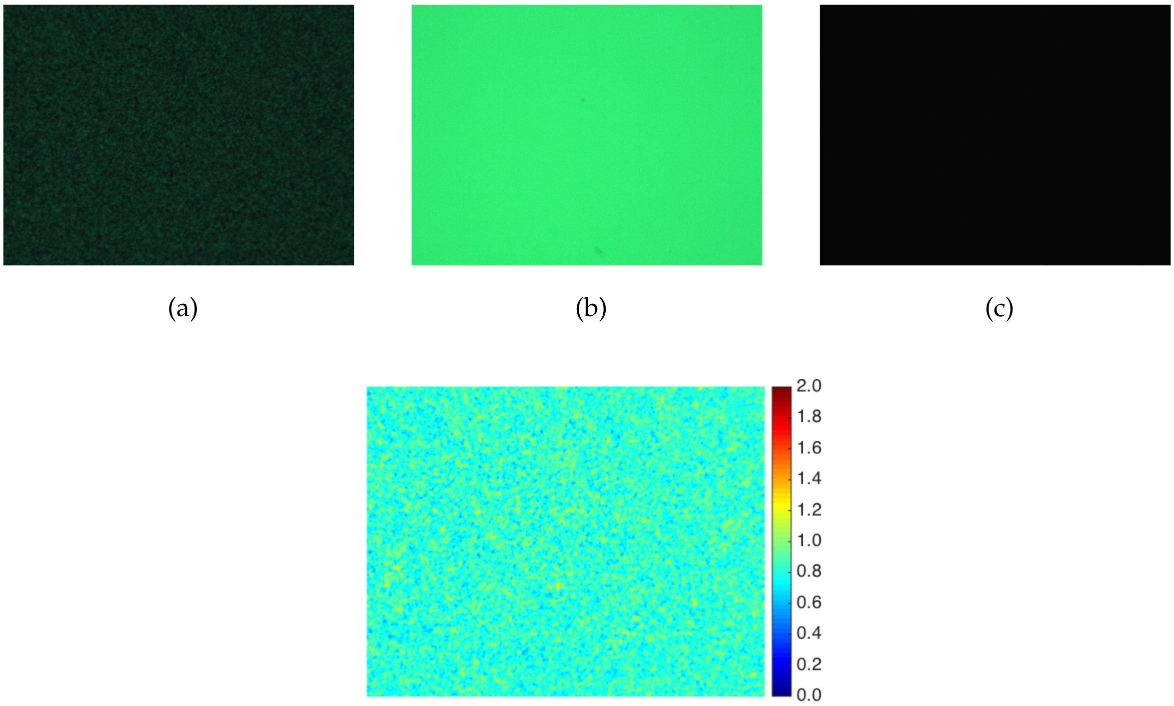

(a) (b) (c)

(d)

Figure 3.6: The substrate (a), background (b), and dark (c) images obtained from the rig shown in figure 3.5. The three images are used to create an absorbance map (d) of the film via equation 3.8.

The absorbance mapping measurement is limited by the pixel count of the camera and the bit-depth of the stored images, both of which should be as high as possible. The pixel count of the camera determines the spacial resolution of the image. A higher pixel count leads to an image with greater detail, allowing smaller features to be mapped out. In addition to the absolute number of pixels in an image, the pixel coverage of the substrate is also important. A high pixel count is of little benefit if the substrate being imaged only constitutes a small fraction of the total image. To ensure the substrate fills the image it is necessary to adjust the focal plane of the camera by varying the distance between the camera's focusing lens and its image sensor. The Pi camera has a fixed lens, but this can be partially unsecured from its holder, bringing the focal plane closer to the image sensor and so ensuring the region of interest on the substrate fills an appreciable fraction of the image. In this way, the optical set up was configured to image an area of 1.33 cm^2 on the substate, using 794 pixels by 590 pixels on the image sensor, implying each pixel monitored an area of 17 μm x 17 μm. Whilst the use of a camera with a higher pixel count than that of the Pi camera would further increase the resolution, this was deemed sufficient for the current application.

The bit-depth of the stored images determines the number of levels used to quantify the intensity of light falling on the pixels, and therefore governs the precision of the absorbance measurements. A higher bit depth provides better intensity resolution and so increases the precision of the absorbance values calculated for each pixel. For the measurements reported here, the resolution of the extracted absorbance values was limited by the capability of the raspberry Pi camera to capture and process digital images. Although the analogue to digital converter in the Pi camera generates a ten bit image, by default the Raspberry Pi processes images as compressed eight bit graphics files to reduce data processing times. To avoid image compression (and consequent loss of information) during image processing, images were saved as ten bit RAW files and were latter demosaiced using software written in MATLAB to extract the relevant pixel information. Recording images in RAW format allows the full ten bits of the image to be exploited and (as we explain below) allows absorbance values of up to 3 to be measured.

The reliability of the absorbance measurements is influenced by many factors, including lamp stability, noise in the image sensor, the mechanical stability of the optical setup, the level of ambient light, and the optical density of the substrate. To reduce noise-related errors in the absorbance measurements, the pixel intensities were averaged over ten repeats measurements for all three of the images used in the calculation. To test the absorbance mapping technique, I first decided to apply it to the absorbance mapping of a series of neutral density filters of known optical density (absorbance). The neutral density filters were chosen as they were expected to be optically uniform with an absorbance that would not vary appreciably with position. The measured distributions in absorbance would therefore indicate the intrinsic standard deviation associated with the technique. This in turn would determine the smallest standard deviation in absorbance that could be measured using this technique. Figure 3.7 shows the distributions in absorbance values for a series of neutral density filters with optical densities of 0.5, 1.0, 1.5 and 2.0, using 1, 10 and 50 averages. It is clear that in all cases,

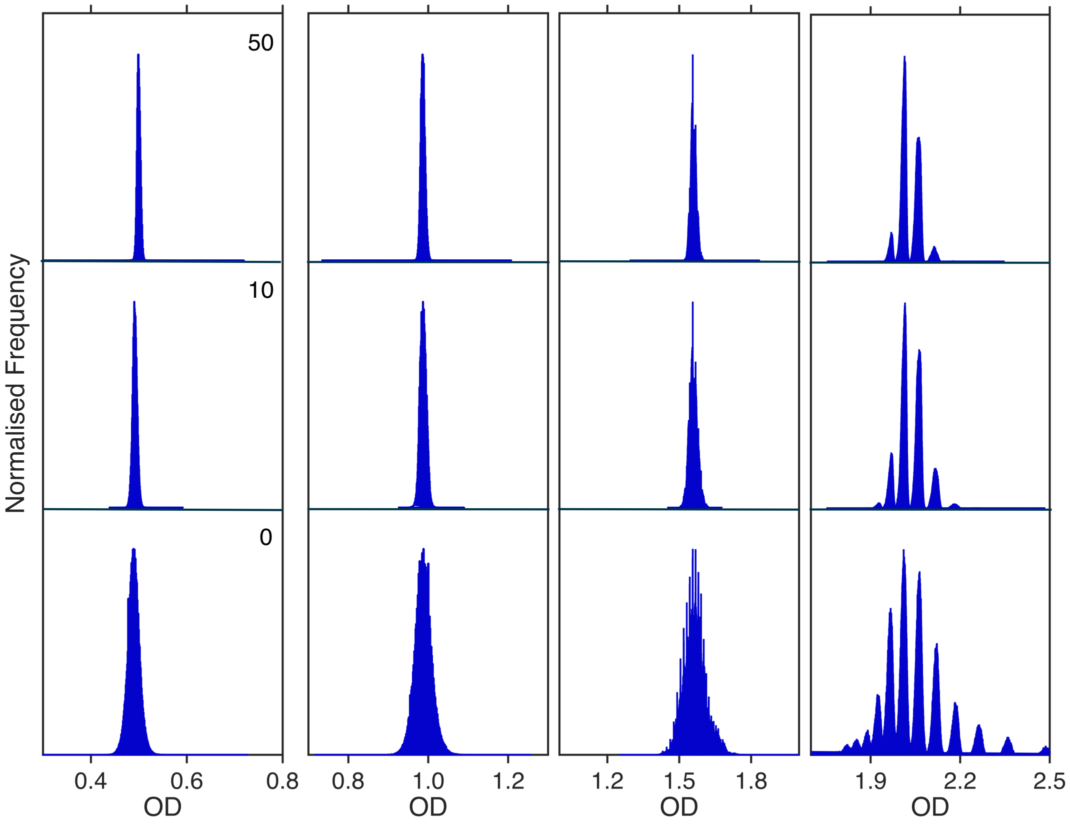

(a) (b) (c) (d)First sub-figure

Figure 3.7: Histograms showing the distributions in absorbance for neutral density filters with optical densities of (a) 0.5 (b) 1.0 (c) 1.5 and (d) 2.0, calculated using equation 3.1, with 1, 10 and 50 averages.

the mean absorbance closely matched the nominal absorbance of the neutral density filter, confirming the general reliability of the technique. As expected, increasing the number of averages reduced the standard deviation in the measured absorbance (due to fluctuations in the lamp intensity and camera response being averaged out). Figure 3.8 shows the standard deviation versus number of averages for a neutral density filter with an optical density of 1.0. The standard deviation decreased monotonically with the number of averages until 30 averages, at which point the standard deviation in absorbance was approximately 0.005. this value corresponds to the real standard deviation of the sample, uncontaminated by measurement noise.

It is clear from figure 3.7 that as the nominal absorbance of the neutral density filter was increased, the variation in the measured absorbance also increased. To better demonstrate these trends, the standard deviation and the relative standard deviation

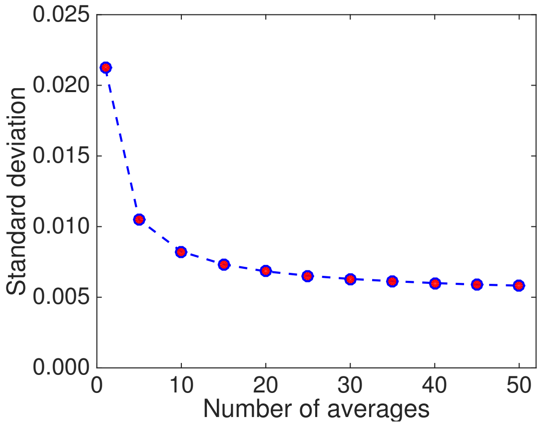

Figure 3.8: A plot showing the standard deviation of the distributions in absorbance vs. the number of averages taken for each of the images used in the absorbance calculation. The data was obtained using a OD 1.0 neutral density filter.

of each of the distributions are plotted against the mean optical density in figure 3.9a. The differences in standard deviation between absorbance measurements made using 10 averages and 50 averages was extremely small. With this in mind, and in the interest of minimising the time taken to complete each measurement, I settled on 10 as the standard number of averages for the absorbance measurement. (Note, owing to the modest processing power of the Raspberry Pi, acquiring a RAW image and transferring it uncompressed to a separate PC for further analysis took $\sim$ 10 s, hence 10 averages took 100 s to acquire).

Although the variation in absorbance was not expected to differ substantially for the various optically smooth filters, the standard deviation increased non-linearly with optical density. This is due to the difficulty of measuring the absorbance of highly absorbing substrates. This is especially clear for the highest optical density filter tested (OD 2.0), shown in figure 3.7d. At high optical densities, the noise associated with the measurement is high and, as a result, the measured absorbance values become quantised.

In principle the maximum optical density that can be measured with the system should be determined by the ten bit resolution of the image sensor. Assuming the system is configured to give a background close to saturation of the sensor (1023 units), the

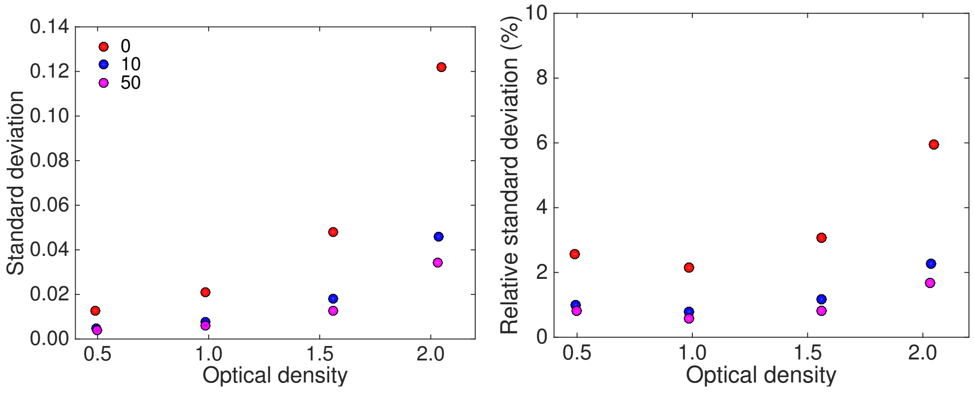

(a)

(b)

Figure 3.9: Plots for neutral density filters showing how (a) the standard deviation and (b) the relative standard deviation of the absorbance distributions varies optical density, for 1, 10 and 50 averages.

minimum (non-zero) level of transmitted light with the filter in place will be one unit, corresponding to an optical density of

$$-\log_{10}\left(\frac{1}{1023}\right) \sim 3 \tag{3.9}$$

In practice, due to the additional noise/jitter in the analogue to digital conversion, the practical upper limit for the optical density is about 2.3. This could be improved by using a better camera with a higher bit depth, but was found to be adequate for the film uniformity measurements described below. Irrespective of the reason for the non-linear relationship between the mean absorbance and the standard deviation of the absorbance distributions, the data provides useful information about the limitations of this measurement. For absorbances determined using 10 averaged images, the minimum measurable standard deviation was around 0.01 for optical densities $\leq$ 1.5, increasing to 0.04 for optical densities in excess of 2. This corresponds to a relative standard deviation in the absorbance of around 1.5-2%, and provides an approximate indication of the limitations of the experimental procedure.

3.3.3 Evaluation of the measurement accuracy

In the earlier discussion it was assumed for simplicity that the light source was monochromatic, although in reality it had a broad emission spectrum spanning from 420 to 650 nm. To obtain a proper estimate of the film thickness, it would be necessary to determine the absorbance at one or more wavelengths, which would require spectral information about the transmitted light $I(\lambda)$, together with the emission spectrum of the filtered light source $I_0(\lambda)$ and the spectral response $S(\lambda)$ of the (green) detector in the camera. The absorbance at a given wavelength could then be determined from:

$$A(\lambda) = -\log_{10}\left(\frac{I(\lambda)S(\lambda)}{I_0(\lambda)S(\lambda)}\right) = -\log_{10}\left(\frac{I(\lambda)}{I_0(\lambda)}\right) \tag{3.10}$$

For the optical profiling technique we ignored the broadband nature of the light source and estimated the absorbance from the following expression

$$A^* = -\log_{10}\left(\frac{I}{I_0}\right) \tag{3.11}$$

where I and I_0 were the signals recorded by a pixel on the digital camera with and without the absorbing sample in place. This is equivalent to estimating the absorbance using the equation

$$A^* = -\log_{10}\left(\frac{\int\limits_{\lambda_a}^{\lambda_b} I(\lambda)S(\lambda)d\lambda}{\int\limits_{\lambda_a}^{\lambda_b} I_0(\lambda)S(\lambda)d\lambda}\right) \tag{3.12}$$

Equations 3.12 and 3.10 are only equivalent for the case where $I(\lambda)$ is monochromatic. Hence, it is important to determine how closely the approximate absorbance, A^*, determined from equation 3.11 differs from the true absorbance, A.

The (true) absorbance, A, of a film of thickness d is related to the (true) absorbance, A_0, of a film of thickness, d_0, by the expression

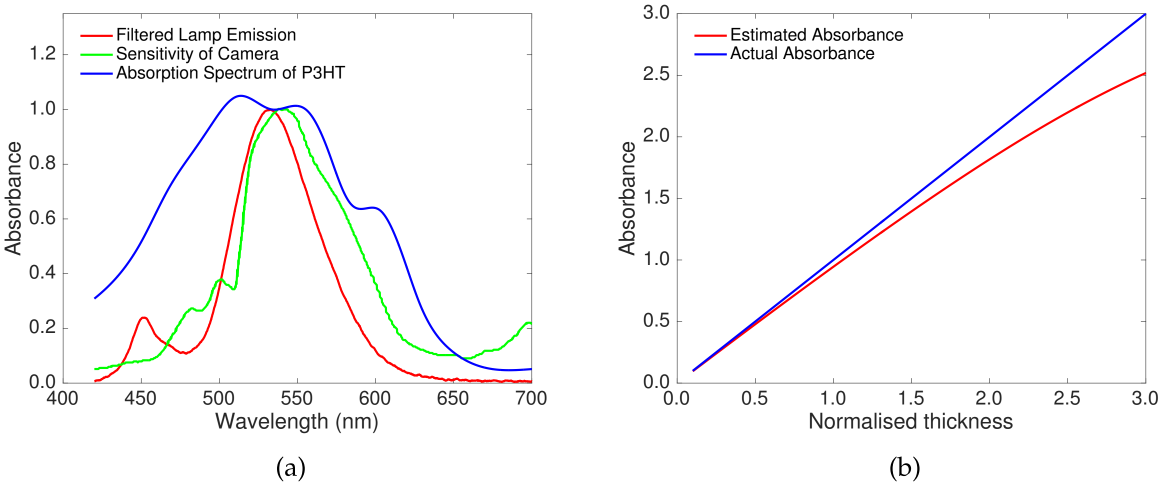

Figure 3.10: Plots showing the filtered emission spectrum of the lamp, the absorption spectrum of the absorbing medium and the sensitivity of the (green) detector in the Pi camera (a) and the true absorbance and the estimated absorbance against normalised film thickness (b).

$$\frac{A}{d} = \frac{A_0}{d_0} \tag{3.13}$$

Substituting equation 3.13 into equation 3.10 and rearranging we obtain

$$I(\lambda) = I_0(\lambda)10^{-\frac{A_0(\lambda)d}{d_0}} \tag{3.14}$$

Substituting equation 3.14 into equation 3.12, we obtain

$$A^* = -\log_{10}\left(\frac{\int_{\lambda_a}^{\lambda_b} I_0(\lambda)10^{-\frac{A_0(\lambda)d}{d_0}} S(\lambda)d(\lambda)}{\int_{\lambda_a}^{\lambda_b} I_0(\lambda)S(\lambda)d(\lambda))}\right) \tag{3.15}$$

Hence, the accuracy of the absorbance estimated by equation 3.12 and therefore equation 3.11, depends on the filtered emission spectrum of the lamp $I_0(\lambda)$, together with the absorption spectrum $A_0(\lambda)$, of the absorbing medium and the sensitivity $S(\lambda)$, of the (green) detector in the Pi camera. These are shown in figure 3.10a.

In figure 3.10b, the true absorbance and the estimated absorbance are plotted against normalised film thickness, using equations 3.13 and 3.12, respectively. The thickness has been normalised such that a thickness of one yields a true absorbance of one at filtered lamp peak of 532 nm. It can be seen that, while the true absorbance is a linear function of the film thickness, the estimated absorbance is a sub-linear function of the film thickness. For the specific optical filtering system chosen, the estimated absorbance is 6 % lower than the true absorbance at OD 1, increasing to a 9 % shortfall at OD 2 and a 20 % short-fall at OD 3.

In practice, the optical set up only permits reliable measurements at optical densities up to 2.3 (see previous chapter) and most films tested in this thesis had optical densities smaller than 1, so the slight errors were considered acceptable to obtain an approximate measure of film uniformity. Had higher accuracy in the optical density been required, it would have been a simple matter to use a narrower band-pass filter on top of the lamp. However, this would have reduced the amount of light falling on each pixel, increasing the noise in the measurement.

3.3.4 Spin coated polymer films

To put the limitations of the technique into context, P3HT films of varying thicknesses were deposited by spin-coating, a technique that is known to produce extremely smooth films (RMS $\leq$ 5 nm). The films were optically profiled using the setup described above. Films with optical densities in the range 0.3-1.2 were obtained by spin-coating at different speeds from solutions of varying concentration. Absorbance histograms for the films are shown in figure 3.11. It becomes progressively more difficult to form uniform films by spin-coating as the film thickness increases, and this difficulty manifests itself in a rapid broadening of the distributions in absorbance for the thicker films shown in figure 3.11. The rate of increase is much faster than that observed for the neutral density filters, implying spatial variations in film thickness. Although the distribution in absorbance for all of the films followed a roughly Gaussian trend, the two thickest films showed asymmetries in their distributions, which is attributable to the visible formation of aggregates in the high concentration (30 mg/ml) of the solutions from which the films were cast.

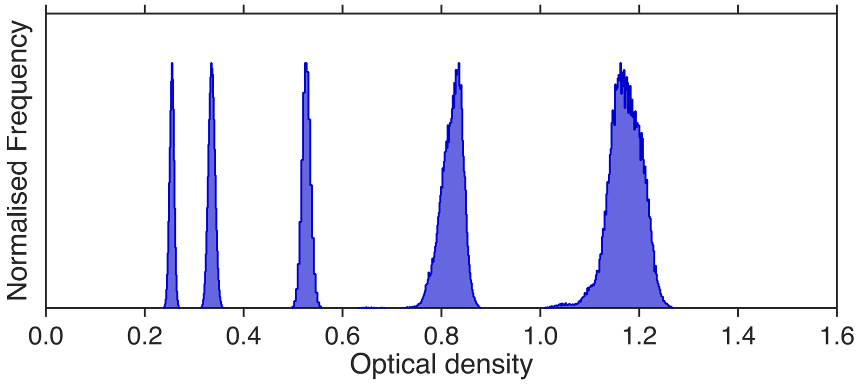

Figure 3.11: Absorbance distributions for spin-coated P3HT films of varying thickness, obtained by casting at different speeds from solutions of varying concentrations.

The standard deviations and relative standard deviations were extracted from the absorbance distributions and plotted against the corresponding mean optical density (see figure 3.12). A linear trend between the mean absorbance and standard deviation can be seen in figure 3.12a. Taking the standard deviation to be an approximate measure of roughness, this behaviour indicates a linear relation between film thickness and film roughness (RMS). Accordingly as can be seen in figure 3.12b, the relative standard deviation does not vary significantly with mean absorbance, and remains flat at $\sim$2.5 %. With the exception of the two thinnest films, which had mean optical densities below those of the filters measured, the standard deviation and relative standard deviation were slightly higher than those measured for the optically smooth filters. This result has important implications for the use of this setup as a means to characterise film uniformity. Whilst the technique is not able to accurately differentiate between films where the roughness (RMS) is $\leq$ 5 nm, the clear differences in standard deviation and relative standard deviation between the spin-coated films and the optically smooth filters demonstrates that it is possible to distinguish between the two. The optical profiling technique is therefore a useful tool for rapidly characterising spray-deposited films where the RMS roughness often exceeds 10 nm.

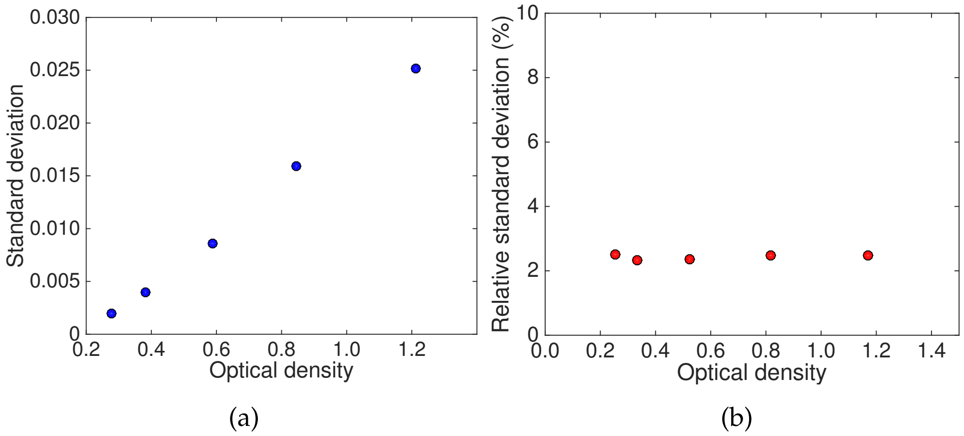

Figure 3.12: Plots showing the standard deviation (a) and relative standard deviation (b) of the absorbance distribution versus the mean optical density for the spin-coated films of P3HT.

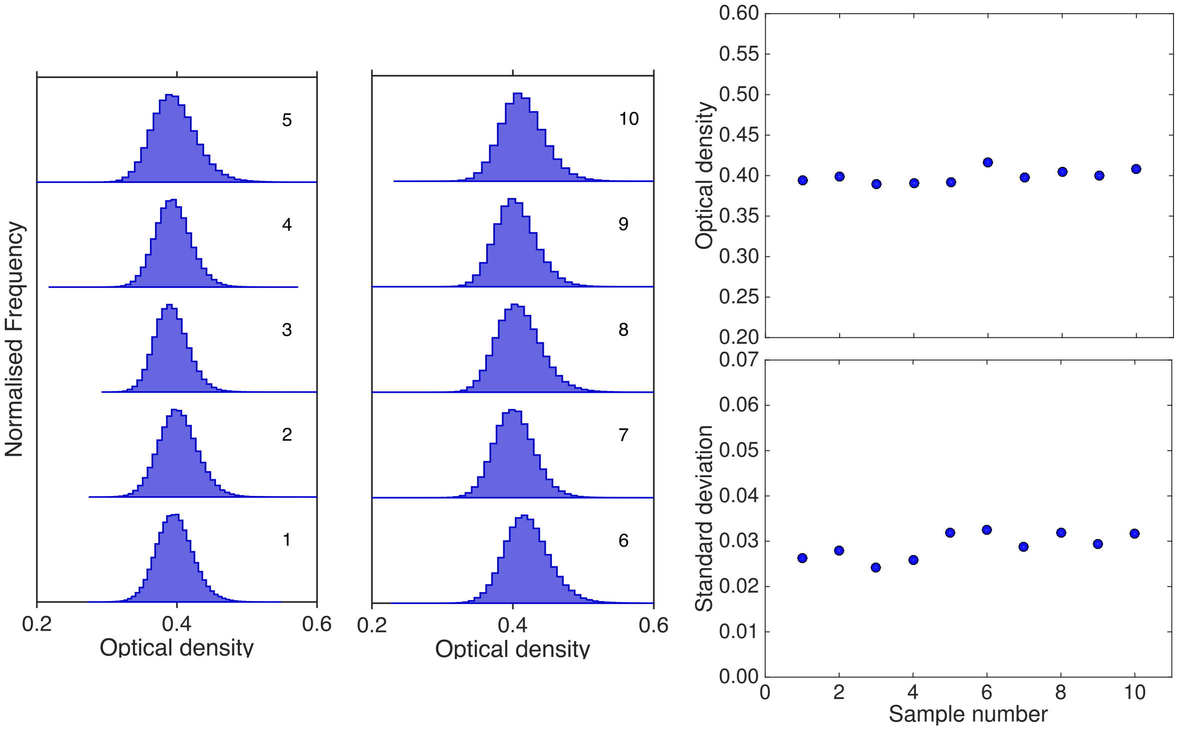

Figure 3.13: Left: The distributions in absorbance for ten spray-coated films deposited using identical processing parameters. Right: Plots showing the (top) standard deviation and (bottom) relative standard deviation of the distribution for each film.

3.3.5 Reproducibility of spray deposited polymer films

Absorbance imaging provides a useful means of quantifying the reproducibility of films deposited using the spray-coater. The distributions in absorbance for ten P3HT films sprayed using identical deposition parameters are shown in figure 3.13, together with plots showing the mean optical density and standard deviation versus sample number. Each film had an optical density of $\sim$0.4 ± 0.03, demonstrating that the spray system is capable of depositing films in a reproducible manner. This provides confidence that any trends observed when deliberately varying spray-deposition parameters are due to genuine effects and are not caused by irreproducibility in the system. Film reproducibility is important not only for the work presented in this thesis, but also for the viability of spray deposition in electronic device manufacturing, where it is essential that the thicknesses of each constituent layer should be consistent for every device.

3.3.6 Large area uniformity of spray-deposited polymer films

Beyond the need for film-to-film reproducibility, uniformity across the same substrate is also a firm requirement. The uniformity of a "large" 2.6 cm x 2 cm film of P3HT was evaluated by optically profiling each quartile of the substrate separately, as shown in figure 3.14a. The absorbance histograms, mean optical density and standard deviation for each quartile are shown in figures 3.14b- 3.14d. Each quartile had a mean optical density of $\sim$0.395 ± 0.008 and a standard deviation of $\sim$0.026 ± 0.002, demonstrating that the spray system is capable of maintaining good uniformity over moderately large areas.

3.3.7 Drying patterns of drop-cast polymer films

Later in this thesis we will sometimes find it useful to study drop-cast films rather than spray-deposited films. This can be useful, for instance, when analysing drying patterns arising from non-uniform evaporation (see section 1.4). Absorbance mapping

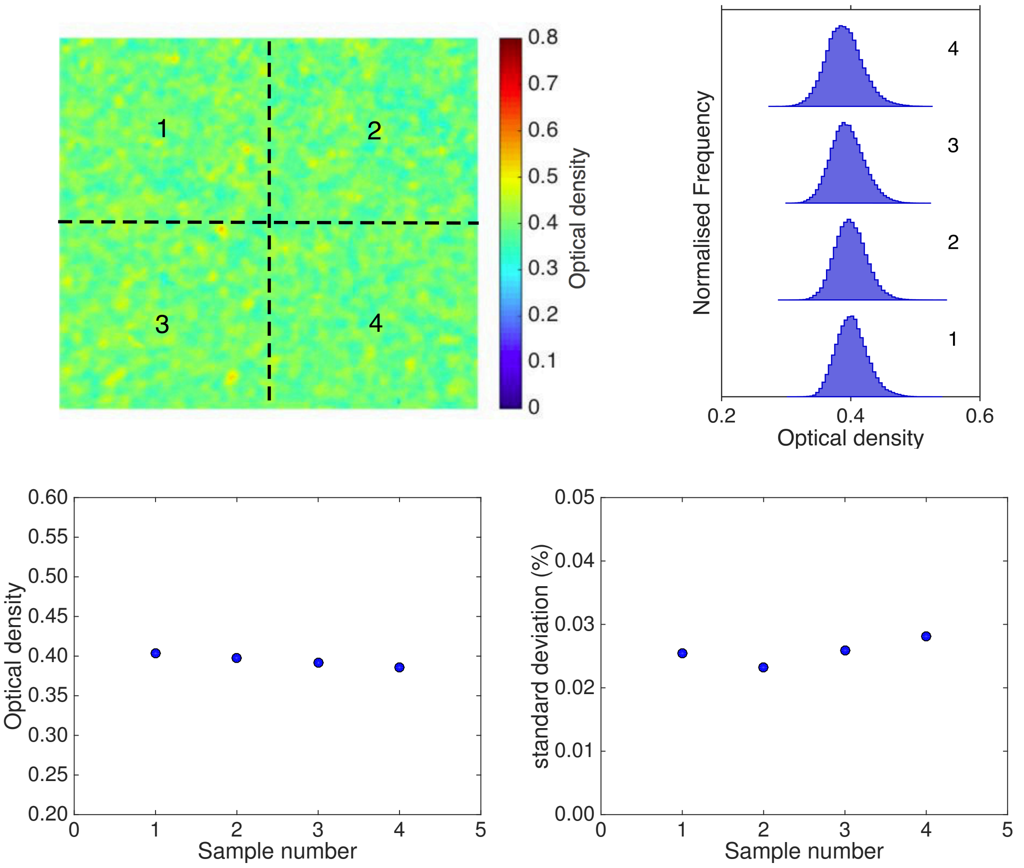

(a) (b)

(c) (d)

Figure 3.14: (a) Absorbance map of a large-area (2.6 cm x 2 cm) spray-coated film, each quartile was measured separately. (b) Absorbance distributions for each quartile of the film. Plots showing the mean optical density (c) and standard deviation (d) extracted from (b).

can also be used to map out the surface profile of drop-cast films to observe patterns such as coffee-staining and mound formation. Illustrative substrate, background and dark images used to create an absorbance map for a drop-cast film are shown in figures 3.15a - 3.15c. The resulting absorbance map is shown in 2D in figure 3.15d and in 3D in figure 3.15e. Here, the effect of coffee-staining is clearly apparent, with the highest optical densities (corresponding to the thickest parts of the film) being situated at the perimeter of the drop, and the lowest optical densities being situated at the centre.

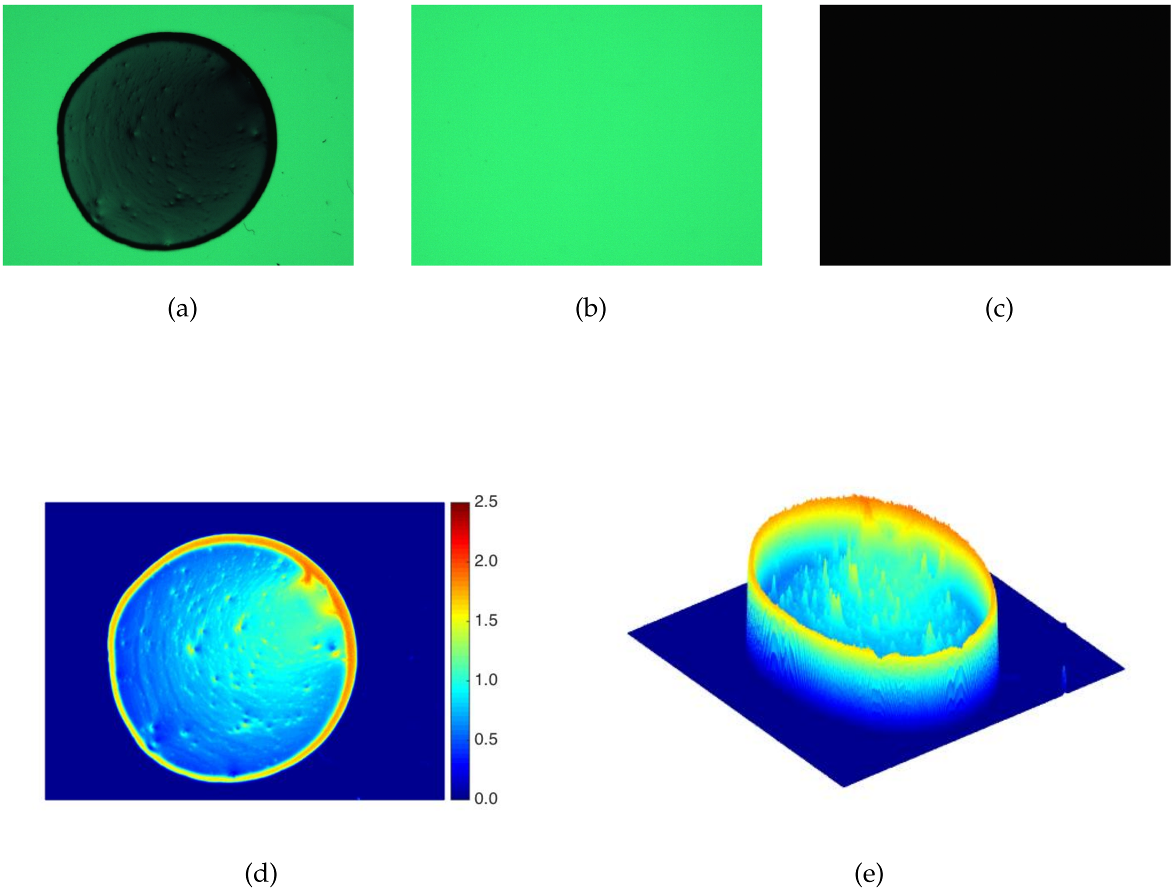

Figure 3.15: The substrate (a), background (b), and dark (c) images used to create 2D (d) and 3D (e) absorbance maps of a drop-cast film.

3.3.8 Summary

The optical profiling method described in this section provides a fast route to characterising the uniformity of thin polymer films of areas up to 1.3 cm^2, in circumstances where the absorption coefficient, k, is spatially invariant. Whilst the resolution of the method is inferior to AFM, it is very useful for characterising the large-area uniformity of spray-coated films, which typically exhibit much rougher surfaces than spin-coated films, and thus, where sub-nanometer resolution is not necessarily required. The optical profiling technique is therefore a useful tool for optimising the smoothness of spray-coated films, and is employed in the next chapter to characterise films deposited using different operating parameters of the rig. As mentioned above, the optical profiling method is also useful for observing the various drying patterns that may form as a result of non-uniform evaporation. It is therefore also used in the next chapter to optimise the composition of the printing ink to promote smooth, pattern-free film formation.

4 Spray-deposition of organic semiconductor films

In this chapter I examine the effects of solution composition (i.e. molecular weight, polymer concentration and the addition of a secondary solvent) on the gelation of the solution, and thus on the viability of spray-depositing solutions of various compositions. I also examine the effects of solution composition and rig operating parameters (i.e. gas flow rate, solution flow rate, raster speed, and substrate temperature) on the uniformity of spray-deposited films of P3HT, as determined by the optical profiling method described in the pervious chapter. Based on these results, I suggest optimum solution and spray-deposition parameters for smooth film formation.

4.1 Ink composition

As a result of the poor solubility of P3HT in o-xylene, gelation is often observed, with the polymer forming aggregates that extend (percolate) through the entire liquid in the solution, resulting in a solid-like gel. The tendency for P3HT (and other conjugated polymers) solutions to gel (in non-chlorinated solvents) has important implications for the printing of active layers: it shortens the time that the ink remains a liquid and can be printed [1], causes clogging of printing machinery, and can influence the morphology and performance of the printed film. However, a small degree of gelation

---

[1] Hoth et al. described this problem in relation to inkjet printing from non-chlorinated solvents, noting they could only run their inkjet printer for 30 minutes before the nozzles became clogged and unusable due to gelation of P3HT in tetralene [102]

can sometimes be beneficial: Krebs et al. for instance, deliberately left newly made solutions of P3HT:PCBM for two hours before use to allow aggregation to occur and thereby presumably achieve an adequate viscosity for slot-die coating [103]. In general, however, gelation is a difficult process to control, and adds another degree of complexity to the formulation of active layer inks. For this reason I tried to minimise gelation in my work by controlling the ink formulation and storage conditions. The gelation of P3HT can be reversed by heating, and is strongly dependent on the ink composition: the molecular weight, regioregularity and concentration of the P3HT have all been shown to play an important role [104]. As such, for the work described here, I prepared multiple ink formulations with a view to achieving optimum film quality and device performance. The gelation temperature and aggregation dynamics of each ink were examined to determine the temperature at which the syringe should be kept during spray-deposition to avoid both aggregation and gelation.

4.1.1 Gel temperature measurement

Aggregation and gelation of P3HT in o-xylene were investigated by static light scattering, using an instrument developed by Dr. Siva Krishnadasan. The instrument incorporated a 650 nm laser diode and photodetector arranged in a 90 ° configuration around a temperature-controlled vial holder as shown in figure 4.1. The system accommodated 3 mL sealed vials, which were typically filled with 2.5 mL of solution. Solutions were heated to 60 °C for 120 minutes to allow the polymer to completely dissolve. The temperature was then reduced at a rate of 4 °C/hr (in 1 °C steps) from 60 to 15 ° C. The scattered light incident on the photodetector was recorded throughout the cooling process, and the data was ”binned” into 1 °C intervals.

A schematic of a typical trace obtained using this technique is shown in figure 4.1b. The shape of the trace may be understood in terms of ordering in the solution as it cools. Initially, the polymer is fully dissolved in solution and polymer-solvent interactions dominate. The signal remains constant as long as the polymer remains fully dissolved. However, as the solution cools, polymer-polymer interactions become more favourable, and the polymer chains begin to interact in solution. For P3HT this results in a gradual, visual colour change from orange to red. As a consequence, the measured intensity of the scattered light decreases slightly (as shown in stage 1 of figure 4.1b). Once the polymer-polymer interactions in the solution are sufficiently strong, nucleation of polymer aggregates can occur. These undissolved particulates scatter the laser light strongly, leading to a sharp increase in the measured signal (stage 2 of figure 4.1b).

After aggregation, the signal is often observed to reduce (stage 3 of figure 4.1b). This behaviour has two possible explanations. One explanation is that, as the solution cools further, the aggregates join together to form a solid gel, causing the signal to drop significantly as a combined consequence of reduced scattering and increased optical absorption. Circumstantial evidence for this explanation is provided by the observation that solutions which showed this behaviour were found to have formed a gel when they were subsequently removed from the instrument, whereas solutions which did not show this behaviour were still found to be in solution when they were removed. However, it should be acknowledged that an alternative explanation is that as the solution cools further, increased aggregation (without gelling) leads to a reduction in the signal as a result of increased optical absorption alone. Further concurrent measurements of the absorption and viscosity of the solution as a function of temperature would be required to establish definitively which of the two explanations is correct. However, it has been assumed in the discussion below that the first explanation is the correct one.

4.1.2 Molecular weight

As expected, the molecular weight of P3HT was found to influence both the temperature of gelation and the aggregation dynamics of the solution. Figure 4.2 shows traces obtained from the light-scattering instrument using solutions (in o-xylene) of different molecular weight P3HT in the range 20-90 kg/mol (see Appendix 7.1 for the molecular weight distributions of each polymer sample). For low molecular weight P3HT (20 kg/-mol), there was no evidence of aggregation or gelation within the temperature range of the measurement. Instead, the signal decreased monotonically with diminishing temperature, consistent with a gradual increase in polymer-polymer interactions in the

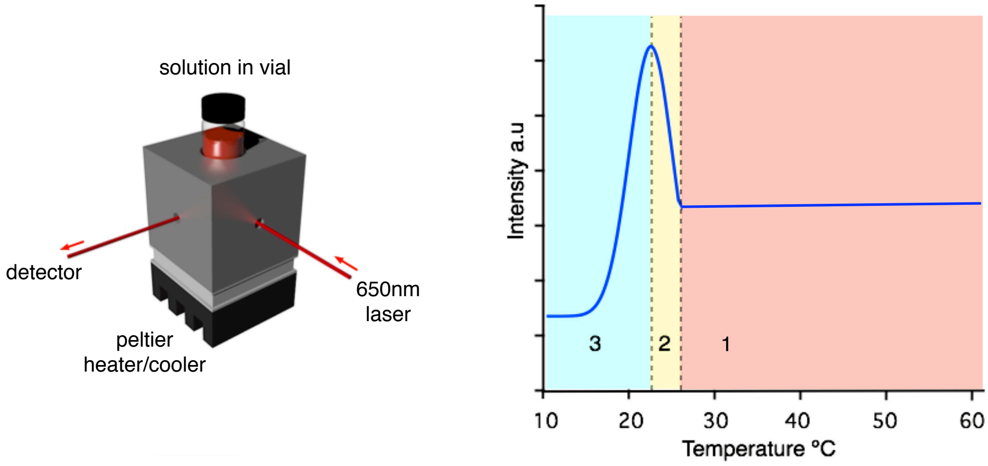

(a) (b)

Figure 4.1: (a) Schematic of the instrument (developed by Dr. Siva Krishnadasan) used to measured the gel temperature of solutions. (b) A typical trace obtained using the light-scattering instrument, showing three regimes: (1) at the highest temperatures the polymer is in solution; (2) as the solution cools aggregation of solid nucleates occurs; (3) further cooling leads to gelation of the polymer solution.

solution. When the molecular weight was increased to 40 kg/mol, similar behaviour was observed until the temperature dropped below 20 °C, at which point a small peak associated with aggregation was seen, followed by a large, fast decrease in signal intensity associated with gelation. On increasing the molecular weight to 65 kg/mol, the peak associated with aggregation increased in magnitude and the gelation temperature also increased to 24 °C. On further increasing the molecular weight of P3HT to 90 kg/mol, the gelation temperature was further increased to 29 °C, but the sharp aggregation peak was not observed.

The reason why the aggregation peak is not observed for the highest molecular weight is not clear. Impurities in the polymer (which exist in the form of oligomers, monomers, reaction byproducts and metal residues from the catalyst) can encourage aggregation. However, each of the P3HT samples was synthesised by the same Grignard metathesis route (by Dr. James Bannock) and purified using the same two-stage Soxhlet extraction process. [2] It is therefore unlikely that impurity levels would vary significantly

---

[2] Acetone was used to remove monomer and salt impurities from the as-synthesised polymer; chloroform was then used to extract the polymer from insoluble impurities. The extracted polymer in

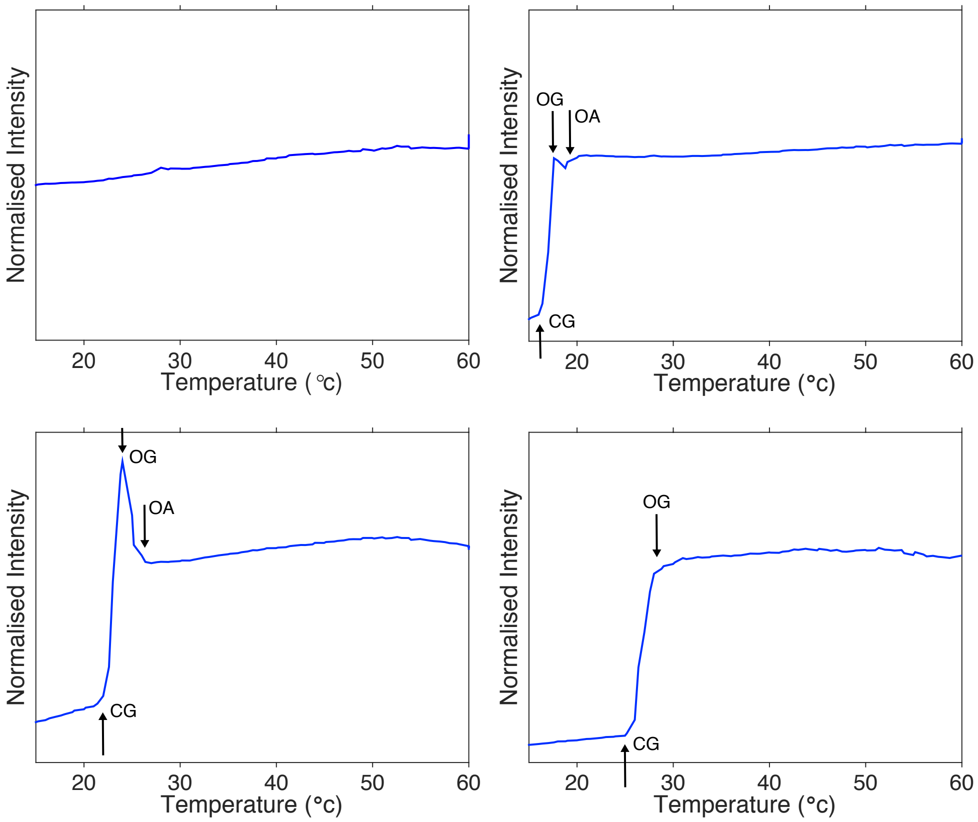

(a) (b)

(c) (d)

Figure 4.2: Traces obtained using the light scattering instrument for 10 mg/ml solutions of P3HT (in o-xylene) with molecular weights of (a) 21 (b) 40 (c) 65 and (d) 90 kg/mol. The arrows on each graph indicate the onset of aggregation (OA), the onset of gelation (OG), and complete gelation (CG), where they could be determined.

between the different molecular weight samples. In the case of the highest molecular weight sample, it is possible that some degree of chain entanglement was present at all temperatures, causing the solution to switch directly from a solution to a gel without the intermediate formation of discrete localised aggregates. Alternatively, the temperature range over which the aggregates exist may have been so narrow that their existence was masked by the rapid onset of gelation. Whatever the reason for the absence of the aggregation peak, the high gelation temperature is potentially

---

chloroform was reprecipitated in cold methanol, and the solvent removed. The purified P3HT was dried under vacuum to remove residual solvent.

undesirable from a processing prospective as it requires external heating, arguing against the use of very high molecular weight material.

The temperatures for the onset of aggregation (OA), the onset of gelation (OG) and complete gelation (CG) were noted (where they could be determined) for each solution as indicated by the arrows drawn on each of the traces of figure 4.2. The three temperatures are plotted versus M_w in figure 4.3. The increase in gelation temperature with M_w is consistent with previous literature reports [104], and is understandable in terms of greater chain entanglement for longer chain materials. The plot also shows that there is a general decrease in the temperature difference between the onset of gelation and complete gelation with increasing molecular weight.

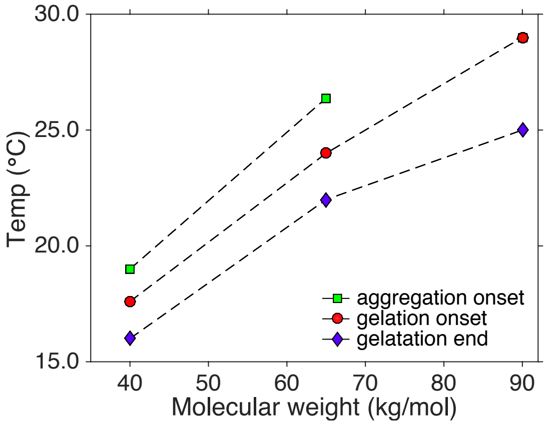

Figure 4.3: A plot showing the temperatures at which aggregation (green squares) and gelation (red circles) begin, and gelation ends (purple diamonds), for molecular weights in the range 40-90 kg/mol.

From the perspective of achieving reliable spray-coating, it appears from figures 4.2 and 4.3, that for the 10 mg/ml solutions investigated, it is either necessary to work with a molecular weight of $\leq$ 20 kg/mol, or else the temperature must be kept above $\sim$30 °C to prevent gelation (and thereby avoid high back pressures and clogging of the spray-head).

The molecular weight (M_w) of P3HT has a strong influence on the electrical performance of devices. It has been demonstrated that, in the solid state, high M_w P3HT has superior charge transport properties to low M_w P3HT [105]. For this reason I decided to work with the highest molecular weight sample of 90 kg/mol, keeping the temperature in the spray-head above 30 °C to avoid gelation. This was achieved by using Kapton microfilm heaters to heat the syringes to a temperature of 35 °C at all times.

4.1.3 Concentration

The concentration of P3HT was also found to influence the gelation and aggregation dynamics. Cooling traces for 90 kg/mol P3HT in o-xylene at various concentrations in the range 5-20 mg/ml are shown in figure 4.4. For the lowest solution concentration (5 mg/ml), no aggregation peak was observed, and the onset of gelation occurred at a relatively low temperature of ∼21 °C. When the concentration was increased to 10 mg/ml, the gelation temperature also increased to 29 °C, but the profile of the cooling trace remained similar in shape. When the concentration was further increased to 15 mg/ml, an aggregation peak appeared in the trace prior to gelation, with the gelation temperature remaining broadly unchanged at 29 °C. At 20 mg/ml, the gelation temperature was further increased to 31 °C and a reduction in the intensity of the aggregation peak was observed.

The temperatures for the onset of aggregation, the onset of gelation and complete gelation (extracted from figure 4.4) are plotted versus solution concentration in figure 4.5. All three temperatures were found to increase with increasing solution concentration, consistent with a greater tendency for 3D network formation at higher concentrations. Furthermore, the temperature difference between the onset of gelation and complete gelation was found to decrease with increasing concentration, which is similar to the behaviour observed previously (in section 4.1.2), for samples of increasing molecular weight.

From a processing prospective, it is clear from figures 4.4 and 4.5 that solutions formulated using 90 kg/mol molecular weight P3HT at concentrations $\geq$ 5 mg/ml must be heated to avoid gelation and aggregation. Hence, for all subsequent work using 90 kg/mol P3HT, the temperature of the syringe was kept at 40 °C using Kapton microfilm heaters.

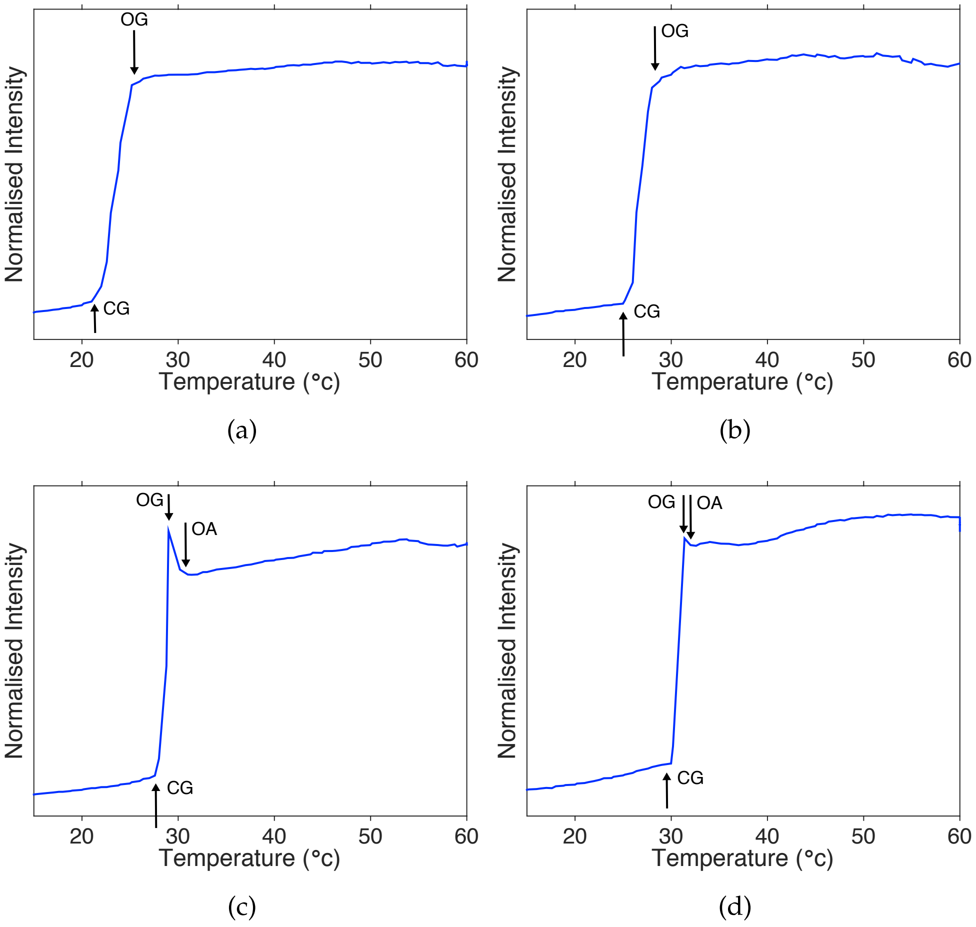

Figure 4.4: Traces obtained using the light-scattering instrument for 90 kg/mol molecular weight P3HT solutions (in o-xylene) with polymer concentrations of (a) 5 (b) 10 (c) 15 and (d) 20 mg/ml. The arrows on each graph indicate the onset of aggregation (OA), the onset of gelation (OG) and complete gelation (CG), where they could be determined.

4.1.4 Use of a secondary solvent

As discussed earlier, a low gelation temperature is preferred to ensure ease of processing during coating. In some circumstances, this can be achieved by careful solvent selection. Unfortunately, there are relatively few non-chlorinated solvents that are suitable for P3HT, combining good solubilising ability (for both P3HT and fullerenes) with high volatility. O-xylene (the solvent used for the measurements in the preceding sections) appears to be one of the best choices in terms of wettability and volatility, but it can be further improved as a solvent for P3HT by the addition of a secondary solvent to reduce the tendency of the solution to gel. Indane is a well known, non-halogenated

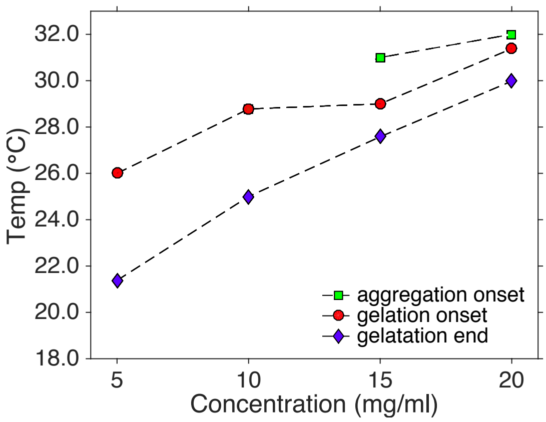

Figure 4.5: A plot showing the temperatures at which aggregation (green squares) and gelation (red circles) begin, and gelation ends (purple diamonds), for 90 kg/mol molecular weight P3HT and solution concentrations of 5-20 mg/ml.

solvent that has been used for depositing the active layer of P3HT:PCBM solar cells. It is miscible with o-xylene and, despite its higher boiling point and surface tension (indane: 176 °C, 34.9 mN/m, o-xylene: 144 °C, 30.10 mN/m), is of interest as a solvent as it is less prone to induce gelation.

Figure 4.6 shows light-scattering traces for 90 kg/mol molecular weight P3HT at solution concentrations of 10 mg/ml using o-xylene/indane solvent mixtures in the range 0-100% indane. As seen previously in figure 4.16b, in the absence of indane, no aggregation peak was observed and the scattering signal decreased monotonically with decreasing temperature until gelation at ∼28 °C, at which point the signal dropped rapidly before plateauing. As the amount of indane was increased first to 20 % and then to 40 %, the shape of the cooling trace remained largely unchanged, although a slight decrease in the gelation temperature was observed to ∼24.5 °C and ∼23 °C respectively. On further increasing the amount of indane to 50 %, the gelation temperature was further decreased to 22 °C and an aggregation peak was observed. As the amount of indane was further increased to 75 % and then to 100 %, the gelation temperature continued to decrease and the aggregation peak increased in magnitude.

The temperatures for the onset of aggregation (where observed), the onset of gelation and complete gelation (extracted from figure 4.6) are plotted against indane concentration in figure 4.7. The gelation onset temperature decreased as the volume percentage

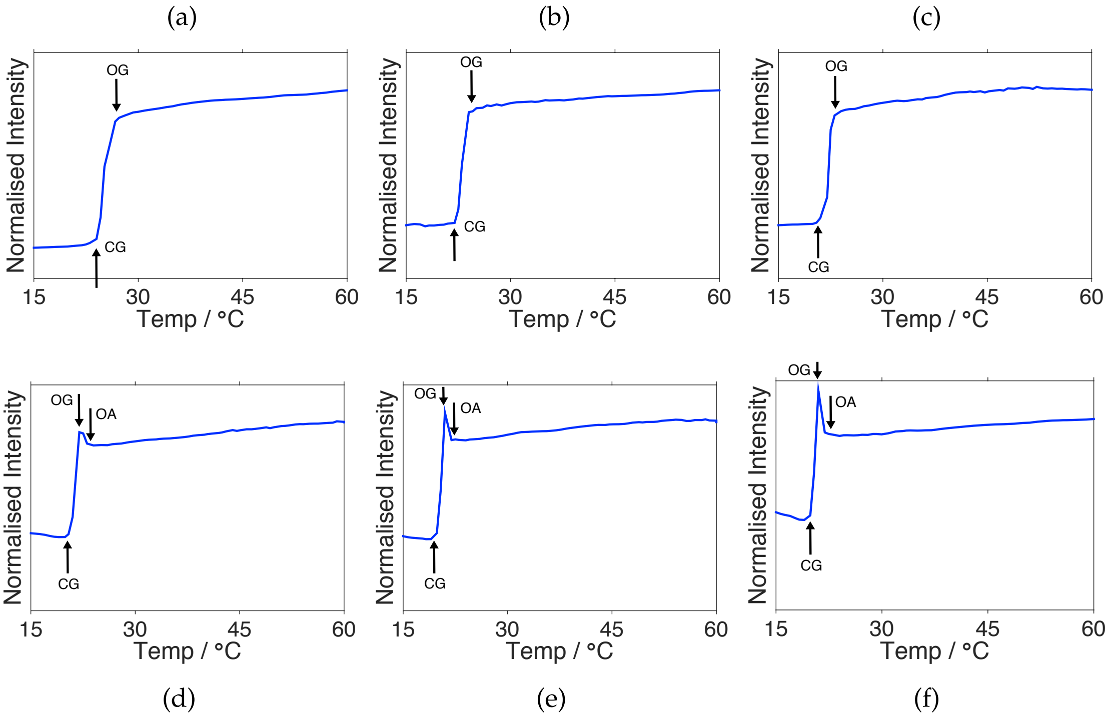

Figure 4.6: Traces obtained using the light-scattering instrument for 10 mg/ml solutions of 90 kg/mol molecular weight P3HT (in o-xylene/indane mixtures) with indane concentrations of (a) 0 (b) 20 (c) 40 (d) 50 (e) 75 and (d) 100 %. The arrows on each graph indicate the onset of aggregation (OA), the onset of gelation (OG) and complete gelation (CG), where they could be determined.

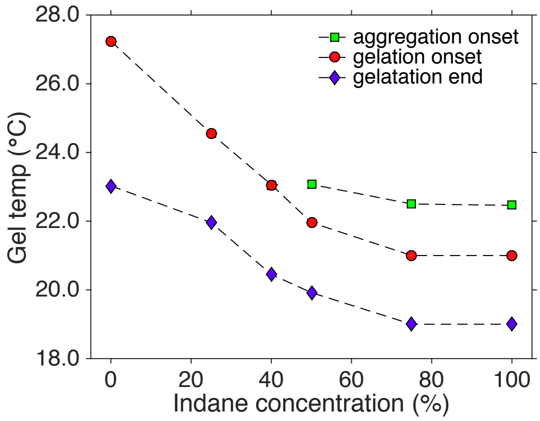

Figure 4.7: A plot showing the temperatures at which aggregation (green squares) and gelation (red circles) begin, and gelation ends (purple diamonds), for 10 mg/ml concentrations of 90 kg/mol molecular weight P3HT in o-xylene with indane concentrations in the range 0-100 %.

of indane was increased, which is potentially beneficial for solution processing as it reduces the likelihood of nozzle clogging and eliminates the need to heat the syringes.

We explore whether its inclusion is helpful or problematic for spray-coating P3HT in section 4.2.3.

4.2 The effect of ink composition on film uniformity

As discussed in section 1.4, when a polymer solution dries, it rarely leaves behind a completely uniform solid film, and a variety of drying patterns are commonly observed. In this section of the thesis, the effect of solution composition on the uniformity of drop-cast and spray-deposited films is examined.

4.2.1 Molecular weight

To investigate the effect of molecular weight on the drying patterns of thin-film P3HT, and thus its effect on film uniformity, 5 mg/ml solutions of P3HT were prepared in o-xylene, using P3HT samples of varying molecular weight in the range 20-90 kg/mol. 1 μL drops of each solution were deposited by drop-casting at room temperature onto glass substrates, and then optically profiled using the setup described in section 3.3. The drying patterns derived from the absorbance maps of each drop-cast film are shown in figure 4.8.

Droplets formed from low molecular weight material (M_w=20 kg/mol) exhibited a prominent coffee stain around the edge of the film, with only a small amount of material present in the centre (a phenomenon explained in section 1.4). When the molecular weight of the P3HT was increased to 40 kg/mol, the resultant film was slightly smaller in size and the coffee-stained edge was less prominent (lower OD), with more of the material being found towards the centre of the film. Faint concentric ring patterns (like those discussed in section 4.3.4) were observed in the space between the droplet edge and the centre. When the molecular weight was increased to 65 kg/mol, coffee-staining was no longer observed since most of the material was deposited in the centre of the drop, giving rise to the characteristic mound-shaped pattern discussed in section 1.4.2, with some faint concentric rings inside the initial edge of the droplet.

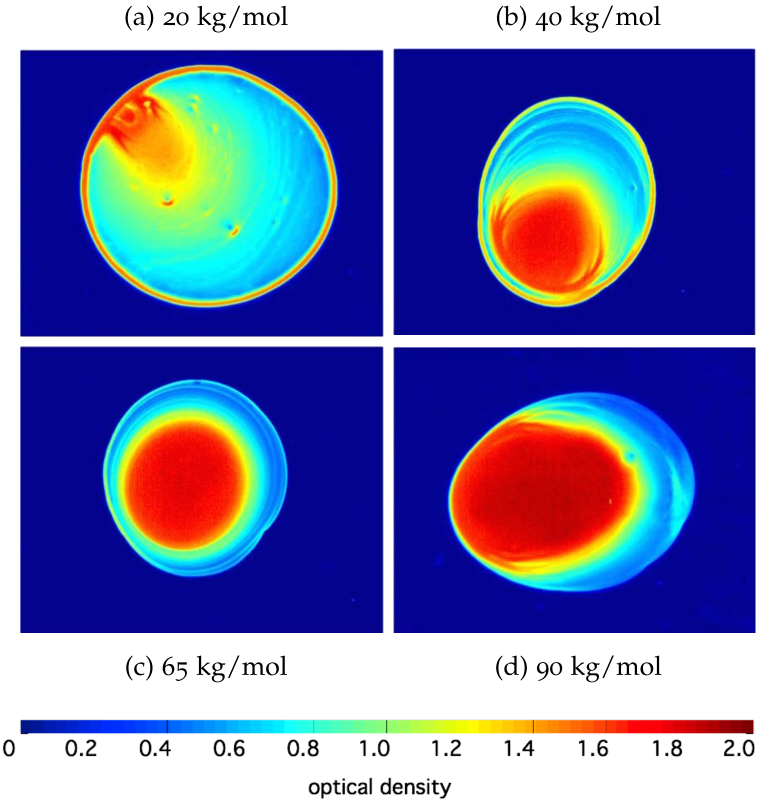

Figure 4.8: Absorbance maps of drop-cast P3HT films deposited from 5 mg/ml solutions in o-xylene with molecular weights of (a) 20 (b) 40 (c) 65 and (d) 90 kg/mol. A clear shift in the drying pattern from coffee-stained to mound-shaped is evident as the molecular weight of the P3HT increases.

Further increasing the molecular weight to 90 kg/mol resulted in a similar mound-like pattern, with most of the material residing in the centre.

The transition from coffee staining to mound formation can be understood in terms of the light-scattering cooling curves shown in figure 4.3. For low molecular weight solutions (M_w= 20 kg/mol), gelation occurs relatively slowly. Dissolved polymer in the bulk solution therefore has time to flow outwards towards the edge of the drop, giving rise to coffee-staining. If gelation occurs quickly (as it does for high molecular weight solutions, the viscosity of the bulk solution increases rapidly as the temperature of the solution drops (due to the combined effects of contact with the low temperature glass substrate and evaporation), suppressing the outward flow of material, and so causing mound formation instead of coffee-staining.

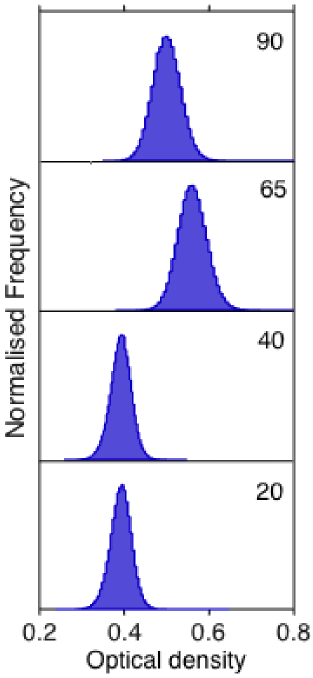

Figure 4.9: Absorbance histograms of films spray-deposited from 5 mg/ml solutions of P3HT (in o-xylene) with molecular weights in the range 20 to 90 kg/mol, using a solution flow rate of 200 μL/min, a gas flow rate of 20 Lpm, and a raster speed of 7.62 mm/s. The molecular weight of the P3HT in kg/mol is indicated at the top right hand corner of each histogram.

Films of P3HT were prepared by spray-coating from the same solutions at room temperature, using a solution flow rate of 200 μL/min, a gas flow rate of 20 Lpm, and a raster speed of 7.62 mm/s. Figure 4.9 shows the absorbance histogram for each film. In rough agreement with the trend observed for drop-cast films, the mean optical density of the sprayed-coated films was higher for higher molecular weight samples (this result is shown in figure 4.10a). Surprisingly, despite the very different drying patterns observed for drop-cast films of varying molecular weight, the standard deviation and relative standard deviation (and hence surface roughness) of the sprayed films did not change appreciably with molecular weight (as shown in figures 4.10b and 4.10c). Additionally, the surface features observed with optical microscopy (see figure 4.11) looked very similar for each film. This suggests that either the drying patterns of large 1 mm droplets are very different from those of smaller ~50 μm droplets, or that the spray-deposition process affects the drying patterns of the droplets, leading to behaviour that is substantially different than for drop-cast droplets.

Variations in drying behaviour with droplet volume could be rationalised in the following way. Evaporation of solvent from a large volume of solution takes longer than it does from a small volume. If the drying patterns are dependent on the time (or the lack of time) available for dissolved material to travel to the edge of the droplet

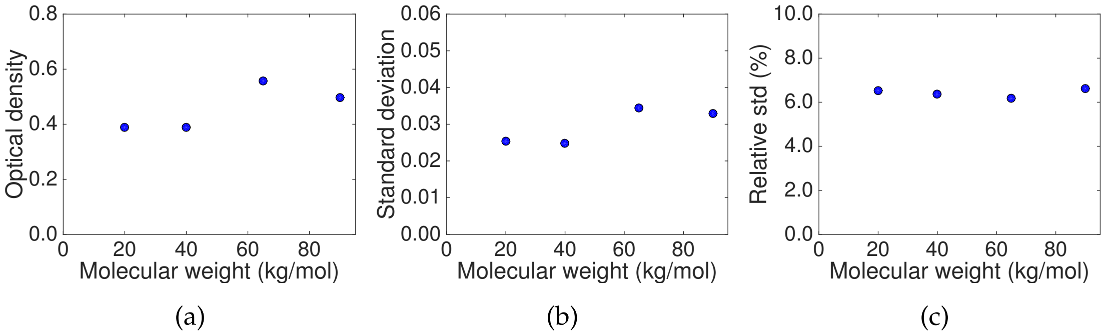

Figure 4.10: Plots showing how the mean optical density (a), the standard deviation (b) and the relative standard deviation (c) of each film varies with the molecular weight of P3HT. (Data extracted from distributions shown in figure 4.9).

before gelation, decreasing the volume of the deposited solution could be expected to result in a reduction in the coffee-stain effect for all molecular weight solutions. At 5 mg/ml, gelation is slow for all molecular weights of P3HT studied. Hence, for very small droplets (like those generated by spray atomisation), complete evaporation of the solvent is likely to occur before the onset of gelation. In this case, the gelation-induced increase in solution viscosity that is responsible for counteracting the outward capillary flow in drop-cast films will not have time to occur, so a coffee-stain will be observed irrespective of the molecular weight of the P3HT. This suppression of gelation in small droplets offers a possible explanation for the similar ″surface roughnesses″ observed for films sprayed from varying molecular weights, and is consistent with the observation of coffee-staining (to varying degrees) for spray-deposited films (as discussed in section 3.1).

The effect of the spray process on the drying patterns of droplets is unclear. The presence of a high velocity carrier gas, the relatively high velocity with which the droplets impact upon the substrate, and the potential for droplet coalescence, are all likely to affect the drying process (and thus the uniformity) of the final coating. The high velocity carrier gas will increase the rate of solvent evaporation, droplets may potentially break-up on impact (resulting in large droplet size variation) and coalescence with adjacent droplets may occur. All of these effects can influence the size and shape of the droplets as is discussed in more detail in section 4.3.

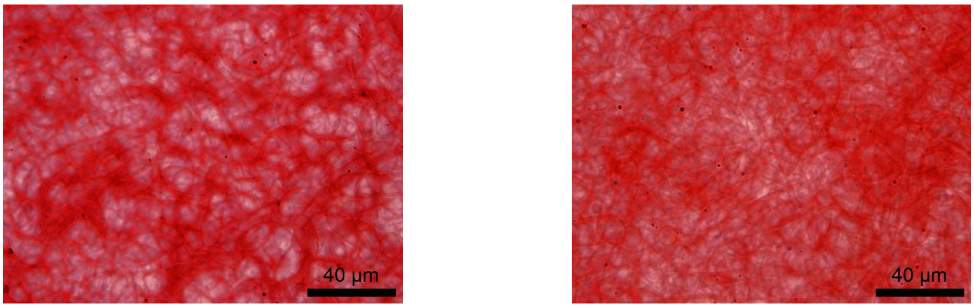

(a) 20 kg/mol (b) 90 kg/mol

Figure 4.11: Optical microscopy images of spray-coated films deposited from solutions of (a) 20 and (b) 90 kg/mol molecular weight P3HT in o-xylene. In both cases droplet-shaped surface features can be seen with "patchy" material distribution.

4.2.2 Concentration

To investigate the effect of solution concentration on the drying patterns of the droplets, solutions of varying concentration in the range 2-15 mg/ml were prepared from each of the different molecular weight polymer samples. 1 μL of each solution was drop-cast at room temperature onto glass substrates in the manner described previously. As before, the droplets were optically profiled using the setup described in section 3.3. The resultant absorbance maps are shown in figure 4.12.

For low molecular weight P3HT (20 kg/mol), a gradual transition from coffee-stained crater to dome-shaped mound was observed as the concentration was increased from 2 to 15 mg/ml. This is shown more clearly by the 3D-absorbance maps in figure 4.13 where, to a first approximation, the local absorbance is proportional to the local height of the film. At 5 mg/ml, conventional coffee-staining was observed with virtually all of the dried material present at the edge of the drop. At 10 mg/ml, the coffee-staining was less severe, with moderate build-up of material at the edge of the droplet to form a thick crust-like ring but a substantial amount of material remaining in the bulk of the droplet. At 15 mg/ml, no ring formation was evident at the edge and a uniform mound shape was observed.

Droplets deposited from M_w= 40 kg/mol P3HT solution showed a similar trend. Low concentrations ($\leq$5 mg/ml) showed a small amount of coffee-staining, with a small

(a) 5 mg/ml (b) 10 mg/ml (c) 15 mg/ml

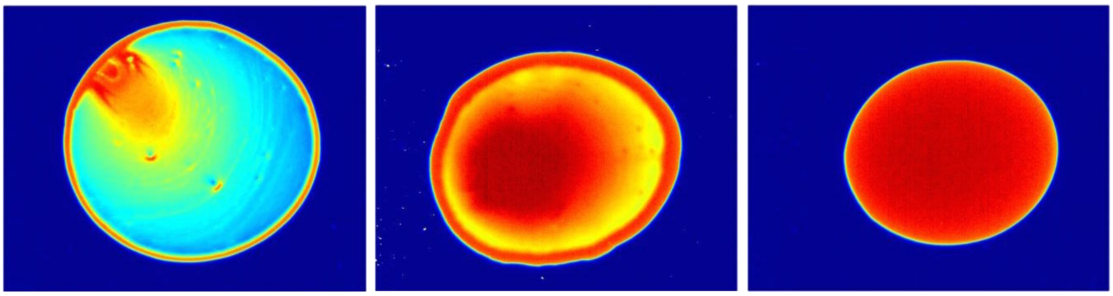

(d) 5 mg/ml (e) 10 mg/ml (f) 15 mg/ml

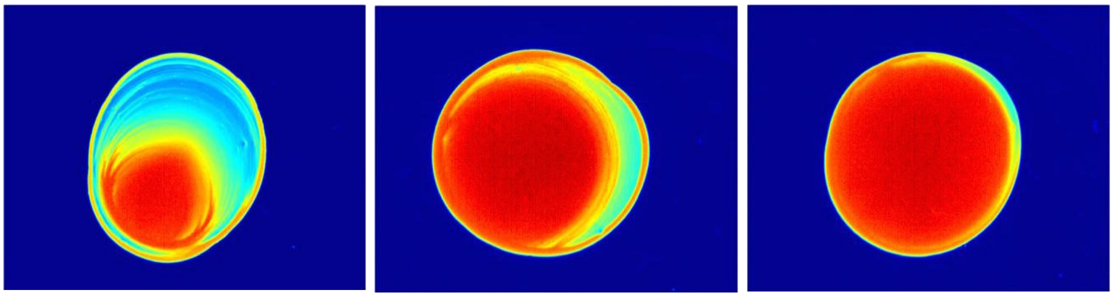

(g) 5 mg/ml (h) 10 mg/ml (i) 15 mg/ml

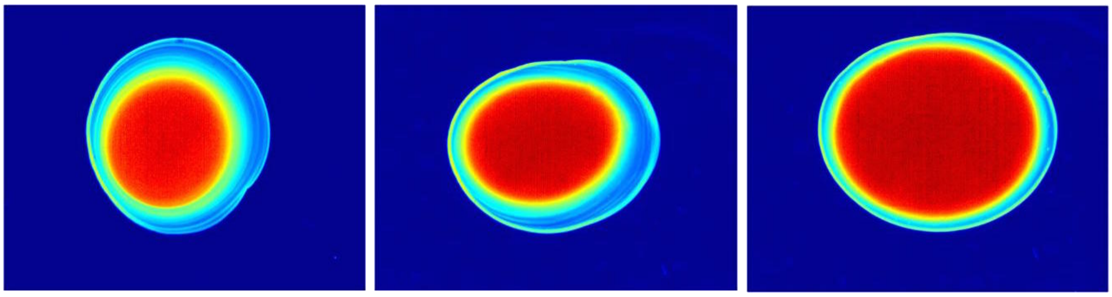

(j) 2 mg/ml (k) 5 mg/ml (l) 7 mg/ml

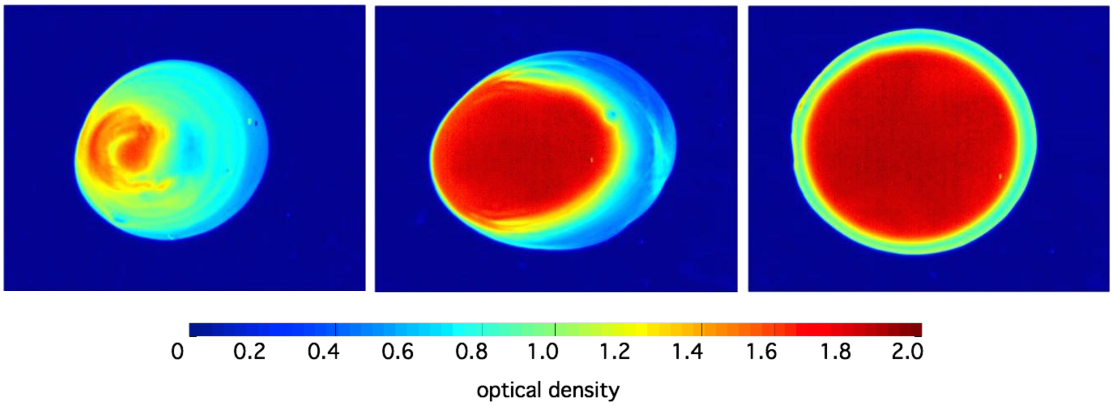

Figure 4.12: Absorbance maps of drop-cast films of 20 kg/mol (a-c) 40 kg/mol (d-f) 65 kg/mol (g-i) and 90 kg/mol (j-l) P3HT solutions in o-xylene, for different solution concentrations.

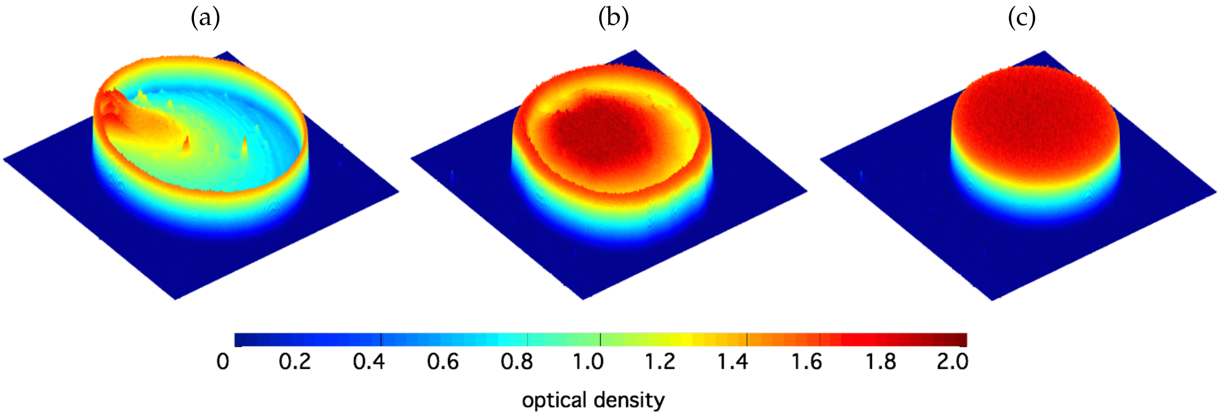

Figure 4.13: 3D absorbance maps of drop-cast films deposited from solutions of 20 kg/mol molecular weight P3HT in o-xylene at polymer concentrations of 5 mg/ml (a) 10 mg/ml (b) and 20 mg/ml (c). The maps show a gradual transition from coffee-stained to mound-shaped film formation on increasing the concentration of the solution.

amount of material left behind in the centre. At 10 mg/ml, coffee-staining was also observed but substantially more material remained in the centre. At 15 mg/ml a mound-shaped deposit was observed with no coffee staining.

Coffee-staining was not observed for any of the droplets deposited from the 65 kg/mol and 90 kg/mol molecular weight solutions. Instead, for low concentrations, a small amount of material accumulated in the centre of the droplet and on increasing the solution concentration, more material was observed in the centre. (Note, that for M_w= 90 kg/mol P3HT, it was not possible to work with concentrations greater than 8 mg/ml since fast gelation within the pipette prevented the polymer from being deposited as a free-flowing solution. Hence, absorbance maps are shown for 2, 5, and 7 mg/ml in figure 4.12j- 4.12l).

The transition from coffee staining to mound formation was explained in the previous section (section 4.2.1) for the situation where solutions had identical weight concentration but contained P3HT of varying molecular weight. Increasing solution concentration has a similar effect to increasing molecular weight, causing the gelation temperature to increase (as seen in the light-scattering cooling curves of section 4.1.3) and accelerating the rate of gelation as the solutions dry. The same explanation can therefore be used to rationalise the effects of solution concentration on the drying pattern. For low molecular weight material at low (5 mg/ml) solution concentrations, sufficient time is available for material transfer to occur radially outwards, resulting in a coffee ring. At higher concentrations, the rate of gelation is much higher, leading to a rapidly increasing solution viscosity that inhibits the outward capillary flow of material to the edge, and so results in mound formation. For higher molecular weight material (90 kg/mol), the rate of gelation is so high that mound formation occurs even at low solution concentrations ($\leq$2 mg/ml). Increasing the concentration beyond 2 mg/ml increases the temperature and speed of solution gelation but does not lead to a substantial change in the shape of the deposit.

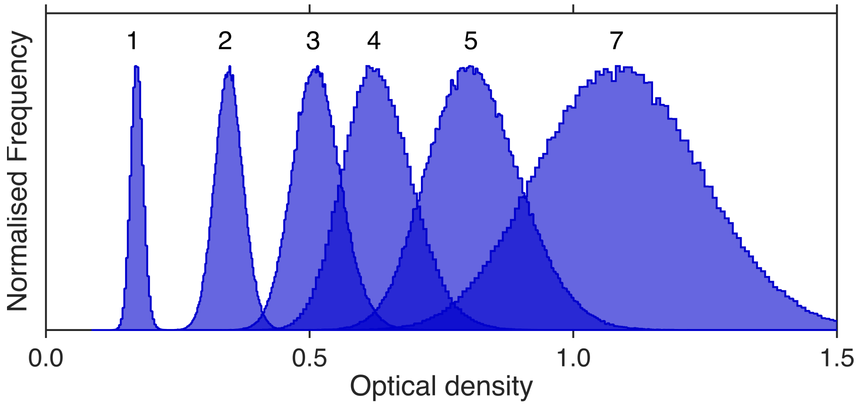

Figure 4.14: Absorbance histograms of films that were spray-deposited from solutions of 90 kg/mol molecular weight P3HT, using a solution flow rate of 200 μL/min, a gas flow rate of 20 Lpm, a raster speed of 10.16 mm/s and solutions concentrations in the range 1 to 7 mg/ml as indicated above each histogram.

Figure 4.14 shows the effect of the solution concentration on the absorbance histograms (shown in figure 4.14) of films that were spray-deposited from 90 kg/mol molecular weight solutions at room temperature, using a solution flow rate of 200 μL/min, a gas flow rate of 20 Lpm and a raster speed of 10.16 mm/s. The concentration of the solution was varied using the multi-solution configuration described in section 2.4.1, using one syringe loaded with 7 mg/ml P3HT in o-xylene and the other syringe loaded with pure o-xylene, and then varying the relative volumetric injection rates from the two syringes, while holding the total volumetric injection rate fixed. Increasing the solution concentration from 1 to 7 mg/ml caused the mean optical density of the film to increase from 0.17 to 1.09. As shown in figure 4.15a, a simple, linear trend was observed between the concentration and the mean optical density. Tailoring the solution concentration therefore offers a potential route to controlling film thickness.

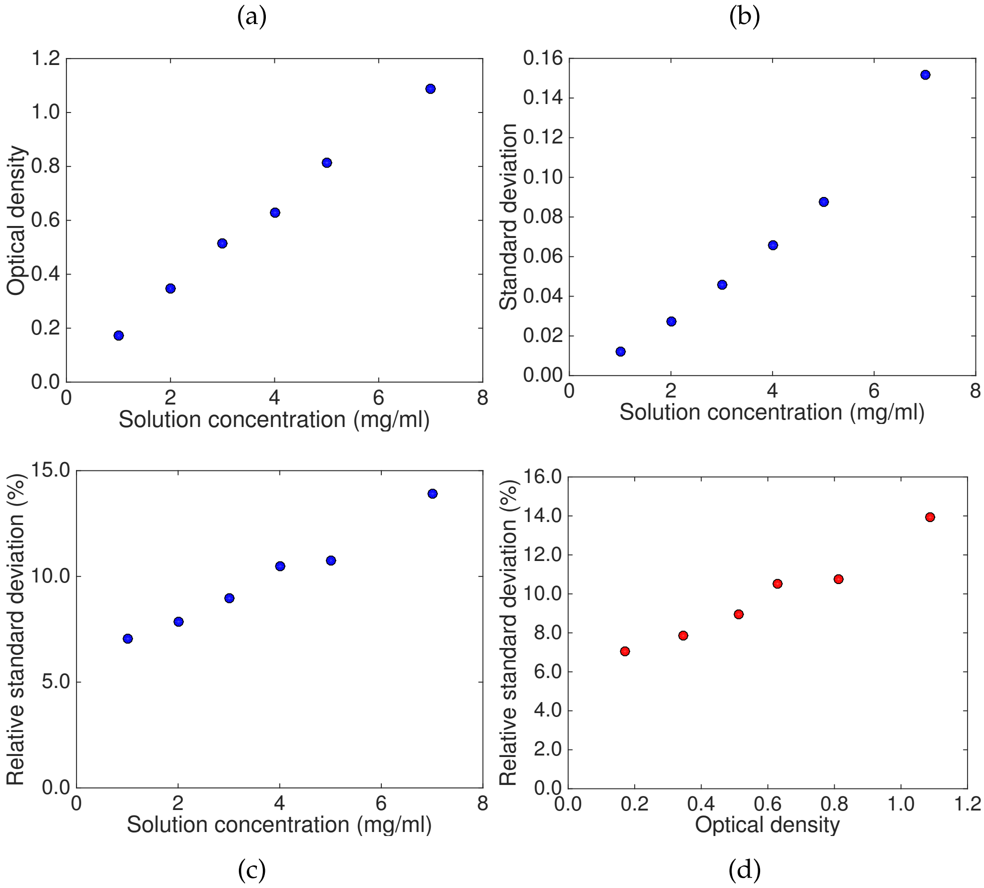

Figure 4.15: Plots showing how the mean optical density (a) the standard deviation (b) and the relative standard deviation (c) of the absorbance distributions vary with increasing solution concentration. (d) shows the relative standard deviation versus the mean optical density.

The standard deviation and relative standard deviation increased with increasing solution concentration, as shown in figures 4.15b and 4.15c, indicating that the thinner films are smoother on a relative basis, than the thicker, more absorbing films (see figure 4.15d). This suggests that using a low solution concentration is favourable for the spray-deposition of uniform films. This is, at first consideration, surprising given the drying behaviour observed for drop-cast films. A more uniform mound shaped deposit seems intuitively more likely to produce smoother films than a deposit with a hollow crater-like topography. The contrasting behaviour observed for the spray-coated films suggests the increased surface roughness at higher solution concentrations is related to the film formation process, rather than the drying behaviour of individual droplets.

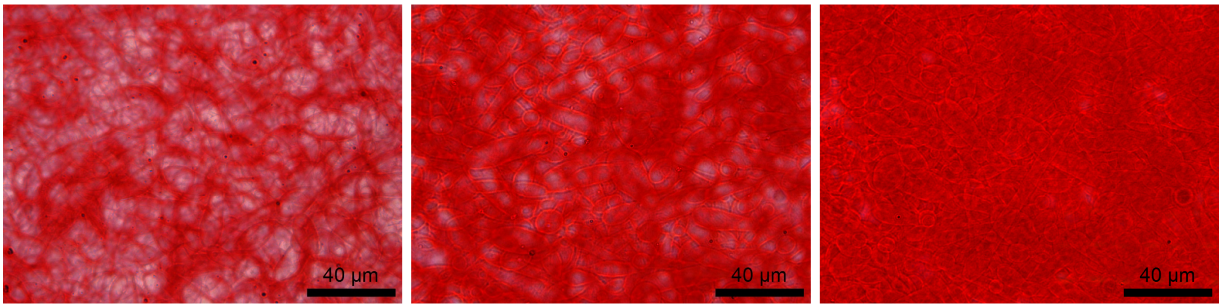

(a) 5 mg/ml (b) 10 mg/ml (c) 20 mg/ml

Figure 4.16: Optical microscopy images comparing the surface morphology of spray-coated films deposited from solution concentrations of 5 mg/ml (a) 10 mg/ml (b) and 20 mg/ml (c).

The formation of a uniform film (as opposed to a random array of uniform dried droplets) during spray deposition relies on droplet coalescence prior to drying/gelation. The way in which the coating takes place is sensitive to both the deposition parameters of the spray system and the ink formulation. To achieve a microscopically uniform film, individual droplets must be deposited in close proximity and spread sufficiently to coalesce into a coherent whole. If the droplets are deposited too far apart (e.g. due to an excessively high spray-head or fast raster) or cannot spread before drying (e.g. due to excessive solution viscosity), a rough coating will result. This point has been previously noted by Steirer et al. [106], who reported that drop coalescence during film formation is key to achieving smooth, uniform films in ultrasonic spray-deposition (using PEDOT:PSS as a coating material). At low (2 mg/ml) concentrations of P3HT, 1 mm drop-cast droplets required at least 5 minutes to dry. Assuming the drying time is also long during spray-coating, the likelihood of droplets having sufficient time to spread and coalesce with neighbouring droplets is high, so a uniform film can be expected. At high concentrations (8 mg/ml), the 1 mm drop-cast solutions were observed to gel within seconds of being deposited. Hence, assuming the gelation time is also short during spray-coating, the likelihood of coalescence will be significantly reduced, leading to a rough film.

From a processing prospective, the requirement for low solution concentration results in more solvent waste, which is undesirable. In practice, however, this is not a great limitation since most conjugated polymers are only soluble in non-chlorinated solvents at low concentrations. The fact that spray-coating can yield relatively ”smooth” films at such low concentrations is an advantage over other coating methods such as screen printing that typically require more concentrated, viscous solutions.

4.2.3 Co-solvent systems

In the previous two sections, it was shown that for large drop-cast ($d \sim 1$ mm) droplets, gelation (and the associated increase in solution viscosity) leads to reduced coffee-staining. However, increased gelation was not found to improve the uniformity of spray-coated films which are formed from droplets of much smaller size. At low concentrations (5 mg/ml), coffee-staining was observed for spray-deposited films for all molecular weights investigated. Although increasing the solution concentration resulted in reduced coffee-staining of drop-cast films, for all molecular weights tested, the uniformity of the spray-coated films actually worsened as the solution became more viscous due to reduced droplet coalescence. Reducing coffee-staining, whilst at the same time encouraging droplet coalescence, appears to be the principal requirement for improving film uniformity. An alternative way to manipulate the drying patterns of droplets which doesn’t rely on an increase in solution viscosity (and hence should not prevent droplet coalescence), is to add a secondary solvent. As discussed in section 1.4.2, a gradient in the surface tension and/or boiling point between the centre and edge of the drying droplet can lead to radial material flow that counteracts or reinforces the outward capillary flow responsible for coffee-staining, depending on the direction of the gradient. The requirements for the secondary solvent include miscibility with the primary solvent as well as the ability to dissolve the solute.

Indane is a common, non-halogenated solvent that has previously been demonstrated as a potential replacement for halogenated solvents such as o-dichlorobenzene for P3HT based devices [107]. Indane is fully miscible with o-xylene and has both a higher boiling point and a higher surface tension (176 °C and 34.9 mN/m versus 144 °C

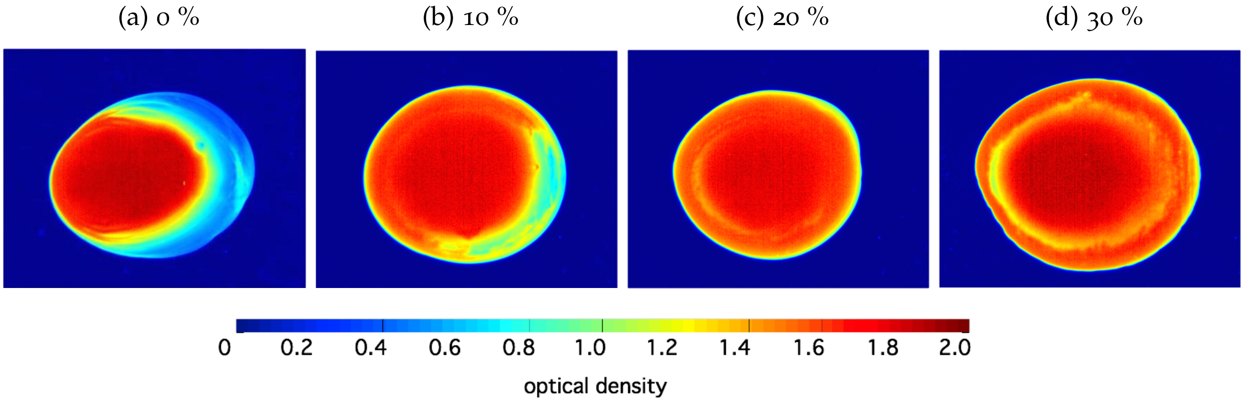

Figure 4.17: Absorbance maps of drop-cast 90 kg/mol P3HT films deposited from 3 mg/ml o-xylene/indane solutions, of varying indane content.

and 30.10 mN/m). Indane is a better solvent for P3HT than o-xylene in terms of it's ability to form a non-gelling solution at room temperature, but is less well suited to spray-deposition at ambient temperatures (due to its higher boiling point). Adding small volume fractions of indane to o-xylene offers a means of reducing the likelihood of gelation without substantially reducing the drying rate of the spray-coated solution. The addition of small amounts of indane ($\leq$40%) to o-xylene has already been shown in section 4.1.4 to reduce the gelation temperature and increase the overall drying time. The addition of indane was consequently expected to increase coffee-staining by increasing the time available for material to travel from the centre of the droplet to the edge (via the evaporation induced capillary flow). In addition to promoting capillary flow, the higher boiling point and higher surface tension of indane relative to o-xylene is also likely to promote outward flow. As the o-xylene evaporates at the edge of the droplet, the surface tension of the solution at the edge is increased (as the indane concentration becomes higher), inducing a surface tension gradient that points out from the centre of the drop to the edge. For solutions that would naturally coffee-stain in pure o-xylene (e.g. for solutions with a P3HT content of <5 mg/ml), the addition of indane would be expected to exacerbate coffee-staining. On the other hand, for solutions that show mound formation in pure o-xylene, this outward flow could improve the uniformity of material distribution and potentially improve the uniformity of sprayed films by enhancing droplet coalescence.

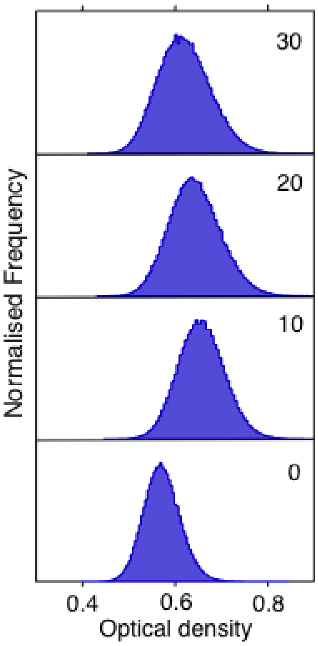

Figure 4.18: Absorbance histograms of 90 kg/mol P3HT films that were spray-deposited from 3 mg/ml solutions, using a gas flow rate of 20 Lpm, raster speed of 7.62 mm/s, solution flow rate of 200 μL/min and indane concentration in the range 0-30 % as indicated at the top right hand corner of each histogram.

Figure 4.17 shows absorbance maps for a series of 1 mm droplets drop-cast from solutions containing 3 mg/ml of 90 kg/mol P3HT, with varying amounts of indane in the range of 0-30 % by volume. With 0 % indane, most of the material accumulated in the centre of the droplet and several, faint concentric rings formed between the centre and edge of the droplet. With 10 % indane, the polymer deposit was less heavily concentrated at the centre, and somewhat more evenly distributed across the full droplet. With 20 % indane, the dried film was more evenly distributed with a relatively flat profile. With a very high indane concentration of 30 %, a mound-shaped centre and a coffee-stained edge were observed, similar to the pattern previously observed for droplets cast from pure o-xylene solutions of intermediate concentration (figure 4.13b).

Figure 4.18 shows the effect of indane concentration on the absorbance histograms of films that were spray-coated from the same solutions, using a solution flow rate of 200 μL/min, a gas flow rate of 20 Lpm and a raster speed of 7.62 mm/s. Increasing the indane concentration had little effect on the mean optical density of the film (figure 4.19a) but caused a marginal increase in the the standard deviation and relative standard deviation of the deposited films (as shown in figures 4.19b and 4.19c). This contrasts with the behaviour of the drop-cast films which showed flatter profiles and improved spreading at higher indane content. The reason for this is unclear and requires further investigation.

Despite the slight increase in surface roughness, spray-coating from a mixed o-xylene/indane solution can still be beneficial due to the reduction in gelation temperature, (which in principle should allow processing at ambient temperatures without heating).

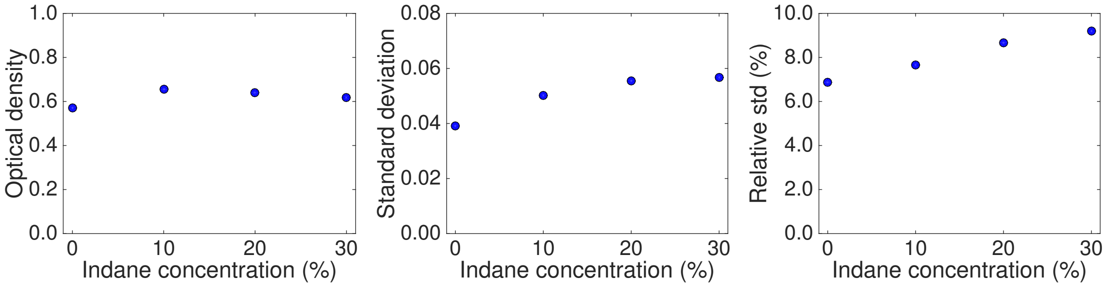

(a) (b) (c)

Figure 4.19: Plots showing how the mean optical density (a) the standard deviation (b) and the relative standard deviation (c) of the absorbance distributions of spray-deposited P3HT films varies with increasing indane concentration.

4.3 The effect of spray parameters on film uniformity

In the previous sections, the effect of ink composition on the film properties were discussed. In the following sections the effect of spray parameters such as gas flow rate, solution flow rate and raster speed are discussed.

4.3.1 Carrier gas flow rate

Increasing the carrier gas flow rate/gas velocity has been reported to improve the uniformity of films for gas-driven spray nozzles due to a decrease in average droplet size [108]. The effect of the carrier gas flow rate on the droplet size was investigated in section 2.3.1, where it was confirmed that higher gas velocities did indeed result

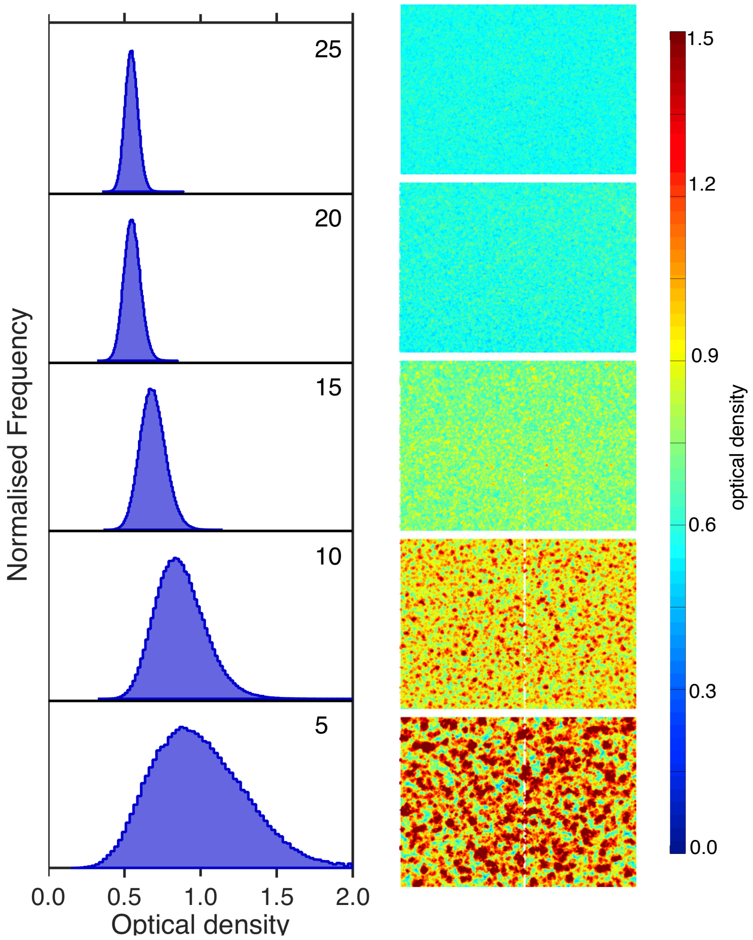

Figure 4.20: Left: absorbance histograms of 90 kg/mol P3HT films that were spray-deposited from 5 mg/ml solutions in o-xylene at room temperature, using a solution flow rate of 200 μL/min, raster speed of 12.7 mm/s and gas flow rate in the range 5-25 Lpm as indicated in the right top hand corner of each histogram. Right: the corresponding absorbance maps of each of the films.

in the production of smaller droplets for the co-axial spray head used in this work. However, the size distributions were obtained for thin, sparse droplet coatings (with widely separated droplets), and so provided no information about the effect of droplet size on the uniformity of dense films. To determine the effect of carrier gas flow rate on film uniformity, P3HT films of molecular weight 90 mol/kg were sprayed from 5 mg/ml o-xylene solutions, using a solution flow rate of 200 μL/min, a raster speed of 12.7 mm/s and a range of carrier gas flow rates from 5 to 25 Lpm. The films were optically profiled using the technique explained in section 3.3. Figure 4.20 shows absorbance maps and histograms for each of the films. Increasing the carrier gas flow rate caused the mean absorbance of the films to decrease from 0.98 to 0.54 and the width of the histograms to narrow substantially, indicating the formation of thinner, more uniform films. Since the liquid flow rate was held constant at 200 μL/min, this is consistent with visibly increased divergence of the spray cone emerging from the spray head, leading to reduced deposition on the small-area substrates.

The effect of carrier gas flow rate on film uniformity and overall film thickness is shown more clearly in figure 4.21, which shows how the mean optical density, standard deviation, and relative standard deviation of the films vary with the gas flow rate. The mean optical density of the film decreased steadily from 0.98 to 0.55 as the flow rate was increased from 5 to 20 Lpm, but remained approximately constant at 0.55 when the flow rate was increased further. The standard deviation followed a similar trend decreasing steadily with carrier gas flow rate until 20 Lpm and plateauing thereafter. This observation is consistent with the change in droplet size reported in section 3.3, where the drop size decreased in magnitude with increasing carrier gas flow rate until reaching an approximate plateau at 20 Lpm. The similarity in the trends confirms that achieving a small droplet size is crucial for forming smooth thin polymer films. The the relative standard deviation of the smoothest film (7.9 %) obtained at the highest gas flow rate is somewhat higher than that achieved by spin coating (2.5 %). In subsequent sections, I describe attempts to further optimise the deposition conditions to narrow this discrepancy.

4.3.2 Solution flow rate

While gas flow rate has a clear influence on film thickness, a more direct way to control the film thickness is to vary the solution flow rate. Figure 4.22 shows for a 5 mg/ml/90 kg/mol P3HT solution, the effect on the absorbance histograms of changing the solution flow rate, using a gas flow rate of 20 Lpm and a raster speed of 12.7 mm/s. Increasing the solution flow rate from 50 to 400 μL/min caused the mean optical density of the film to increase linearly from 0.2 to 1.3 (as shown in figure 4.23a).

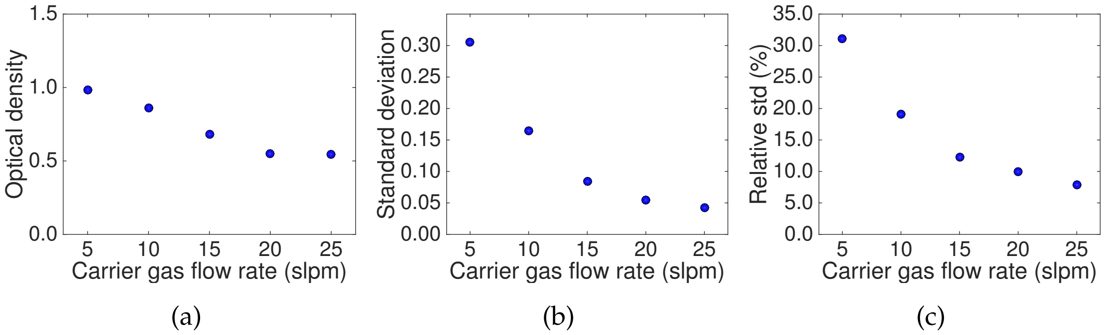

Figure 4.21: Plots showing how the mean optical density (a) the standard deviation (b) and the relative standard deviation (c) of the absorbance distributions of spray-deposited films varies with gas flow rate. Data was extracted from figure 4.20

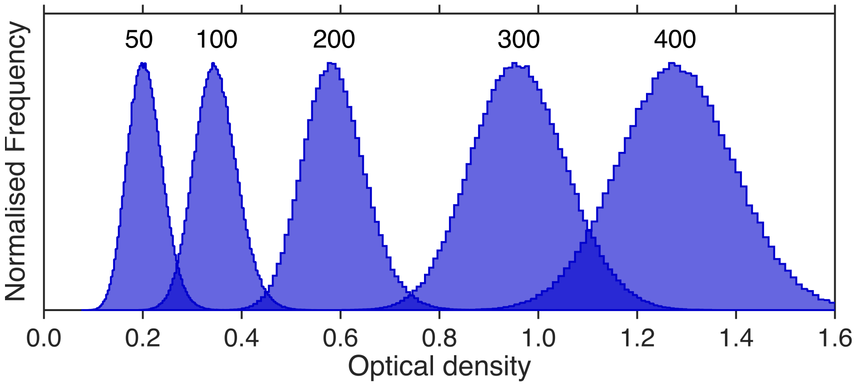

Figure 4.22: Absorbance histograms of 90 kg/mol P3HT films that were spray-deposited from 5 mg/ml solutions, using a gas flow rate of 20 Lpm, raster speed of 10.16 mm/s and solution flow rate in the range 50-400 μL/min as indicated above each histogram.

Due to this linear behaviour, modification of the solution flow rate offers a simple and effective way of controlling film thickness.

The standard deviation in the absorbance also increased with increasing solution flow rate, indicating an increase in the absolute film roughness (figure 4.23b). Interestingly, the relative standard deviation decreased with increasing solution flow rate (see figures 4.23c and 4.23d), indicating that the thicker spray-coated films are smoother, on a relative basis, than the thinner films. This suggests that, irrespective of the target film thickness, a high solution flow rate is favourable for the deposition of uniform films.

As discussed in section 4.3.2, the size of the droplets generated by the nozzle was not significantly affected by the flow rate of the solution. Therefore another effect

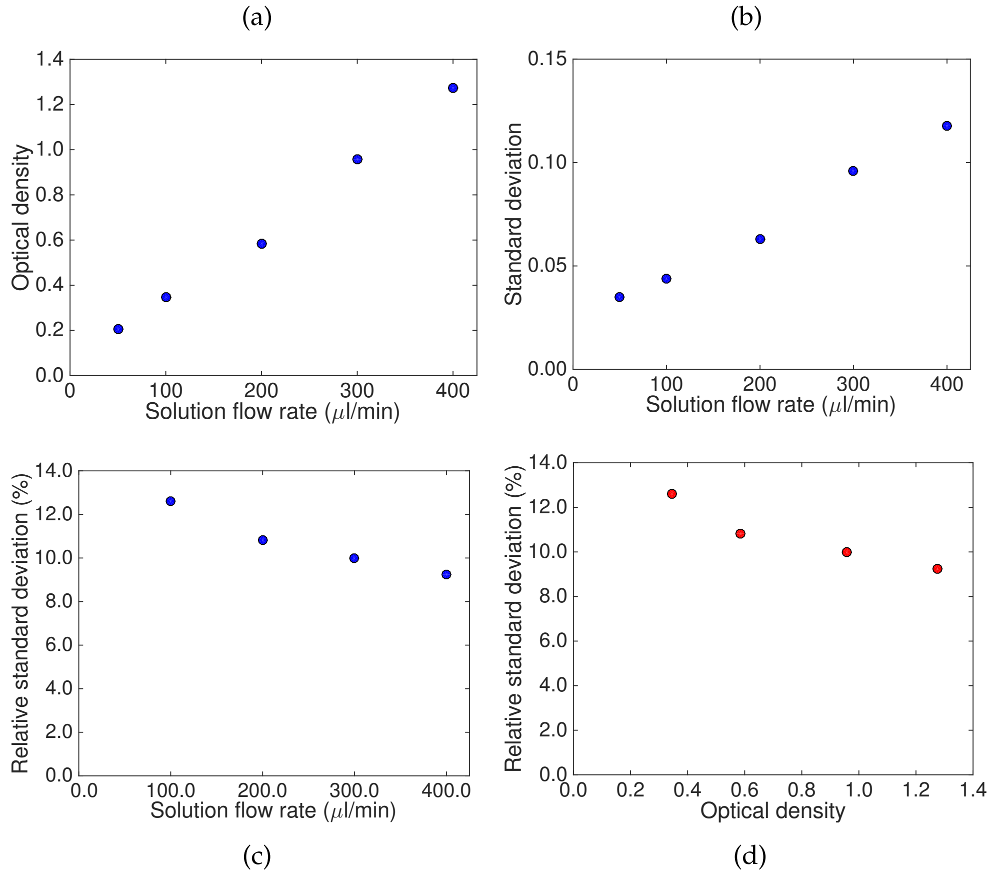

Figure 4.23: Plots showing how the mean optical density (a) the standard deviation (b) and the relative standard deviation (c) of the absorbance distributions vary with increasing solution flow rate. (d) shows how the relative standard deviation varies with respect to the mean optical density of each film.

must be responsible for the relative reduction in surface roughness with increasing solution flow rate. The most likely reason is a difference in the film formation process for films sprayed at low and high solution flow rates. The formation of a uniform film (as opposed to a random array of dried droplets) during spray deposition relies on droplet coalescence prior to drying. Droplets can either be successively stacked onto the substrate as isolated drops that dry individually, or else they may be deposited in close proximity and coalesce into a single, uniform, wet layer that dries after coalescence. At low solution flow rates, the total volume of solution deposited is low, and it is likely that the droplets will form spatially isolated ”islands” on the surface of the substrate, forming domains that dry independently, with poor interconnectivity. At

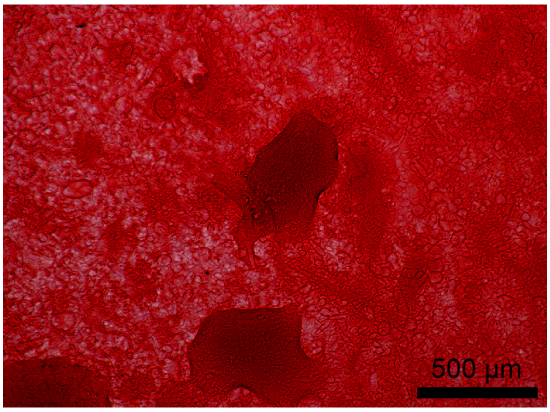

Figure 4.24: Optical microscopy image showing the effect of solution ”pooling” on a spray-deposited film. Pooling was caused by using a high solution flow rate of 800 μL/min.

high deposition rates, by contrast a continuous wet layer can form, leading to smoother films.

Although using high solution flow rates is beneficial for achieving good film uniformity, from a device perspective, this is only practical if low concentration inks are used, otherwise excessively thick films will be obtained, resulting in poor device performance [3]. (The effect on film uniformity of varying solution concentration was discussed in section 4.2.2). If excessively high flow rates are employed, the rate of solution deposition can exceed the evaporation rate of the solvent, resulting in solution ”pooling” (the formation of thick uneven puddles of solution), which leads to an irregular and sometimes discontinuous surface morphology on drying [18]. Elevated substrate temperatures can sometimes prevent solution pooling by increasing the rate of solvent evaporation to compensate for the increased deposition rate. However, balancing the two variables can be challenging. (The effect of varying substrate temperature on film uniformity is discussed in more detail in section 4.3.4).

Although solution pooling was not observed for the range of solution flow rates (50-400 μL/min) presented in figures 4.23 and 4.22, it was observed for solution flow rates $\geq$ 800 μL/min. This is shown in the optical micrograph of figure 4.24, for a 5 mg/ml solution concentration at room temperature. In practice however, the high solution

---

[3] Using high raster speeds is an alternative way to avoid excessively thick films but is not conducive to smooth film formation (as discussed in section 4.3.3).

flow rates for which "pooling" was observed are not necessary to achieve the typical film thicknesses needed for device applications (e.g. active layer films typically have mean optical densities close to unity).

4.3.3 Raster speed

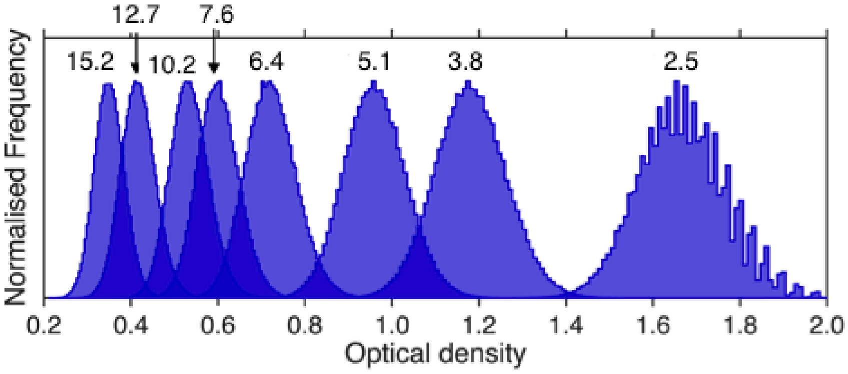

Figure 4.25: Absorbance histograms of 90 kg/mol P3HT films spray-deposited from 5 mg/ml o-xylene solutions, using a solution flow rate of 200 μL/min, gas flow rate of 20 Lpm, and various raster speeds in the range 2.5-15.2 mm/s as indicated above each histogram.

The raster speed offers a complementary means of controlling film thickness as it affects the time the spray-head spends at any given location. The total volume of solution deposited onto the substrate therefore depends on both the rate at which the solution is dispensed and the rate at which the nozzle is transported across the substrate. For all measurements reported here, a single-pass method was employed. Figure 4.25 shows absorbance histograms for 90 kg/mol P3HT films sprayed from 3 mg/ml o-xylene solutions, using a solution flow rate of 200 μL/min, a gas flow rate of 20 Lpm and raster speeds in the range of 2.5 to 15.2 mm/s. The mean absorbance, standard deviation and relative standard deviation are plotted versus raster speed in figures 4.26a- 4.26c, while the relative standard deviation is plotted against the mean optical density, in figure 4.26d.

As expected, the mean optical density decreased with increasing raster speed, consistent with the reduced volume of material deposited per unit area. The standard deviation also decreased with increasing raster speed, consistent with a decrease in absolute roughness (see figure 4.26b). The relative standard deviation, by contrast, increased with raster speed (see figure 4.26c), indicating an increase in relative roughness. This suggests that a slower raster speed is favourable for the formation of uniform films. Since the solution flow rate, gas flow rate and capillary size were the same in each case, implying identical droplet size distributions, it is clear that other factors (in particular droplet coalescence) are important in determining film roughness.

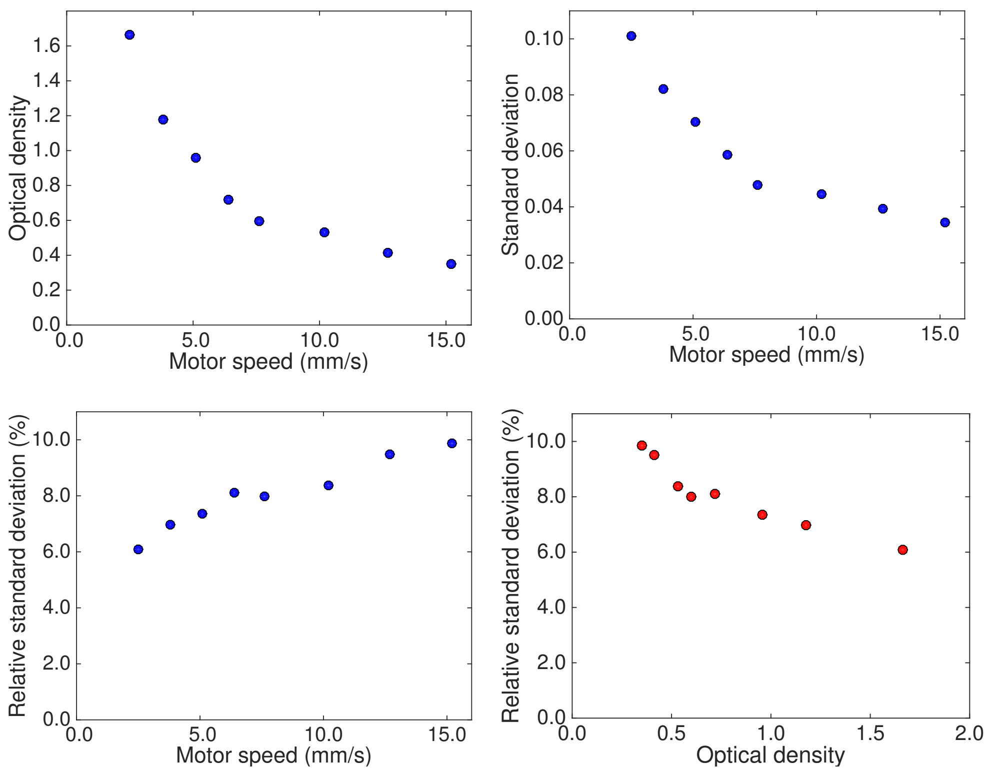

(a) (b)

(c) (d)

Figure 4.26: Plots showing how the mean optical density (a) the standard deviation (b) and the relative standard deviation (c) of the absorbance distributions vary with increasing raster speed. (d) shows how the relative standard deviation varies with respect to the mean optical density of each film.

This variation in surface morphology arising from the change in raster speed is also evident from the optical microscope images of figure 3.1, where it can also be seen that a fast raster speed results in a low droplet density across the substrate (and thus a reduced likelihood of droplet coalescence), resulting in a film that is riddled with discrete coffee-ring-like structures. At slower deposition speeds, the higher resulting droplet density increases the likelihood of coalescence before drying, leading to a thicker, more homogenous film.

4.3.4 Temperature

To investigate the effect of substrate temperature on film morphology, solutions of P3HT in o-xylene (1 μL of 90 kg/mol P3HT at 5 mg/ml) were drop cast onto substrates at different temperatures in the range 22-160 °C, after which, they were optically profiled using the setup described in section 3.3. Absorbance maps of the deposited drops are shown in figure 4.27. For droplets deposited at room temperature ($\sim$22 °C), classic coffee staining was observed, with most of the material being deposited in a single ring around the edge of the drop. At higher substrate temperatures in the range 60-120 °C, the dried films displayed multiple rings - an effect that, as perviously noted, has been reported in the literature for lightly pinned drops of particle suspensions [70]. This effect was discussed briefly in section 1.4.2, and is attributable to intermittent pinning and de-pinning of the contact edge during drying.

Given the wide range of patterns observed over the investigated temperature range, it is unsurprising that both the surface roughness and thickness of sprayed films varied substantially with substrate temperatures. Figure 4.28 shows absorbance histograms for films sprayed using a solution flow rate of 200 μL/min, a gas flow rate of 20 Lpm and a raster speed of 12.7 mm/s, at substrate temperatures in the range 22-160 °C, from the same 90 kg/mol, 5 mg/ml o-xylene solutions. Figures 4.29a and 4.29b show the mean optical density, standard deviation and relative standard deviation of the films versus the substrate temperature. For temperatures above 50 °C, the mean optical density and standard deviation of the films increased with increasing substrate temperature. Interestingly, this 50 °C transition temperature coincides with the lowest temperature at which multiple coffee rings were observed for the drop cast films, suggesting a potential connection between the two observations. It is important to stress again, however, that the large volumes of solution deposited during drop casting (1 μL) may behave quite differently than the small (< 0.01 μL) droplets generated by spray-deposition.

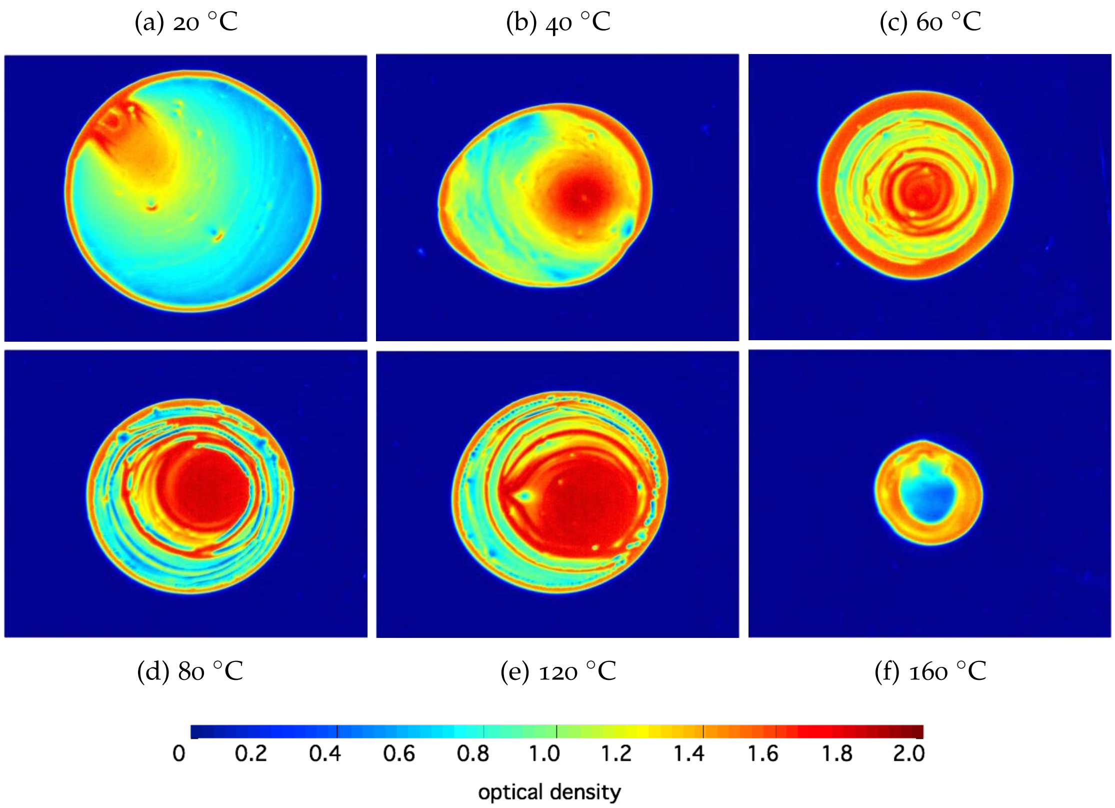
(a) 20 °C (b) 40 °C (c) 60 °C

(d) 80 °C (e) 120 °C (f) 160 °C

Figure 4.27: Absorbance maps of drop-cast films deposited from 5 mg/ml o-xyelene solutions, using 90 kg/mol P3HT at substrate temperatures of (a) 20 (b) 40 (c) 60 (d) 80 (e) 120 and (f) 160 °C.

The influence of the substrate temperature on the likelihood of coalescence provides an alternative/additional explanation for the observed increase in film roughness with increasing substrate temperature. As well as causing multiple ring formation within individual drops, increasing the substrate temperature may also reduce the likelihood of coalescence with other, neighbouring drops due to excessively fast drying. Previous reports relating to the effects of substrate temperature on the surface morphology and structural features of spray-deposited polymer films have emphasised the importance of balancing the evaporation rate with the solution flow rate in order to prevent film formation by successive stacking of dried droplets at one extreme and pooling at the other. A number of reports have discussed the optimum substrate temperature to achieve uniform film characteristics for various polymer and solvent combinations [106, 109]. It has been suggested that the substrate temperature should be close to the boiling

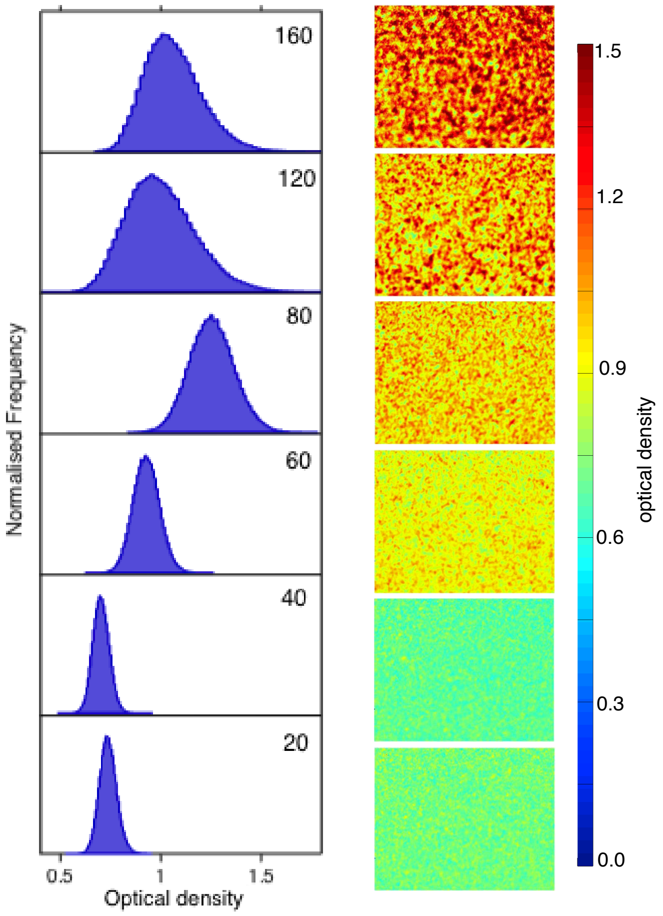

Figure 4.28: Left: absorbance histograms of 90 kg/mol P3HT films that were spray-deposited from 5 mg/ml solutions in o-xylene, using a solution flow rate of 200 μL/min, gas flow rate of 20 Lpm, raster speed of 12.7 mm/s, and substrate temperatures in the range 20-160 °C as indicated in the right top hand corner of each histogram. Right: the corresponding absorbance maps of each of the films.

point of the solvent [109]. Steirer et al. for instance, were able to achieve uniform films of ultrasonically spray-deposited PEDOT:PSS (70 nm thick) with a minimum surface roughness of 4 nm as measured by optical profilometry [106]. However, due to the already elevated evaporation rate of the solvent caused by the high carrier gas velocity used for atomisation in this work, and the observed increase in film roughness on increasing substrate temperature, heating the substrate to the boiling point of

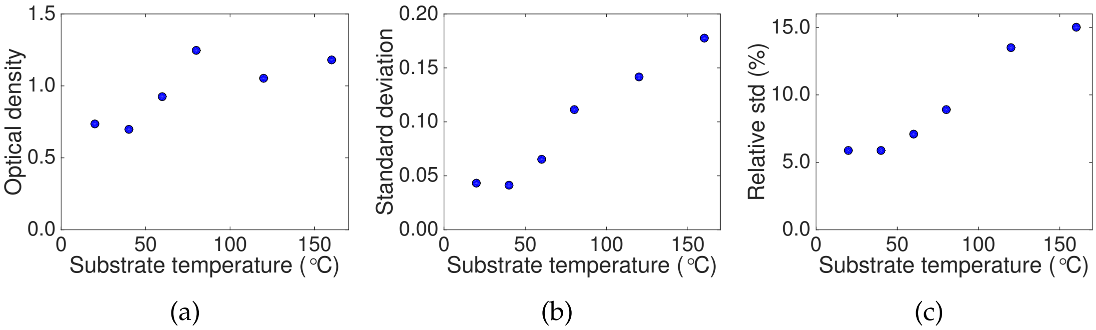

Figure 4.29: Plots showing how the mean optical density (a) the standard deviation (b) and the relative standard deviation (c) of the absorbance distributions of spray-deposited P3HT films vary with increasing substrate temperature.

the solvent was not a viable option here, and thus the substrate was kept at room temperature for subsequent work presented in this thesis.

4.4 Summary

In this chapter the molecular weight of the polymer, the solution concentration and the addition of indane as a secondary solvent, were all shown to have a strong influence on both the process of solution gelation (and thus, the processability of a solution) and the material distribution of drop-cast films. However, only the solution concentration was shown to have an appreciable effect on the uniformity of spray-deposited films.

Light-scattering measurements indicated that the solution should ideally be dilute (polymer concentration <5 mg/ml), consist of low molecular weight polymer (20 kg/-mol), and contain a small amount (<40 %) of indane in order to avoid solution gelation and clogging of the spray-head.

In contrast to the improved material distribution observed for drop-cast films, the uniformity of spray-deposited films was insensitive to the polymer molecular weight. It was suggested that evaporation of the solvent from the tiny spray droplets occurred before gelation could occur and thus, the benefits of solution gelation on material distribution were not felt. In contrast to the behaviour of drop-cast films, an increase in solution concentration caused the uniformity of spray-deposited films to worsen. In this case, it was assumed that gelation did occur, but that it was detrimental to droplet coalescence, causing less uniform film formation.

This chapter also examined the effects of the operating parameters of the spray rig on the uniformity of spray-deposited films of P3HT in o-xylene. The smoothest films were formed using higher gas (>15 Lpm) and solution flow rates (>300 μL/min), and lower raster speeds (<7 mm/s), at room temperature. This was attributed to smaller droplet generation and increased droplet coalescence.

Based on the results of this chapter, a firm requirement of the solution for both smooth film formation and ease of processing is low solution concentration (<5 mg/ml). Optimum spray-deposition operating parameters include: a gas flow rate of 20 Lpm, a solution flow rate greater than 200 μL/min, a raster speed that is as low as possible (preferably <5 mm/s) and room temperature deposition. In the next chapter, we use these optimum process parameters to fabricate OPV devices with a spray-coated P3HT:PCBM active layer.

5 Organic photovoltaics

In this final chapter I describe the fabrication, characterisation and analysis of organic devices, in which the P3HT/PCBM active layer was deposited by spray-coating from the non-chlorinated solvent o-xylene, using the spray system and optimised processing conditions described in previous chapters. Before doing so I will briefly summarise the operating principles of OPV devices, and review pertinent prior work on spray-coated OPV devices from the literature.

5.1 Organic heterojunctions

Photovoltaic devices convert a flux of incident photons into an electronic current. Three steps are necessary for the generation of electrical power in a photovoltaic device:

1. Absorption of photons by the photoactive material(s);
2. Photoinduced charge separation, leading to the generation of mobile carriers;
3. Collection of electrons at one electrode and holes at the opposite electrode.

A variety of organic photovoltaic device architectures have been reported, but here we focus exclusively on the most widely used and most efficient architecture: the polymer/fullerene bulk heterojunction solar cell. In their simplest form, polymer/fullerene bulk heterojunction organic solar cells are based on a single phase-separated blend of a semiconductor polymer and a soluble fullerene derivative (~100-200 nm), sandwiched between between two electrodes (of which at least one must be transparent in order for light to pass through). Numerous nanoscale interfaces are formed between the polymer and the fullerene, which are chosen to have offset frontier orbitals. The highest occupied molecular orbital (HOMO) and lowest unoccupied molecular orbital (LUMO) of the polymer are chosen to be higher in energy (i.e. less negative with respect to the vacuum level) than those of the fullerene. Upon absorption of a photon by the polymer (the fullerene is typically only weakly absorbing), an electron is excited from the HOMO level to the LUMO level, forming a tightly bound exciton with the hole left behind in the HOMO level. The (neutrally charged) exciton diffuses through the polymer domain in which it was generated, and in the course of its migration may reach a polymer/fullerene interface, where it may dissociate via an ultrafast electron transfer process from the polymer to the fullerene. A schematic of exciton dissociation into free charge carriers at the bulk heterojunction interface, is shown in figure 5.1a.

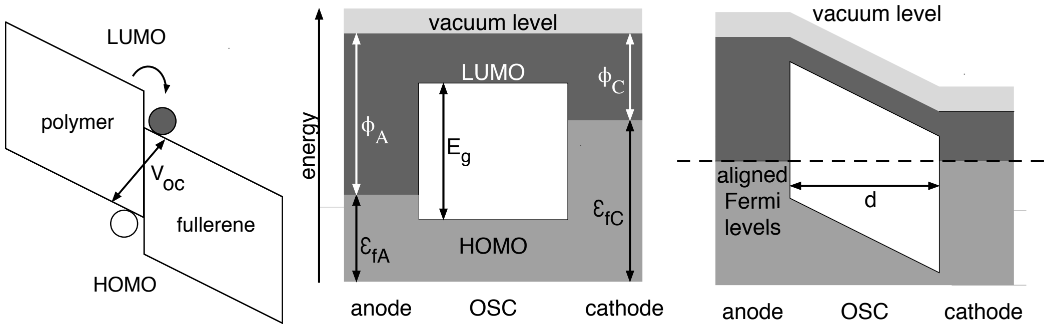

(a) exciton dissociation (b) before contact (c) after contact

Figure 5.1: (a) Exciton dissociation into free charge carriers at the bulk heterojunction (b-c) A simple model of a bulk heterojunction organic solar cell, where the polymer/fullerene blend is presented as a single semiconductor, with its HOMO derived from the polymer and its LUMO from the fullerene. The organic layer is sandwiched between electrodes with differing work functions. At equilibrium, the Fermi levels of the electrodes equalise, thus developing a "built-in" electric field.

After electron transfer, a "charge-transfer" exciton is formed, in which the electron and hole are spatially separated on different moieties, but a residual Coulombic interaction remains between them. If the charge-transfer exciton has sufficient excess energy, it may overcome its Coulombic binding and dissociate into free carriers. Following exciton dissociation, the constituent charges are driven in opposite directions by the electric field inside the device to their respective electrodes. The electric field is set up as a result of the different work functions of the two electrodes, and is created when the device is in equilibrium and the Fermi-levels of the two electrodes are equalised (the low work function cathode essentially donates electrons to the high work function anode, raising the Fermi level of the anode relative to the cathode until they are equal). The two electrode materials are chosen to have substantial work function differences to maximise the internal electric field, e.g. indium tin oxide (ITO), the most widely used transparent anode material, has a work function of ~4.5 eV, while calcium, a common cathode material, has a work function of ~ 2.9 eV. Under illumination and in the absence of an external voltage, the built-in field drives free electrons along the fullerene network towards the cathode, and the holes along the polymer network towards the anode.

Due to the low intrinsic carrier density, the built-in field may be regarded as constant throughout the organic layer [110]. The electric strength E_{bi} is given by

$$E_{BI} = -\frac{V_{BI}}{d} \tag{5.1}$$

where d is the thickness of the organic semiconductor and V_{BI} is the built-in potential. To a first approximation, V_{BI} is determined by the difference in the electrode work functions [110]:

$$V_{BI} = -\frac{\Phi_A - \Phi_C}{e} \tag{5.2}$$

The situation can be modified, however, by pinning [111, 112]. The Fermi level of the cathode becomes pinned to the LUMO level of the acceptor if it lies higher in energy, and the Fermi level of the anode becomes pinned to the HOMO level of the donor if it lies lower in energy. Hence, the biggest voltage that can be developed across the device is determined by the energy difference between the LUMO level of the acceptor and the HOMO level of the donor. For P3HT:PCBM devices, pinning usually occurs at the cathode due to the deep-lying LUMO level of the fullerene [113].

A schematic of a bulk-heterojunction device in the presence of the built-in internal field is shown in figure 5.1c, where the polymer/fullerene blend is presented as a single semiconductor, with its HOMO derived from the polymer and its LUMO from the fullerene.

5.2 Current-voltage characteristics

The application of an external bias V between the anode and the cathode modifies the internal field strength in accordance with equation 5.3.

$$E = \frac{V - V_{BI}}{d} \tag{5.3}$$

The measured current response of a solar cell (J_{light}) may be considered to be the sum of an injected current (J_{dark}) and a photogenerated current (J_{ph}). J_{light} is altered as the voltage is increased from zero at short circuit, to a value above that of the built-in voltage ($V > V_{BI}$). The flow of both injected (J_{dark}) and photogenerated (J_{ph}) charge carriers is explained below as a function of applied voltage, with respect to competing diffusion and drift currents.

5.2.1 Dark conditions

We start by considering the behaviour of the device in the dark for which $J_{ph} = 0$. At equilibrium ($V = 0$), the high electron density at the low work function cathode causes electrons to diffuse from the cathode towards the anode. The internal electric field causes an electron drift current that opposes this diffusion current such that the net dark current flow is zero ($J_{dark} = 0$). (A similar argument applies to the holes, which have a high density at the high work function anode). For reverse bias conditions ($V < 0$), the internal electric field is larger, and the negative drift current overcomes the diffusion current, resulting in a small, negative net current ($J_{dark} < 0$). For applied voltages slightly above zero ($V > 0$), the electric field strength and the resulting drift current is reduced, and the positive diffusion current dominates, resulting in a positive dark current ($J_{dark} > 0$). For an external voltage equal to the built-in voltage ($V = V_{BI}$), the internal electric field is zero and the dark current is solely dependent upon the contribution from the positive diffusion current. As the applied voltage is increased further such that $V > V_{BI}$, the direction of the internal electric field is switched. The resulting drift current no longer opposes the diffusion current, but instead reinforces

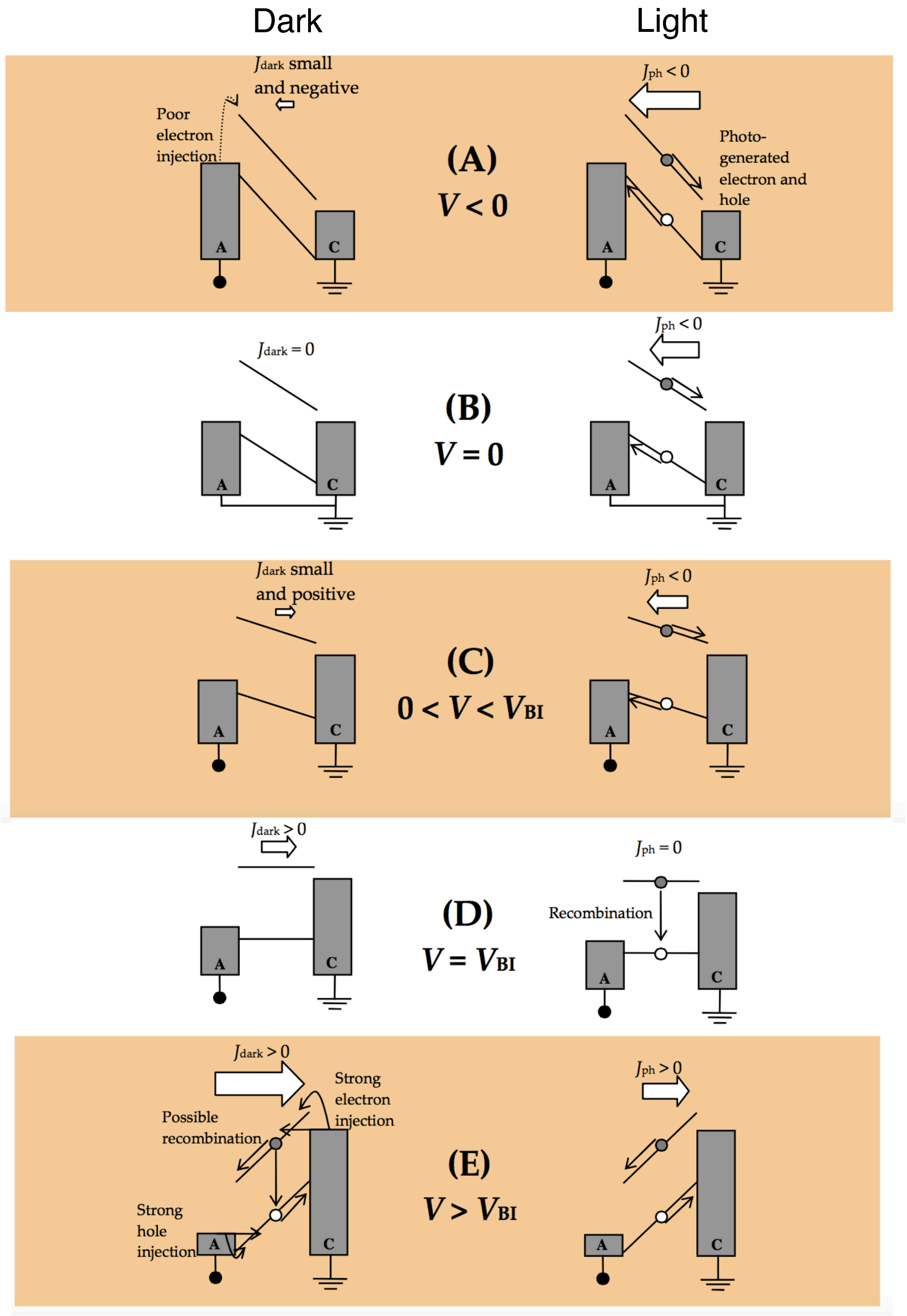

Figure 5.2: A schematic diagram illustrating the direction of current flow at various applied voltages, taken from [114].

its positive contribution to the overall dark current. The switch in direction of the electric field also enables an additional mechanism for charge injection in the form of tunnelling through the triangular energy barrier (see figure 5.2*E*), leading to a sharp positive increase in the dark injection current.

5.2.2 Under illumination

As noted above, the photogenerated current, J_{ph}, has its origins in exciton dissociation upon photoabsorption, leading to the generation of free charge-carriers. For $V \leq 0$ (see figure 5.2), the electric field causes the electrons and holes to migrate preferentially to the cathode and anode, respectively, resulting in a negative photogenerated current ($J_{ph} < 0$) that grows in magnitude with increasing field strength. When the applied voltage is greater than zero, it opposes the built-in potential, resulting in a reduced electric field strength. As a result the photogenerated charges are swept out of the device less rapidly, leading to increased carrier loss by electron-hole recombination and a diminished photocurrent. At $V = V_{BI}$ the electric field is cancelled, and the photogenerated carriers migrate equally (by diffusion) to the two electrodes, resulting in a net photogenerated current of zero ($J_{ph} = 0$). For $V > V_{BI}$, the reversal of the electric field causes the photogenerated electrons and holes to migrate preferentially to the anode and cathode, respectively, resulting in a positive photocurrent ($J_{ph} > 0$) that increases in magnitude with increasing field strength. If the electric field strength is sufficiently high, the positive photocurrent becomes limited by the rate of photogeneration of excitons rather than the field strength, and so the photogenerated current saturates. The measured photocurrent can then be understood as a summation of the dark and photogenerated current curves.

The above description applies when a solar cell is subjected to an external bias, using e.g. a battery. For a solar cell under illumination, the measured voltage cannot be lower than zero and cannot be higher than V_{BI}, meaning the solar cell operates only in the fourth quartile of the $J - V$ curve.

5.3 Characterising device performance

Several solar cell performance indicators can be obtained directly from the $J_{light} - V$ characteristics of the device (see figure 5.3), namely: the short-circuit current J_{SC}, the open-circuit voltage V_{OC}, the fill factor FF and the power conversion efficiency PCE.

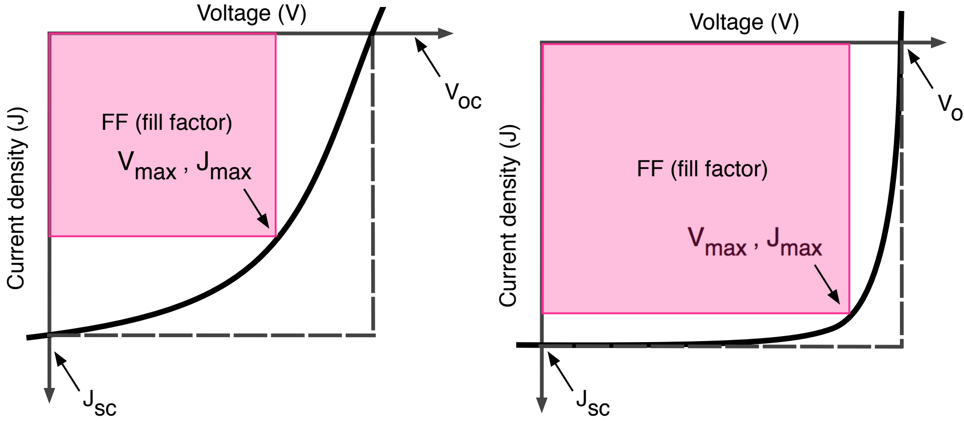

(a) low fill factor. (b) high fill factor.

Figure 5.3: Current density vs. voltage (J-V) of a solar cell.

The short-circuit current is the maximum photocurrent produced by the solar cell, when there is no external voltage (or photocurrent) applied, and the open-circuit voltage is the maximum voltage delivered by the solar cell, when the current is zero. Both of these modes of operation yield zero power. The fill factor is a parameter which, in conjunction with V_{OC} and J_{SC}, determines the maximum power from a solar cell, and is defined as:

$$FF = \frac{P_{max}}{V_{OC} J_{SC}} \tag{5.4}$$

Graphically, the FF is a measure of the "squareness" of the solar cell and is the ratio between the maximum power generated by the solar cell (pink area in figure 5.3), and the power at V_{OC}, J_{SC} (grey-dotted area in figure 5.3). The FF is determined by the competition between sweep-out of the photogenerated carriers and the recombination of carriers to the ground state.

The efficiency of a solar cell is the most commonly used parameter for quantifying device performance. It is defined as the fraction of incident optical power, P_{in}, which is successfully converted to electrical power:

$$PCE = \frac{J_{SC}V_{OC}FF}{P_{in}} \tag{5.5}$$

The incident optical power is usually an approximation of the AM 1.5 solar spectrum (i.e., the spectrum of the solar radiation received on the surface of the earth 100 mW/cm^2).

5.4 Loss mechanisms

It is sometimes instructive to model a photovoltaic cell using an equivalent circuit of the form shown in figure 5.4. The equivalent circuit comprises several components: a current source representing the negative current due to the photogenerated flux of electrons and holes; a diode accounting for the injection current flowing through the active layer semiconductors, with the direction of its symbol indicating forward bias; a shunt resistance (R_{sh}) accounting for current flow through Ohmic shorts or shunts between the two electrodes (typically caused by metallic filaments formed during evaporation of the top electrode); and a series resistance (R_0) accounting for the resistance of the two electrodes, in particular the transparent electrode.

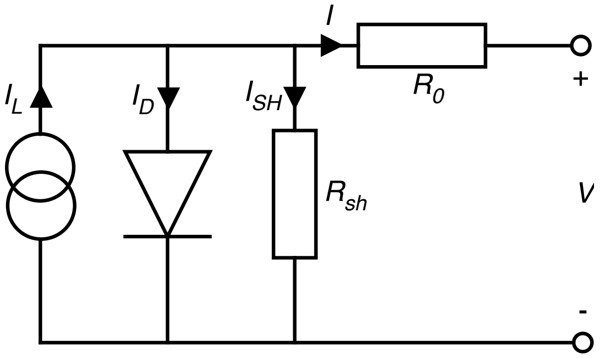

Figure 5.4: An equivalent circuit diagram for the photodiodes.

The series resistance can be obtained from the $I - V$ curve in figure 5.4 by

$$R_0 = \left(\frac{dV}{dI}\right)_{I \to 0} \tag{5.6}$$

This series resistance leads to an unwanted voltage across the electrode(s), causing energy dissipation, and should ideally be zero. The shunt resistance is given by

$$R_{sh} = \left(\frac{dV}{dI}\right)_{V \to 0} \tag{5.7}$$

This resistance accounts for leakage in the device caused by imperfections in the film such as electrical shorts through pinholes and exciton recombination. These leakage phenomena decrease the net current generated by the device, so ideally the shunt resistance should be infinite.

The often rough and inhomogeneous films associated with spray coating can negatively affect both the series and shunt resistance by generating pinholes and associated shunts that decrease the shunt resistance, and by leading to poor electrical contact between the electrodes and active layer materials, increasing the series resistance. Attaining a continuous and moderately smooth film is therefore important for attaining good device performance. However, as we discuss below, it is more important for the film to be continuous than smooth, and high PCEs can be obtained even for relatively rough films.

5.5 Spray-deposited organic bulk heterojunction solar cells

The use of spray-coating to prepare organic devices (and OPV devices in particular) has received increasing interest over the past few years. There are many reports of the electrode layers [106, 115–119], the hole transport layer [120, 121], the electron transport layer [122], and/or the organic active layer [10, 109, 120, 123–129] being deposited using either gas-driven or ultrasonic spray systems. The work reported in this thesis is specifically concerned with the deposition of polymer-based active layers. In the following few pages, I provide a brief overview of previous work relating specifically to polymer-based active layers.

The first report describing the use of spray-coating to deposit the active layer focused on evaporative spray deposition from an ultra-dilute solution (1 ppm), consisting of a functionalised fullerene and a poly-p-phenylenevinylene PPV derivative in the non-toxic solvent, tetrahydrofurane (THF) [130]. Whilst the method required an evacuated chamber (which is likely to be incompatible with low cost, large-area fabrication), it allowed the fabrication of smooth polymer films and resulted in devices with power conversion efficiencies of 0.69 %. The report is of interest as one of very few attempts to spray-deposit the active layer from an environmentally friendly solvent.

Later work focused on the fabrication of OPV devices in air (i.e. without the need for an evacuated chamber), using conventional handheld gas-driven spray heads (of the type described in section 1.3) to deposit a P3HT:PCBM active layer from the (chlorinated) solvent chlorobenzene [123]. A power conversion efficiency of 2.83 % was reported, comparable to equivalent devices spin-coated in air but lower than spin-coated devices fabricated under inert atmosphere conditions (3.9 %). Interestingly, the 2.8 % PCE was achieved in spite of a relatively high RMS roughness of 52 nm, which as noted above suggests that exceptional film smoothness is not required for achieving good device performance. The authors concluded that the performance could be further improved by taking additional precautions to avoid air degradation.

The influence of the spray-gun settings was studied by Girotto et al. [125] for gas-driven systems. They compared single-pass and multiple-pass deposition. In the single-pass case the airbrush was kept approximately 3 cm above the substrate, and was moved in parallel lines over the desired area, using a high solution flow rate of 800 μL/min. In the multiple-pass case, the airbrush was kept approximately 10 cm above the substrate and passed over the desired area multiple times, using a lower solution flow rate of 20 μL/min. Films spray-coated using the single pass technique resulted in higher device efficiencies (2.8 %) than those sprayed using the multiple pass technique (0.4 %).

The difference was attributed to the smoother, more homogeneous films produced using the single pass technique, which resulted in fewer pinholes and improved phase separation between the P3HT and PCBM domains, leading to improved carrier collection at the electrodes.

Careful tuning of the solvent and post-annealing conditions has previously been reported by Green et al. to improve the homogeneity of spray-coated (P3HT:PCBM) films deposited using a gas-driven spray head [124]. Active layers deposited from chlorobenzene were found to be significantly smoother and more homogenous than those prepared from p-xylene, chloroform and toluene. In this case, however, the smoother films did not result in appreciably higher device efficiencies, all of which were below 2.4 %. Steirer et al. subsequently studied the effect of solvent selection on active layers deposited by ultrasonic spray-coating [128]. They found that films sprayed from chlorobenzene resulted in higher device efficiencies than those sprayed from p-xylene (3.2 % and 1.2 %, respectively). The improvement was attributed to the large difference in film morphologies. Large crystalline aggregates (>100 μm in diameter) were observed in films sprayed from p-xylene, which caused extreme phase separation of the active layer components and thus reduced exciton dissociation (due to the lack of intimate mixing), and increased charge carrier recombination.

The use of solvent mixtures, in which one solvent has a high boiling point and the other has a low boiling point, has been previously shown to improve the performance of devices with active layers deposited using gas-driven spray heads. For instance, using a 68:32 blend by volume of orthodichlorobenzene, oDCB, and 1,3,5-trimethylbenzene, mesitylene, increased the PCE from 1.9 % for pure oDCB to 3.1 % for the blend [120]. The authors attributed the improvement to a reduction in the RMS roughness from 67.9 nm for the single solvent system to 24.1 nm for the blend as a result of a favourable change in the drying and wetting behaviours of the solution, which led to improved droplet coalescence. Girotto et al. studied the same solvent mixture for ultrasonically spray-deposited P3HT:PCBM active layers, and were able to achieve an RMS roughness of 6.9 nm and a device performance of 3.53 %, comparable to spin-coated devices cast from the same solution (3.62 %). However, unlike Hoth et al., they attributed the improved device performance to enhanced spreading of the liquid on the substrate due to outward Marangoni flows, caused by the lower surface tension of the secondary solvent in addition to the difference in their boiling points. From the above reports, it is clear that both the film homogeneity/smoothness and microscopic ordering are important for achieving high performance devices.

Finally we note that, a PCE as high as 5.8 % has been reported for OPVs in which the spray-coated active layer comprised a low-bandgap donor material (poly[4,8-bis(1-pentylhexyloxy)benzo[1,2-b:4,5-b′]dithiophene-2,6-diyl- alt-2,1,3-benzoxadiazole-4,7-diyl) and PCBM [131]. This work demonstrates that spray-coating is applicable to the latest generation of high performance materials as well as the widely studied P3HT/fullerene system examined in this thesis.

Overall, spray-deposition of the active layer, from non-chlorinated solvents has not been widely studied, and reports where non-chlorinated solvents such as xylene and toluene were used, conclude that such solvents are unfavourable for device fabrication due to relatively poor device performance. However, the deposition parameters used in these reports were specifically optimised for film formation from solutions consisting of chlorinated solvents (orthodichlorobenzene). It is possible that the same parameters are not optimum for film formation from solutions consisting of other solvents which have different surface tensions and boiling points. The dismissal of non-chlorinated solvents for spray deposition at this stage, is therefore premature. The devices presented in this chapter offer an alternative perspective on the applicability of non-halogenated solvents for device fabrication.

5.6 OPV fabrication

Solar cells with the structure: ITO/PEDOT:PSS/P3HT:$PC_{60}BM$/Ca/Al, were fabricated using a variety of deposition processes (every process except the spray deposition of the active layer was carried out by Dr. Neil Treat). Poly(3,4-ethylenedioxythiophene)-poly(styrenesulfonate), PEDOT:PSS (Clevios PVP AI 4083), was spin-coated at 4000 rpm onto 2 cm^2, pre-patterned indium tin oxide, ITO, glass substrates (purchased from

Merck Display Technologies) and annealed in nitrogen at 175 °C to form a 35-40 nm thin film.

The addition of octanedithiol, ODT, to P3HT:fullerene blends has been reported as a method for achieving higher performance OPV devices by encouraging phase separation during deposition. It acts as a good solvent for PCBM and a poor solvent for P3HT, resulting in segregation during deposition to form an as-cast blend that contains purer domains of the two materials, with a high degree of molecular order than ODT-free films. Chen et al. found that the optimum concentration of ODT for improving as-cast device efficiency was 3 % by volume, due to a greater short-circuit current and fill factor [132]. As such, a 2.5 mg/mL solution of P3HT in o-xylene was mixed with a 2.5 mg/mL solution of $PC_{60}BM$ (Solenne, used as supplied) in o-xylene (97 % volume) and ODT (3 % volume), to form a 1:1 (by mass) blend of P3HT:$PC_{60}BM$.

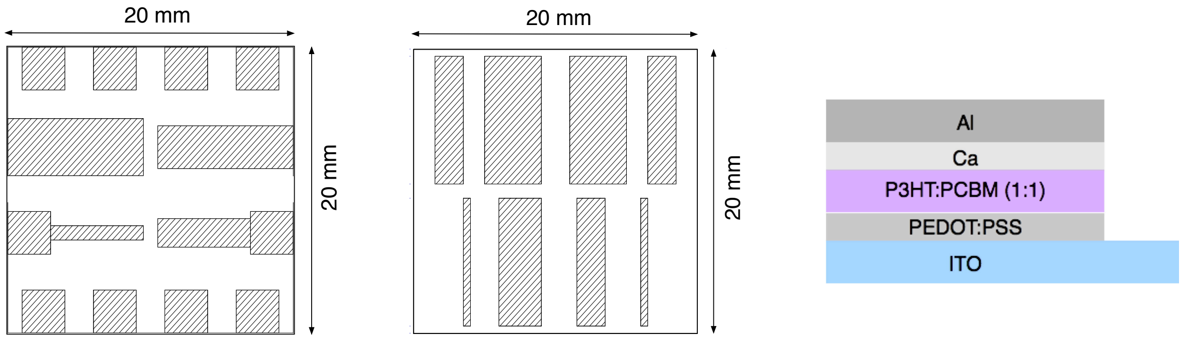

(a) (b) (c)

Figure 5.5: Substate patterns for the anode, ITO (a) and the cathode, Al (b) and a schematic showing the composite materials of the OPV device stack (c).

The polymer:fullerene solutions were spray-coated without filtration to form films with optical densities in the range of ~0.25 to ~0.5. Using the results obtained for pure polymer films (see chapter 4) as a guideline, the chosen spray-deposition operating parameters were as follows: a raster speed of 5.1 mm/s, a solution concentration of 1.25 mg/ml, a gas flow rate of 20 Lpm, and a solution flow rate in the range of 100-200 μL/min. The resulting films were annealed at 160 °C for 10 minutes. Cathodes consisting of 15 nm calcium capped with 80 nm aluminium were evaporated onto the active layer under a vacuum of 10^{-6} mbar, forming eight cells, ranging in size from

0.5 to 16 mm^2 on a single substrate. The electrode patterns and final device stack are shown in figure 5.5.

The current-voltage response of devices were recorded with a Keithley 2400 Source Meter. The voltage source was programmed to sweep through a user-defined voltage range in fixed steps of 20 mV. Upon advancing to a new voltage, 20 successive current readings were made, following which the average was calculated. Measurements were performed under AM 1.5G illumination with an intensity of 100 mW cm^2 from a solar simulator (Model SS50A, Photo Emission Tech., Inc.) to obtain the photocurrent. The light source used was a 180 Watt xenon arc lamp (Photo Emission Tech.); the intensity was calibrated using a standard silicon photodiode calibrated at the Energy research Center of the Netherlands (ECN).

5.7 Characteristics of spray-deposited P3HT:PCBM blends

The spray-deposited fullerene/polymer films on glass were optically profiled as previously described, and the resulting absorbance histograms are shown in figure 5.6. As expected, increasing the solution flow rate from 100 to 200 μL/min caused a linear increase in the mean optical density from 0.24 to 0.47, consistent with the behaviour for pure polymer films reported in section 4.3.2. The standard deviation also increased linearly with the mean optical density of the films (as shown in figure 5.6f), indicating that thicker films were less smooth on an absolute basis than thin ones. Interestingly, the relative standard deviation of the films did not change substantially with film thickness as shown in figure 5.6g. This differs from the behaviour reported in section 4.3.2 for pure polymer films, where a decrease in the mean optical density of the film resulted in an exponential-like increase in the relative standard deviation. This difference is most likely due to the much narrower range of solution flow rates used for the deposition of bulk heterojunctions, and the use here of a substantially lower solution concentration and a slower raster speed (1.25 mg/ml polymer:fullerene vs 5 mg/ml polymer and 5.1 mm/s vs 12.7 mm/s). These conditions were selected to

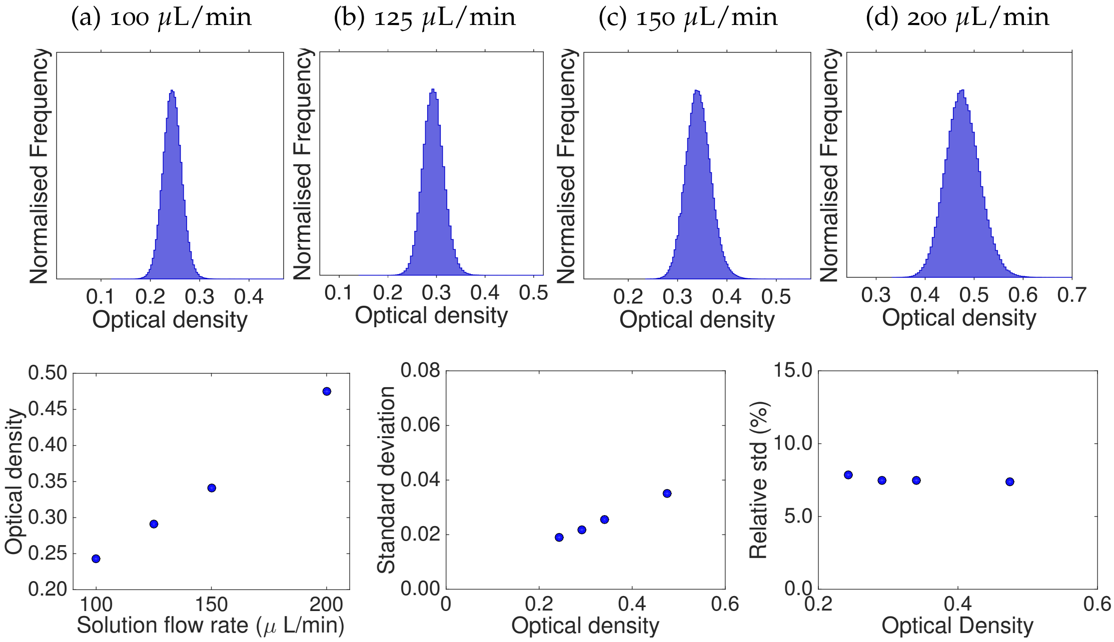

(e) (f) (g)

Figure 5.6: Absorbance histograms of 90 kg/mol P3HT films spray-deposited from 1.25 mg/ml o-xylene/ODT solutions, using a gas flow rate of 20 Lpm, raster speed of 5.1 mm/s and solution flow rates of (a) 100 (b) 125 (c) 150 and (d) 200 μL/min. Plots showing how the mean optical density (e) of the absorbance distributions vary with increasing solution flow rate and how the standard deviation (f) and the relative standard deviation (g) varies with respect to the mean optical density of each film.

promote droplet coalescence as discussed in the previous chapter. The roughly constant relative standard deviation indicates that deposition of homogeneous films is possible using spray-coating, even for very thin films. Similar behaviour was observed for pure polymer films deposited by spin-coating, where the relative standard deviation was also found to be insensitive to optical density/thickness (see section 3.3.4). The relative standard deviation of spray-deposited bulk heterojunction films was measured to be roughly three times higher than for spin-coated P3HT films (7.5 vs 2.5).

Atomic force microscopy was also used to image a 90 μm x 90 μm region of each spray-deposited polymer/fullerene film to provide nanoscale resolution of the surface features (see figure 5.7). All of the films exhibited coffee-stained, droplet-shaped surface features that were similar in size and independent of film thickness, consistent with the use of the same carrier gas flow rate for each of the sprayed films. The RMS

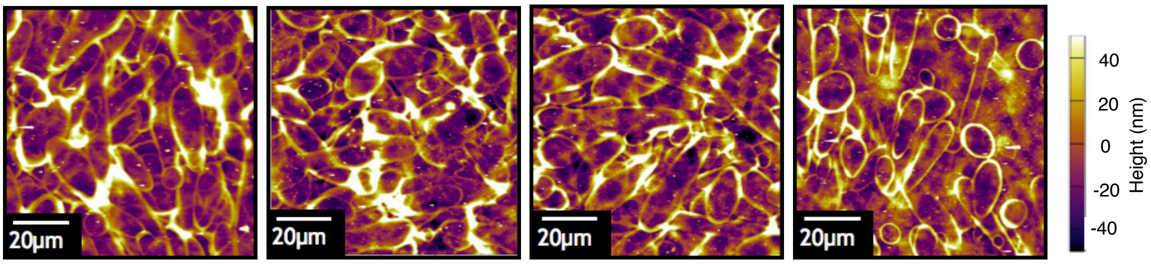

(a) 0.25 (b) 0.30 (c) 0.35 (d) 0.47

Figure 5.7: Atomic force microscopy images of the spray-deposited active layers, each showing droplet-shaped surface features.

roughness of the films did not change significantly with the mean optical density, fluctuating in the range of 23-31 nm (see figure 5.8). This differs from the results of the optical profiling measurement (where the standard deviation increased with optical densities/film thickness). The techniques however, measure surface roughness on very different length scales, with optical profiling being better suited to profiling the macroscopic roughness of large spray-coated films.

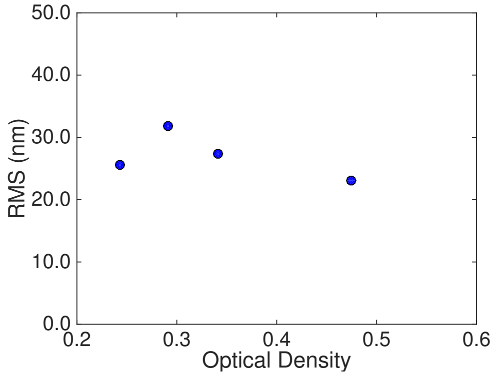

Figure 5.8: A plot showing the RMS roughness of each spray-deposited active layer as determined by AFM with respect to the mean optical density of the film.

Figure 5.9a shows current density versus voltage ($J - V$) curves for four 12 mm^2 devices of varying OD, under illumination and in the dark. The corresponding device parameters are summarised in table 5.9c. The dark $J - V$ curves are shown on a logarithmic scale in figure 5.9b. The key device parameters for each of the devices are summarised in figure 5.10. The thinnest bulk heterojunction film (OD 0.27) exhibited a significant leakage current, with a low shunt resistance of 1.82E+03 Ωcm^2, suggesting the active layer was insufficiently smooth/continuous to avoid pinhole formation between the two contacts. However, as the active layer thickness was increased, the leakage current decreased and the shunt resistance increased by three orders of magnitude, reaching 1.07E+06 Ωcm^2 for the OD 0.47 device (see figure 5.10e), consistent with a reduction in pinholes/shorts. Increased shunt resistance reduces localised heating inside the device that can both reduce device efficiency and cause thermal degradation. Thus, the thicker spray-deposited active layers (OD $\geq$ 0.25) are better suited for device applications.

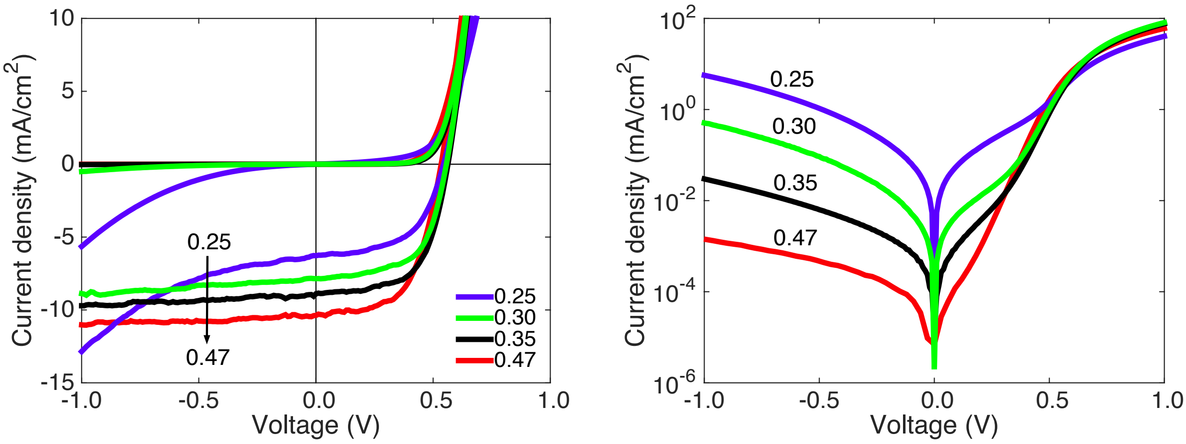
(a)

(b)

Optical density	PCE (%)	J_{SC} (mA/cm^2)	FF (%)	V_{OC} (mV)	R_{sh} (Ωcm^2)
0.25	1.90	6.28	56	556	1.82E+03
0.30	2.64	7.86	60	557	2.24E+04
0.35	3.04	8.89	61	563	1.26E+05
0.47	3.21	10.37	58	534	1.07E+06

Figure 5.9: Current density versus voltage curves for four devices with spray-deposited active layers of varying OD under illumination and in the dark (a,b). A table (below) showing the corresponding device parameters.

When the devices were operated under illumination, the current density was found to increase substantially with increasing active layer thickness (see figure 5.12c), consistent with increased photon absorption. This is evident from figure 5.10f which shows a steady and smooth increase in J_{SC} with the percentage of photons absorbed (determined from the mean optical density of each film). The fill factor, FF, did not change substantially with thickness (see figure 5.12a), indicating that all of the films were sufficiently thin (and hence the electric field was sufficiently high) to achieve efficient, photogeneration and extraction in all cases. The average FF of the four devices was ~59 %, a value that is comparable to FFs observed for high-performing P3HT:PCBM devices with spin-coated active layers [133].

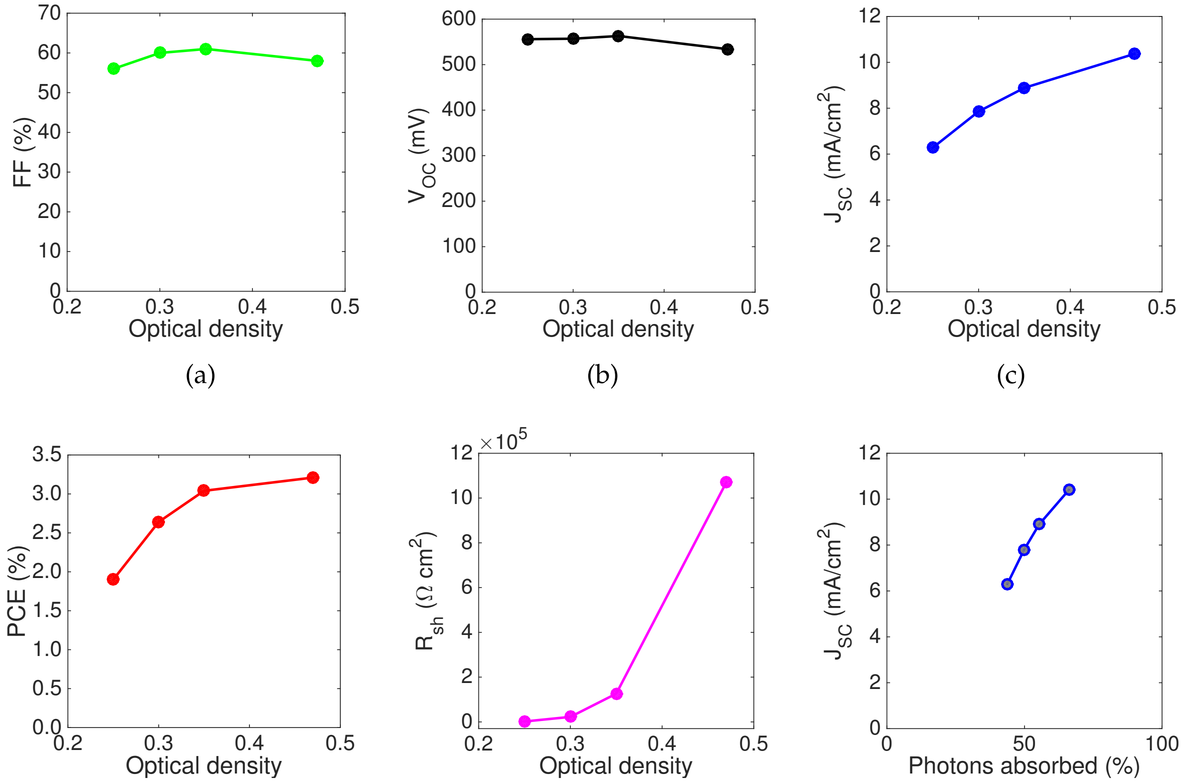

(a) (b) (c)

(d) (e) (f)

Figure 5.10: Plots showing how the (a) FF, (b) V_{OC}, (c) J_{SC}, (d) PCE and (e) R_{SH} of each device varies with the spray-deposited active layer thickness. (f) A plot showing how the J_{SC} of each device varies with the percentage of photons absorbed (determined from the mean optical density of each film) by each active layer.

The V_{OC} did not change substantially with the thickness of the active layer (see figure 5.12b), consistent with the fact that the open-circuit voltage V_{OC} of bulk-heterojunction devices is determined by the active layer and electrode materials [134], which are common to all devices. The average V_{OC} of 553 mV was on the low side for optimised P3HT:PCBM bulk heterojunction devices, which have typical V_{OC} values in the range of 550-650 mV [133]. Kitchen et al. found that by varying the molecular orientation of the aggregate P3HT relative to the PCBM layer, from highly edge-on (conjugated ring plane perpendicular to the interface plane) to appreciably face-on (ring plane parallel to the interface), the V_{OC} was increased [135]. The effect was attributed to a shift in the highest occupied molecular orbital (HOMO) energy level of P3HT. It is possible that spray-deposition favours face-on packing but further investigation would be required to confirm this.

As a result of the increase in J_{SC} with increasing active layer thickness, and despite the relatively high surface roughness of the spray-deposited films, the device efficiency increased to a reasonably high value of 3.2 % for the thickest film (see figure 5.12d). It is therefore evident from this data that, providing the active layer is continuous (resulting in a high shunt resistance), high device efficiency can be achieved even with relatively rough films.

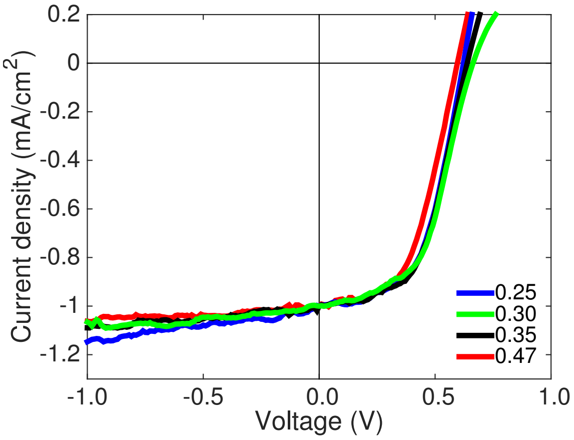

Figure 5.11: The corrected photocurrent for the four 12 mm^2 devices of varying OD, whose "RAW" J-V characteristics are shown in figure 5.9. The corrected photocurrent of each device was calculated by subtracting the dark current from the photocurrent.

Further insight into the device operation can be obtained by subtracting the dark current from the photocurrent to obtain a so-called "corrected photocurrent" [114]. The corrected photocurrent curves for the four devices were very similar in shape, indicating that the charge generation and recombination processes are similar in all cases. Slight differences were observed in the zero-crossing of the corrected photocurrent from 600 to 660 mV. From the highest value measured, it follows that the V_{OC} of a real device could potentially be increased up to around 660 mV by further process optimisation. If this were to happen it would be possible to realise device efficiencies of up to 3.3 %. It is also worth pointing out that the similarity in the shapes of the corrected photocurrents is indirect evidence for the relatively high levels of control that spray coating can deliver, with all devices exhibiting the same intrinsic device characteristics.

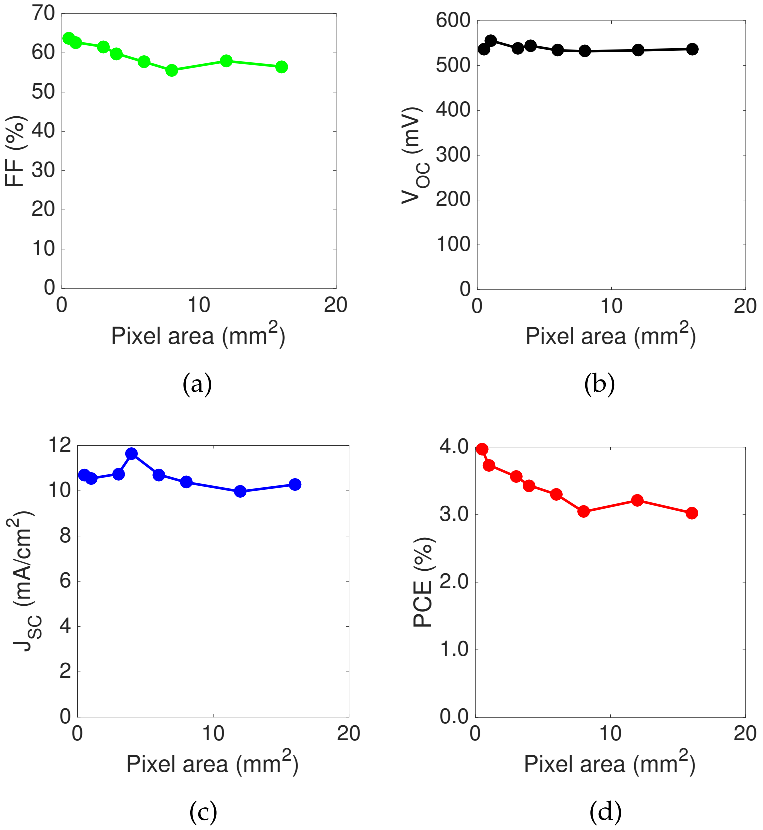

(a) (b) (c) (d)

Figure 5.12: Plots showing the variation of (a) FF, (b) V_{OC}, (c) J_{SC} and (d) PCE with pixel area, using spray-deposited P3HT:PCBM active layers with an optimised optical density of 0.47.

Finally, although spray-deposition is of interest as a large area coating technique, it is known that the performance of ”large” devices (such as the 12 mm^2 devices used above) is limited by the relatively high sheet resistance of ITO. The effects of changing the pixel area can be seen in figure 5.12, which shows the variation of FF, V_{OC}, J_{SC}, and device efficiency for the thickest (and best performing) spray-deposited active layer (OD 0.47). With the exception of V_{OC} which remains approximately constant, all parameters show a gradual decrease with increasing pixel area. The $J-V$ curve for the smallest (0.5 mm^2), most efficient device and the corresponding device performance parameters are shown in figure 5.13. The measured PCE of 4 % compares very favourably with spin-coated P3HT:PCBM devices. To my knowledge this is amongst the highest value reported using non-chlorinated solvents. Gas-driven spray-coating from non-chlorinated processing solvents, therefore appears to be a very viable method for fabricating devices.

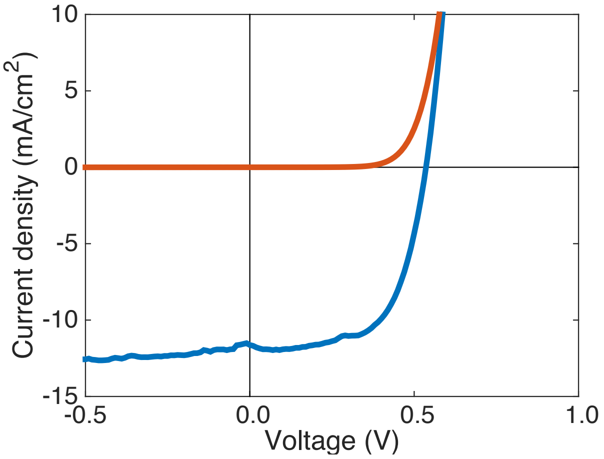

PCE (%)	4.00
J_{SC} (mA/cm^2)	11.63
FF (%)	64
V_{OC} (mV)	536
R_{sh} (Ωcm^2)	9.53E+04

Figure 5.13: J-V characteristics of the best (PCE) performing spray-coated device, and the corresponding device performance parameters.

6 Conclusions and Further Work

6.1 Conclusions

In this thesis I have described work undertaken to develop a fully-automated gas-driven spray-deposition system, specifically designed for the deposition of thin semi-conducting polymer films for device applications. A coaxial gas-driven spray-head was developed for generating ultra-fine mists with mean droplet diameters of 18 μm. The physical parameters affecting the droplet size were investigated. The droplet size was found to be most strongly influenced by the carrier-gas flow rate, with smaller droplets generated at higher rates. When operated under optimum conditions, the average size and polydispersity of droplets generated using the spray-head were comparable to (or better than) those generated using more complex ultrasonic spray-heads. Hence I reasoned that gas-driven spray-heads should be as capable as ultrasonic systems of depositing smooth, homogenous polymer films, contrary to common assertions in the literature.

To complement the spray-head, a fully-automated system was developed for spray-deposition, with fine control over operating parameters including x-y-z spray-head positioning, transportation speed, solution and gas flow rates, and hotplate temperature. Three modes of operation were incorporated into the design for maximum versatility. The single-and multiple-solution modes enabled the deposition of single solutions and solution mixtures from a single spray-head, whilst the multi-spray-head mode allowed several films of different materials to be deposited sequentially using two (or more) separate spray-head and solution channels.

A separate focus of this work was the development of a low cost optical characterisation technique for spray-deposited and drop-cast polymer films, using a band-pass filter (centred at 540 nm), a white light photography box and a Raspberry Pi camera. The technique was based on a two-dimensional approximate absorption measurement of a polymer film, calculated using the pixel signals of a set of photographic images. For materials where the extinction coefficient, k, is independent of the local film morphology, mapping the absorption of a film is equivalent to mapping its thickness variation. Hence, the technique provides a fast route to characterising the uniformity of "large-area" polymer films, yielding an X-Y resolution of $\sim$20 μm^2 when mapping films of approximate area 1.3 cm^2. The technique was found to be well suited to characterising the large-area uniformity of spray-coated films whose surfaces were rougher than those of spin-coated films, and for determining their average optical density.

To determine the optimum solution composition for spray-deposition of P3HT films, the aggregation and gelation dynamics of various P3HT/o-xylene solutions were investigated by static light scattering, using an instrument developed by Dr. Siva Krishnadasan. The measurements indicated that the solution should be dilute (polymer concentration $<$5 mg/ml), ideally consist of low molecular weight polymer ($\leq$20 kg/-mol), and contain a small amount ($<$40 %) of indane, in order to avoid solution gelation and clogging of the spay-head. For higher weight material, it was found to be necessary to heat the solutions to 40 °C to avoid gelation.

The optical profiling technique was used to determine the smoothness of drop-casted and spray-coated films, deposited from different solution compositions, using different operating parameters of the rig. Drop-cast films deposited from higher solution concentrations and solutions comprising higher molecular weight P3HT showed a reduction in coffee-staining and improved radial material uniformity. The improved material distribution was attributed to faster gelation of the solutions, which reduced the outward flow of solute and so inhibiting coffee staining. The addition of small amounts of indane also improved the material distribution of drop-cast films, and was attributed to favourable manipulation of material flow within the droplet as it dried.

In contrast to the improved material distribution observed for drop-cast films, the uniformity of spray-deposited films remained largely unchanged for solutions of increasing polymer molecular weight. It was suggested that because gelation was slow for these solutions, evaporation of the solvent was likely to take place before significant flow had occurred and thus, there was no improvement in material distribution arising from gelation of the solution. In contrast to the behaviour of drop-cast films, the uniformity of spray-deposited films was found to be highest for low concentration solutions. It was proposed that although gelation had occurred at high solution concentrations, it may be detrimental to droplet coalescence, causing less uniform film formation. Increasing the indane concentration caused a marginal decrease in the uniformity. Again, this contrasts with the behaviour of the drop-cast films, which showed flatter profiles and improved spreading at higher indane content. The reason for this however, is unclear and requires further investigation.

The effects of the operating parameters of the spray rig on the uniformity of spray-deposited films of P3HT in o-xylene were also examined. It was found that the smoothest films were formed at room temperature, using higher gas and solution flow rates, and lower raster speeds. This was attributed to the generation of smaller droplets and increased droplet coalescence.

Based on the optical profiling results obtained for pure P3HT films, the solution composition and deposition parameters were tailored for uniform and smooth bulk heterojunction P3HT:PCBM films. The final coating solution consisted of 1.25 mg/ml of 90 kg/mol molecular weight P3HT in o-xylene/ODT. A raster speed of 5.1 mm/s, a gas flow rate of 20 Lpm, and a solution flow rate in the range of 100-200 μL/min were chosen as optimum deposition parameters. The relative standard deviation of spray-deposited bulk heterojunction films was measured to be roughly three times higher than for spin-coated P3HT films, and the RMS roughness of the films, determined by AFM measurements on a 90 μm x 90 μm length scale, was $<$30 nm. Despite the relatively high surface roughness of the spray-deposited films (compared to spin-coated films), a maximum device efficiency of 4.0 % was achieved for the thickest bulk heterojunction film. The results indicated that, providing the active layer was continuous (resulting in a high shunt resistance), high device efficiency could be achieved even with relatively rough films, spray-coated from non-chlorinated processing solvents. This is one of the highest values reported for spray-coated bulk heterojunction films, cast from non-chlorinated solvents.

6.2 Further optimisation of spray-deposited polymer films

Despite the high device performance achieved using relatively rough spray-coated bulk heterojunction films, further reduction in the surface roughness would likely be beneficial to minimise localised heating inside the device that can cause thermal degradation and to allow easier coating by subsequent layers in the device stack. Further optimisation of the surface topography may be possible by optimising multiple deposition/solution composition parameters in parallel. For example, the effect of the solution flow rate and the raster speed of the spray-head on the film uniformity may be linked as in both cases the degree of droplet coalescence is affected. Rather than holding either one of them constant, the optimum conditions might only be found by varying them simultaneously.

The device efficiencies achieved in this work suggest that film uniformity is not the most important requirement for achieving high device efficiencies. Since OPV performance is critically dependent on the phase-separated nanomorphology of the active layer, it may be useful to investigate the effects of the spray conditions on the nanostructure of the blended layer (rather than film uniformity alone). Key analytical techniques for doing this range from X-ray diffraction and spectroscopy to electron microscopy and scanning probe microscopy [136].

6.3 Exploiting the functionality and additional applications of the spray-rig

Of the three operational modes of the spray-rig (described in chapter 2.4.1), only two were used for the work reported here. The single-solution mode was regularly used to deposit films of P3HT from one solution using a single spray head, and the multi-solution mode was occasionally used to mix two solutions of different composition or concentration before depositing (with a single spray-head) to investigate the effects of polymer concentration or solvent composition on film uniformity. Overall however, the functionality of the multi-solution mode was not fully exploited, and the multi-spray-head mode was not used at all.

The multi-solution mode offers the potential for depositing films with a horizontal or vertical composition gradient. Vertical composition gradients in bulk heterojunction films with increasing acceptor concentration closer to the cathode have been shown to benefit solar cell performance in the case of both polymer and small-molecule devices [137–139]. Vertical gradient doping of the active layer can be achieved with the multi-solution mode by depositing sequential layers using different delivery rates for the two different solutions (e.g. one containing the solution to be doped (i.e. P3HT in o-xylene) and the other containing the dopant solution (PCBM o-xylene)). Additionally, horizontal doping could be achieved in a similar way by depositing a single layer and changing the delivery rates of the two solutions during deposition.

In this work we focused exclusively on deposition of the active layer, however the rig could also be used to spray-coat other electronic materials, including those used for the electrode layers, the hole transport layers, and the electron transport layers of organic devices. Common materials used for these functional layers include metal oxides, metal nanoparticles and metal nanowires. The film formation process for solutions of these materials are different to those of polymer solutions and thus, would require separate consideration and optimisation. The multi-spray-head mode of the rig was developed to allow multiple functional layers of a device to be deposited sequentially by spray-coating.

6.4 Combining polymer synthesis with spray deposition

The spray-head was designed and assembled with solution inlet connectors and tubing sizes that match those used in the continuous droplet-based microfluidic reactors used elsewhere at Imperial to synthesise P3HT [140]. This raises the interesting prospect of fabricating a continuous in-line process that can both synthesise and deposit the active layer materials. The idea would be to build a system which accepts the reactants/catalysts/monomer for the synthesis of P3HT, and then produces a smooth homogenous polymer film.

There are currently two major obstacles which prevent this from happening. Firstly, in-line purification of the polymer is necessary before it can be directly applied to solutions without any intermediary processes [141]. Secondly, there may be a need to switch solvent from the best choice for synthesis to the best choice for coating. Despite these challenges however, the combination of polymer synthesis and thin film deposition appears to be quite feasible and such a development could further reduce the processing steps involved in device fabrication, bringing us closer to a fully automated, single-step process.

References

1. Forrest, S. R. The path to ubiquitous and low-cost organic electronic appliances on plastic. *Nature* **428,** 911–918. ISSN: 0028-0836 (2004).
2. Chen, S., Manders, J. R., Tsang, S.-W. & So, F. Metal oxides for interface engineering in polymer solar cells. *J. Mater. Chem.* 24202–24212. ISSN: 0959-9428 (2012).
3. Guldi, D. M. & Sgobba, V. Carbon nanostructures for solar energy conversion schemes. *Chem. Commun.* **47,** 606–610. ISSN: 1364-548X (2011).
4. Hecht, D. S., Hu, L. & Irvin, G. Emerging transparent electrodes based on thin films of carbon nanotubes, graphene, and metallic nanostructures. *Adv. Mater.* **23,** 1482–513. ISSN: 1521-4095 (Apr. 2011).
5. Poodt, P., Knaapen, R., Illiberi, A., Roozeboom, F. & van Asten, A. Low temperature and roll-to-roll spatial atomic layer deposition for flexible electronics. *J. Vac. Sci. Technol. A Vacuum, Surfaces, Film.* **30,** 01A142. ISSN: 07342101 (2012).
6. Norrman, K., Ghanbari-Siahkali, a. & Larsen, N. B. 6Studies of spin-coated polymer films. *Annu. Rep. Prog. Chem., Sect. C.* **101,** 174. ISSN: 0260-1826 (2005).
7. Chan, S.-H. *et al.* Morphology Evolution of Spin-Coated Films of Poly(thiophene-phenylene-thiophene) and [6,6]-Phenyl-C_{71}-butyric Acid Methyl Ester by Solvent Effect. *Macromolecules* **43,** 3399–3405. ISSN: 0024-9297 (2010).
8. Sandström, A., Dam, H. F., Krebs, F. C. & Edman, L. Ambient fabrication of flexible and large-area organic light-emitting devices using slot-die coating. *Nat. Commun.* **3,** 1002. ISSN: 2041-1723 (2012).

9. Voigt, M. M. *et al.* Gravure printing inverted organic solar cells: The influence of ink properties on film quality and device performance. *Sol. Energy Mater. Sol. Cells* **105,** 77–85. ISSN: 09270248 (2012).

10. Na, S.-I. *et al.* Fully spray-coated ITO-free organic solar cells for low-cost power generation. *Sol. Energy Mater. Sol. Cells* **94,** 1333–1337. ISSN: 09270248 (Aug. 2010).

11. Zhang, B., Chae, H. & Cho, S. M. Screen-Printed Polymer:Fullerene Bulk-Heterojunction Solar Cells. *Jpn. J. Appl. Phys.* **48,** 020208. ISSN: 0021-4922 (2009).

12. Krebs, F. C. *et al.* A complete process for production of flexible large area polymer solar cells entirely using screen printing-First public demonstration. *Sol. Energy Mater. Sol. Cells* **93,** 422–441. ISSN: 09270248 (2009).

13. Krebs, F. C. Fabrication and processing of polymer solar cells: A review of printing and coating techniques. *Sol. Energy Mater. Sol. Cells* **93,** 394–412. ISSN: 09270248 (Apr. 2009).

14. Galagan, Y. *et al.* Technology development for roll-to-roll production of organic photovoltaics. *Chem. Eng. Process. Process Intensif.* **50,** 454–461. ISSN: 02552701 (May 2011).

15. Dang, M. T., Hirsch, L. & Wantz, G. P3HT:PCBM, Best Seller in Polymer Photovoltaic Research. *Adv. Mater.* **23,** 3597–3602. ISSN: 09359648 (Aug. 2011).

16. Engle, R. *Advantages of ultrasonic spray coatings of biomaterials onto devices and implantables* 2010. <`http://www.sono-tek.com/wp-content/uploads/2012/01/Sono-Tek-ISCST-Symposium.pdf`>.

17. Lefebvre, A. H. *Atomization and sprays* (Taylor and Francis, 1989).

18. Lonakar, G. S., Mahajan, M. S., Ghosh, S. S. & Sali, J. V. Modeling thin film formation by Ultrasonic Spray method: A case of PEDOT:PSS thin films. *Org. Electron.* **13,** 2575–2581. ISSN: 15661199 (Nov. 2012).

19. Tenent, R. C. *et al.* Ultrasmooth, large-area, high-uniformity, conductive transparent single-walled-carbon-nanotube films for photovoltaics produced by ultrasonic spraying. *Adv. Mater.* **21,** 3210–3216. ISSN: 09359648 (2009).

20. S. Gilje, S. Han, M. W. A Chemical Route to Graphene for Devie Applications. *Nano Lett.* **7,** 3394–3398 (2007).

21. Schulz, F., Franzka, S. & Schmid, G. Nanostructured surfaces by deposition of metal nanoparticles by means of spray techniques. *Adv. Funct. Mater.* **12,** 532–536. ISSN: 1616301X (2002).

22. Scardaci, V., Coull, R., Lyons, P. E., Rickard, D. & Coleman, J. N. Spray deposition of highly transparent, low-resistance networks of silver nanowires over large areas. *Small* **7,** 2621–2628. ISSN: 16136810 (2011).

23. Adamopoulos, G., Thomas, S., Bradley, D. D. C., McLachlan, M. A. & Anthopoulos, T. D. Low-voltage ZnO thin-film transistors based on Y2O3 and Al2O3 high-k dielectrics deposited by spray pyrolysis in air. *Appl. Phys. Lett.* **98,** 123503. ISSN: 00036951 (2011).

24. Felton, L. A. Mechanisms of polymeric film formation. *Int. J. Pharm.* **457,** 423–7. ISSN: 1873-3476 (Dec. 2013).

25. Lavernia, E. J. & Wu, Y. *Spray atomization and deposition* 3rd ed. (Chichester: Wiley, 1997).

26. Shi, D., Li, M. & Christofides, P. D. Diamond Jet Hybrid HVOF Thermal Spray: Rule-Based Modeling of Coating Microstructure. *Ind. Eng. Chem. Res.* **43,** 3653–3665. ISSN: 0888-5885 (2004).

27. Hermanson, J. *Vaporization of liquid droplets in supersonic flow* <`https://www.aa.washington.edu/research/combustion/research/supersonic`>.

28. Mariotte, E. *Traité du mouvement des eaux et autres corps fluides* (Chez J. Jombert, 1686).

29. Plateau, J. A. F. *Statique expérimentale et théorique des liquides soumis aux seules forces moléculaires* (Gauthier-Villars, 1873).

30. Rayleigh, L. On the stability, or instability, of certain fluid motions. *Proc. London Math. Soc.* **x,** 57–72. ISSN: 0024-6115 (1879).

31. Rayleigh, L. On the instability of cylindrical fluid surfaces. *Philos. Mag. Ser. 5* **34,** 177–180. ISSN: 1941-5982 (1892).

32. Safran, S. A. & Srolovitz, D. J. Kinetics of Instabilities in Solid Films. *Europhys. Lett.* **2,** 61–66. ISSN: 0295-5075 (2007).

33. Lin, S. P. & Reitz, R. D. Drop and Spray Formation From a Liquid Jet. *Annu. Rev. Fluid Mech.* **30,** 85–105. ISSN: 0066-4189 (Jan. 1998).

34. Birouk, M. & Lekic, N. Liquid Jet Breakup in Quiescent Atmosphere: A Review. *At. Sprays* **19,** 501–528. ISSN: 1046-5111 (2009).

35. Gennes, D. statics and dynamics. *Am. Phys. Soc.* **57** (1985).

36. Harkins, W. D. & Feldman, A. Films. The spreading of liquids and the spreading coefficient. *J. Am. Chem. Soc.* **44,** 2665–2685. ISSN: 0002-7863 (1922).

37. Fowkes, F. M. *Contact Angle, Wettability, and Adhesion* (ed Fowkes, F. M.) 112–135. ISBN: 0-8412-0044-0. doi:`10.1021/ba-1964-0043`. <`http://pubs.acs.org/doi/book/10.1021/ba-1964-0043`> (AMERICAN CHEMICAL SOCIETY, WASHINGTON, D.C., Jan. 1964).

38. Fox, H. & Zisman, W. The spreading of liquids on low energy surfaces. I. polytetrafluoroethylene. *J. Colloid Sci.* **5,** 514–531. ISSN: 00958522 (1950).

39. Good, R. J. A Thermodynamic Derivation of Wenzel's Modification of Young's Equation for Contact Angles; Together with a Theory of Hysteresis. *J. Am. Chem. Soc.* **74,** 5041–5042. ISSN: 0002-7863 (1952).

40. Roisman, I. V., Rioboo, R. & Tropea, C. Normal impact of a liquid drop on a dry surface: model for spreading and receding. *Proc. R. Soc. A Math. Phys. Eng. Sci.* **458,** 1411–1430. ISSN: 1364-5021 (June 2002).

41. Range, K. & Feuillebois, F. Influence of Surface Roughness on Liquid Drop Impact. *J. Colloid Interface Sci.* **203,** 16–30 (1998).

42. A.L. Yarin. Drop Impact Dynamics: Splashing, Spreading, Receding, Bouncing... *Annu. Rev. Fluid Mech.* **38,** 159–192. ISSN: 0066-4189 (Jan. 2006).

43. Xu, L., Zhang, W. & Nagel, S. Drop Splashing on a Dry Smooth Surface. *Phys. Rev. Lett.* **94,** 184505. ISSN: 0031-9007 (May 2005).

44. D. Nuyttens, M. De Schampheleire, P. Verboven, E. Brusselman & D. Dekeyser. Droplet Size and Velocity Characteristics of Agricultural Sprays. *Trans. ASABE* **52,** 1471–1480. ISSN: 2151-0040 (2009).

45. Mundo, C., Sommerfeld, M. & Tropea, C. Droplet-wall collisions: Experimental studies of the deformation and breakup process. *Int. J. Multiph. Flow* **21,** 151–173. ISSN: 03019322 (1995).

46. Rioboo, R., Tropea, C. & Marengo, M. Outcomes from a drop impact on solid surfaces. *Atomization and Sprays* **11.** ISSN: 1044-5110 (2001).

47. Guéna, G., Poulard, C., Voué, M., De Coninck, J. & Cazabat, a. M. Evaporation of sessile liquid droplets. *Colloids Surfaces A Physicochem. Eng. Asp.* **291,** 191–196. ISSN: 09277757 (2006).

48. R. G. Picknett and R. Bexon. The Evaporation of Sessile or Pendant Drops in Still Air. *J. Colloid Interface Sci. Vol.* **61** (1977).

49. Lopes, M. C. & Bonaccurso, E. Evaporation control of sessile water drops by soft viscoelastic surfaces. *Soft Matter* **8,** 7875. ISSN: 1744-683X (2012).

50. Deegan, R. *et al.* Contact line deposits in an evaporating drop. *Phys. Rev. E* **62,** 756–765. ISSN: 1063-651X (July 2000).

51. Morse, H. W. On Evaporation from the Surface of a Solid Sphere . *Proc. Am. Acad. Arts Sci.* **45,** 363–367. ISSN: 01999818 (1910).

52. Langmuir, I. The evaporation of small spheres. *Phys. Rev.* **12,** 368–370. ISSN: 0031899X (1918).

53. Hu, H. & Larson, R. G. Evaporation of a sessile droplet on a substrate. *J. Phys. Chem. B* **106,** 1334–1344. ISSN: 10895647 (2002).

54. Popov, Y. Evaporative deposition patterns: Spatial dimensions of the deposit. *Phys. Rev. E* **71,** 036313. ISSN: 1539-3755 (Mar. 2005).

55. Deegan, R. D., Bakajin, O. & Dupont, T. F. Capillary flow as the cause of ring stains from dried liquid drops. *Nature* **389,** 827–829 (1997).

56. Baldwin, K. a., Roest, S., Fairhurst, D. J., Sefiane, K. & Shanahan, M. E. R. Monolith formation and ring-stain suppression in low-pressure evaporation of poly(ethylene oxide) droplets. *J. Fluid Mech.* **695,** 321–329. ISSN: 0022-1120 (Feb. 2012).

57. Willmer, D., Baldwin, K. A., Kwartnik, C. & Fairhurst, D. J. Growth of solid conical structures during multistage drying of sessile poly(ethylene oxide) droplets. *Phys. Chem. Chem. Phys.* **12,** 3998–4004. ISSN: 1463-9084 (Apr. 2010).
58. Baldwin, K. A., Granjard, M., Willmer, D. I., Sefiane, K. & Fairhurst, D. J. Drying and deposition of poly(ethylene oxide) droplets determined by Péclet number. *Soft Matter* **7,** 7819. ISSN: 1744-683X (2011).
59. Jung, Y., Kajiya, T., Yamaue, T. & Doi, M. Film Formation Kinetics in the Drying Process of Polymer Solution Enclosed by Bank. *Jpn. J. Appl. Phys.* **48,** 031502. ISSN: 0021-4922 (Mar. 2009).
60. Ozawa, K., Nishitani, E. & Doi, M. Modeling of the Drying Process of Liquid Droplet to Form Thin Film. *Jpn. J. Appl. Phys.* **44,** 4229–4234. ISSN: 0021-4922 (June 2005).
61. Okuzono, T., Kobayashi, M. & Doi, M. Final shape of a drying thin film. *Phys. Rev. E* **80,** 021603. ISSN: 1539-3755 (Aug. 2009).
62. Still, T., Yunker, P. J. & Yodh, A. G. Surfactant-induced Marangoni eddies alter the coffee-rings of evaporating colloidal drops. *Langmuir* **28,** 4984–4988. ISSN: 07437463 (2012).
63. Liu, C., Bonaccurso, E. & Butt, H.-J. Evaporation of sessile water/ethanol drops in a controlled environment. *Phys. Chem. Chem. Phys.* **10,** 7150–7. ISSN: 1463-9076 (Dec. 2008).
64. Sefiane, K., Tadrist, L. & Douglas, M. Experimental study of evaporating water-ethanol mixture sessile drop: Influence of concentration. *Int. J. Heat Mass Transf.* **46,** 4527–4534. ISSN: 00179310 (2003).
65. Poulard, C. & Damman, P. Control of spreading and drying of a polymer solution from Marangoni flows. *Europhys. Lett.* **80,** 64001. ISSN: 0295-5075 (Dec. 2007).
66. Hu, H. & Larson, R. G. Analysis of the effects of marangoni stresses on the microflow in an evaporating sessile droplet. *Langmuir* **21,** 3972–3980. ISSN: 07437463 (2005).

67. Eres, M., Weidner, D. & Schwartz, L. Three-dimensional direct numerical simulation of surface-tension-gradient effects on the leveling of an evaporating multicomponent fluid. **35,** 1859–1871. ISSN: 0743-7463 (1999).

68. Sultan, E., Boudaoud, A. & Amar, M. B. Evaporation of a thin film: diffusion of the vapour and Marangoni instabilities. **543,** 183–202. ISSN: 0022-1120 (2004).

69. Hu, H. & Larson, R. G. Marangoni effect reverses coffee-ring depositions. *J. Phys. Chem. B* **110,** 7090–4. ISSN: 1520-6106 (Apr. 2006).

70. Adachi, E., Dimitrov, A. S. & Nagayama, K. Stripe Patterns Formed on a Glass Surface during Droplet Evaporation. *Langmuir* **11,** 1057–1060. ISSN: 0743-7463 (Apr. 1995).

71. Shmuylovich, L., Shen, A. & Stone, H. Surface morphology of drying latex films: multiple ring formation. *Langmuir,* 3441–3445 (2002).

72. Li, Y.-F., Sheng, Y.-J. & Tsao, H.-K. Solute concentration-dependent contact angle hysteresis and evaporation stains. *Langmuir* **30,** 7716–23. ISSN: 1520-5827 (July 2014).

73. Freed-Brown, J. Evaporative deposition in receding drops. *Soft Matter* **10,** 9506–10. ISSN: 1744-6848 (Dec. 2014).

74. Budrene, E. O. & Berg, H. C. Complex patterns formed by motile cells of Escherichia coli. *Nature* **349,** 630–3. ISSN: 0028-0836 (Feb. 1991).

75. Maeda, H. Observation of Spatially Rhythmic Patterns from Evaporating Collagen Solution Droplets. *Langmuir* **16,** 9977–9982. ISSN: 0743-7463 (Dec. 2000).

76. De Gennes, P. G. Solvent evaporation of spin cast films:"crust" effects. *Eur. Phys. J. E Soft Matter Biol. Phys.* **7,** 31–34. ISSN: 1292-8941 (2002).

77. Ozawa, K., Okuzono, T. & Doi, M. Diffusion process during drying to cause the skin formation in polymer solutions. *Japanese J. Appl. Physics, Part 1 Regul. Pap. Short Notes Rev. Pap.* **45,** 8817–8822. ISSN: 00214922 (2006).

78. Okuzono, T., Ozawa, K. & Doi, M. Simple model of skin formation caused by solvent evaporation in polymer solutions. *Phys. Rev. Lett.* **97,** 1–4. ISSN: 00319007 (2006).

79. Okuzono, T. & Doi, M. Effects of elasticity on drying processes of polymer solutions. *Phys. Rev. E - Stat. Nonlinear, Soft Matter Phys.* **77,** 1–4. ISSN: 15393755 (2008).

80. Sheetz, D. P. Formation of films by drying of latex. *J. Appl. Polym. Sci.* **9,** 3759–3773. ISSN: 1097-4628 (1965).

81. Kajiya, T., Nishitani, E., Yamaue, T. & Doi, M. Piling-to-buckling transition in the drying process of polymer solution drop on substrate having a large contact angle. *Phys. Rev. E* **73,** 011601. ISSN: 1539-3755 (Jan. 2006).

82. Pauchard, L. & Allain, C. Stable and unstable surface evolution during the drying of a polymer solution drop. *Phys. Rev. E. Stat. Nonlin. Soft Matter Phys.* **68,** 052801. ISSN: 1063-651X (2003).

83. Pauchard, L. & Allain, C. Buckling instability induced by polymer solution drying. *Europhys. Lett.* **62,** 897–903. ISSN: 0295-5075 (2007).

84. Head, D. Modeling the elastic deformation of polymer crusts formed by sessile droplet evaporation. *Phys. Rev. E* **74,** 021601. ISSN: 1539-3755 (Aug. 2006).

85. Sick, V. High speed imaging in fundamental and applied combustion research. *Proc. Combust. Inst.* **34,** 3509–3530. ISSN: 15407489 (2013).

86. McCarthy, M. & Molloy, N. Review of stability of liquid jets and the influence of nozzle design. *Chem. Eng. J.* **7,** 1–20. ISSN: 03009467 (1974).

87. Vahedi Tafreshi, H. & Pourdeyhimi, B. The effects of nozzle geometry on waterjet breakup at high Reynolds numbers. *Exp. Fluids* **35,** 364–371. ISSN: 07234864 (2003).

88. Fansler, T. D. & Parrish, S. E. Spray measurement technology: a review. *Meas. Sci. Technol.* **26,** 012002. ISSN: 0957-0233 (Jan. 2015).

89. Black, D. L., McQuay, M. Q. & Bonin, M. P. Laser-based techniques for particle-size measurement: A review of sizing methods and their industrial applications. *Prog. Energy Combust. Sci.* **22,** 267–306. ISSN: 03601285 (1996).

90. Bachalo, W. D. & Houser, M. J. Phase/doppler spray analyzer for simultaneous measurements of drop size and velocity distributions. *Optical Engineering* **23,** 583–590. ISSN: 0091-3286 (1984).

91. Widmann, J. F. Phase Doppler interferometry measurements in water sprays produced by residential fire sprinklers. *Fire Safety Journal* **36,** 545–567. ISSN: 03797112 (2001).

92. Ghandhi, J. B. & Heim, D. M. An optimized optical system for backlit imaging. *Rev. Sci. Instrum.* **80,** 80–83. ISSN: 00346748 (2009).

93. Mayer, W. O. H. Coaxial atomization of a round liquid jet in a high speed gas stream : *Experiments in Fluids* **16** (1994).

94. Lorenzetto, G. E. & Lefebvre, a. H. Measurements of Drop Size on a Plain-Jet Airblast Atomizer. *AIAA J.* **15,** 1006–1010. ISSN: 0001-1452 (1977).

95. Nukiyama, S. & Tanasawa, Y. *Experiments on the Atomization of Liquids in an Air Stream: Reports 1 to 6* (Defence Research Board, Department of National Defence, 1950).

96. Rizk, N. K. & Lefebvre, a. H. Spray characteristics of spill-return atomizers. *Journal of Engineering for Gas Turbines and Power* **1,** 200–204. ISSN: 0748-4658 (1985).

97. Varga, C. M., Lasheras, J. C. & Hopfinger, E. J. Initial breakup of a small-diameter liquid jet by a high-speed gas stream. *J. Fluid Mech.* **497,** 405–434. ISSN: 00221120 (Dec. 2003).

98. Jiang, D.-J. *et al.* Modeling atomization of a round water jet by a high-speed annular air jet based on the self-similarity of droplet breakup. *Chem. Eng. Res. Des.* **90,** 185–192. ISSN: 02638762 (Feb. 2012).

99. Liu, H.-F. *et al.* Effect of liquid jet diameter on performance of coaxial two-fluid airblast atomizers. *Chem. Eng. Process: Process Intensification.* **45,** 240–245. ISSN: 02552701 (2006).

100. Marco R. Cavallaria and José E. E. Izquierdoa and Estrella F. G. Rodríguezb and Marcelo A. Pereira-da-Silvac & Fonseca, F. J. Optical absorbance of P3HT thin films used to estimate simultaneously thin-film thickness and morphology for gas sensing. *Proc. SPIE* **9568,** 1–9 (2015).

101. Palma-cando, A. U., Frontana-uribe, B. A. & Luis, J. Control of thickness of PEDOT electrodeposits on Glass / ITO electrodes from organic solutions and its use as anode in organic solar cells. *Procedia Chem.* **12,** 92–99. ISSN: 1876-6196 (2014).

102. Hoth, C. N., Schilinsky, P., Choulis, S. A. & Brabec, C. J. Printing highly efficient organic solar cells. *Nano Lett.* **8,** 2806–13. ISSN: 1530-6984 (Sept. 2008).

103. Krebs, F. C. All solution roll-to-roll processed polymer solar cells free from indium-tin-oxide and vacuum coating steps. *Org. Electron.* **10,** 761–768. ISSN: 15661199 (Aug. 2009).

104. Koppe, M. *et al.* Influence of Molecular Weight Distribution on the Gelation of P3HT and Its Impact on the Photovoltaic Performance. *Macromolecules* **42,** 4661–4666. ISSN: 0024-9297 (July 2009).

105. Brinkmann, M. & Rannou, P. Effect of Molecular Weight on the Structure and Morphology of Oriented Thin Films of Regioregular Poly(3-hexylthiophene) Grown by Directional Epitaxial Solidification. *Adv. Funct. Mater.* **17,** 101–108. ISSN: 1616301X (2007).

106. Steirer, K. X. *et al.* Ultrasonically sprayed and inkjet printed thin film electrodes for organic solar cells. *Thin Solid Films* **517,** 2781–2786. ISSN: 00406090 (Feb. 2009).

107. Schmidt-Hansberg, B. *et al.* Investigation of non-halogenated solvent mixtures for high throughput fabrication of polymer–fullerene solar cells. *Sol. Energy Mater. Sol. Cells* **96,** 195–201. ISSN: 09270248 (Jan. 2012).

108. Chen, W. *et al.* The Measurement of Spray Quality for Pan Coating Processes. *J. Pharm. Innov.* **3,** 3–14. ISSN: 1872-5120 (Mar. 2008).

109. Abdellah, A., Fabel, B., Lugli, P. & Scarpa, G. Spray deposition of organic semiconducting thin-films: Towards the fabrication of arbitrary shaped organic electronic devices. *Org. Electron.* **11,** 1031–1038. ISSN: 15661199 (June 2010).

110. Malliaras, G., Salem, J., Brock, P. & Scott, C. Electrical characteristics and efficiency of single-layer organic light-emitting diodes. *Phys. Rev. B* **58,** R13411–R13414. ISSN: 0163-1829 (1998).

111. Lane, P. a., Brewer, P. J., Huang, J., Bradley, D. D. C. & DeMello, J. C. Elimination of hole injection barriers by conducting polymer anodes in polyfluorene light-emitting diodes. *Phys. Rev. B* **74,** 125320. ISSN: 1098-0121 (2006).

112. Tengstedt, C. *et al.* Fermi-level pinning at conjugated polymer interfaces. *Appl. Phys. Lett.* **88,** 053502. ISSN: 00036951 (2006).

113. Brabec, C. J. *et al.* Origin of the open circuit voltage of plastic solar cells, Adv. *Funct. Mater.* **11,** 374–380 (2001).

114. Ooi, Z. E. *On the corrected photocurrent of organic bulk heterojunction solar cells* PhD thesis (2008). <`http://spiral.imperial.ac.uk/retrieve/9659/license.txt`>.

115. Girotto, C., Rand, B. P., Steudel, S., Genoe, J. & Heremans, P. Nanoparticle-based, spray-coated silver top contacts for efficient polymer solar cells. *Org. Electron.* **10,** 735–740. ISSN: 15661199 (July 2009).

116. Hau, S. K., Yip, H.-L., Leong, K. & Jen, A. K.-Y. Spraycoating of silver nanoparticle electrodes for inverted polymer solar cells. *Org. Electron.* **10,** 719–723. ISSN: 15661199 (July 2009).

117. Lim, Y.-F. *et al.* Spray-deposited poly(3,4-ethylenedioxythiophene):poly(styrenesulfonate) top electrode for organic solar cells. *Appl. Phys. Lett.* **93,** 193301. ISSN: 00036951 (2008).

118. Margulis, G. Y. *et al.* Spray Deposition of Silver Nanowire Electrodes for Semi-transparent Solid-State Dye-Sensitized Solar Cells. *Adv. Energy Mater.* **3,** 1657–1663. ISSN: 16146832 (Dec. 2013).

119. Bolink, H. J., Coronado, E., Orozco, J. & Sessolo, M. Efficient Polymer Light-Emitting Diode Using Air-Stable Metal Oxides as Electrodes. *Adv. Mater.* **21,** 79–82. ISSN: 09359648 (Jan. 2009).

120. Hoth, C. N. *et al.* Topographical and morphological aspects of spray coated organic photovoltaics. *Org. Electron.* **10,** 587–593. ISSN: 15661199 (July 2009).

121. Girotto, C., Moia, D., Rand, B. P. & Heremans, P. High-Performance Organic Solar Cells with Spray-Coated Hole-Transport and Active Layers. *Adv. Funct. Mater.* **21,** 64–72. ISSN: 1616301X (Jan. 2011).

122. Lewis, J. E., Lafalce, E., Toglia, P. & Jiang, X. Over 30% transparency large area inverted organic solar array by spray. *Sol. Energy Mater. Sol. Cells* **95,** 2816–2822. ISSN: 09270248 (Oct. 2011).

123. Vak, D. *et al.* Fabrication of organic bulk heterojunction solar cells by a spray deposition method for low-cost power generation. *Appl. Phys. Lett.* **91,** 081102. ISSN: 00036951 (2007).

124. Green, R. *et al.* Performance of bulk heterojunction photovoltaic devices prepared by airbrush spray deposition. *Appl. Phys. Lett.* **92,** 033301. ISSN: 00036951 (2008).

125. Girotto, C., Rand, B. P., Genoe, J. & Heremans, P. Exploring spray coating as a deposition technique for the fabrication of solution-processed solar cells. *Sol. Energy Mater. Sol. Cells* **93,** 454–458. ISSN: 09270248 (Apr. 2009).

126. Kim, J.-S. *et al.* Performance Optimization of Polymer Solar Cells Using Electrostatically Sprayed Photoactive Layers. *Adv. Funct. Mater.* **20,** 3538–3546. ISSN: 1616301X (Oct. 2010).

127. Shao, M. *et al.* High-performance organic field-effect transistors with dielectric and active layers printed sequentially by ultrasonic spraying. *J. Mater. Chem. C* **1,** 4384. ISSN: 2050-7526 (2013).

128. Steirer, K. X. *et al.* Ultrasonic spray deposition for production of organic solar cells. *Sol. Energy Mater. Sol. Cells* **93,** 447–453. ISSN: 09270248 (Apr. 2009).

129. Tait, J. G., Rand, B. P. & Heremans, P. Concurrently pumped ultrasonic spray coating for donor:acceptor and thickness optimization of organic solar cells. *Org. Electron.* **14,** 1002–1008. ISSN: 15661199 (Mar. 2013).

130. Ishikawa, T., Nakamura, M., Fujita, K. & Tsutsui, T. Preparation of organic bulk heterojunction photovoltaic cells by evaporative spray deposition from ultradilute solution. *Appl. Phys. Lett.* **84,** 2424. ISSN: 00036951 (2004).

131. Nie, W. *et al.* High efficiency organic solar cells with spray coated active layers comprised of a low band gap conjugated polymer. *Appl. Phys. Lett.* **100,** 083301. ISSN: 00036951 (2012).

132. Chen, H. Y. *et al.* Fast-grown interpenetrating network in poly(3-hexylthiophene): Methanofullerenes solar cells processed with additive. *J. Phys. Chem. C* **113,** 7946–7953. ISSN: 19327447 (2009).

133. Marrocchi, A., Lanari, D., Facchetti, A. & Vaccaro, L. Poly(3-hexylthiophene): synthetic methodologies and properties in bulk heterojunction solar cells. *Energy Environ. Sci.* **5,** 8457. ISSN: 1754-5692 (2012).

134. Scharber, M. C. *et al.* Design Rules for Donors in Bulk-Heterojunction Solar Cells—Towards 10% Energy-Conversion Efficiency. *Adv. Mater.* **18,** 789–794. ISSN: 0935-9648 (Mar. 2006).

135. Kitchen, B. *et al.* Tuning Open-Circuit Voltage in Organic Solar Cells with Molecular Orientation. *ACS Appl. Mater. Interfaces* **7,** 13208–16. ISSN: 1944-8252 (June 2015).

136. Giridharagopal, R. & Ginger, D. S. Characterizing Morphology in Bulk Heterojunction Organic Photovoltaic Systems. *J. Phys. Chem. Lett.* **1,** 1160–1169. ISSN: 1948-7185 (2010).

137. Arias, A. C. *et al.* Vertically segregated polymer-blend photovoltaic thin-film structures through surface-mediated solution processing. *Appl. Phys. Lett.* **80,** 1695–1697. ISSN: 00036951 (2002).

138. Snaith, H. J., Greenham, N. C. & Friend, R. H. The origin of collected charge and open-circuit voltage in blended polyfluorene photovoltaic devices. *Adv. Mater.* **16,** 1640–1645. ISSN: 09359648 (2004).

139. Xue, J., Rand, B. P., Uchida, S. & Forrest, S. R. A Hybrid Planar-Mixed Molecular Heterojunction Photovoltaic Cell. *Adv. Mater.* **17,** 66–71. ISSN: 0935-9648 (2005).

140. Bannock, J. H. *et al.* Continuous Synthesis of Device-Grade Semiconducting Polymers in Droplet-Based Microreactors. *Adv. Funct. Mater.* **23,** 2123–2129. ISSN: 1616301X (May 2013).

141. Bannock, J. H., Phillips, T. W., Nightingale, A. M. & DeMello, J. C. Microscale separation of immiscible liquids using a porous capillary. *Anal. Methods* **5,** 4991. ISSN: 1759-9660 (2013).

7 Appendix 1: Molecular weight distribution

Molecular weight distributions of the four separate batches of P3HT used in this thesis for drop-casting and spray-coating. P3HT:PCBM bulk heterojunction device-grade films from o-xylene were fabricated from the 90K sample.

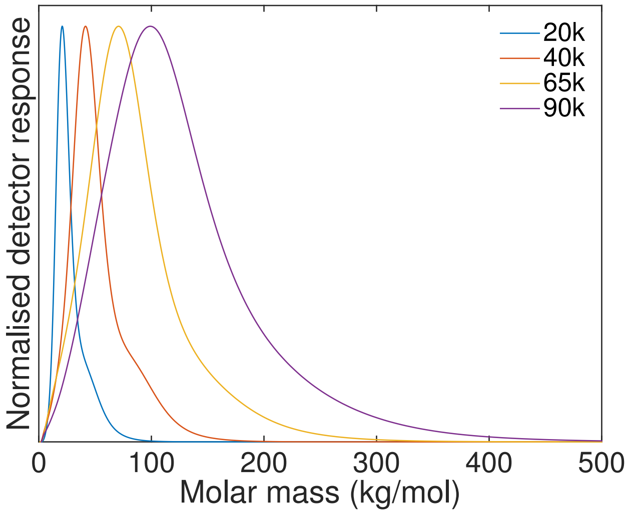

Figure 7.1: Series of RI-SEC chromatograms for the various molecular weights of P3HT used in this thesis.

8 Appendix 2: Arduino code for spray automation

This appendix describes the Arduino scripts used to run the spray-deposition rig. Some of the code described here is adapted (where mentioned) from standard libraries, which are freely available online.

Three Arduinos are used in the spray automation process to provide sufficient digitals pins to connect to the various pieces of rig hardware and to separate the mains power supply to the hotplate from the other electronic components. The main controller (an Arduino Yun) controls the stepper motors and the actuator responsible for the $x - y - z$ motion of the nozzle, and the mass flow controller. It also transmits signals to and receives signals from the two other Arduinos (Uno) used to control the hotplate, a display and a dual rate syringe pump.

8.1 Main controller: Arduino Yun

Figure 8.1 shows how the Arduino Yun is connected to the electronic components responsible for the motion of the nozzle.

```
//Rig Routine 1

#include <AccelStepper.h>
#include <SoftwareSerial.h>

// RX, TX
```

8 Appendix 2: Arduino code for spray automation

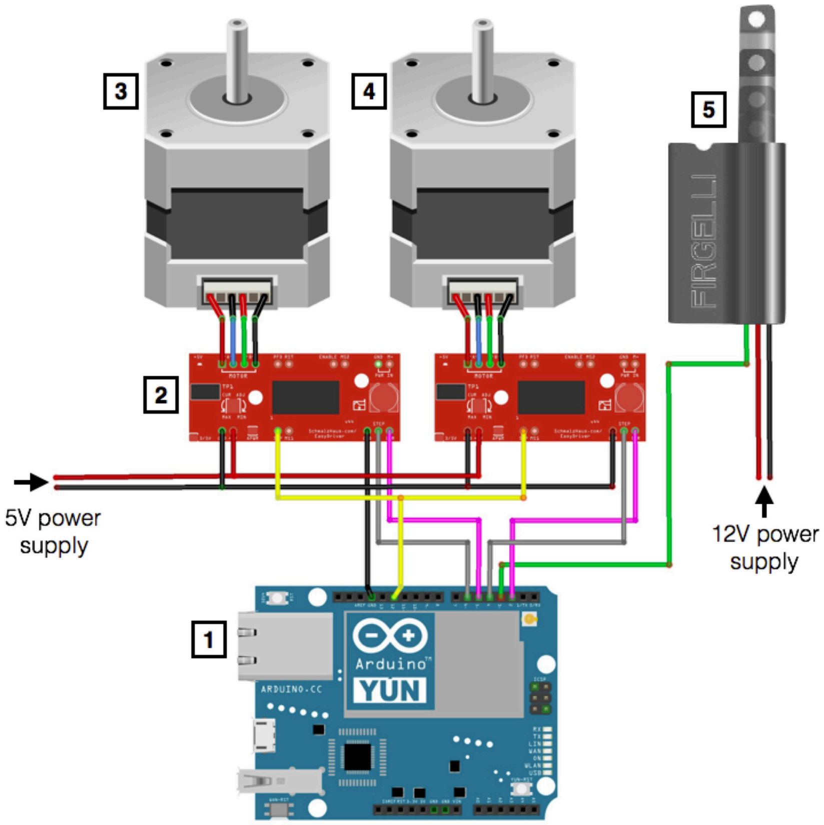

Figure 8.1: Schematic showing the electrical connections between the Arduino Yun and the motors responsible for the motion of the spray nozzle. [1] Arduino Yun. [2] EasyDriver, stepper motor drivers (Sprakfun). [3] Stepper motor responsible for motion along the *x*-axis. [4] Stepper motor responsible for motion along the *y*-axis. [5] Linear actuator (Firgelli) responsible for motion along the *z*-axis (RobotShop).

```
SoftwareSerial syringePump(9,7);
SoftwareSerial hotPlate(11, 13);
SoftwareSerial MFC(10, 8);

AccelStepper stepper_y(1, 2, 4);
AccelStepper stepper_x(1, 5, 6);

//motor positions
int pos1 = 3200;
int pos2 = 0;
int pos3 = -5600;
int pos4 = -900;
int pos5 = -4300;
long lastposition =0;
```

```
//long x = −100;
long y = 200;

//MFC variables
char *outputCharArray;
String commandString;

//motor sleep
int SLEEP = 12;

void setup() {

  syringePump.begin(9600);
  hotPlate.begin(9600);
  MFC.begin(9600);
  Serial.begin(9600);
  hotPlate.listen();

  //move actuator to start position
  analogWrite(3,0);
  delay(10000);
  pinMode(SLEEP, 12);
  digitalWrite(SLEEP, HIGH);

  //Set syringe diameter
  syringePump.print(”DA15.9”);
  delay(100);
  syringePump.print(”DB15.9”);
  delay(100);

  //Set flow rate and units
  //Units are one of Meaning
  //
  //UM  l /mn
  //
  //UH  l /hr
  //
  //MM ml/mn
```

```
  //
  //MH ml/hr

  syringePump.print("FA200UM");
  delay(100);
  syringePump.print("FB0UM");
  delay(100);

  //Set motor speeds
  stepper_y.setMaxSpeed(300);
  stepper_y.setAcceleration(50000);
  stepper_x.setMaxSpeed(500);
  stepper_x.setAcceleration(10000);

  //motor sleep
  digitalWrite(SLEEP, LOW);

  //set up MFC
  commandString = "!Gasi7";  //1 Argon, 7 Nitrogen
  Talk2MFC(commandString);
  delay(10);
  commandString = "!Fscl100";
  Talk2MFC(commandString);
  delay(10);
//  commandString = "!Unts";
//  Talk2MFC(commandString);

  //set height
  analogWrite(3,150);
  //delay(1000);

}

void loop() {

  //hotplate variables
  double temp = 20.00;
  double annealTemp = 20.00;
```

```
String realTemp; // do not change
long waitTime;
long warmupTime = 30000; //ten minutes
long interruptTime = 30000; //one minute
long annealTime = 1200000; // 20 minutes

int i = 1; // do not change, layer counter

int layerNo = 1; //number of sprayed layers

//warm-up hotplate
hotPlate.print(temp);
waitTime = warmupTime;
hotplateWait(waitTime, realTemp);


for ( ; i <= layerNo; i++)
  {
    //MFC on
    commandString = "!Setr20";
    Talk2MFC(commandString);
    delay(100);

    //syringe pump on
    syringePump.print("R");
    delay(100);
    syringePump.print("R");

    delay(5000);

    rasterMe();

    //pump off
    syringePump.print("S");
    delay(100);

    //MFC off
    commandString = "!Setr0";
```

```
      Talk2MFC(commandString);

      endPos();

      //resume constant temperature
      waitTime = interruptTime;
      hotplateWait(waitTime, realTemp); //warm-up hotplate
    }

  //move actuator to rest position
  analogWrite(3,0);
  delay(10000);

  //Anneal time
  hotPlate.print(annealTemp);
  waitTime = annealTime;
  hotplateWait(waitTime, realTemp);
  if (hotPlate.available()){hotPlate.read();}

//void loop close
}

void rasterMe(){

  int x = -100;
  int y = -2800;

  digitalWrite(SLEEP, HIGH);
  delay(100);

  while(x > -2000){

  stepper_y.moveTo(pos1);
  while(stepper_y.distanceToGo() != 0){
  stepper_y.run();}

//  Serial.print(stepper_x.currentPosition());
//  Serial.print('\t');
```

```
//  Serial.println(stepper_y.currentPosition());

  stepper_x.moveTo(pos4+x);
  while(stepper_x.distanceToGo() != 0){
  stepper_x.run();}

//  Serial.print(stepper_x.currentPosition());
//  Serial.print('\t');
//  Serial.println(stepper_y.currentPosition());

  stepper_y.moveTo(pos2);
  while(stepper_y.distanceToGo() != 0){
  stepper_y.run();}

//  Serial.print(stepper_x.currentPosition());
//  Serial.print('\t');
//  Serial.println(stepper_y.currentPosition());

  stepper_x.moveTo(pos4+x-100);
  while(stepper_x.distanceToGo() != 0){
  stepper_x.run();}
//
//  Serial.print(stepper_x.currentPosition());
//  Serial.print('\t');
//  Serial.println(stepper_y.currentPosition());

  x = x - 200;

  }

  digitalWrite(SLEEP, LOW);
  delay(100);

}

void endPos(){

  digitalWrite(SLEEP, HIGH);
```

```
  delay(100);

  stepper_y.moveTo(pos1);
  while(stepper_y.distanceToGo() != 0){
  stepper_y.run();}

  stepper_x.moveTo(pos2);
  while(stepper_x.distanceToGo() != 0){
  stepper_x.run();}

  stepper_y.moveTo(pos2);
  while(stepper_y.distanceToGo() != 0){
  stepper_y.run();}

  digitalWrite(SLEEP, LOW);
  delay(100);
}

void queryHotplate(String &H)
  {
    //Serial.println("function");
    if (hotPlate.available())
      {
        H = "";
        char d = hotPlate.read();
        delay(1);
        if (d == '?')
          {
            while (hotPlate.available())
                {
                  char d = hotPlate.read();
                  delay(10);
                  H +=d;
                 }
          }

      }
  }
```

```
void hotplateWait(long waitTime, String realTemp)
  {
    long startTime = millis();
    long duration = (millis() - startTime);

    while(duration < waitTime)
      {
        queryHotplate(realTemp);
        syringePump.print("?");
        syringePump.print(realTemp);
        Serial.println(realTemp);
        delay(10);
        Serial.print("\t");
        duration = millis() - startTime;
//        syringePump.print(duration);
        Serial.println(duration);
        delay(1000);
      }
      syringePump.write("\r\n");
  }



 void Talk2MFC(String commandString){

        unsigned int LRC = {0x00};
        unsigned int inputArray[20];
        int stringLength = commandString.length();
        unsigned int dummy;

        //convert inputString to array of integers
        for (int i = 0; i < commandString.length(); i++)
        {
                char x = commandString.charAt(i);
                inputArray[i] = int(x);
```

```
    }

    //easy integer to ASCII conversion
    char digits[19] = {'0', '1', '2', '3', '4', '5', '6', '7',
         '8','9', 'A', 'B', 'C', 'D', 'E', 'F'};

    //sum up individual bytes
    for (int i = 0; i < stringLength; i++)
    {LRC = inputArray[i]+LRC;}
    LRC = ~LRC; //calculate 1s complement
    LRC += 1; //convert to 2s complement
    LRC = LRC & 0xFF; //retain lowest byte of LRC only

    //add LRC to command;
    dummy = (LRC & 0xF0)/16; // calculate highest four bits of LRC
    commandString += digits[dummy];
    dummy = (LRC & 0x0F); //calculate lowest four bits of LRC
    commandString += digits[dummy];
    //convert to char array
    char* outputCharArray = (char *)commandString.c_str();

    //Send and Receive
    Serial.print("Evaluated as:");
    Serial.println(outputCharArray);
    MFC.write(outputCharArray);
    MFC.write("\r\n");
    delay(1000);

   if (MFC.available()){
        String msg = "";
        for (int i=0; i<100; i++) {
             char ch = MFC.read();
             msg += ch;
             delay(30);
        }
      Serial.println(msg);
  }
}
```

8.2 Secondary controller: Arduino Uno

The secondary controller (Arduino Uno) controls the syringe pumps and the display panel, which shows the temperature of the hotplate. Figure 8.2 shows the electrical connections between the Arduino Uno, the syringe pump, and the display, as well as the electrical connections between the Arduino Yun and mass flow controller. It also shows the electrical connections used for communicating between the main and secondary controllers.

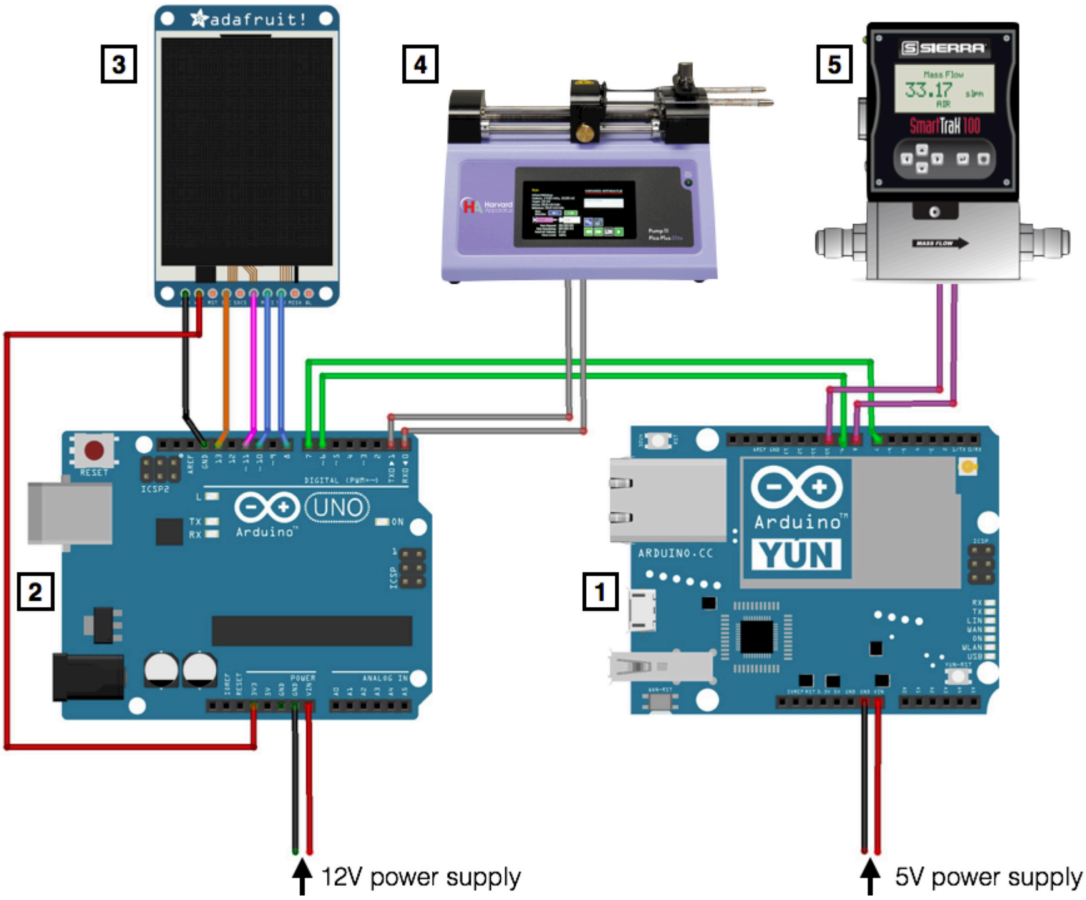

Figure 8.2: Schematic showing the electrical connections associated with the secondary controller. [1] Arduino Yun. [2] Secondary controller (Arduino uno). [3] 1.8″ Colour TFT LCD display (Adafruit). [4] Dual rate syringe pump (Harvard Apparatus). [5] Mass flow controller (Sierra).

```
//syringePumpSlave
#include <SoftwareSerial.h>
// RX, TX
SoftwareSerial Yun(6,7);
```

```
//Screen
//Use these pins for the shield!
#define sclk 13
#define mosi 11
#define cs   10
#define dc   8
#define rst  0

#include <Adafruit_GFX.h>    // Core graphics library
#include <Adafruit_ST7735.h> // Hardware-specific library
#include <SPI.h>

#if defined(__SAM3X8E__)
    #undef __FlashStringHelper::F(string_literal)
    #define F(string_literal) string_literal
#endif



Adafruit_ST7735 tft = Adafruit_ST7735(cs, dc, mosi, sclk, rst);
float p = 3.1415926;
String message;

void setup() {

   Serial.begin(9600, SERIAL_8N2);
   Yun.begin(9600);

   Serial.write("01MODPRO\r\n");
   delay(100);
   Serial.write("01PARON\r\n");
   delay(100);
   Serial.write("01DIRINF\r\n");
   delay(100);

// setup screen
  tft.initR(INITR_GREENTAB); // initialize a ST7735R chip, green tab
  uint16_t time = millis();
```

```
  tft.fillScreen(ST7735_BLACK);
  time = millis() - time;

  tft.setRotation(3);
  tft.setTextWrap(false);
  tft.fillScreen(ST7735_BLACK);
  tft.setCursor(0, 30);
  tft.setTextColor(ST7735_WHITE);
  tft.setTextSize(2);

}

void loop() {

  String temperature;

    if (Yun.available())
      {
      char i = Yun.read();
      delay(1);

      switch(i){

    case 'R':
    GoGoPump();
    break;

    case 'S':
    achtung();
    break;

    case 'F':
    flow();
    break;

    case 'D':
    diameter();
    break;
```

```
    case '?':
    updateTemp(temperature);
    updateScreen(temperature);
    break;

//      case 'd':
//      updateTime(timer);
//      process = "HEATING";
//      updateScreen(temperature, timer);
//      delay(1000);
//      break;




  }

    }}

    void GoGoPump(){
      Serial.write("01RUN\r\n");
      delay(10);
    }

    void achtung(){
      Serial.write("01STP\r\n");
      delay(10);
      Serial.write("01DIRREV\r\n");
      delay(10);
      Serial.write("01RUN\r\n");
      delay(2000);
      Serial.write("01STP\r\n");
      delay(10);
      Serial.write("01DIRINF\r\n");
      delay(10);
```

```
    }

    void flow(){
      Serial.write("01RAT");
      char d = Yun.read();
      delay(1);
      if (d == 'A'){
        Serial.write("A");
      }
      else{
        Serial.write("B");
      }
      while (Yun.available()){
      char m = Yun.read();
      Serial.write(m);
        delay(1);
          }
          Serial.write("\r\n");
          delay(100);
    }


//Query flow rate
void queryFlowRate()
    {
      Serial.write("01RAT");
      char d = Yun.read();
      delay(1);
      if (d == 'A'){
        Serial.write("A");
      }
      else{
        Serial.write("B");
      }
        delay(10);
        Serial.write("\r\n");
        delay(10);
//          String D = "";
```

```
//          while (Serial.available())
//               {
//                 char m = Serial.read();
//                 D += m;
//                 delay(1);
//                }
//          delay(1);
//          Yun.print(D);
//          delay(10);
     }


void diameter()
        {
         Serial.write("01DIA");
         char d = Yun.read();
         delay(1);
                if (d == 'A'){
         Serial.write("A");
         delay(1);
       }
       else{
         Serial.write("B");
         delay(1);
       }
          while (Yun.available()){
          Serial.write(Yun.read());
           delay(1);
           }
           Serial.write("\r\n");
          delay(100);
        }

void updateTemp(String &H)
  {
    H = "";
    while (Yun.available())
          {
```

```
            char d = Yun.read();
            Serial.print(d);
            delay(10);
           H +=d;
            }

        H = H.substring(0,5);



//         Serial.println(H);
//         tft.println(H);
//        delay(1000);
  }

void updateTime(String &T)
  {
    T = "";
    while (Yun.available())
          {
            char d = Yun.read();
            Serial.print(d);
            delay(10);
            T +=d;
            }
  }

void updateScreen(String temperature)
  {
    tft.fillScreen(ST7735_BLACK);
    tft.setCursor(0, 30);
    tft.print(temperature);
    tft.print(char(248));
    tft.println("C");

  }
```

8.3 Hotplate controller: Arduino Uno

The hotplate controller (Arduino Uno) controls the temperature of the hotplate using a thermocouple, the mains power supply and a solid state relay. The electrical connections between the Arduino and the components are shown in figure 8.3.

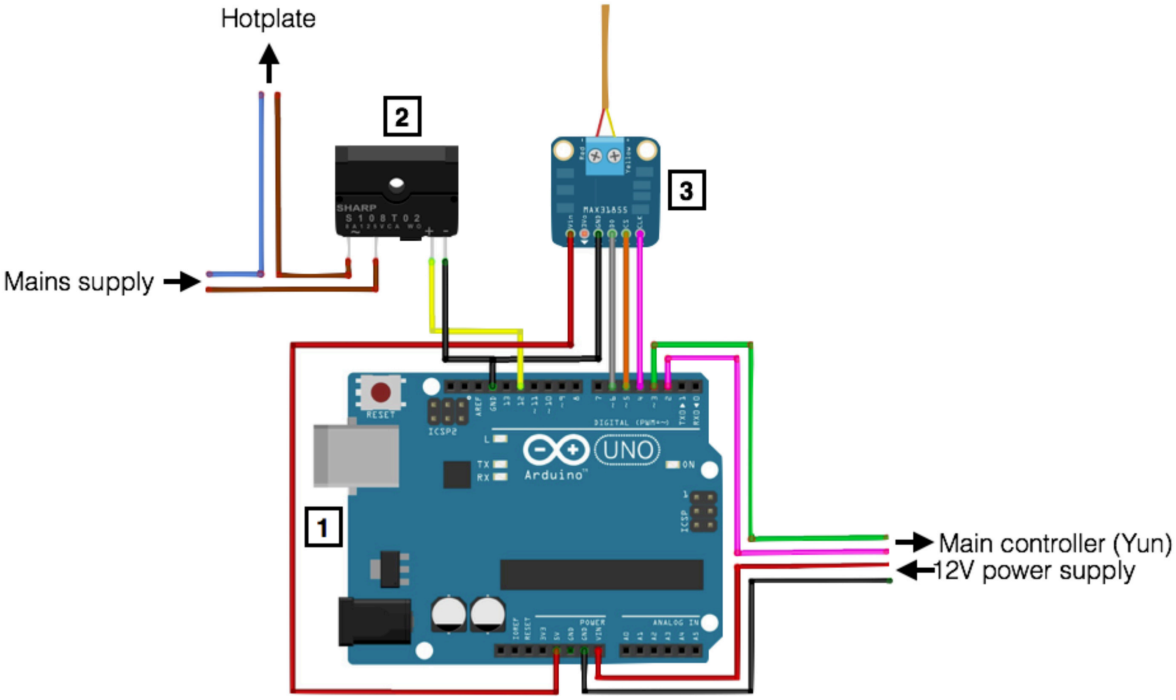

Figure 8.3: Schematic showing the electrical connections between the Arduino Uno and the hotplate apparatus. [1] Arduino Uno. [2] Solid state relay. [3] Thermocouple Amplifier MAX31855 (Adafruit).

```
#include <PID_v1.h>
#define RelayPin 12
#include "Adafruit_MAX31855.h"
#include <SoftwareSerial.h>
// RX, TX
SoftwareSerial Yun(10, 9);


//Define Variables we'll be connecting to
double Setpoint, Input, Output;
int thermoDO = 3;
int thermoCS = 4;
int thermoCLK = 5;
```

```
int i = 1;
//pinMode(12, OUTPUT);

//Specify the links and initial tuning parameters
PID myPID(&Input, &Output, &Setpoint,18,9.5,0.24, DIRECT);

Adafruit_MAX31855 thermocouple(thermoCLK, thermoCS, thermoDO);

int WindowSize = 5000;
unsigned long windowStartTime;
void setup()
{

 Yun.begin(9600);

  windowStartTime = millis();

  //initialize the variables we're linked to
  Setpoint = 20;

  //tell the PID to range between 0 and the full window size
  myPID.SetOutputLimits(0, WindowSize);
  myPID.SetSampleTime(9000);

  //turn the PID on
  myPID.SetMode(AUTOMATIC);

  Serial.begin(9600);

  Serial.println("MAX31855 test");
  // wait for MAX chip to stabilize
  delay(500);

  pinMode(RelayPin,OUTPUT);

}

void loop()
```

```
{

  Input = thermocouple.readCelsius();
  if(Input != Input){
  }
  else{
  myPID.Compute();

  /**********************************************
   * turn the output pin on/off based on pid output
   **********************************************/
  unsigned long now = millis();
  if(now - windowStartTime>WindowSize)
  { //time to shift the Relay Window
    windowStartTime += WindowSize;
  }
  if(Output > now - windowStartTime)
  {digitalWrite(RelayPin,HIGH);}
  else {digitalWrite(RelayPin,LOW);}

  if (Yun.available()){
   // read it all
  char msg[100] = "";
  int i = 0;
  while (Yun.available()) {
    char ch = Yun.read();
    //Serial.print(ch);
    //Serial.print("-");
    msg[i] = ch;
    delay(30);
    i++;
  }
    Setpoint = atof(msg);
//      Serial.println(msg);
    Serial.println(Setpoint);
//      Serial.print("\t");
    //Serial.println(msg.toInt());
    //Setpoint = (double) msg.toInt();
```

```
    //Serial.print("Setpoint:");
    //Serial.println(Setpoint);
    }
//
//  //Serial.print("INPUT:");
  Serial.print(Input);
//  Serial.print("\t");
//  //Serial.print("OUTPUT:");
//  Serial.print(Output);
//  Serial.print("\t");
//  //Serial.print("RELAY:");
//  Serial.print(digitalRead(RelayPin));
//  Serial.println("\t");

    Yun.print("?");
    Yun.print(Input);
    delay(1000);

//  }

}}
```